Mantle-Melting at High Pressure - Experimental Constraints on Magma Ocean Differentiation

Von der Fakultät für Biologie, Chemie und Geowissenschaften
der Universität Bayreuth

zur Erlangung der Würde eines
Doktors der Naturwissenschaften
- Dr. rer. nat. -

genehmigte Dissertation

vorgelegt von
Diplom-Mineraloge Christian Liebske
aus Hameln

Bayreuth, Mai 2005

Die vorliegende Arbeit wurde in der Zeit von August 2001 bis Januar 2005 am Bayerischen Geoinstitut der Universität Bayreuth angefertigt.

Vollständiger Abdruck der von der Fakultät für Biologie, Chemie und Geowissenschaften der Universität Bayreuth genehmigten Dissertation zur Erlangung des akademischen Grades eines Doktors der Naturwissenschaften (Dr. rer. nat.).

Prüfungsausschuss:
Prof. F. Seifert, Universität Bayreuth (Vorsitzender)
Prof. D. C. Rubie, Universität Bayreuth (1. Gutachter)
Prof. H. Keppler, Universität Bayreuth (2. Gutachter)
Prof. J. Breu, Universität Bayreuth
Prof. S. Peiffer, Universität Bayreuth

Datum der Einreichung der Dissertation: 14. Januar 2005
Datum des wissenschaftlichen Kolloquiums: 11. Mai 2005

Hiermit erkläre ich, daß ich die vorliegende Arbeit selbständig verfaßt und keine anderen als die von mir angegebenen Quellen und Hilfsmittel benutzt habe. Ferner erkläre ich, daß ich nicht anderweitig mit oder ohne Erfolg versucht habe eine Dissertation einzureichen. Ich habe keine gleichartige Doktorprüfung an einer anderen Hochschule endgültig nicht bestanden.

Bayreuth, Mai 2005

Mantle-Melting at High Pressure - Experimental Constraints on Magma Ocean Differentiation

Von der Fakultät für Biologie, Chemie und Geowissenschaften
der Universität Bayreuth

zur Erlangung der Würde eines
Doktors der Naturwissenschaften
- Dr. rer. nat. -

genehmigte Dissertation

vorgelegt von
Diplom-Mineraloge Christian Liebske
aus Hameln

Bayreuth, Mai 2005

Contents

Abstract

In this study geochemical processes and geophysical parameters have been investigated that are relevant to the crystallisation of a deep magma ocean, that likely existed in the final stages of the Earth's accretion.

The melting relations of potential magma ocean compositions, such as peridotitic and chondritic bulk compositions, have been investigated using multianvil apparatus at pressures of 25-26 GPa and temperatures ranging from ∼2100°C to ∼2400°C. Compositional effects on the melting relations have been investigated by varying bulk Mg/Si and Mg/(Mg+Fe) ratios (the latter is denoted as Mg-number, Mg#). At 26 GPa, peridotite liquids show a crystallisation sequence of ferropericlase (Fp) followed down temperature by Mg-silicate perovskite (MgPv) + Fp, which is in contrast to the sequence of MgPv followed by MgPv + Fp in chondritic composition. The melting relations along the different compositions depend primarily on the bulk Mg/Si ratio and not on the Mg#. Melting relations and eutectic compositions have been studied in the simple binary MgO-SiO_2 system between 10 and 26 GPa using the multianvil apparatus. Combining the new results with previously published data shows that the eutectic composition between Mg_2SiO_4 and $MgSiO_3$ phases, up to ∼20 GPa, moves towards MgO with increasing pressure. Between ∼20 and ∼23 GPa the direction in which the eutectic is moving with pressure reverses. At higher pressures, however, this trend is again reversed and the eutectic composition moves towards MgO. The multiple changes in the direction in which the eutectic is moving as a function of pressure explains qualitatively the differences in liquidus phase relations in the more complex peridotite and chondrite compositions.

The effect of bulk chemical composition on the partitioning of major, minor and trace elements between MgPv and coexisting silicate melts has been investigated by electron microprobe analysis and secondary ion mass spectrometry. MgPv/melt partition coefficients for Mg (D_{Mg}) and Si (D_{Si}) are related to the melt Mg/Si ratio such that

D_{Si} becomes lower than D_{Mg} at chondritic Mg/Si melt ratios. This shows that the Earth's upper mantle Mg/Si ratio is unlikely to be derived from chondrites as a result of MgPv fractionation. Partition coefficients of tri- and tetravalent elements increase with increasing Al concentration of MgPv. A crystal chemical model indicates that Al^{3+} substitutes predominantly onto the Si-site in MgPv, but most other elements substitute onto the Mg-site. This is consistent with a charge-compensating coupled cation-substitution mechanism. A crystal fractionation model, based on upper mantle refractory lithophile element ratios (Ca/Sc and Yb/Ca), is developed to constrain the amount of MgPv and Ca-silicate perovskite (CaPv) that could have fractionated during a Hadean magma ocean event and could still be present as a chemically distinct heterogeneity in the lower mantle today. It is shown that a fractionated crystal pile composed of 96% MgPv and 4% CaPv could comprise up to 13 wt% of the entire mantle.

$Fe^{3+}/\sum Fe$ ratios have been determined for MgPv, crystallised at temperatures slightly below and above the peridotite solidus, using Mössbauer and electron-energy-loss spectroscopy. The amount of Fe^{3+} in MgPv is positively correlated to the Al concentration of this phase. This is consistent with the aforementioned charge-compensating coupled substitution mechanism. In the recovered samples, homogeneously distributed Fe-rich metal, mostly on the sub-micron scale, has been observed on grain boundaries, although the MgPv has $Fe^{3+}/\sum Fe$ ratios between 0.2 and ~0.5. This suggests that the amount of Fe^{3+} in MgPv is independent of the oxygen fugacity and that the presence of Fe-rich metal in the samples is the result of the disproportionation of FeO to Fe_2O_3 and Fe-metal. This has many possible implications for the mantle oxidation state and the mantle geochemistry during magma ocean solidification.

The viscosity of peridotite liquid, as an analogue for a magma ocean composition, has been investigated at high pressure using in-situ falling sphere viscometry, by combining a multianvil technique with synchrotron radiation. A newly developed capsule

has been used to improve the precision of viscosity measurements performed on low viscosity liquids. Experiments have been performed between 2.5 and 13 GPa at temperatures between 2043 to 2523 K. Measured viscosities range from 0.018 (±0.003) to 0.13 (±0.01) Pa s. Up to 9 GPa the data indicate an isothermal increase in viscosity with increasing pressure but viscosity then decreases between 9 and 13 GPa at constant temperature. The observed change in the pressure dependence of the viscosity is probably associated with structural changes in the liquid upon compression. The new high-pressure results are combined with 1-bar viscosity data for peridotite liquid (Dingwell et al. 2004), and a non-Arrhenian Vogel-Fulcher-Tamman (VFT) equation, to which an empirical pressure-dependent term has been added, is presented to parameterise all experimental data. This approach reproduces measured viscosities excellently with an average deviation of 0.08 $\log_{10}$-units. The model can be used to calculate magma ocean viscosities to depths of ∼400 km. When likely magma ocean temperatures are considered, the calculated viscosities down to transition zone pressure are extremely low and comparable to water at room temperature.

The results of the different aspects of this study have been used to investigate magma ocean crystallisation and its effect on the geochemistry and the evolution of the Earth's mantle.

Zusammenfassung

In der vorliegenden Arbeit wurden verschiedene geochemische Prozesse und ein geophysikalischer Parameter untersucht, die relevant für die Kristallisation eines Magmaozeans sind, der mit großer Wahrscheinlichkeit während der späteren Akkretionsphase der Erde existierte.

Zunächst wurden die Schmelzbeziehungen von möglichen Magmaozeanzusammensetzungen, wie z.B. peridotitische und chondritische Zusammensetzungen, in Vielstempelpressen bei Drücken von 25-26 GPa und Temperaturen zwischen 2100 und 2400°C untersucht. Um Effekte der chemischen Zusammensetzung untersuchen zu können, wurden Mg/Si und Mg/(Mg+Fe) Verhältnisse (das letztere wird als Mg-Nummer, Mg#, bezeichnet) in den Ausganszusammensetzungen variiert. Bei 26 GPa kristallisierten peridotitische Schmelzen in der Reihenfolge Ferroperiklas (Fp), gefolgt bei niedrigeren Temperaturen von Mg-Silikat-Perowskit (MgPv) plus Fp. Dies steht im Kontrast zu einer Sequenz von MgPv gefolgt von MgPv + Fp, die in chondritischen Zusammensetzungen beobachtet wurde. Die Schmelzphasenbeziehungen hängen in erster Linie vom Mg/Si Verhältnis ab und nicht von der Mg#. Die Schmelzbeziehungen und eutektischen Zusammensetzungen wurden im binären System MgO-SiO_2 zwischen 10 und 26 GPa mittels Vielstempelpressen untersucht. Der Vergleich von diesen neuen experimentellen Daten mit Resultaten aus der Literatur zeigt, daß sich die eutektische Zusammensetzung zwischen den Mg_2SiO_4 und $MgSiO_3$ Phasen bis ∼20 GPa in Richtung von MgO verschiebt. Zwischen ∼20 und ∼23 GPa ändert sich diese Richtung, und das Eutektikum verschiebt sich mit zunehmenden Druck in Richtung der $MgSiO_3$ Komponente. Bei höheren Drücken wird diese Richtungsänderung erneut umgekehrt und die eutektische Zusammensetzung verschiebt sich wieder zur MgO Komponente. Die mehrfachen Richtungsänderungen in der Verschiebung der eutektischen Zusammensetzung mit zunehmenden Druck beschreiben qualitativ die Schmelzphasenbeziehungen in den chemisch komplexeren peridotitischen und chondritischen Zusammensetzungen.

Der Effekt der chemischen Zusammensetzung auf die Verteilung von Haupt-, Neben- und Spurenelementen zwischen MgPv und koexistierenden silikatischen Schmelzen wurde untersucht. Die Proben wurden mit der Elektronenstrahlmikrosonde und Sekundär-Ionisations-Massenspektroskopie analysiert. Die Verteilungskoeffizienten zwischen MgPv und Schmelze für Mg (D_{Mg}) und Si (D_{Si}) sind abhängig vom Mg/Si Verhältnis der Schmelze, sodaß D_{Si} bei chondritischen Mg/Si Verhältnissen kleiner wird als D_{Mg}. Das bedeuted, daß das heutige Mg/Si Verhältnis des oberen Erdmantels nicht durch Fraktionierung von MgPv von einer chondritischen Magmaozeanzusammensetzung entstanden sein kann. Die Verteilungskoeffizienten von drei- und vierwertigen Elementen werden größer mit zunehmender Al-Konzentration im MgPv. Ein kristallchemisches Modell zeigt, daß Al^{3+} überwiegend auf die Si-Position im MgPv substituiert, andere Elemente jedoch vorwiegend auf die Mg-Position. Dies ist konsistent mit einem ladungsausgleichenden, gekoppelten Kationenaustausch. Ein Kristallfraktionierungsmodell, das auf Verhältnissen von refraktären lithophilen Elementen (Ca/Sc und Yb/Ca) basiert, wird angewandt, um die Menge von MgPv und Ca-Silikat-Perowskit (CaPv) zu bestimmen, die möglicherweise während der Kristallisation des Magmaozeans fraktionierte und ein chemisches Reservoir bildete, das noch immer im unteren Erdmantel existieren könnte. Eine solche Kristallakkumulation könnte bis zu 13 Gew% des gesamten Erdmantels ausmachen, wenn es aus 96% MgPv und 4% CaPv besteht.

$Fe^{3+}/\sum Fe$ Verhältnisse von Mg-silikat Perowskiten, die bei Temperaturen nahe dem Peridotit-Solidus kristallisierten, wurden mittels Mösserbauer- und Elektronen-Energie-Verlust Spektroskopie bestimmt. Der Gehalt an Fe^{3+} im MgPv steigt mit zunehemder Konzentration von Al in diesem Mineral, was im Einklang mit dem bereits erwähnten gekoppelten Kationaustausch ist. In den Versuchsprodukten wurde an den Korngrenzen gleichmäßig verteiltes Fe-reiches Metall mit durchschnittlichen Korngrößen im Submikrometerbereich entdeckt, obwohl die Mg-Silikat Perowskite

$Fe^{3+}/\sum Fe$ Verhältnisse von 0.2 bis ∼0.5 aufweisen. Dies deutet darauf hin, daß der Gehalt an Fe^{3+} im MgPv unabhängig von der Sauerstofffugazität ist, und daß die Bildung von Fe-reichem Metall in den Proben auf die Disproportionierung von FeO zu Fe_2O_3 und metallischem Fe zurückzuführen ist. Die Kristallisation eines Magmaozeans im Stabilitätsfeld vom MgPv hat möglicherweise wichtige Implikationen für den Oxidationszustand und die Geochemie des Erdmantels.

Die Viskosität von geschmolzenem Peridotit als ein Analogmaterial für eine Magmaozeanzusammensetzung wurde bei hohen Drücken mit einer 'in-situ' Methode und der Kombination einer Vielstempelpressentechnik mit Synchrotron-Strahlung gemessen. Eine neu entwickelte Probenkapsel verbesserte hierbei die Präzision der gemessenen Viskositäten für niedrig-viskose Schmelzen. Die Experimente wurden bei Drücken von 2.5 bis 13 GPa und Temperaturen zwischen ∼1800 und ∼2250°C durchgeführt. Die gemessenen Viskositäten variieren von 0.018 (±0.003) bis 0.13 (±0.01) Pa s. Die Daten lassen darauf schließen, daß die Viskosität bei konstanter Temperatur bis zu 9 GPa mit wachsendem Druck ansteigt, jedoch zwischen 9 und 13 GPa bei isothermen Bedingungen abnimmt. Die Veränderung in der Druckabhängigkeit der Viskosität ist wahrscheinlich auf strukturelle Modifikationen in der Schmelze während der Kompression zurückzuführen. Die neuen Ergebnisse wurden mit Viskositätsdaten, die bei Umgebungsdruck gemessen wurden (Dingwell et al. 2004), kombiniert und ein empirisches Viskositätsmodell wurde verwendet, um die gemessenen Viskositätsdaten zu beschreiben. Dieses Modell reproduziert experimentell bestimmte Viskositäten mit einer durschnittlichen Abweichung von nur 0.08 $\log_{10}$-Einheiten. Das Modell kann dazu verwendet werden die Viskositäten eines Magmaozeans bis zu einer Tiefe von etwa 400 km zu berechnen. Bei den hohen Temperaturen, die möglicherweise in einem Magmaozean geherrscht haben, wären die Viskositäten bis zu Drücken der Übergangszone vergleichbar mit der Viskosität von Wasser bei Raumtemperatur.

Die Resultate der verschiedenen Untersuchungen dieser Arbeit werden verwendet, um

die Kristallisation eines Magmaozeans zu untersuchen, und um die Effekte auf die Goechemie des Erdmantels und seine Evolution zu verstehen.

Chapter 1

Introduction

1.1 The Structure of the Earth's Mantle

The structure of Earth's mantle has been investigated by research in the fields of geochemistry, seismology and experimental petrology. The mantle can be divided into concentric regions, which are distinguished by abrupt changes in seismic wave velocities caused by phase transitions of mineral phases at specific pressures (or depths). Xenoliths derived from depths of 100-200 km indicate that the upper mantle is predominately of peridotitic composition (see Table 1.1), which implies that the upper mantle is mainly composed of $(Mg, Fe)_2SiO_4$ olivine, ortho- and clinopyroxene ($(Mg, Fe)SiO_3$, $(Mg, Fe, Ca)SiO_3$) and an aluminous phase which, depending on the pressure, can be plagioclase, spinel or $(Mg, Fe, Ca)_3Al_2Si_3O_{12}$ garnet. A diagram indicating mineral proportions and phase transitions to lower mantle pressures is given in Figure 1.1.

The seismic discontinuity at 410 km or 13.5 GPa, which separates the upper mantle from the transition zone, is attributed to the phase transition of olivine to its high pressure polymporh wadsleyite (e.g. Katsura and Ito 1989, Morishima et al. 1994). Wadsleyite transforms within the transition zone at approximately 520 km to another $(Mg, Fe)_2SiO_4$ polymorph ringwoodite (e.g. Katsura and Ito 1989). The $CaSiO_3$ component of majoritic garnet exolves and forms Ca-silicate perovskite (CaPv) at 17-18

Table 1.1: Typical peridotite composition after McDonough and Sun (1995)

Compound	**Peridotite** (wt% oxides)
SiO_2	44.9
TiO_2	0.2
Al_2O_3	4.4
Cr_2O_3	0.4
FeO	8.0
MnO	0.1
MgO	37.7
CaO	3.5
NiO	0.4
Na_2O	0.2
total	100.0

GPa (Canil 1994). The sharp seismic discontinuity at 670 km defines the top of the lower mantle and is attributed to the transition of ringwoodite (Rwd) to $(Mg, Fe)SiO_3$ perovskite (referred to as Mg-silicate perovskite or MgPv) plus the oxide phase ferropericlase (Mg,Fe)O (Fp) (Ito and Takahashi 1989). This phase transition is accompanied by the dissolution of the Al_2O_3 component of majoritic garnet into MgPv (Wood 2000). A peridotitic lower mantle would consequently be composed of approximately 79 wt% aluminous MgPv, 16 wt% Fp and approximtely 5 wt% CaPv (Wood 2000). A detailed review of phase transitions and stable mineral phases in the Earth's mantle as a function of pressure can be found in Fei and Bertka (1999).

1.2 The Magma Ocean Hypothesis

Although knowledge about the present day structure of Earth's mantle has greatly improved over the last decades, the formation of the mantle and evolution over the entire history of the Earth is not well understood. Models for the formation of the

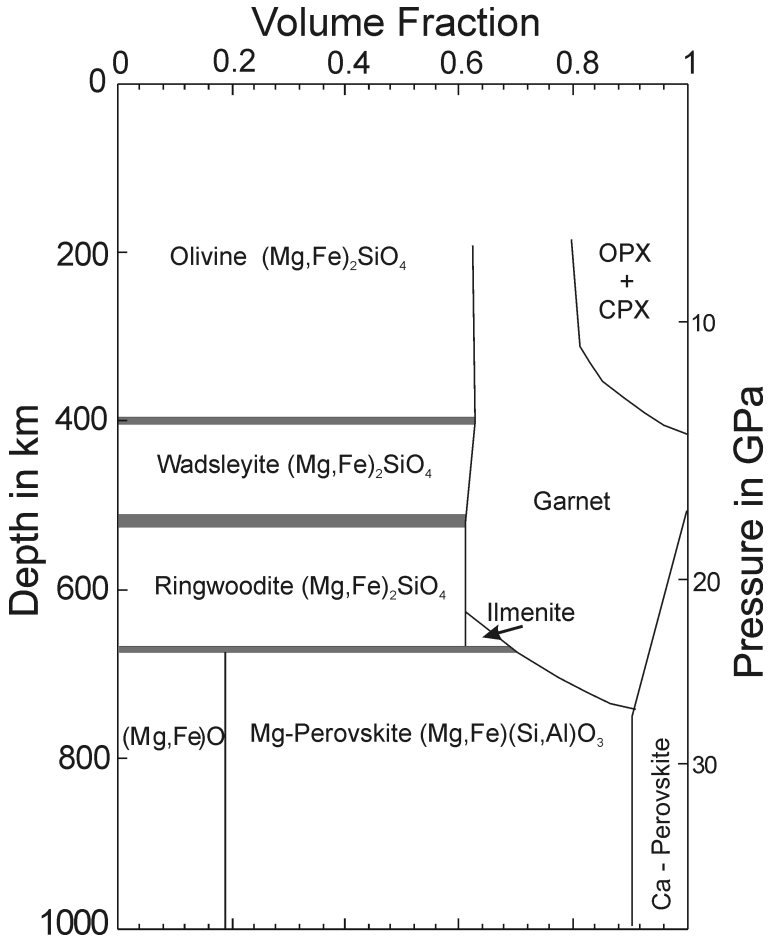

Figure 1.1: Schematic diagram showing the volume proportions of mantle minerals as a function of depth. The proportions are valid for a mantle of a homogeneous peridotitic chemical composition. Modified after Irifune (1994).

Earth propose a period of substantial melting of the planet during the later stages of accretion. Main supporting evidence for this is given by $^{182}Hf/^{182}W$ decay systematics, which indicate that core-formation ceased approximately 30 Ma after formation of the solar system (Kleine et al. 2002) and was therefore quite rapid. Tungsten isotope data also indicate that chondritic core-forming material in the later stages of accretion equilibrated to a significant extend with the silicate Earth (Kleine et al. 2004). Since transport properties and chemical equilibration mechanisms are orders of magnitude faster in the liquid state, both processes are only feasible under participation of sig-

nificant amounts of mantle melting and the formation of a magma ocean. The energy required for melting parts of the Earth most likely originated from kinetic energy released during the growth of the proto-Earth by impacts of numerous smaller asteroids or even small-planet sized bodies. In particular, the extremely high energies involved in a probable moon-forming 'giant impact' event would have most likely melted Earth's entire mantle (e.g. Melosh 1990, Tonks and Melosh 1993).

The concept of a terrestrial magma ocean is also supported by geochemical features of the upper mantle. Partition coefficients of moderately- and highly siderophile ('iron-loving') elements between core-forming liquids and silicate melts determined at ambient pressure suggest that such elements should have partitioned almost entirely into the Earth's core. The relatively high abundance of such elements observed in the upper mantle, however, can be explained if equilibrium between core-forming metal and silicate liquid took place at pressures corresponding to the top of the lower mantle, because experimentally determined metal/silicate partitioning coefficients reach appropriate values, that are consistent with the observed element abundances in the upper mantle (e.g. Li and Agee 1996, Righter and Drake 1997, Bouhifd and Jephcoat 2003).

1.3 Magma Ocean Crystallisation

Melting planet-forming material is a very efficient processes, that enabled chemical differentiation to occur throughout the entire history of the Earth, as it still takes place today, e.g. in volcanic eruptions. The existence of a deep terrestrial magma ocean during the Hadean (4.5-3.8 Ga before present) may have led to significant chemical differentiation and possibly stratification of the mantle by crystal fractionation

as envisaged in Figure 1.2. Assuming that a deep magma ocean existed implies that there are essentially three possibilities for the evolution of the Earth's mantle from the Hadean until the present day. Firstly, crystal fractionation took place and formed a chemically distinct reservoir that is still present in the mantle today and was thus not remixed with the overlying mantle by subsequent solid-state convection. Secondly, crystal fractionation took place but mantle convection rehomogenised the crystal accumulate and the overlying mantle either completely or to a large extend. Thirdly, the magma ocean crystallised without causing any significant amount of fractionation and thus without initial mantle differentiation. The third possibility could have occurred if i.e. crystals were suspended in the liquid due to turbulent convection of the magma ocean (e.g. Tonks and Melosh 1990, Solomatov and Stevenson 1993b, see section 1.5). In order to reconcile a number of geochemical and geophysical observations, it has been suggested that the Earth's lower mantle may contain a chemically distinct region below a depth of approximately 1600 km (Kellogg et al. 1999, van der Hilst and Karason 1999). The existence of this region was proposed in order to explain the common geochemical inference of an undegassed and undepleted mantle source region that may also be enriched in radiogenic heat producing elements. Fractional crystallisation of a magma ocean has been considered as one possible mechanism for the formation of such a reservoir. Information on the state of mantle differentiation during the Hadean has been derived from radiogenic isotope geochemistry. Although no rock samples from the Hadean are preserved, parent-daughter Sm-Nd relationships and Hf-Nd isotope systematics obtained from Archean rocks (3.8-2.5 Ga) support the hypothesis of early differentiation of the Earth's mantle (e.g. Galer and Goldstein 1991, Bowring and Housh

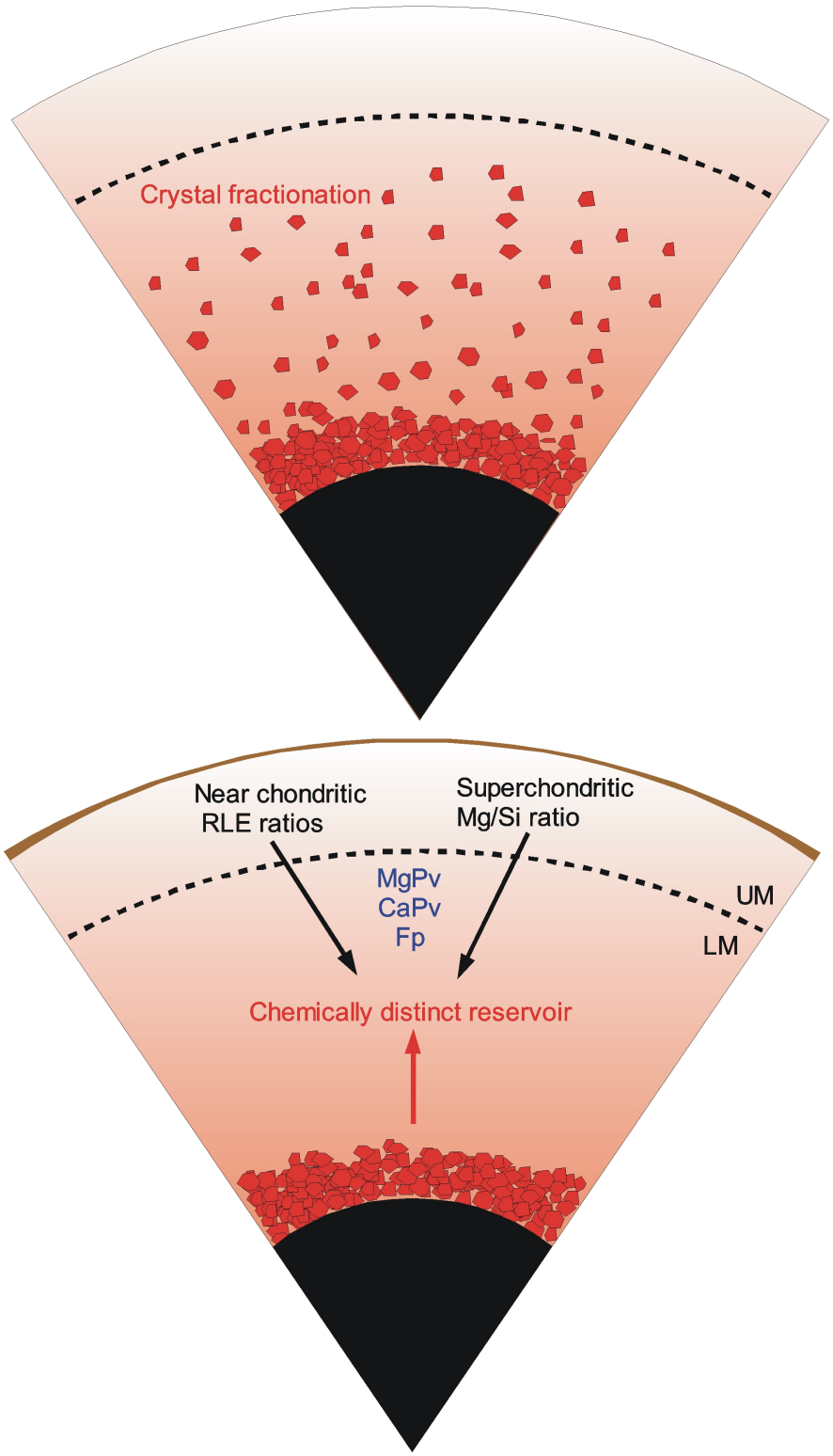

Figure 1.2: Possible process during magma ocean crystallisation. Crystal fractionation at lower mantle pressure takes place and results in the formation of a chemically distinct reservoir in the lower mantle. See text for details.

1995, Albarede et al. 2000, Boyet et al. 2003, Caro et al. 2003). It is therefore possible that these early mantle differentiation events were related to magma ocean processes and possibly to fractional crystallisation and it is also possible that products of that event still remain in the lower mantle today.

In order to test possible consequences of the crystallisation of a magma ocean on the mantle geochemistry, knowledge is required on the order in which minerals crystallise from a magma ocean as a function of depth and composition. Likely magma ocean compositions are typical peridotite compositions, which are assumed to be very similar to the bulk silicate Earth (e.g. Hart and Zindler 1986, McDonough and Sun 1995), or chondrite meteorite compositions. Chondritic compositions are primarily defined by lower Mg/Si ratios compared to peridotites but may also have lower bulk Mg#'s (Mg#: Mg-number, defined as the molar Mg/(Mg+Fe) ratio). Understanding of the liquidus phase relations of such compositions is therefore the first step to model the crystallisation of a deep Hadean magma ocean. MgO and SiO_2 are the most important components in both peridotite and chondrite compositions and their sum in a peridotite bulk composition is greater then 85 mol%. Detailed knowledge of melting relations along the binary MgO-SiO_2 system as function of pressure with focus on the compositional range between Mg_2SiO_4-$MgSiO_3$ (which covers peridotitic and chondritic Mg/Si ratios) must therefore provide a fundamental understanding of melting relations in the chemically more complex peridotite and chondrite compositions, and possibly also allows to predict the liquidus phases outside experimentally accessible pressure ranges. Once the most likely liduidus phases are determined, the partitioning major, minor and trace elements between crystallising phases and the residual silicate melt

provides important geochemical constraints on how much of a crystal reservoir may exist in a chemically distinct reservoir in the lower mantle today, or if such a reservoir may have resisted subsequent solid-state mantle convection.

1.3.1 Liquidus Phase Relations of Peridotites and Chondrites

Previous studies, that investigated liquidus phase relations of peridotite compositions, showed that olivine is the liquidus phase at pressures below approximately 13-16 GPa (e.g. Takahashi and Scarfe 1985, Takahashi 1986, Scarfe and Takahashi 1986, Takahashi et al. 1993, Walter 1998) but that it is replaced by majoritic garnet (majorite, Mj) at higher pressures (Ito and Takahashi 1987, Herzberg et al. 1990, Zhang and Herzberg 1994). Majorite is the liquidus phase up to approximately 22-23 GPa, where it is replaced by ferropericlase (Zhang and Herzberg 1994, Trønnes and Frost 2002). Recently, Ito et al. (2004) reported melting relations for a peridotite composition up to 35 GPa and found that Mg-silicate perovskite (MgPv) becomes the liquidus phase at approximately 31 GPa. Figure 1.3 summarises reported peridotite liquidus phase relations at lower mantle pressures. If a magma ocean extended well in the present-day lower mantle or possibly to the core-mantle boundary as indicated in Figure 1.2, which is likely in case a giant impact occurred, then the most likely candidates for crystal fractionation are the lower mantle phases MgPv, Fp and CaPv. Thus, understanding of the melting relations in this pressure range may be crucial for investigating effects of deep magma ocean crystallisation.

Melting relations for Fe-rich (relative to peridotite) chondritic compositions have been reported by Agee (1990), Agee et al. (1995), Trønnes (2000) and Asahara et al. (2004). Pressures below 16 GPa have only been investigated by Agee et al. (1995) who found

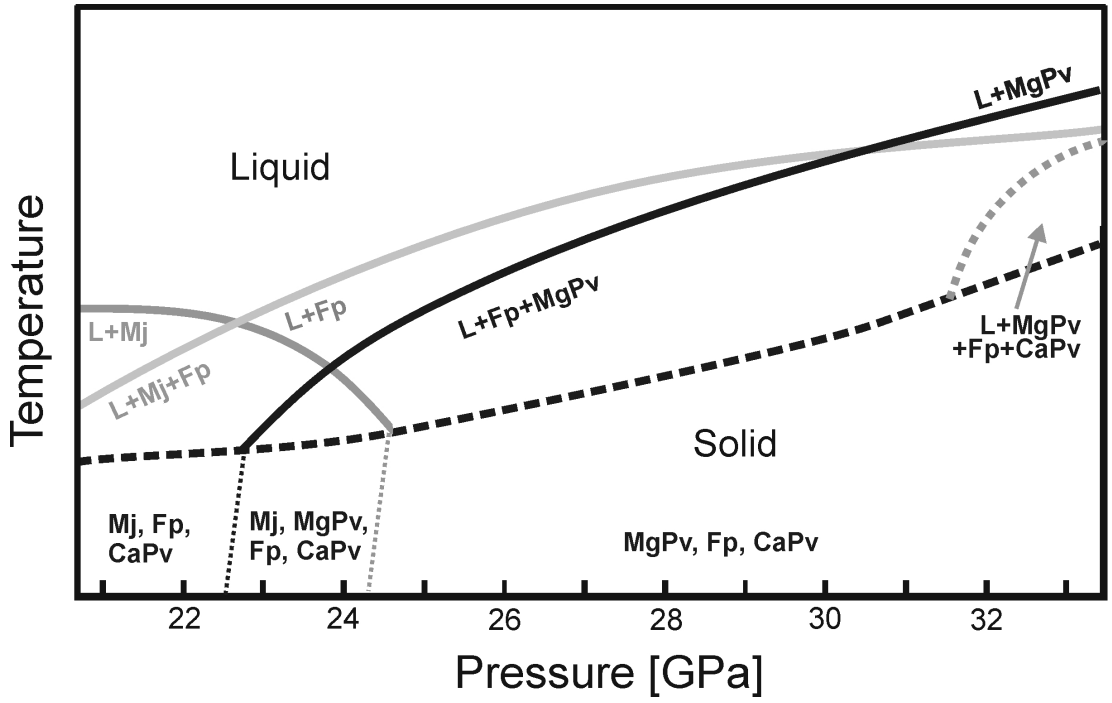

Figure 1.3: Summary of peridotite liquidus phase relations slightly below and at lower mantle pressures inferred from melting experiments of Trønnes and Frost (2002) and Ito et al. (2004). The black dashed line marks the solidus. Black and grey lines above the solidus indicate the stability fields of crystallising phases. Abbreviations: Mj, majorite; MgPv, Mg-silicate perovskite; CaPv, Ca-silicate perovskite; Fp, ferropericlase; L, liquid. For example, at 26 GPa the first phase that crystallises from a peridotitic melt is Fp (light grey line) followed down temperature by Fp plus MgPv (black line). The temperature scale is in the order of 2100-2500°C.

a transition from olivine to garnet between 13 and 14 GPa. At higher pressures garnet (Mj) is regarded as the liquidus phase up to approximately 24-25 GPa. Although Agee (1990) and Agee et al. (1995) observed a transition to Fp on the liquidus above 25 GPa, Asahara et al. (2004) describe a direct change of the liquidus phase from Mj to MgPv between 24-25 GPa.

Melting experiments on a model CI-chondritic mantle composition with peridotitic Mg#'s of approximately 0.9 have been performed by Ohtani et al. (1986), Ohtani and Sawamoto (1987) and Ito et al. (2004). Herzberg et al. (1990) reported a change in liquidus phase from olivine to majorite at approximately 10 GPa in experiments

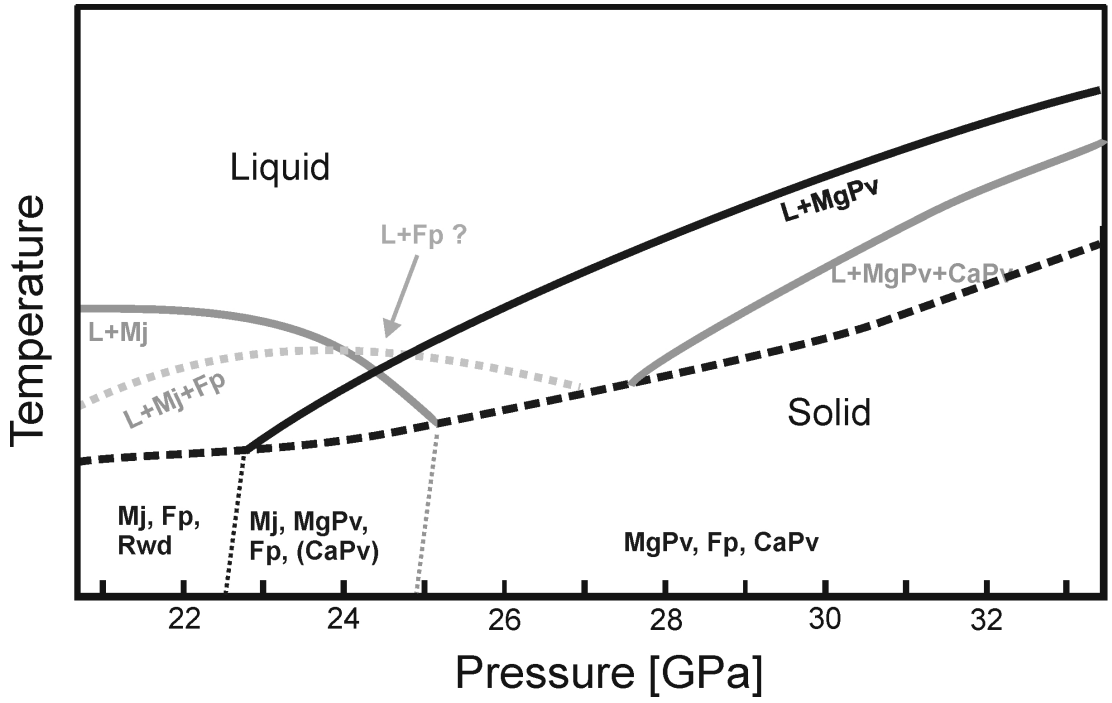

Figure 1.4: Summary of chondrite liquidus phase relations slightly below and at lower mantle pressures inferred from previous studies. The starting compositions had nearly constant Mg/Si but varying Mg#'s. The black dashed line marks the solidus. Black and grey lines above the solidus indicate the stability fields of crystallising phases. The stability field of Fp on the liquidus in chondritic compositions is not well constrained by previous studies. Abbreviations: Mj, majorite; MgPv, Mg-silicate perovskite; CaPv, Ca-silicate perovskite; Fp, ferropericlase; L, liquid.

performed on an Fe-free model chondrite composition, while this transition has been observed by Ohtani et al. (1986) between 12 and 15 GPa. Mj is also observed as the liquidus phase up at 25 GPa (Ohtani and Sawamoto 1987). Ito et al. (2004) reported the transition from majorite to MgPv as liquidus phase to take place below 28 GPa. A comparison of the liquidus phase relations between peridotite and chondrite bulk compositions shows differences in the stability fields of the liquidus phases. The stability field of majorite is slightly expanded in the chondrite bulk composition towards both lower and higher pressures, relative to peridotite. The stability field of ferropericlase in peridotite compositions extends over a larger pressure range than in chondritic com-

positions, although the discrepancies between the results of Agee (1990), Agee et al. (1995) and Asahara et al. (2004) need to be clarified. However, despite the relatively large number of studies that investigated melting relations of peridotite and chondrite compositions, the origin of the changes in liquidus phase relations at various pressures along the two compositions has not been systematically explored.

It should be mentioned that the melting relations in chemically complex peridotite and chondrite compositions are derived from quenched high-pressure melting experiments performed in strong thermal gradients. The proposed melting relations rely therefore on the interpretation of quench textures. This approach involves large uncertainties in reported temperatures and in the stability fields of liquidus phases. For example, some inconsistency exists about the Clapeyron-slope of the peridotite liquidus at pressures between 10-15 GPa. In this pressure interval Scarfe and Takahashi (1986) and Takahashi (1986) reported a negative slope, which however, has not been confirmed in a subsequent study (Zhang and Herzberg 1994).

1.3.2 Liquidus Phase Relations along the Binary Mg_2SiO_4-$MgSiO_3$

The differences in melting relations between peridotite and chondrite compositions must be related to the different chemical compositions. The similarity between melting relations of chondrite compositions with different bulk Mg#'s, indicates that the differences relative to peridotite compositions are related to the Mg/Si ratio. Because MgO and SiO_2 are the most important components in both compositions, the melting relations along this binary system should provide a more systematic understanding of melting relations in the chemically more complex peridotite and chondrite composi-

tions.

Bowen and Anderson (1914) investigated the system MgO-SiO_2 at ambient pressure and found that $MgSiO_3$ enstatite melts incongruently to Mg_2SiO_4 forsterite and liquid containing 51.1 mol% SiO_2 at 1562°C. Boyd et al. (1964) performed melting experiments on $MgSiO_3$ up to 5 GPa and noted that the melting reaction changes to congruent melting at an elevated pressure below 0.54 GPa, which has later been estimated to be 0.13 GPa by Chen and Presnall (1975). The congruently melting behaviour of $MgSiO_3$ has been confirmed up to lower mantle pressures by e.g. Kato and Kumazawa (1985a) (3, 7 GPa), Presnall and Gasparik (1990) (10-16.5 GPa), Kato and Kumazawa (1985b) (20 GPa) and Ito and Katsura (1992) (21-25 GPa).

Liu and Presnall (1990) estimated the eutectic composition between Mg_2SiO_4 and $MgSiO_3$ at 2.3 GPa to be located at 19.8 wt% Mg_2SiO_4, which corresponds to 46.5 mol% SiO_2. Other studies demonstrated that the eutectic melt composition becomes progressively more MgO-rich with increasing pressure to about 16 GPa (Kato and Kumazawa 1985a, 1990, Presnall and Gasparik 1990). The most recent data on the Mg_2SiO_4-$MgSiO_3$ eutectic were presented by Presnall et al. (1998), who reported compositions of 21 and 32 wt% Mg_2SiO_4 (46.3 and 44.4 mol% SiO_2) at 2 and 16.5, respectively, in good agreement with the aforementioned studies. At higher pressures, of approximately 20-23 GPa, data reported by Kato and Kumazawa (1986) and Gasparik (1990) also indicate an increasing Mg_2SiO_4 component with increasing pressure of the eutectic compositions, although the latter two studies reported relatively large uncertainties in either pressure or composition. Above 16.5 GPa the previously reported data do therefore not allow a precise description of the eutectic composition as

a function of pressure.

Bowen and Anderson (1914) measured the melting temperature of forsterite to be 1898°C at ambient pressure. Davis and England (1964) studied the melting curve of forsterite up to 4 GPa using a piston cylinder apparatus. Melting experiments at higher pressures in the forsterite stability field have been performed using multianvil apparatus by Ohtani and Kumazawa (1981), Kato and Kumazawa (1985a,c, 1986), Presnall and Walter (1993) and Kato et al. (1998). Some discrepancies have been revealed about the beginning of incongruent melting of forsterite to periclase plus liquid, which has been reported to occur at 8.5 GPa (Kato et al. 1998), 10.1 GPa (Presnall and Walter 1993) and below 12.7 GPa (Ohtani and Kumazawa 1981). At pressures higher than 15 GPa forsterite is observed to melt incongruently to phase anhydrous B (AnhB, $Mg_{14}Si_5O_{22}$) and liquid, which is followed by the reaction AnhB + liquid = periclase + liquid at higher temperatures (Kato and Kumazawa 1986, Presnall and Walter 1993). The stability of AnhB at higher pressures is, however, not well studied. Although Ohtani et al. (1998) reported data on melting of a $(Mg_{0.9}, Fe_{0.1})_2SiO_4$ olivine composition between 18-25 GPa no systematic investigation of the melting curve of pure Mg_2SiO_4 to its stability limit (defined by the breakdown to MgPv+periclase) has been performed.

1.3.3 Geochemical Constraints on Fractional Magma Ocean Crystallisation

The extend of large-scale chemical differentiation by crystal fractionation, as depicted in Figure 1.2, is constrained by a number of geochemical observations. Chemical analysis of primitive upper mantle rocks show that many ratios of refractory lithophile elements

(RLE's, e.g. rare earth elements, Be, Al, Ca, Sc, Ti, Sr, Y, Zr, Nb, Ba, Hf, Th, U) are very similar to those observed in CI-chondrite meteorites (e.g. McDonough and Sun 1995, O'Neill and Palme 1998, and references therein). This observation has been interpreted to indicate that the Earth formed from CI-chondrite-like material. Crystal fractionation, however, wouled have changed the chemical composition of the residual liquid, that eventually solidified as the upper mantle. If fractionation from a crystallising magma ocean took place and led to formation of a chemically distinct reservoir, which is still present in the lower mantle today, then the extend of this process has not shifted upper mantle RLE ratios outside their chondritic bounds (defined by the uncertainty on the RLE ratios). If a magma ocean extended well below 670 km depth, and possibly to the core-mantle boundary, then the most likely candidates for crystal fractionation are the lower mantle phases MgPv, Fp and CaPv. It should be mentioned that a particularly attractive aspect of $(Mg, Fe)(Si, Al)O_3$ perovskite fractionation is that this could have produced a lower mantle which is enriched in Si relative to the upper mantle, which must have formed from the residual liquid. This could therefore be an explanation for the observation, that the Mg/Si ratio of the upper mantle is significantly lower compared to the value for CI-chondrites, from which the Earth probably formed (Ringwood 1979).

A number of previous studies have investigated element partition coefficients between Mg-silicate perovskite (MgPv), the most abundant lower mantle phase, and silicate melts in peridotitic compositions and compared refractory lithophile element (RLE) ratios of the residual liquid with observed ratios in the present day upper mantle (e.g. Kato et al. 1988b,a, Drake et al. 1993, McFarlane et al. 1994, Hirose et al. 2004,

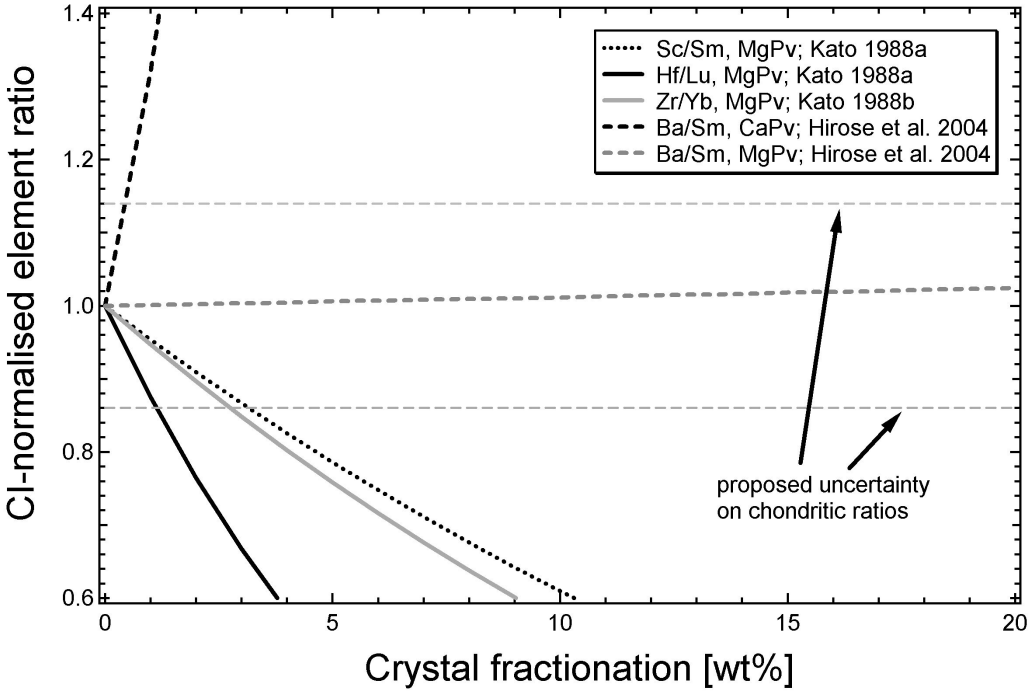

Figure 1.5: Results on previous estimates on MgPv and CaPv fractionation based on chondritic ratios of refractory lithophile elements after data from Kato et al. (1988b,a) and Hirose et al. (2004).

.

Corgne et al. 2004, Walter et al. 2004). Results of Kato et al. (1988b) and Kato et al. (1988a), as an example, are summarised in Figure 1.5. This figure shows the evolution of selected refractory lithophile element ratios, that are believed to be present in CI-chondritic proportions in the upper mantle, as a function of the weight fraction of crystallised and fractionated Mg-silicate perovskite (MgPv). The figure indicates that small amounts (<4 wt%) of MgPv fractionation would shift Sc/Sm, Hf/Lu and Zr/Yb ratios outside their chondritic bounds. Therefore it has been argued that MgPv fractionation took place only to a very minor extend or never occurred (Kato et al. 1988b,a). It should be noted, that application of a recently developed mineral/melt partitioning model (the 'lattice strain model', Blundy and Wood 1994, see section 3.4.1) to the data of Kato et al. (1988b) and Kato et al. (1988a) indicates that partition

coefficients for Zr and Sc are most likely heavily overestimated. Revision of those data, however, could significantly change the conclusions about the likely proportion of MgPv fractionation. More recent experimental studies have also investigated trace element partitioning between Ca-silicate perovskite and melt in addition to MgPv (Hirose et al. 2004, Corgne et al. 2004). Results from Hirose et al. (2004) for CaPv and MgPv are also plotted in Figure 1.5. Hirose et al. (2004) used the evolution of the Ba/Sm ratio and demonstrated that MgPv crystallisation may have fractionated essentially the complete mantle, because this element ratio is insensitive to MgPv fractionation. CaPv fractionation, however, would shift the Ba/Sm ratio outside the chondritic bound after less than 1 wt% crystallisation. Fractionation of mixtures of these minerals would plot in between the two extremes. Hirose et al. (2004) argued that the total amount of combined MgPv and CaPv fractionation likely did not exceed 6 wt% of the total mantle, although they did not present a discussion about likely relative proportions of the two phases. An additional problem is that especially Ba especially is a highly incompatible element in low pressure melting processes (e.g. Salters and Stracke 2004), such that this element has certainly been fractionated by formation of the continental crust. Therefore, element ratios involving Ba cannot be considered chondritic in a primitive upper mantle. Other recent polymineralic fractionation models came to the conclusions that the lower mantle could contain between 5-13 wt% of fractionated material without perturbing the geochemical signature of RLE's in the primitive upper mantle (Corgne and Wood 2002, Corgne et al. 2004, Walter et al. 2004). Approximately 60 wt% MgPv fractionation, on the other hand, would be required to explain the super-chondritic Mg/Si ratio of the upper mantle (e.g. Kato et al. 1988b).

The Earth most likely accreted from a range of chondritic materials (O'Neill and Palme 1998) and there is a priori no reason to assume that a magma ocean must have been of a primitive upper mantle peridotitic composition. However, trace element partitioning data between Mg-silicate perovskites and silicate liquids have only been measured in peridotite bulk compositions. Thus, possible variation in element partition as a result of changing bulk Mg/Si ratios or bulk Mg#'s has not been systematically explored in previous work. Furthermore, the effect of changing concentrations of major elements in the liquid during crystallisation has also not been considered in previous fractionation models.

1.4 The Oxidation State of the Earth's Mantle

The distribution of ferric (Fe^{3+}) and ferrous (Fe^{2+}) iron between olivine, orthopyroxene (opx) and spinel in mantle xenoliths can be used to constrain the oxygen fugacity fO_2 of Earth's upper mantle, using the reaction (e.g. O'Neill and Wall 1987):

$$6Fe_2SiO_{4,olivine} + O_2 = 6FeSiO_{3,opx} + 2Fe_3O_{4,spinel}. \quad (1.1)$$

Application of this reaction shows that most spinel-peridotites fall within a range of +1 to -2 $\log_{10}$-units of the 'quartz-fayalite-magnetite' (QFM) oxygen buffer (e.g. O'Neill and Wall 1987, Ballhaus et al. 1991) The bulk $Fe^{3+}/\sum Fe$ ratios of such rocks are on the order of 0.03. Analysis of ancient volcanic rocks indicate the the oxygen fugacity of the upper mantle has been remained nearly constant since the early Archean (Delano 2001, Canil 2002, Li and Lee 2004). During core-formation, however, the equilibrium of metallic core-forming liquids with silicates imposed a very low oxygen fugacity (close to the iron-wüstite (IW) oxygen buffer), which should have resulted in a bulk silicate

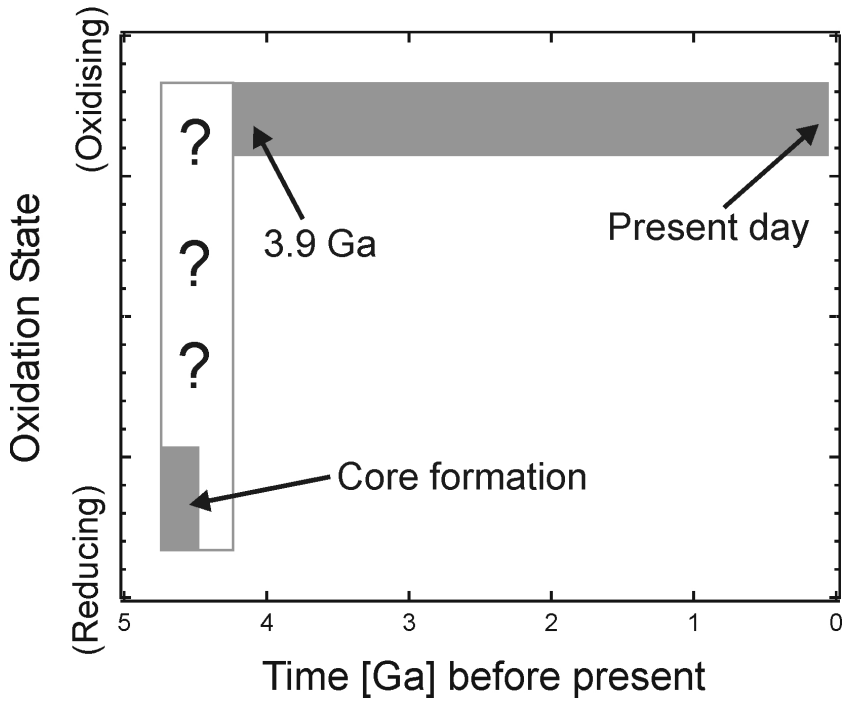

Figure 1.6: Schematic diagram showing the evolution of the Earth's upper mantle redox state over the entire history of the Earth. Redrawn after Delano (2001).

$Fe^{3+}/\sum Fe$ ratio of zero. It should be noted that the present day upper mantle fO_2 is about 5 to 8 orders of magnitude higher than the oxygen fugacity at the IW oxygen buffer. This implies that the bulk oxygen content of the upper mantle and possibly of the bulk silicate Earth has been raised between core-formation and the crystallisation of Archean rocks, as indicated in Figure 1.6, which shows schematically the evolution of the Earth's redox state.

Redox processes that occurred during formation of the lower mantle, possibly during crystallisation of a magma ocean, may be relevant to this oxidation event. A number of experimental studies have shown that aluminous Mg-silicate perovskite (MgPv) can accommodate significant amounts of ferric iron (McCammon 1997, Xu et al. 1998, Frost and Langenhorst 2002, McCammon et al. 2004) even at low oxygen fugacities (Lauter-

bach et al. 2000, Frost et al. 2004a). Except for two data points from McCammon et al. (2004), no $Fe^{3+}/\sum Fe$ measurements on MgPv that has crystallised from a peridotitic bulk composition have been performed. Furthermore, only samples quenched from conditions close to a present-day mantle geotherm have been investigated, but no data from higher temperatures, as they prevailed during magma ocean crystallisation, are available. Lauterbach et al. (2000) and Frost et al. (2004a) suggested that even at very low oxygen fugacity the ferric iron in MgPv under subsolidus conditions may be produced by the disproportionation of ferrous to ferric iron plus metal, according to the reaction

$$3FeO_{System} = Fe_2O_{3,MgPv} + Fe_{Metal}, \tag{1.2}$$

which thus results in the precipitation of metallic iron in the presence of MgPv with high ferric iron contents. Although the net oxygen content in this reaction remains unchanged when the equilibrium lies on the right-hand side of Equation 1.2, the physical separation of Fe_2O_3 and Fe would create a local disequilibrium of the oxygen distribution in the Earth. The question arises if such a process could have occurred during formation of lower mantle by magma ocean crystallisation, possibly involving fractionation of a MgPv dominated crystal accumulate. However, to answer this question the systematics of redox processes in the lower mantle at melting temperatures need to be investigated. It is therefore important to determine at melting conditions whether MgPv contains high amounts ferric iron even at a low oxygen fugacity, as it has been observed under subsolidus temperatures.

1.5 Viscosity of a Magma Ocean

The viscosity of a magma ocean as a function of pressure (or depth) is a crucial parameter in modelling fluid dynamical properties and magma ocean dynamics. Tonks and Melosh (1990) argued that crystal fractionation in a magma ocean may have been efficiently suppressed by the high convective velocities related to a turbulent convecting magma ocean. They also noted that the possibility of crystal fractionation only weakly depends on gravitational forces, but is strongly influenced by viscosity. Solomatov and Stevenson (1993b) found that a critical parameter in modelling crystal suspension or settling is the crystal size, which an the other hand, depends also on the viscosity of the liquid (Solomatov and Stevenson 1993a). In these studies, the viscosity of the silicate melt was assumed to be on the order of $10^{-3} - 10^{-1}$ Pa s. The effect of pressure on the viscosity, however, has not been taken into account in the modelling. The viscosity of a magma ocean was also an important parameter in a recent study of metal/silicate equilibration mechanisms (Rubie et al. 2003), in which the viscosity was estimated based on experimental measurements on $CaMgSi_2O_6$ liquid (Reid et al. 2003) as an analogue material, but it was assumed to be constant with pressure.

The chemical composition of a magma ocean is not known with certainty, and it may have varied i.e. due to crystallisation, volatilisation or due to extraction of FeO into core-forming liquids (Rubie et al. 2004), but it is likely that it was similar to a present day peridotite or bulk mantle composition, at least during the final stages prior to solidification. Viscosity data for a peridotitic composition have only been reported from measurements performed at 1 bar (Dingwell et al. 2004), and no viscosity data exist from measurements at high pressure, as they would be applicable to a magma

ocean.

1.5.1 Liquid Structure and the Effect of Pressure on Viscosity

The effect of pressure on viscosity reflects the response of the melt structure to compression. The viscosity of simple ionic or metallic liquids increases with increasing pressure, which is consistent with the 'free volume theory' of Cohen and Turnbull (1959). In this model, the free volume within a liquid of hard spheres is defined as the volume of a cage around a molecule (constrained by neighbouring atoms) minus its own volume. Compression of a simple liquid will result in a decrease of interatomic distances and therefore in a decrease of the free volume. This reduces the number of statistical redistributions of the free volume that provide voids that are necessary for structural rearrangements. Hence, the viscosity of such liquids increases with increasing pressure. Experimental studies by Kushiro et al. (1976) and Kushiro (1976), however, showed that the viscosity of silicate melts of andesite and jadite ($NaAlSi_2O_6$) compositions actually decrease with increasing pressure. This 'anomalous' effect of pressure on viscosity is therefore inconsistent with models that consider liquids as an ensemble of hard spheres. The structure of a silicate liquid depends strongly on the chemical composition and may qualitatively be described by the degree of depolymerisation. In a first approach a silicate melt can be understood as an arrangement of silicon cations, which are covalently bonded to oxygen to form SiO_4^{4-} tetrahedra. The oxygen anions may either be bonded to other TO_4 tetrahedra (whereas T denotes a tetrahedrally coordinated cation, e.g. Si^{4+} or Al^{3+}, termed 'network-formers') or to a 'network-modifying' cation, such as Na^+ or Mg^{2+}. In the former case the oxygen is called a 'bridging oxygen', which contributes to a three-dimensional network of tetrahedra, while in the latter

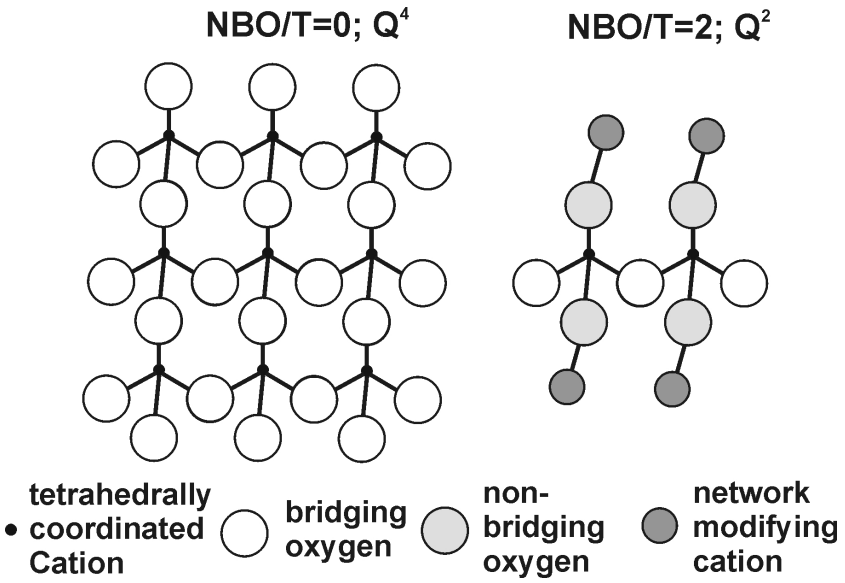

Figure 1.7: Schematic diagram showing the concept of NBO/T and the Q^n speciation. See text for details. Redrawn after Mysen (2003).

case the oxygen is termed a 'non-bridging oxygen' (NBO), which has a depolymerising effect on the liquid. The degree of polymerisation can be expressed as NBO/T, which denotes the ratio of the number non-bridging oxygens to the number of tetrahedrally coordinated cations (e.g. Mysen 1991). Schematic examples of silicate melt structures and the concept of NBO/T are shown in Figure 1.7. Values of NBO/T can range from 0 to 4, corresponding to a fully polymerised to a completely depolymerised melt. It is emphasised that NBO/T is purely based on the stoichiometry of the bulk composition, and does not reflect the actual cation coordinations in a melt, because the latter also depend on temperature, pressure and composition. Nonetheless, this approach allows, at least qualitatively, the relation between transport properties of silicate liquids and the degree of depolymerisation to be described. Depolymerised liquids are usually less viscous than more polymerised melts, because of the lower concentration of three-dimensionally connected and relatively rigid TO_4 tetrahedra. A more detailed

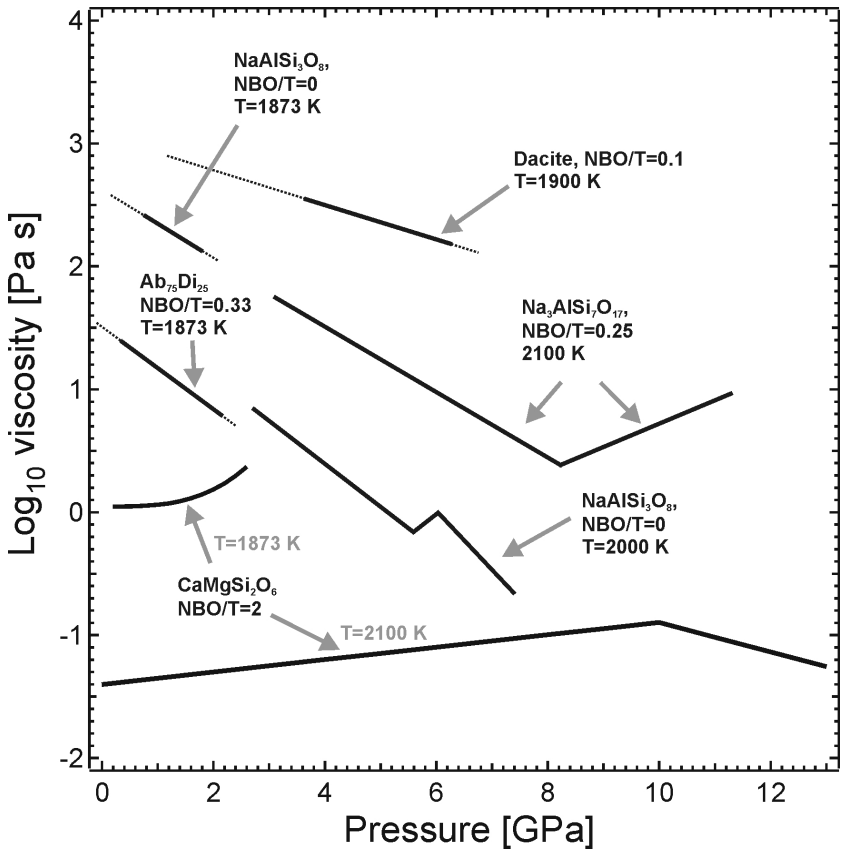

Figure 1.8: Plot of melt viscosity as a function of pressure for some silicate liquids derived from experimental studies. Data sources: $NaAlSi_3O_8$ (Ab), $CaMgSi_2O_6$ (Di), $Ab_{75}Di_{25}$ (Ab and Di components in mol%) at 1873 K, Brearley et al. (1986); $CaMgSi_2O_6$ at 2100 K, Reid et al. (2003); $NaAlSi_3O_8$ at 2000 K, Mori et al. (2000); $Na_3AlSi_7O_{17}$, Poe et al. (1997); dacite-liquid, Tinker et al. (2004). Data from Poe et al. (1997) have been recalulated from oxygen self-diffusion data using Equation 1.3.

characterisation of silicate melt structures is provided by means of NMR spectroscopy, which allows the determination of relative abundances of 'Q^n' species, where n ($0 \leq$ n ≤ 4) is the number of bridging oxygens bonded to a tetrahedrally coordinated cation Q (e.g. Mysen 2003).

The degree of depolymerisation has strong influence on the viscosity of silicate melts but also on the effect of pressure on the viscosity of such liquids. Viscosity measurements performed on melt compositions along the join $NaAlSi_3O_8$ (albite-composition, NBO/T=0) - $CaMgSi_2O_6$ (diopside-composition, NBO/T=2) at pressures below 3 GPa

have shown that the pressure dependence of the viscosity changes from negative (decrease in viscosity with increasing pressure at constant temperature) to positive (increase in viscosity with pressure at constant temperature) with increasing degree of depolymerisation (e.g. Brearley et al. 1986, Scarfe et al. 1987, Behrens and Schulze 2003, Persikov and Bukhtiyarov 1999). Other studies performed at pressures up to 15 GPa have also shown maxima and minima of transport properties of silicate melts as pressure increases (e.g. Poe et al. 1997, Tinker and Lesher 2001, Persikov and Bukhtiyarov 1999, Mori et al. 2000, Reid et al. 2001, 2003), especially between 5 to 10 GPa. Maxima in cation diffusion-rates, for example, have also been reported in early computer simulation studies on silicate liquids (Angell et al. 1982, 1983). Some results of earlier experimental studies performed on melts with different degrees of depolymerisation are summarised in Figure 1.8. Spectroscopic methods applied to silicate glasses obtained from high pressure experiments and molecular dynamics simulations show evidence for increasing coordination numbers of network-forming cations, such such Al^{3+} and Si^{4+}, to five- and/or sixfold coordinated species as pressure increases (e.g. Stebbins and McMillan 1989, Wolf et al. 1990, Yarger et al. 1995, Xue et al. 1991, Stebbins and Poe 1999, Bryce et al. 1999, Suzuki et al. 2002, Lee et al. 2004). Other spectroscopic and computational studies also reported changing T-O bond angles and distances upon compression (e.g. Kubicki et al. 1992, Poe et al. 2001, Suzuki et al. 2002). Liu et al. (1988) suggested that diffusive displacement in silicate liquids may involve intermediate fivefold-coordinated silicon. A schematic diagram of an oxygen-diffusion mechanism is shown in Figure 1.9. The diffusion mechanism is initiated when a non-bridging oxygen of the SiO_4 tetrahedra A (probably with three other bridging oxygens) impinges on

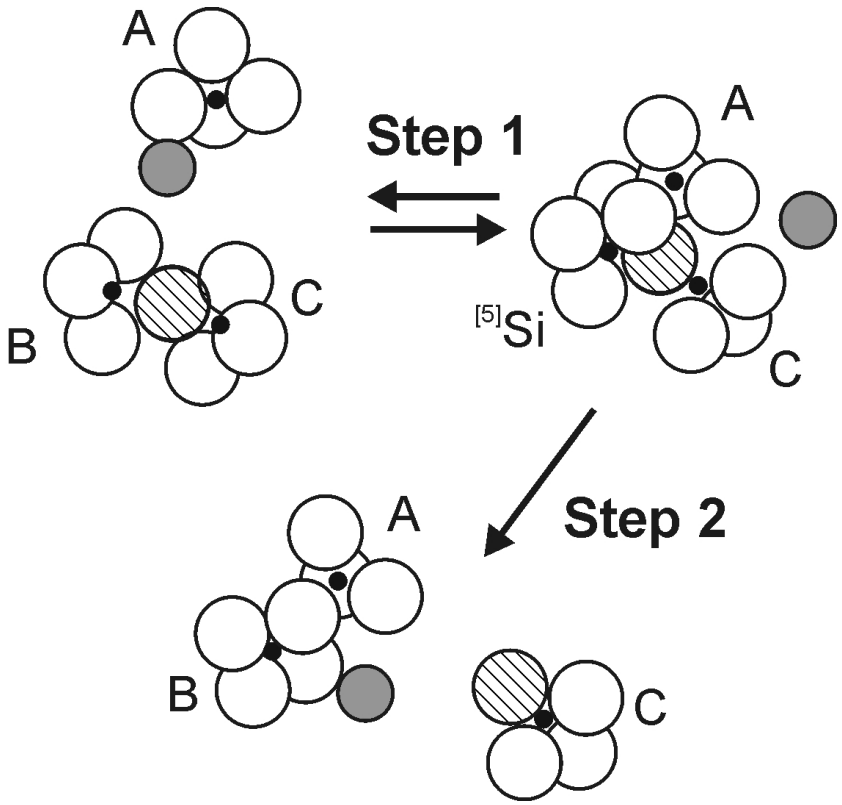

Figure 1.9: Diagram showing the cooperative oxygen diffusion mechanism. Symbols are as in Figure 1.7. The hatched circle is the diffusing oxygen anion. Redrawn after Farnan and Stebbins (1994)

a tetraheda B, where all oxygens are bridging oxygens (e.g. to tetrahedra C among others). In this situation B transforms to an intermediate five-fold coordinated species ($^{[5]}$Si, step 1). Diffusion occurs when $^{[5]}$Si dissociates and an oxygen that was initially bonded to B (shown as hatched circle) is now associated with a neighbouring tetrahedra such as C (step 2). A similar mechanism may also be envisaged for the formation of five-fold coordinated Al. Poe et al. (1997) suggested that such a process could cause the observed maximum in the rate of oxygen self-diffusion in $Na_3AlSi_7O_{17}$ liquid at around 8 GPa (see Figure 1.8), because at this pressure the population of five-fold coordinated Al (derived from spectroscopy) also reached a maximum relative to other species. The increase of higher coordinated species with pressure is therefore

consistent with increasing diffusivity in the liquid, which on the other hand implies that viscosity decreases, since diffusivity D and viscosity η are inversively correlated. This relationship may be described by the following expression (Eyring 1936):

$$\eta = \frac{k_B T}{\lambda D}, \tag{1.3}$$

which is known as *Eyring equation*, where k_B is the Boltzmann constant ($1.38 \cdot 10^{-23}$ JK^{-1}), T the absolute temperature and λ is the 'jump distance', which is usually assumed to be equivalent to the diameter of the diffusing species. The applicability of this relationship to silicate melts has been demonstrated by e.g. Rubie et al. (1993) and Poe et al. (1997) for some simple relatively, polymerised sodium-aluminum silicate liquids and by Reid et al. (2001) and Reid et al. (2003) for depolymerised $CaMgSi_2O_6$ melt. However, it is emphasised that at present no experimental, spectroscopic or computational study is able to resolve unambiguously the nature of the negative pressure dependence of silicate liquids, which most likely also involves different mechanisms for different melt compositions.

Most previous experimental studies that have investigated the viscosity of silicate liquids at high pressure presented results for relatively polymerised melts (NBO/T«2). In order to relate physical properties of a liquid to structural changes, many studies have used compositions for which spectroscopic data, obtained from high-pressure glasses, were available (e.g. Poe et al. 1997) or for which molecular dynamics simulation is applicable (e.g. Suzuki et al. 2002). Such an approach usually restricts the experiments to be performed on compositions along simple binaries or ternaries but precludes chemically more complex compositions, especially when they are iron-bearing. Only few experimental data are available for depolymerised melts, such as for $CaMgSi_2O_6$ liq-

uid (NBO/T=2), especially at pressures higher than 3 GPa (Reid et al. 2003). This is related to the experimental difficulties in investigating low-viscosity liquids at very high temperatures. The most significant problems are described later in section 5.1. A liquid of peridotitic composition, however, has an NBO/T ratio of approximately 2.5 and is therefore probably the most depolymerised naturally occurring silicate liquid composition. Knowledge ot the viscosity of a liquid of such a composition as a function of pressure is therefore not only important for understanding magma ocean processes, but will also provide new insights into transport properties of silicate liquids in general.

1.6 Aims of this Study

The aim of this work is to study processes that are relevant to the crystallisation of a deep Hadean magma ocean. Although previous studies have worked on problems that are related to magma ocean crystallisation, the following aspects are not well understood and have been therefore investigated in this study:

- The effects of changing bulk composition on the liquidus phase relations of peridotites and chondrites have not been investigated systematically in previous studies. Therefore, variations of bulk Mg/Si ratios and Mg#'s, as probably the most important unknowns in an initial magma ocean composition, have been studied. Due to the difficulties in interpreting liquidus phase relations in chemically complex multi-component systems, melting relations and eutectic compositions along the simple binary MgO-SiO_2 system have been investigated as an analogue composition. This leads to a more fundamental understanding of mantle-melting at high pressure. In the simple system, the temperature interval between the solidus

and the liquidus can be more precisely determined, which enables depths intervals, over which crystallisation takes place in a magma ocean, to be estimated (Chapter 2).

- Although mineral/melt partition coefficients for Mg-silicate perovskite have been reported in previous work, the bulk composition in earlier studies was usually constant and peridotitic (e.g. Kato et al. 1988b, Hirose et al. 2004, Walter et al. 2004). Investigating compositional effects on element partitioning, however, enables fractionation models to be developed, that are applicable to a variety of magma ocean compositions and which also consider changing liquid compositions during crystallisation (Chapter 3).

- The Al-concentration of MgPv has a significant effect on the incorporation of ferric iron, which is probably independent of oxygen fugacity. At temperature conditions close to a present-day mantle-geotherm, it has been observed that FeO disproportionates to Fe_2O_3 and Fe-metal at sufficiently low oxygen fugacities (Lauterbach et al. 2000, Frost et al. 2004a). In order to investigate if such a process may have influenced the oxidation state of the mantle during magma ocean crystallisation, detailed knowledge of the redox-systematics of MgPv at solidus temperatures is required (Chapter 4).

- Transport properties of potential magma ocean liquids as a function of pressure are poorly constrained by previous studies. Therefore, the viscosity of peridotite liquid, as a magma ocean composition, has been investigated as a function of pressure. Those data may be used to improve modelling of magma ocean dynamics,

and to determine if crystal fractionation may have occurred during magma ocean crystallisation (Chapter 5).

Chapter 2

Melting Relations in the Earth's Interior

2.1 Introduction

If a magma ocean crystallised at conditions corresponding to the present-day lower mantle, the order in which phases crystallise from the liquid determines how the geochemistry of residual liquid evolved during cooling. Therefore, knowledge of the liquidus phase relations of potential magma ocean compositions, such as peridotite and chondrite compositions, is required. Although melting relations of such compositions have been investigated in previous studies, there are a number of complexities and discrepancies, which have not been resolved in previous work. The melting relations of chondritic compositions at lower mantle pressure have not been revealed unambiguously, as demonstrated by discrepancies concerning the stability field of ferropericlase between the studies of Agee (1990), Agee et al. (1995) and Asahara et al. (2004). No systematic description of melting relations of peridotite and chondrite compositions as function of pressure has been presented in previous studies. Melting relations and eutectic compositions along the binary MgO-SiO_2, as a simple analogue for the more complex peridotite chondrite compositions, are not well constrained from previous

studies at transition zone and lower mantle pressures.

In this chapter, new results on liquidus phase relations in peridotite and chondrite compositions with varying Mg/Si ratios and bulk Mg#'s at pressures of 25-26 GPa are presented. An attempt is made to describe the liquidus phase relations of complex chemical compositions as a function of pressure by comparison with eutectic melt compositions and phase relations in the simple binary MgO-SiO_2 system. For this purpose, melting relations and eutectic melt compositions especially between the components Mg_2SiO_4 and $MgSiO_3$ have been investigated at pressures ranging from 16 to 26 GPa. Investigation of a simple binary also allows application of the phase rule

$$P + F = C + 2, \tag{2.1}$$

which, at chemical equilibrium, provides information on the number of stable phases P for a given number of components C in a system, if thermodynamic parameters such as pressure, temperature or composition (the number of defined parameters constrain the variance F) are known. The phase rule places constraints on univariant reactions and invariant points, which most likely could not be resolved from high-pressure melting experiments performed on complex multicomponent compositions.

2.2 Experimental Methods

2.2.1 Preparation of starting materials

Experiments in this study were performed on complex multicomponent peridotite and chondrite compositions and on samples along the binary MgO - SiO_2 system. A fertile peridotite and CI-chondrite analogue (low Mg/Si and high Fe/Mg ratios relative

to the fertile peridotite; with total Fe as FeO) starting composition (taken from McDonough and Sun 1995) were fabricated from analytical grade oxides and carbonates. Reagents were ground together under alcohol and then decarbonated by heating slowly to 1000°C. Nominal major and minor element concentrations, Mg/Si ratios and Mg#'s are reported in Table 2.1. A selection of trace elements at the 100-500 ppm level was added using atomic absorption standard solutions (see Table 2.1). Powder and doped aqueous solutions were homogenized in an agate mortar and were subsequently devolatilised at 400°C. Pressed pellets of this powder were reduced in a gas mixing furnace at an oxygen fugacity about two log units below the quartz - fayalite - magnetite (QFM) oxygen buffer at 1100°C for 48 hours. Three further ultramafic compositions were prepared to investigate compositional effects on phase relations and element partitioning (see Chapter 3). To study the effect of varying bulk Mg/Si ratios at a constant bulk Mg# (Mg-number, defined as atomic Mg/(Mg+Fe) ratio) SiO_2 was added to the initial fertile peridotite composition to produce Mg/Si ratios corresponding to a CI-chondrite and an enstatite-chondrite (referred to as CI-mantle and EC-mantle compositions, respectively). Furthermore an Al-enriched peridotite composition with a total Al_2O_3 concentration of 7 wt% was prepared by adding Al_2O_3 to the initial peridotite composition.

Synthetic forsterite (Fo, Mg_2SiO_4), enstatite (En, $MgSiO_3$) and quartz (Qz, SiO_2) were used as basic components for starting compositions in the investigation of the MgO - SiO_2 binary. While the SiO_2 component was available as glass (from company *Schott*), the Fo and En components were prepared by thoroughly mixing and grinding appropriate amounts of analytical grade MgO and SiO_2 under ethanol. The forsterite

Table 2.1: Nominal chemical compositions of peridotitic and chondritic starting materials and trace element concentrations.

	Fertile Peridotite	Al-rich Peridotite	CI-Chondrite analogue	CI-mantle	EC-mantle
SiO_2	44.9	43.7	34.0	49.3	56.1
TiO_2	0.2	0.2	a)	0.2	0.2
Al_2O_3	4.4	7.0	2.4	4.1	3.5
Cr_2O_3	0.4	0.4	0.6	0.3	0.3
FeO	8.0	7.8	34.8	7.4	6.4
MnO	0.1	0.1	0.4	0.1	0.1
MgO	37.7	36.7	23.9	34.7	30.1
CaO	3.5	3.4	1.9	3.3	2.8
NiO	0.4	0.3	a)	0.2	0.2
Na_2O	0.2	0.2	2.0	0.3	0.3
total	100.0	100.0	100.0	100.0	100.0
Mg/Si	1.25	1.25	1.05	1.05	0.80
Mg#	0.89	0.89	0.55	0.89	0.89

a) added as trace element
trace element concentrations (in ppm, by weight):
Li, 500; Be, 200; B, 200; K, 200; Sc, 500; Co, 100; Ga, 100; Rb, 100; Sr, 100; Y, 200; Zr, 100; Nb, 100; Ba, 100; La, 200; Ce, 200; Nd, 200; Sm, 200; Eu, 200; Lu, 200; Hf, 200; Pb, 200; Th, 200; U, 200.

starting material was then pressed into a pellet, fired at 1600°C for 20 h and then ground to a fine powder. This procedure was repeated to ensure complete reaction to Fo. The enstatite was prepared as a glass by melting the powder at 1600°C in a Pt crucible. The crucible was quenched after 2 h by dropping into water. Optical investigation of the glass revealed negligible amounts of quench crystals, forming during quenching. The glass was then ground to fine powder. Intermediate compositions between Fo, En and Qz were prepared by appropriate mixing of the three components. The following compositions were prepared: Fo_{100}, $Fo_{75}En_{25}$, $Fo_{50}En_{50}$, $Fo_{34}En_{66}$, $Fo_{25}En_{75}$, $Fo_{9}En_{91}$, En_{100}, $En_{80}Qz_{20}$, $En_{75}Qz_{25}$ and $En_{50}Qz_{50}$, where the subscripts indicate mol% of each component.

2.2.2 High-Pressure Synthesis

High-pressure experiments in this study were performed using multianvil presses. The method is based on two stages of anvils, which concentrate a large force, generated by a conventional hydraulic press, on a relatively small octahedral pressure medium. Details and descriptions of this technique can be found in Kawai and Endo (1970), Rubie (1999) and Frost et al. (2004b). The pressure medium, made from MgO doped with 5 wt% Cr_2O_3, contains an encapsuled sample, a heating element and a thermocouple and is compressed by a set of eight corner-truncated tungsten-carbide cubes (first stage anvils). This set of cubes is then compressed by six outer tool-steel anvils (second stage), which are driven by a hydraulic press in an uniaxial direction. A sketch of the technique and a typical pressure cell are presented in Figure 2.1. In this study, presses capable of producing loads of 1000, 1200 and 5000 tonnes have been used to generate pressures up to 26 GPa, corresponding to pressures in the upper part of

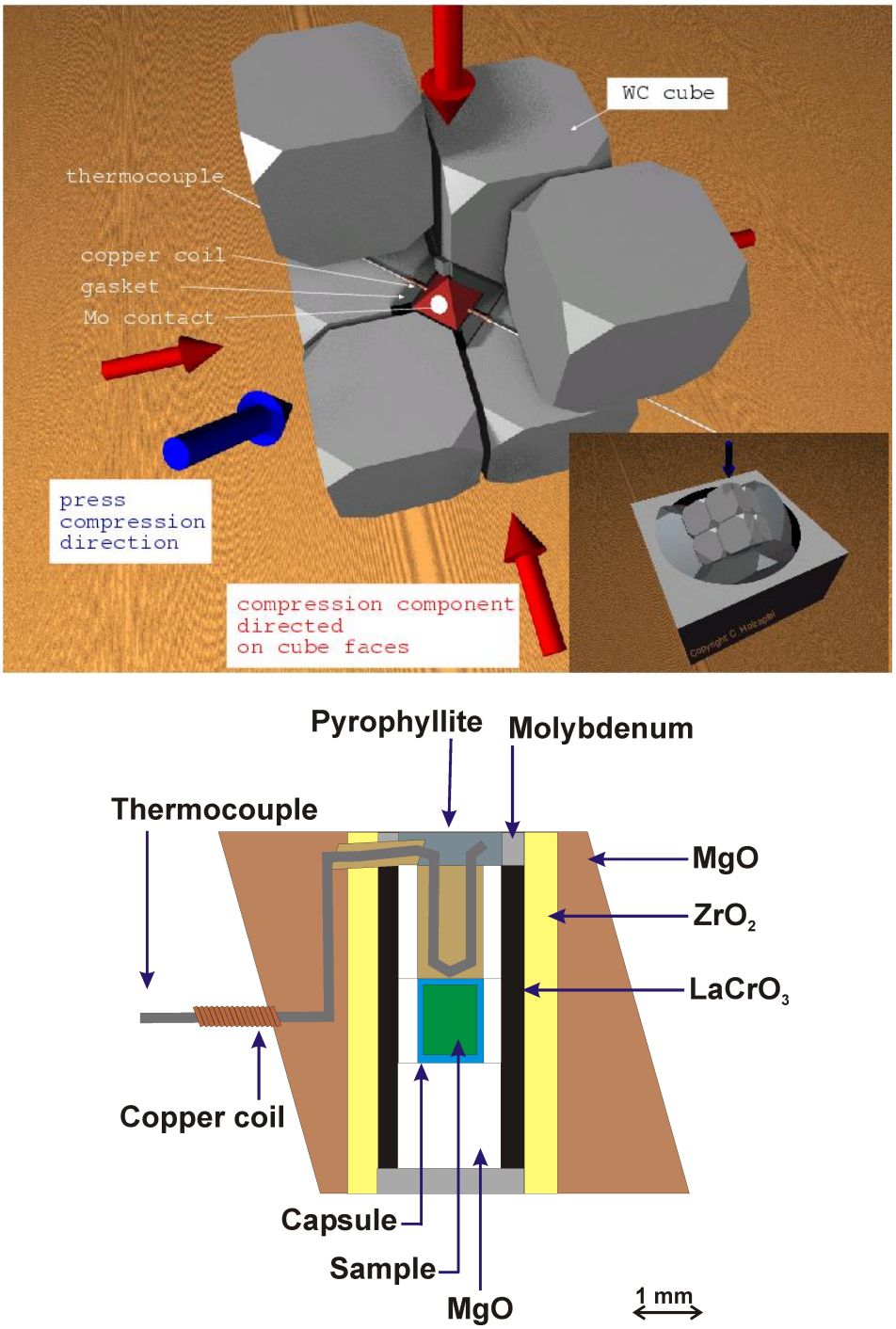

Figure 2.1: Upper image: schematic setup of a multianvil experiment, reproduced with permission from Holzapfel (2004). The compression directions of the press and the six outer anvils are indicated by arrows. The small picture in the right bottom corner shows the arrangement of the inner tungsten-carbide anvils in the hydraulic press. Lower image: cross-section of a typical pressure cell (10/4; see text for details)

the Earth's lower mantle. Although the maximum sample pressure does not increase with increasing maximum load of the multianvil press, the 5000 tonne press allows significantly larger pressures cells to be used at a given pressure, relative to those utilised in the 1000 and 1200 tonnes presses. This advantage provides the possibility to reduce thermal gradients within the samples and to improve the determination of sample-temperatures as described below (see also Frost et al. 2004b).

Different pressure cell/anvil-truncation configurations, covering various pressure ranges and sample volumes, have been used in this study. The 18/11 (octahedral edge length/tungsten-carbide anvil truncation in mm) and 18/8 pressure cells were used in the 5000 tonne press in combination with 54 mm tungsten-carbide anvils. These pressure cells contain stepped $LaCrO_3$ heaters to minimise thermal gradients (see Rubie 1999), which are surrounded by ZrO_2 sleeves for thermal insulation. The capsule dimension in both pressure cells is 2 mm in diameter and up to 3.5 mm in length. The run pressure is determined from a calibration curve which relates the pressure of univariant phase transitions at given temperatures to the load applied by the multianvil press. For the 18/11 and 18/8 configurations high-temperature calibrations between 1000-1900°C are based on phase transitions in $CaGeO_3$, SiO_2, Mg_2SiO_4 and $MgSiO_3$. Details of the pressure calibration of the 5000 tonne press are given by Frost et al. (2004b). Maximum pressures that can be achieved are approximately 18-19 GPa using the 18/11 cell and 23-24 GPa using the 18/8 configuration.

Pressures up to 26 GPa were achieved in 1000 and 1200 tonnes presses using 32 mm tungsten carbide cubes with corner truncations of 8, 4, 3.5 and 3 mm. Up to approximately 14-15 GPa a 14/8 pressure cell with a stepped $LaCrO_3$ heater and sample

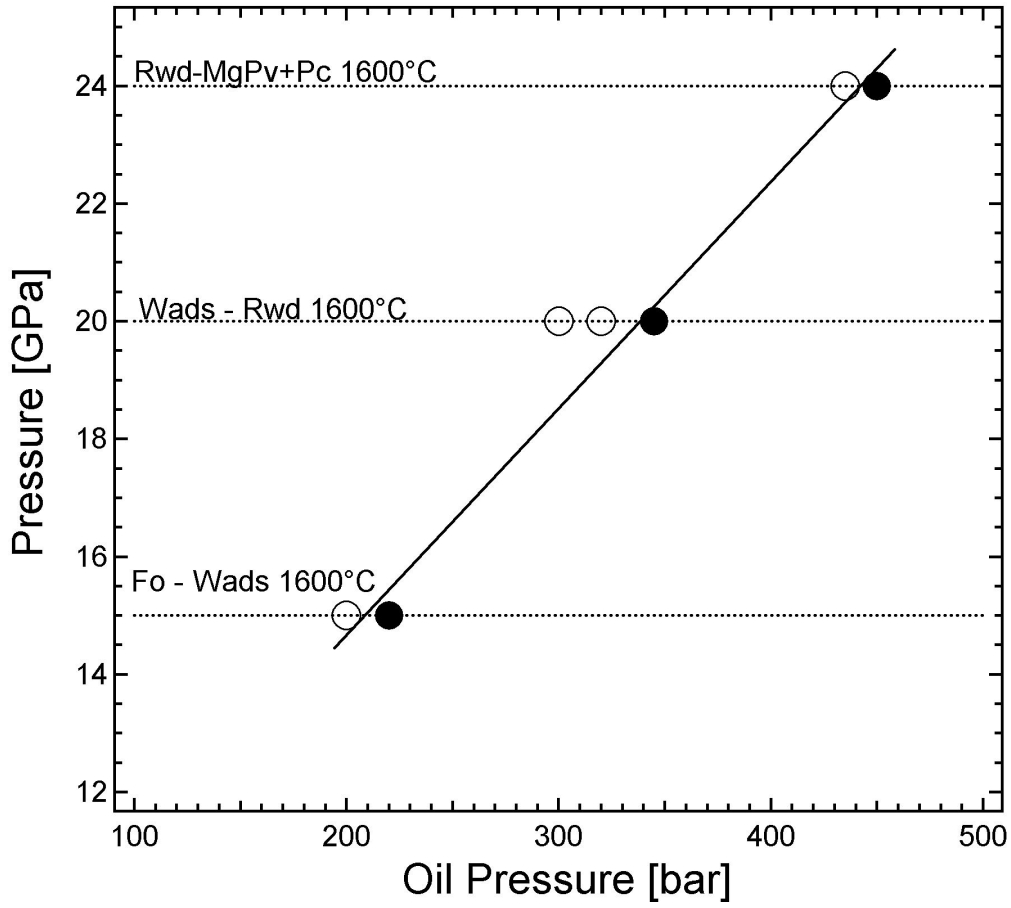

Figure 2.2: Pressure calibration curve of the 10/4 pressure cell. Run pressures are defined by phase transitions in Mg_2SiO_4. The x-axis of this diagram corresponds to the hydraulic pressure applied to the multianvil press.

dimensions of up to 1.6 mm in diameter were used. Details of the pressure calibration for this assembly are given by Mosenfelder et al. (2000). The 10/4 assembly with a straight $LaCrO_3$ heater and ZrO_2 thermal insulation was employed up to 24 GPa. Sample dimensions are 1 mm in diameter and 1 mm in length. The pressure calibration for this assembly at 1600°C is based on phase transformations in Mg_2SiO_4, such as forsterite (Fo) to wadsleyite (Wads) at 15 GPa (Morishima et al. 1994), wadsleyite to rindwoodite (Rwd) at 21 GPa (Katsura and Ito 1989) and the ringwoodite to Mg-silicate perovskite (MgPv) plus periclase (Pc) transformation at 24 GPa (Ito and

Takahashi 1989). The calibration curve of this pressure cell is shown in Figure 2.2. Pressures of 25 and 26 GPa have been reached using 10/3.5 and 8/3 pressure cells with a straight $LaCrO_3$ heater but no insulating ZrO_2. The sample dimensions are identical to the 10/4. The high temperature pressure calibration is based on liquidus phase relations in peridotite compositions and on the Al-content of Mg-silicate perovskite (Trønnes and Frost 2002).

Samples were encapsuled in Re-metal or graphite. Re-metal capsules were either produced from 25 μm thick foil or were spark eroded from solid Re-rods having diameters of 1 or 2 mm. In the latter procedure up to four sample chambers with diameters of approximately 250 μm were eroded in a single capsule (see Figure 2.3), providing the possibility of investigating several different starting compositions simultaneously at identical pressure and temperature conditions.

Temperatures in all assemblies were measured using axially inserted $W_{97\%}Re_{3\%}$ - $W_{75\%}Re_{25\%}$. The effects of pressure and temperature on the 'electromotive force' (*emf*) generated by a thermocouple are not well known. Experiments performed by Mao and Bell (1971) in a piston-cylinder apparatus up to 4 GPa and 1500°C, indicate that temperatures reported by W/Re thermocouples underestimate the real temperature ($\sim$30°C), with the effect becoming more pronounced with increasing pressure and temperature. Based on the latter study, Irifune (2002) argued that temperatures in a multianvil apparatus at $\sim$24 GPa and 1600°C are underestimated by not more than $\sim$80°C. This is a similar estimate compared with a value of $\sim$100°C at 22 GPa and 2400-2500°C, reported by Zhang and Herzberg (1994), which is based on the results of melting experiments performed in multianvil apparatus and laser-heated diamond

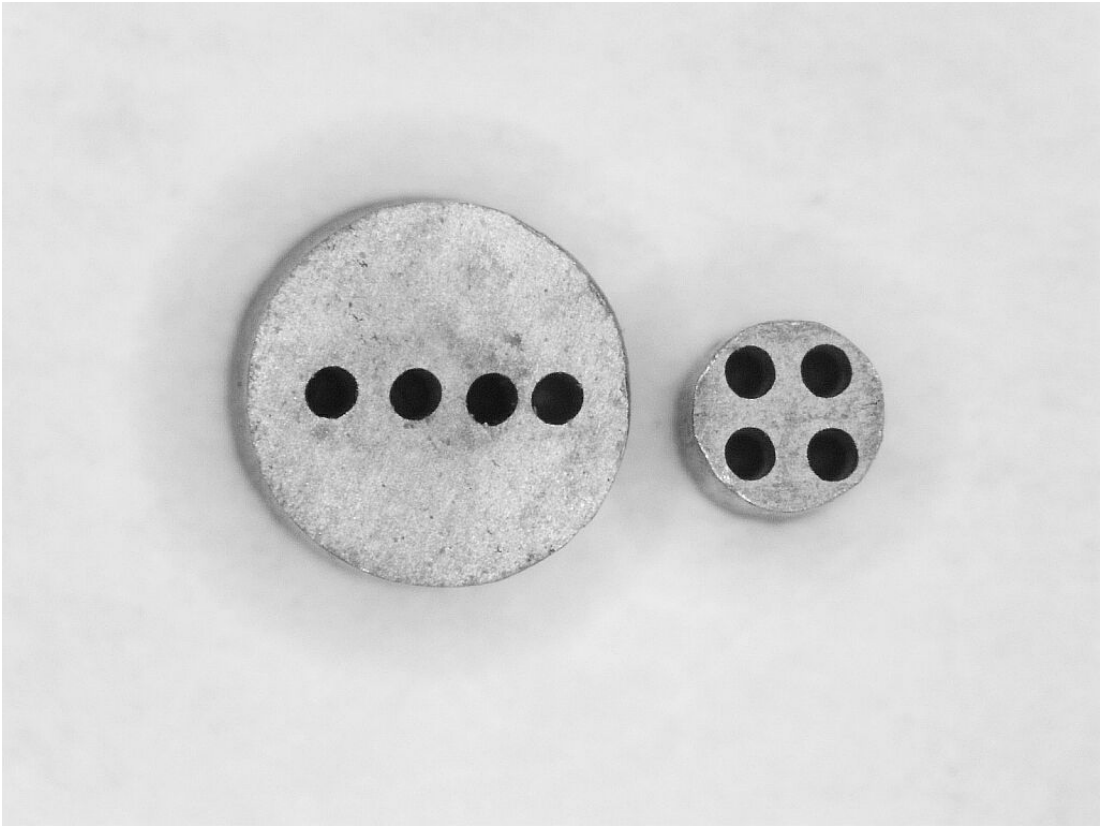

Figure 2.3: Examples of Re multi-chamber capsules produced by spark-erosion. Diameters of the capsules are 2 and 1 mm, respectively. Capsule heights were usually close to 1 mm. Sample chambers are approximately 250 μm in diameter. The left capsule can be used in the 18/8 assembly up to 24 GPa, while the smaller 1 mm capsule can be used up to 26 GPa using 10/4 or 8/3 pressure cells. Due to relatively small thermal gradients in pressure cells with stepped furnaces (18/11, 18/8) up to two multi-chamber capsules could be used in a single experiment.

anvil cells, respectively. However, Walter et al. (1995) pointed out that the effects of pressure and temperature on the thermocouple *emf* depend also critically on the experimental setup. In this study, no correction on the thermoucouple *emf* has been applied. The accuracy of reported temperatures is therefore not determined, but real temperatures are possibly on the order of $\sim$100°C higher than measured values.

Thermocouple wire of 260 μm diameter was used in the 18/11, 18/8 and 14/8 pressure cells, while 130 μm wire was used in 10 or 8 mm octahedra. The precision in run temperatures reported by the thermocouples in the 18 and 14 mm pressure cells is

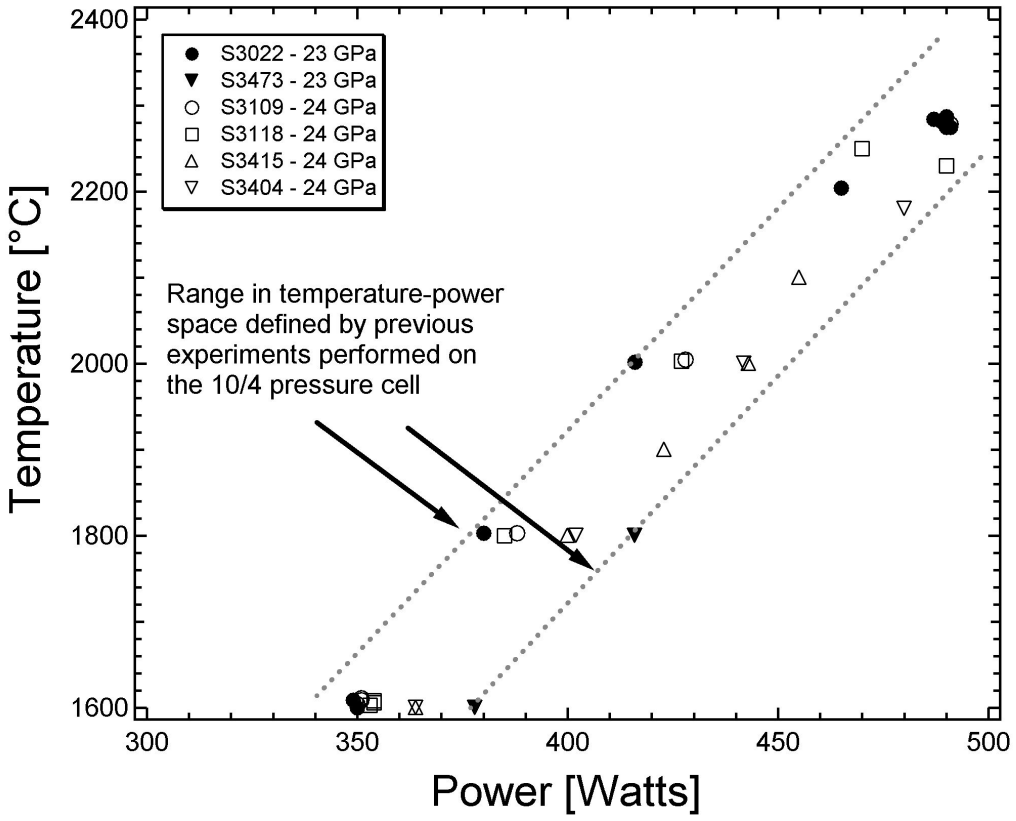

Figure 2.4: Temperature versus electrical power relationship for the 10/4 pressure cell. Run numbers correspond to experiments performed along the join Mg_2SiO_4-$MgSiO_3$.

estimated to be on the order of ±30°C. Precisions in reported temperatures in the 10 and 8 mm cells are estimated to be on the order ±50°C. In the small 10 and 8 mm pressure cells thermocouples sometimes failed during compression or during heating to the final temperature. In such cases the temperature was estimated from the electrical power to the furnace. Temperature-power relationships from other experiments performed on the same pressure cells have then been used for estimating run temperatures. The temperature-power calibration for the 10/4 assembly is shown in Figure 2.4. The uncertainty in the run temperature according to this approach is probably on the order of ±150°C. It is emphasised that temperatures reported by the thermocouples in the small 10 and 8 mm pressure cells represent temperature values at a specific point

along the thermal gradient and not necessarily the temperatures at the hotspot or sample temperatures. Bolfan-Casanova (2000) reported thermal gradients in the 10/4 pressure cell (measured by a second thermocouple) ranging from 85°C/mm at a nominal run temperature of 1200°C up to 170°C/mm at 1650°C. It is likely that thermal gradients at temperatures required for melting peridotite or chondrite compositions at lower mantle conditions (>2000°C) exceed 200 or 250°C/mm, especially in the even smaller 8/3 assembly. A direct comparison of temperatures among different experiments performed in a thermal gradient is therefore only possible, if the thermocouple in each experiment has the same position relative to a reference point, such as the hotspot of the furnace. Since this cannot be ensured, reported temperatures in 10 or 8 mm pressure cells should only be considered semi-quantitatively at melting conditions. Nonetheless, the multichamber technique allows different samples to be exposed to a thermal gradient in the same experiment, which provides information about relative melting temperatures based on the observed melt fractions in different starting compositions. Comparison of run textures and temperature-power relationships do therefore allow a self-consistent description of melting temperatures.

Experiments performed on the chemically complex peridotite and chondrite compositions (see section 2.4.3) using 10/3.5 and 8/3 pressure cells were performed without thermocouples. In addition to the relatively low reliability of thermocouples under lower-mantle melting temperatures (Trønnes and Frost 2002), the insertion of a thermocouple itself may cause an asymmetric temperature distribution in the pressure cell (Walter et al. 2004). Another problem is that the thermocouple may also cause damage to soft graphite capsules during compression. Temperature-power relationships for the

10/3.5 and 8/3 assemblies are less well constrained than those for the 10/4 assembly. Run temperatures leading to partially molten samples were estimated on the basis of reported solidus and liquidus temperatures for peridotites and chondrites by Trønnes and Frost (2002), Trønnes (2000) and Asahara et al. (2004). The uncertainty in temperature estimated for the solid-liquid boundary within the capsules (see section 2.4.2) in this approach is most likely on the order of the solidus-liquidus temperature interval, which is estimated to be approximately 150°C based on the aforementioned studies.

In order to perform experiments under nearly anhydrous conditions all ceramic parts of the pressure cell were fired at 1000°C prior to assembling the pressure cell. Sample powders were continuously stored in a vacuum oven at 220°C. After assembling the pressure cell, it was stored in the vacuum oven before it was used, usually the next day. The assemblage was first pressurised at room temperature, the temperature was then raised at a rate of approximately 100°C/min to the final temperature. Experiments were quenched by shutting off the electrical power to the furnace. Runs were then decompressed gradually over a period of 14-18 h.

Recovered run products were mounted in epoxy resin and then ground and polished for analytical investigations. In the case of graphite containers, the capsule material transformed to diamond under the experimental conditions. During decompression of the experiments the diamonds usually fractured strongly, such that the samples could be retrieved by removal of diamond pieces.

2.3 Analytical Techniques

Mineral phases were identified by micro-Raman spectroscopy using a *Dilor Labram* confocal spectrometer operating a 20 mW HeNe-Laser with a wavelength of 632.82 nm. Details of this technique are reported in McMillan and Hofmeister (1988). Spectra were obtained in backscattering mode under an optical microscope. Reference spectra were taken from McMillan et al. (1996) and references therein.

Major and minor element concentrations of coexisting phases were determined by electron microprobe analysis (EMPA). A detailed introduction to this analytical technique is given by Reed (1975). Samples in this study were analysed by either a four-spectrometer *Cameca SX-50* or a five-spectrometer *Jeol JXA-8200* microprobe. Samples were coated with a 6-10 μm thick carbon layer to avoid electrical charging of the surfaces. Analyses were performed using an acceleration voltage of 15 kV and variable beam currents and diameters depending on the investigated phases. Mineral phases were analysed with beam currents of 10-15 nA and a focused electron beam of approximately 2 μm. Silicate melts, which consist entirely of an intergrowth of quench crystals when quenched at the conditions used in this study, were measured with beam currents of 15-50 nA and beam diameters ranging from 10 to 50 μm. Counting times were 20 s on the peak and 10 s on the background for each element. Internal correction routines of the microprobes were used for data reduction and evaluation of element concentrations. The following synthetic minerals and oxides were used as standards for both microprobes: Si, Mg: enstatite; Al: spinel; Ca: wollastonite; Fe: wüstite or Fe-metal; Ti, Mn: $MnTiO_3$; Ni: NiO; Cr: Cr_2O_3; Na: albite; Re: metal.

Water concentrations in some experiments investigating Mg_2SiO_4-wadsleyite were de-

termined by Fourier-transform infrared (FTIR) spectroscopy using a *Bruker IFS 120* HR high resolution FTIR spectrometer coupled with a *Bruker* IR microscope. Measurements in the near-infrared (NIR) region were carried out on doubly-polished 100-150 μm thick sections using a tungsten light source and a CaF_2 beam-splitter. 200 scans were accumulated for each spectra. Water concentrations were derived by integrating absorption bands using the calibration of the extinction coefficients of Paterson (1982) and density factors reported in Bolfan-Casanova et al. (2000).

2.4 Results and Discussion

2.4.1 Estimation of Water Contents

In order to estimate the likely amount of water present in the experiments of this study, FTIR measurements on Mg_2SiO_4 wadsleyite samples were performed. Under subsolidus conditions wadsleyite can accommodate significant amounts of water (e.g. Smyth 1987, Kohlstedt et al. 1996) and its H_2O content measured on subsolidus high-pressure multianvil samples gives some indication of whether significant amounts water were present during the experiments. Spectra were measured on two subsolidus assemblages synthesised at 16 GPa, 1800°C for 20 min (S2942) and 22 GPa and 2000°C for 10 min (S2952), respectively. In both runs the Mg_2SiO_4 forsterite powder transformed completely to wadsleyite. In each experiment 10 spectra at different positions in the sample were measured. Average water concentrations of 170 $\pm$50 (S2942) and 70 $\pm$5 ppm (by weight) (S2952) were derived from integration of absorption bands between 3650 and 3180 cm^{-1}. Due to the relatively short run times it cannot be confirmed that complete hydration of the crystals occurred. However, the run- times were consistent

with those of most experiments in this study. It is therefore concluded, that the water concentrations in these samples most likely did not exceed 1000 ppm or 0.1 wt% water. Similar maximum water concentrations are therefore expected for other experiments performed in this study as a result of similar sample preparation procedures as described in section 2.2.2.

2.4.2 Interpreting Melting Experiments From Quench Textures

Thermal gradients are difficult to avoid in high-pressure multianvil experiments. Although such gradients can be minimised by the use of stepped heating elements (as in 18/11 and 18/8 pressure cells), their presence still has an influence on the local distribution of solids and melts in the sample capsule. Melting experiments performed in the presence of thermal gradients usually lead to complete separation of the solid and the liquid phases. This process has been investigated in detail, by Lesher and Walker (1988) for example, and can be portrayed using a simple phase diagram between the components A and B, as shown in Figure 2.5. A sample capsule containing the composition a_0 is exposed to a temperature range, which covers conditions from superliquidus to subsolidus as a result of the thermal gradient (indicated by the grey bar). According to the phase diagram the liquidus phase is A, but the liquid becomes more B-rich with decreasing temperature. Thus a compositional gradient in the liquid evolves along the thermal gradient. Because the liquid is interconnected, diffusion takes place in order to eliminate the compositional gradient. This mass flux, that occurs as a result of a compositional gradient along a thermal gradient, has been termed 'saturation gradient chemical diffusion' (Lesher and Walker 1988). The mass flux, however, leads to diffusion of component B towards the hot part of the capsule, such that this region

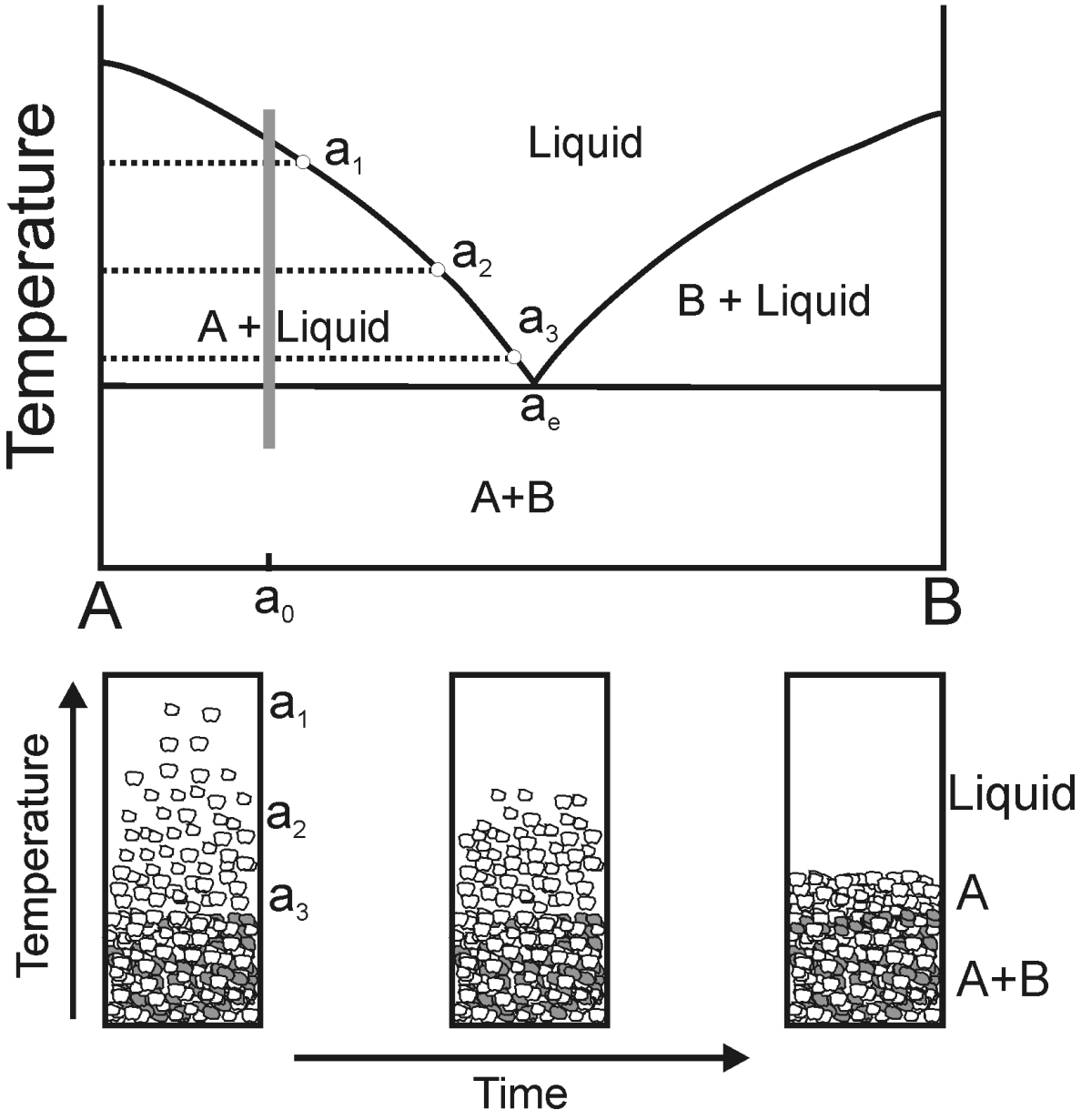

Figure 2.5: Upper part: schematic phase diagram to explain the textural evolution of a melting experiment in a thermal gradient. Lower part: the corresponding textural evolution in the sample capsule as a function of time. See text for details.

becomes oversaturated in the liquidus crystals A, which is consequently compensated by dissolution of this phase. On the other hand phase A must precipitate in the colder part of the capsule to maintain the local equilibrium. The situation in the sample capsule is shown in the lower part of Figure 2.5. At an initial time t=0 the capsule consists of an subsolidus phase assemblage (A, white crystals; B, grey crystals), and the liquidus region with a decreasing proportion of A with increasing temperature. Over time the liquidus region shrinks as a result of saturation gradient chemical diffusion and dissolution of A in the hot part and crystallisation of this phase in the cold part. This process proceeds until complete separation of crystals and liquid takes place, with the latter having an equilibrium composition somewhere between a_0 and the eutectic composition a_e. This melt composition corresponds to the temperature at the crystal-liquid boundary. The run texture then consists of a region of pure liquid, a layer of A and the subsolidus assemblage of A plus B (Figure 2.5, lower right). From the experimental run texture the sequence of crystallisation for the bulk composition a_0 can be interpreted as liquid plus A followed down temperature by A plus B (abbreviated as Liq-[A]-[A,B]), which is consistent with the phase diagram. Such a melting experiment may therefore be regarded as an isobaric section of a phase diagram, except that a single liquid composition is attained, that tends towards the eutectic composition. It is emphasised that the separation of liquid and solid in a thermal gradient is not significantly influenced by gravitational forces (e.g. Schmidt and Ulmer 2004, Presnall and Walter 1993). An additional process that may influence experimental run textures is related to compositional gradients within a liquid (known as 'Soret-effect'; Chipman 1926, Lesher and Walker 1988) as a result of the thermal gradient, such that it may

lead to a bulk chemical gradient in the sample. However, compositional gradients in the liquid are difficult to resolve in experiments where the melt does not quench to a glass, because of the relatively large standard deviations of averages, that are related to the analysis of quench crystals. Presnall and Walter (1993) reported no measurable compositional gradient in a melt obtained from an experiment performed on Mg_2SiO_4, indicating that compositional variations in such liquids may be absent or very small. It is therefore assumed that the Soret-effect has no resolvable effect on the present results. In a chemically complex peridotite or chondrite composition the thermal gradients lead to the segregation of the silicate melt and the creation of zones of solid phases. These zones most likely reflect the relative crystallisation sequence with decreasing temperature down the thermal gradient (e.g. Zhang and Herzberg 1994) as it has been described above. Critical for the evaluation of the phase relations for different chemical compositions is the correct identification of the liquidus phase for a given bulk composition. Experimentally, a liquidus phase in samples with no or weak thermal gradients is properly identified by the presence of a minor proportion of crystals coexisting with a large melt pool, which is chemically almost identical to the bulk composition. These conditions were not achieved in the experiments of this study and the liquidus phase is determined by making the assumption that it is the phase that is the closest to the melt pool. This approach is discussed further at the end of section 2.4.4.

2.4.3 Melting of Peridotites and Chondrites at Lower Mantle Conditions

Experiments on peridotite and chondrite bulk compositions were performed in 10/3.5 and 8/3 assemblies at approximately 25 and 26 GPa, respectively. Experimental run

conditions and the crystallising phase assemblages are summarised in Table 2.2. Run temperatures of experiments that show partial melting are estimated to be on the order of 2250°C for peridotite compositions (H2026, H2033a, S3237, S3242) and chondrite compositions with peridotitic Mg#'s (H2144) based on data from Trønnes and Frost (2002). The run temperature of the most Fe-rich CI-chondritic sample was probably ∼2100°C (Trønnes 2000, Asahara et al. 2004). The chemical compositions of coexisting phases are given in Appendix *A*. The partitioning of major, minor and trace elements between solid phases and liquids is discussed in Chapter 3. Backscattered electron images of recovered run products are shown in Figures 2.6 and 2.7.

Three slightly different peridotite compositions were investigated. Experiments H2026 and S3242 were performed on the 'normal' fertile peridotite model composition in a Re and graphite capsule, respectively. Run H2033a was enriched in Al_2O_3 (7 wt%, Re-capsule) and S3237 contained additional metallic Fe (∼30 wt%) and was performed in a graphite capsule. These three compositions, however, crystallised with an identical sequence of Fp on the liquidus followed down temperature by MgPv + Fp (abbreviated as Liq-[Fp]-[Fp, MgPv]), consistent with reported phases relations from Trønnes and Frost (2002) extrapolated to 25-26 GPa (see their Figure 1). It is interesting to note, that no significant layering of solid phases took place in experiment S3242 (see Figure 2.6), which indicates that saturation gradient chemical diffusion was not sufficient to complete separation over the runtime of the experiment, possibly as a result of the small liquid region, which indicates temperatures just above the solidus. Fp and MgPv crystallise almost cotectic in the liquid, but slightly more Fp crystals are present close to the melt pool, seen on the left side of the image. The Al-enriched peridotite

Table 2.2: Run conditions of melting experiments performed on peridotitic and chondritic compositions

Run#	**Pressure cell**	**Starting material**	**Capsule material**	**t (min)**	**Phase assemblage**
S3237	10/3.5	Peridotite+Fe^0	graphite	12	Liq-[Fp]-[Fp,MgPv,(CaPv)]
S3242	10/3.5	Peridotite	graphite	12	Liq-[Fp]-[Fp,MgPv,(CaPv)]
H2026	8/3	Peridotite	Re	10	Liq-[Fp]-[Fp,MgPv]
H2029	8/3	CI-chondrite	Re	16	Liq-[MgPv]-[MgPv, Fp]
H2033a	8/3	Al-rich peridotite	Re	10	Liq-[Fp]-[Fp,MgPv,(CaPv)]
H2144EC	8/3	EC mantle	Re double	15	Liq-[MgPv]
H2144CI	8/3	CI mantle	Re double	15	Liq-[St]-[St, MgPv, (CaPv)]

Pressure: 10/3.5 - 25 GPa; 8/3 - 26 GPa
Temperatures: peridotite and CI-, EC-mantle 2250°C, CI-chondrite 2100°C, see section 2.2.2 for details
Abbreviations: Liq: Liquid; MgPv: Mg-silicate perovskite; Mj: Majorite
Fp: ferropericlase; St: Stishovite; CaPv: Ca-silicate perovskite

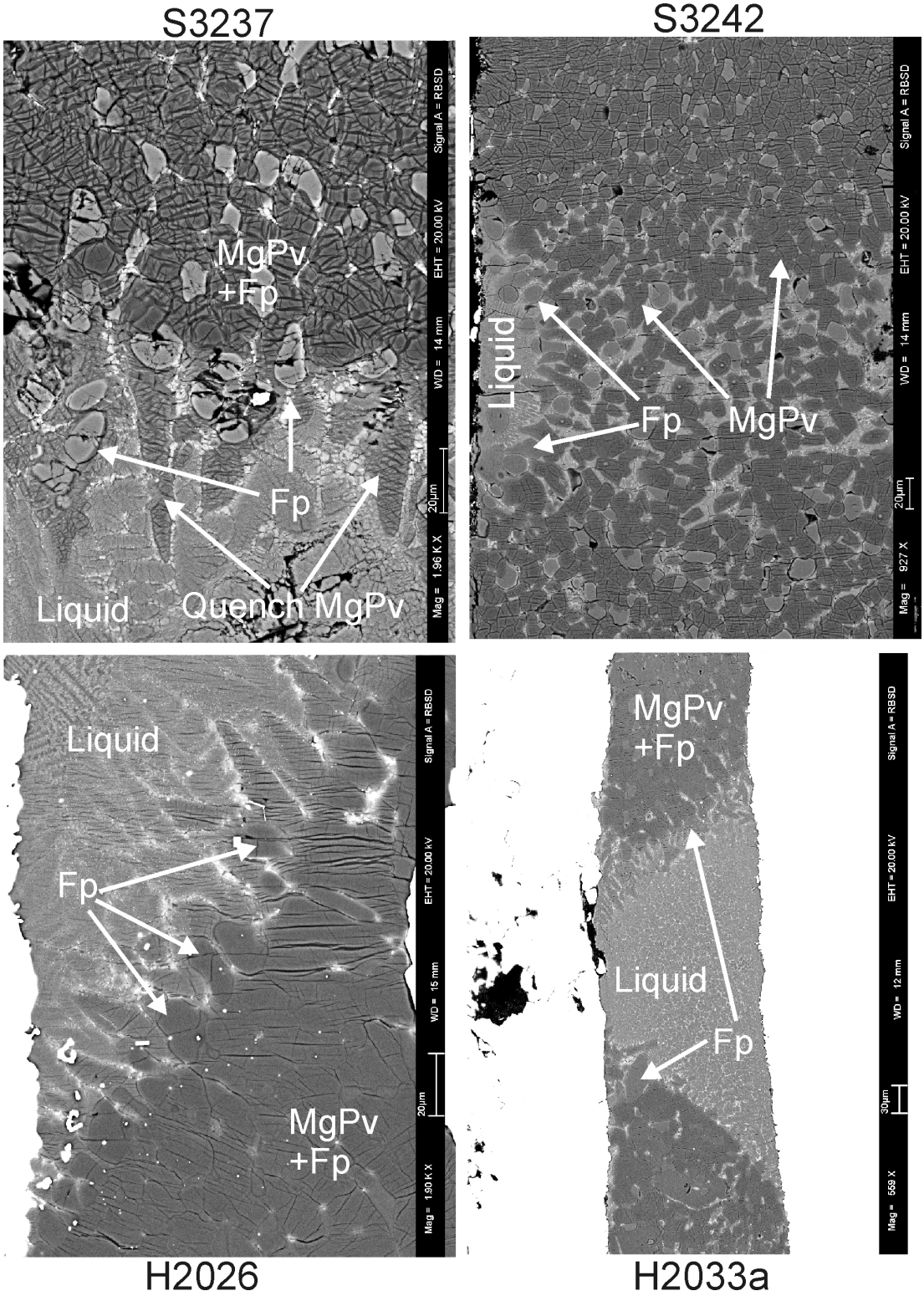

Figure 2.6: Backscattered electron (BSE) images of the peridotite samples produced at 25-26 GPa. In all samples ferropericlase (Fp) is the first phase, that crystallises down the thermal gradient followed by Fp and MgPv. See Table 2.2 for starting compositions.

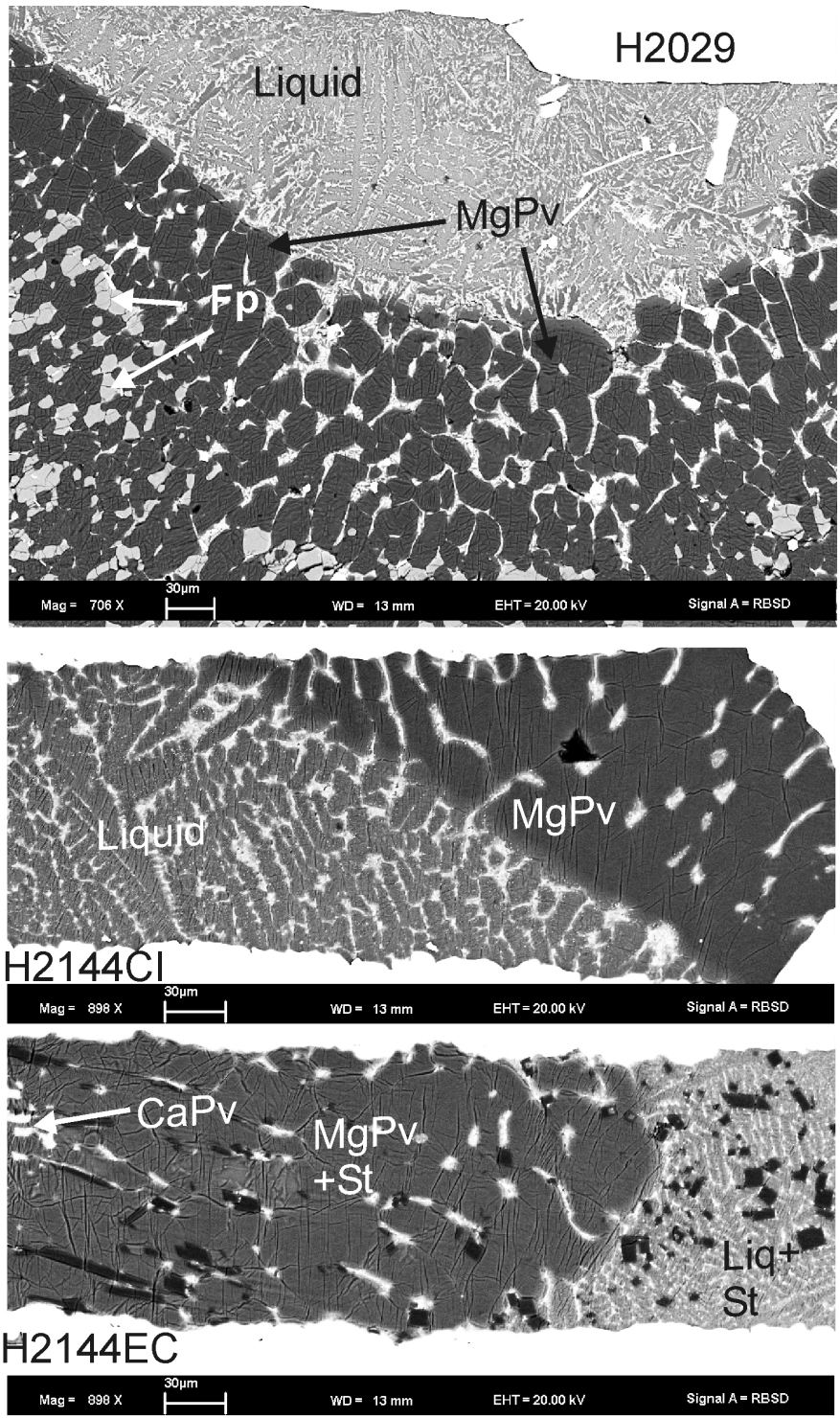

Figure 2.7: Chondritic samples synthesised in the 8/3 pressure cell at 26 GPa. The first crystallising phases down the thermal gradient in CI-chondritic samples are MgPv and St in the EC-chondritic sample. See Table 2.2 for starting compositions.

sample (H2033a) also contained majoritic garnet (Majorite, Mj) close to the liquidus. Although the pressure in all three melting experiments was above the majorite stability field for peridotite (Trønnes and Frost 2002), adding Al_2O_3 to H2033a has clearly expanded the majorite stability field, resulting also in an increased MgPv Al_2O_3 content in this experiment relative to the other MgPv compositions. The fact that the sample containing metallic Fe (S3237) shows an identical crystallisation sequence to the experiments in Re capsules implies that oxygen fugacity has no resolvable effect on the phase relations under these condition, assuming that the lower bulk Mg# of S3237, caused by oxidation of some Fe-metal, has no influence on the crystallisation sequence. The similarity of results obtained from melting experiments performed in graphite and Re-metal capsules also supports this conclusion.

Three different chondritic compositions have been studied in high-pressure melting experiments. H2029 is a CI-chondrite analogue composition, characterised by a lower Mg/Si ratio and lower Mg# compared to the fertile peridotite composition (see Table 2.1). Run H2144 was performed in a Re two-chamber capsule containing the CI-mantle and EC-mantle compositions with peridotitic Mg#'s of 0.89 but Mg/Si ratios of 1.05 and 0.80, respectively. In contrast to peridotitic compositions no Fp has been observed to be in direct contact with the melt pool in any of the chondritic compositions. In H2029 the first Fp grains were observed to crystallise approximately 100 μm away from the interface between the melt pool and the first crystallising phase which was MgPv (Figure 2.7). Thus the crystallisation sequence in H2029 is Liq-[MgPv]-[MgPv, Fp]. MgPv was also identified as the liquidus phase in the CI-mantle composition of H2144, but no Fp was observed along the thermal gradient. The EC-mantle sample

with the highest SiO_2 content showed stishovite (St) crystals floating in the silicate melt and solid regions consisting predominately of MgPv plus St with small amounts of CaPv in the coldest part of the charge (Figure 2.7). The crystallisation sequence is therefore determined to be Liq-[St]-[St,MgPv,(CaPv)]. Fp was also not observed in sample H2144EC.

2.4.4 The Effect of Pressure on Liquidus Phase Relations

Previous studies have shown that the liquidus phase in a peridotite bulk composition changes with pressure from olivine to majoritic garnet (Mj) at approximately 13-15 GPa (e.g. Takahashi 1986, Herzberg et al. 1990, Zhang and Herzberg 1994) and from Mj to ferropericlase (Fp) at about 22-23 GPa (Zhang and Herzberg 1994, Trønnes and Frost 2002). A recent study performed by Ito et al. (2004) at pressures up to 35 GPa indicates that the liquidus phase changes from Fp to Mg-silicate perovskite (MgPv) at 31 GPa (see Figure 1.3).

Melting relations in chondritic compositions at transition zone and/or lower mantle pressures have shown consistently that majoritic garnet is the liquidus phase up to approximately 24-25 GPa. The observation of Agee (1990) and Agee et al. (1995) that ferropericlase becomes the liquidus phase in compositions with low bulk Mg#'s (around 0.6) is not confirmed by the present experiments. In this study MgPv is the liquidus phase at 26 GPa in experiment H2029, in agreement with Asahara et al. (2004). Ito et al. (2004) reported experiments on a CI-chondrite model composition, that bracket a transition from majorite to MgPv on the liquidus between 22 and 28 GPa, which is thus consistent with the observation of MgPv as the liquidus phase in experiment H2144CI, which was performed at 26 GPa. The appearance of Fp on the liquidus in a

chondritic composition as observed by Agee (1990) and Agee et al. (1995), if it occurs at all, must be restricted to a relatively small pressure range of 1-2 GPa (see Figure 1.4). This is a remarkably small interval when compared to peridotitic compositions, where Fp is the liquidus phase over a pressure interval of approximately 8 GPa, i.e. from 23.5 GPa (Trønnes and Frost 2002) to ∼31 GPa (Ito et al. 2004). As Fp is the most FeO rich phase in both compositions it seems unlikely that the increased bulk Mg# will expand the Fp stability field in peridotite compositions relative to Fe-rich chondrite compositions. In fact, the CI-mantle composition with a peridotitic Mg# (H2144CI) shows no Fp in the solid region of the sample, which indicates that a high Fe-content (as in H2029) actually stabilises Fp.

The change in liquidus phase relations of chemically complex peridotite and chondrite compositions may be envisaged on simple phase diagrams in the system MgO-$MgSiO_3$ and is most likely related to the changes in the eutectic composition with increasing pressure. Liquidus phases are constrained by the location of the eutectic composition relative to the peridotite or chondrite bulk compositions, as shown schematically in Figure 2.8 along the join MgO-$MgSiO_3$. As the eutectic composition moves towards Mg_2SiO_4 as pressure increases to those of the transition zone (e.g. Presnall et al. 1998), the eutectic composition becomes more MgO-rich than either the chondrite or peridotite bulk compositions, which results in $MgSiO_3$ Mj being on the liquidus for both compositions (Figure 2.8a). Although there are no measurements of eutectic-like melt compositions in such chemically complex systems from high-pressure melting experiments, the observed phase relations in peridotites and chondrites suggest that the shift in the eutectic composition must change direction. With increasing pressure the

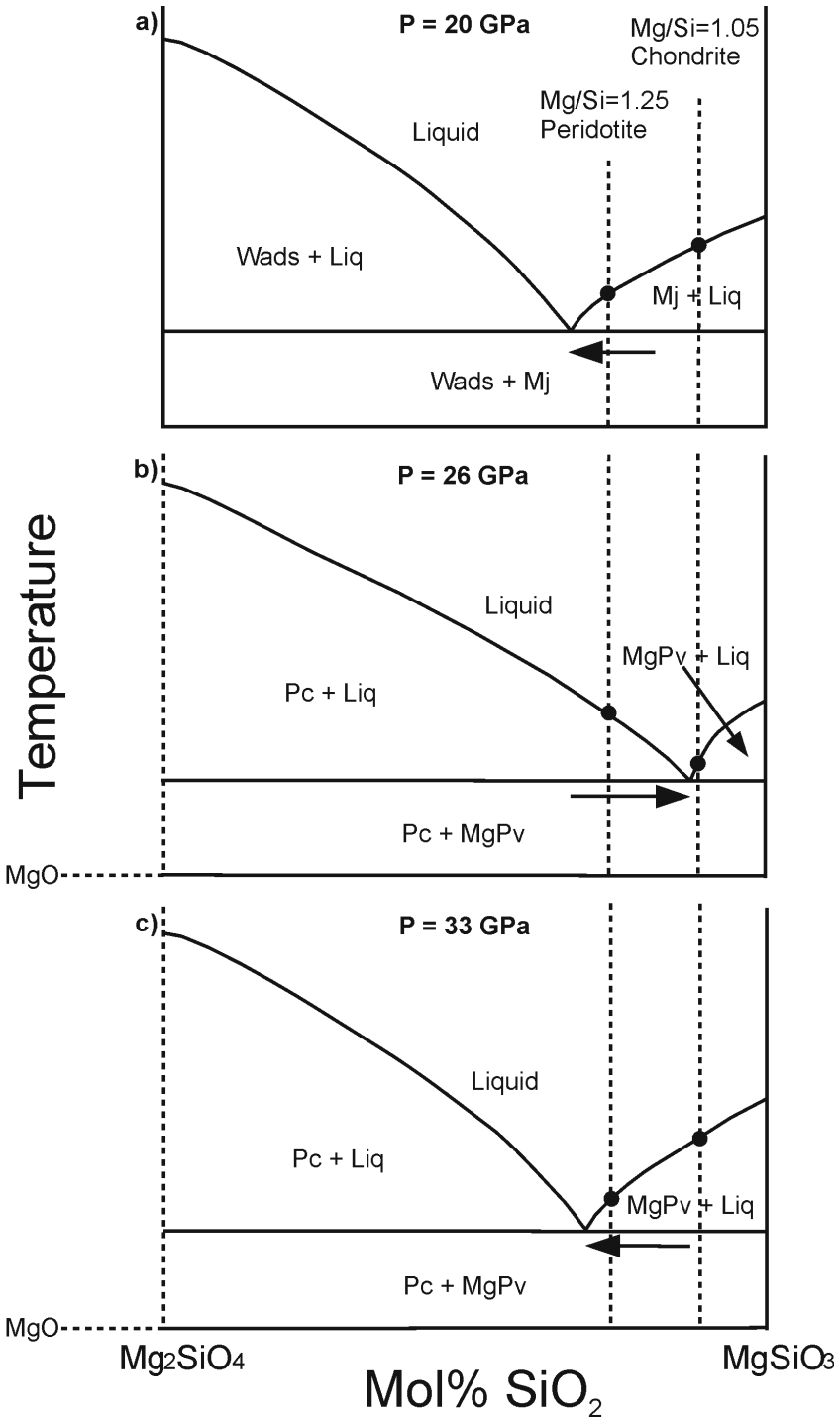

Figure 2.8: Phase diagrams along the MgO-$MgSiO_3$ join at a) 20 GPa, b) 25 GPa and c) 33 GPa, inferred from Presnall et al. (1998) and melting relations in peridotites and chondrites. Differences in phase relations between those compositions can be rationalised by their different bulk Mg/Si ratios and changes in the eutectic melt composition with pressure. Arrows indicate the direction in which the eutectic is moving at each pressure.

eutectic must move quite sharply towards MgPv between approximately 23 and 25 GPa, since ferropericlase appears on the liquidus. The situation at approximately 25 GPa is shown in Figure 2.8b where Fp is on the liquidus in the peridotite composition, while the chondrite composition is very close to the eutectic and may have either Fp or MgPv on the liquidus, depending on the exact bulk composition. Above 25 GPa the liquidus stability field of MgPv must expand at the expense of Fp as a result of a shift in the eutectic composition towards MgO again, because MgPv becomes the liquidus phase in a peridotite composition (Ito et al. 2004) at 31 GPa (Figure 2.8c). From this it follows that the equivalent cotectic composition in a complex system must cross any peridotitic composition twice between 23 and 33 GPa. This behaviour likely contributes to a relatively shallow pressure dependence of the liquidus temperature over this region, which would be consistent with the melting temperatures observed by Ito et al. (2004) between 20 and 30 GPa.

The description of the phase relations presented here depends critically on the correct identification of the liquidus phase. Thermal gradients and possibly compositional gradients in the capsules may complicate the evaluation of liquidus phase relations from experimental run textures. Nonetheless, the consistency between phase relations reported in different experimental studies is remarkable and, in addition, some studies have carefully evaluated crystallisation sequences using experiments performed at isobaric conditions but varying temperatures (e.g. Trønnes and Frost 2002). This consistency clearly supports the proposed melting systematics to explain liquidus phase relations in peridotite and chondrite compositions based on their different Mg/Si ratios. However, a more detailed investigation of eutectic compositions and basic phase

relations is presented in the following sections.

2.4.5 Melting in the System MgO-SiO_2

The liquidus phase relations of multi-component peridotite and chondrite compositions should be primarily determined by the liquidus phase relations along the joins of their major components SiO_2, MgO, FeO, Al_2O_3 and CaO. In order to test the proposed systematics in liquidus phase relations of peridotite and chondrite compositions, additional melting experiments in the system MgO-SiO_2 have been performed. Along this binary the particular attention has been paid to the compositional range between Mg_2SiO_4 and $MgSiO_3$. In particular, knowledge of the chemical composition of the eutectic at a given pressure allows the liquidus phase to be predicted for a specific bulk composition as described in the previous section.

At a given pressure, using the multichamber technique, different starting compositions along the binary can be melted at identical experimental conditions. Measured melt compositions and observed liquidus phases can then be used to construct phase diagrams. It is emphasised that this method of studying melting relations at high pressure provides the best possible consistency between the results of melting different chemical compositions. Experiments along the join MgO-SiO_2 have been performed at 16, 23, 24 and 26 GPa. Additional melting experiments on Mg_2SiO_4 compositions have also been carried out between 10 and 24 GPa.

Melting Along the Join MgO-SiO_2 at 16 GPa

Four experiments at 16 GPa have been performed in the 5000 tonne press at temperatures between 2160°C and 2360°C using Re multi-chamber capsules. Experimental

conditions, identified mineral phases and melt compositions are summarised in Table 2.3. Melt compositions presented in this section (2.4.5) were normalised to 100 mol%. Temperature measurements in the 18/11 pressure cell are believed to be significantly more reliable than values obtained from the smaller pressure cells as a results of the use of thicker and more stable thermocouple wire and the stepped $LaCrO_3$ heater, which reduces thermal gradients (Frost et al. 2004b). Run temperatures recorded by the thermocouples varied within ±10°C of the reported values during the experiments. Recovered samples were prepared as polished sections, such that all sample chambers were exposed parallel to the cylindrical axis of the capsules in order to observe the phase relations along the thermal gradient. Experiments Z282 and 294 have been performed with two capsules each containing three samples chambers, while experiments Z295 and Z297 contained one capsule having four chambers. A backscattered electron image of run Z282, as an example of such recovered multichamber capsules, is shown in Figure 2.9.

Experiment Z294 was performed at the lowest temperature of 2160°C. Two sample chambers of this experiment, containing $Fo_{25}En_{75}$ and $Fo_{50}En_{50}$ mixtures (given in mol%), contain partial melts (Figure 2.10). The sample chamber containing the $Fo_{50}En_{50}$ composition contains only a small amount of melt in equilibrium with wadsleyite (Wads), indicating a run temperature only slightly above the solidus, which was therefore estimated to be 2150 ±30°C. This temperature is in good agreement with estimates of Kato and Kumazawa (1990) of $T_{eutectic}$=2130°C at 15 GPa but lower than values of 2240-2250°C reported by Presnall and Gasparik (1990). The measured liquid composition is, within error, identical to the melt in the chamber containing

Table 2.3: Run conditions of melting experiments performed along the join MgO-SiO_2 at 16 GPa using the 5000 tonne press. Starting materials were forsterite (Fo), enstatite (En) and quartz (Qz) components and mixtures of them (given in mol%). Element concentrations are given in mol% and are normalised to 100%. *n* denotes the number of analyses.

run	**P [GPa]**	**T [°C]**	**t [min]**	**Mixture**	**Phases**	**n**	**SiO_2**	**MgO**	**Mg/Si**
Z282	290bar	2220	5	Fo	Liq - AnhB	15	42.7 (1.8)	57.3 (2.5)	1.34 (8)
	16GPa			Qz	St		-	-	-
				En	Liq		-	-	-
				En25Qz75	Liq-[St]	21	51.3 (5)	48.7 (1.0)	0.97 (2)
				Fo75En25	Liq-[AnhB]	22	42.1 (1.2)	57.9 (1.9)	1.38 (6)
				Fo	Liq-[AnhB]	17	42.1 (9)	57.9 (9)	1.37 (4)
Z294	290bar	2160	10	Peridotite	Liq-[Mj]-[Mj,Fp]	-	-	-	-
	16GPa			En	Mj	-	-	-	-
				Fo25En75	Liq-[Mj]	38	44.1 (7)	55.9 (1.0)	1.27 (3)
				Pc85Qz15	[Pc, Wads]	-	-	-	-
				En75Qz25	[Mj, St]	-	-	-	-
				Fo50En50	Liq-[Wads]	7	45.5 (2.4)	54.5 (4.1)	1.20 (11)
Z295	290bar	2360	2	En50Qz50	Liq	14	53.1 (9)	46.9 (1.4)	0.88 (3)
	16GPa			Fo	Liq	20	44.0 (3)	56.0 (4)	1.27 (1)
				En75Qz25	Liq	18	48.1 (3)	51.9 (4)	1.08 (1)
				Fo75En25	Liq	16	45.3 (7)	54.7 (1.1)	1.21 (3)
Z297	290bar	2270	3	En50Qz50	Liq-[St]	10	51.0 (8)	49.0 (1.2)	0.96 (3)
	16GPa			Fo100	Liq-[Pc]	20	41.4 (1.0)	58.6 (1.3)	1.42 (5)
				Fo50En50	Liq-[Pc]	23	40.3 (6)	59.7 (9)	1.48 (3)
				En75Qz25	Liq	34	54.9 (3)	45.1 (4)	0.82 (1)

Abbreviations: Liq: Liquid, Pc: Periclase, St: Stishovite, Mj: Majorite
AnhB: Anhydrous B, Wads: Wadsleyite

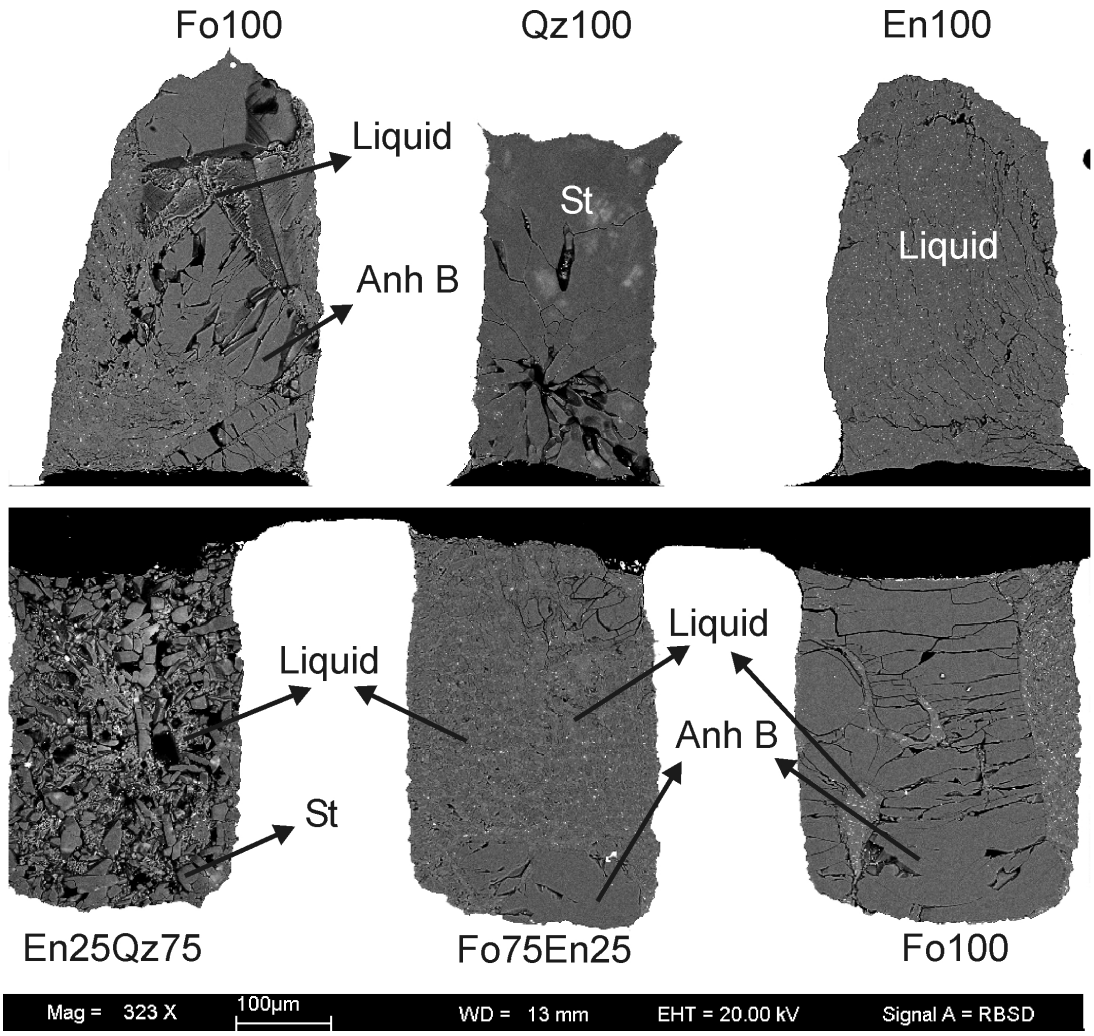

Figure 2.9: Backscattered electron (BSE) image of run Z282 performed in the 5000 tonne press in a 18/11 pressure cell using two Re multi-chamber capsules. The figure is composed from two different images, but shows the relative position of the two capsules during the experiment. Sample capsules were separated by Re-foil discs. Five different compositions have been used. For comparison, in each capsule one Fo_{100} composition has been added to check for identical melt compositions.

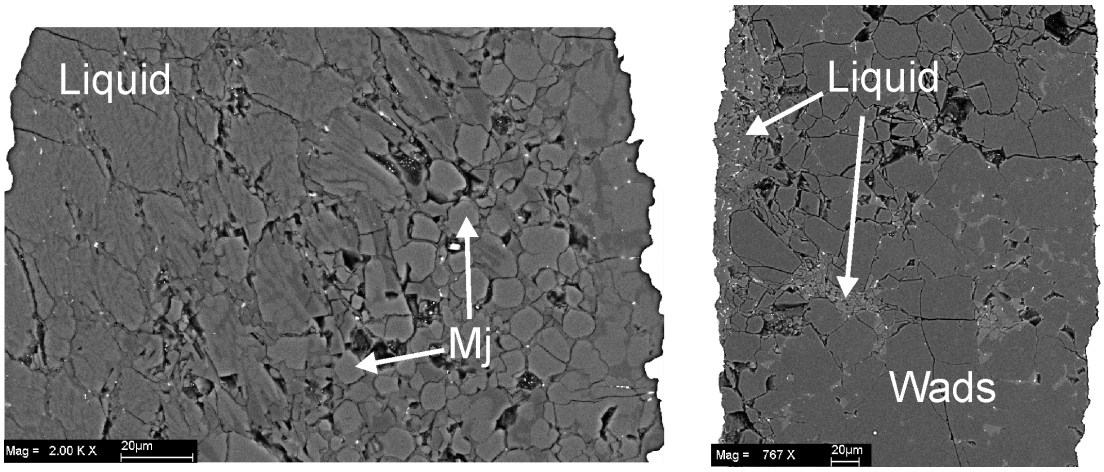

Figure 2.10: BSE images of sample chambers of run Z294 initially filled with $Fo_{25}En_{75}$ (left) and $Fo_{50}En_{50}$ (right)

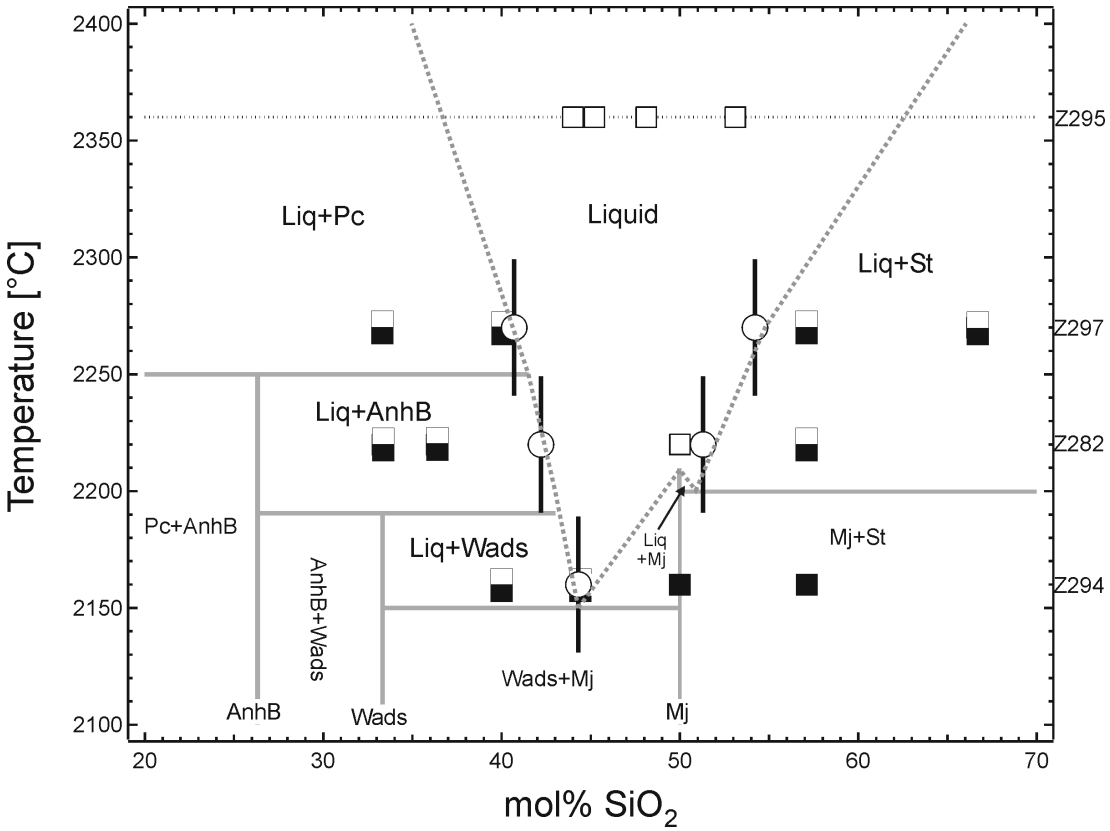

Figure 2.11: Phase diagram along the join MgO-SiO_2 at 16 GPa inferred from high-pressure multi-chamber experiments. Open squares indicate compositions of completely molten samples, filled squares those of solid samples. Half-filled rectangles represent the starting compositions of partially molten samples and open circles with error bars their weighted average melt compositions. Liquidus curves were interpolated linearly to the melting points of pure MgO and SiO_2 at 16 GPa (Zerr and Boehler 1994, Belonoshko and Dubrovinsky 1995).

the $Fo_{25}En_{75}$ mixture, which has majorite (Mj) on the liquidus. The weighted average melt composition, which should be very close to the eutectic composition, has a SiO_2 content of 44.3 ±0.7 mol% (MgO and SiO_2 were normlised to 100%), which is in good agreement with a previously measured value of 44 mol% SiO_2 (Presnall and Gasparik 1990). This experiment also contained the fertile peridotite composition, which showed a crystallisation sequence of Liq-[Mj]-[Mj,Fp], which is consistent with the liquidus phase for the $Fo_{25}En_{75}$ composition, which has a Mg/Si ratio identical to that of the peridotite. The melt fraction in the complex composition is slightly higher compared with the melt fraction in the simple binary system.

The stable mineral phases and the melt compositions have been used to construct a phase diagram which is shown in Figure 2.11. At 16 GPa wadsleyite melts incongruently to a Mg-rich phase with the composition 26.5±0.1 mol% SiO_2 and 73.5±0.1 mol% MgO plus liquid. The solid composition is very close to the ideal stochiometry of phase anhydrous B (AnhB) ($Mg_{14}Si_5O_{22}$, 26.3 mol% SiO_2 and 73.7 mol% MgO; e.g. Finger et al. 1991), which has also been observed in melting experiments in previous studies (e.g. Kato and Kumazawa 1986, Presnall and Gasparik 1990, Presnall and Walter 1993) at similar pressures. Phase anhydrous B was therefore identified by stoichiometry. At temperatures between 2220 and 2270°C the melting reaction changes from wadsleytite = AnhB + liquid to AnhB + liquid = periclase (Pc) + liquid. The univariant boundary between Pc+Liq and liquid has been interpolated linearly between the melting temperature of pure MgO of ∼3200°C at this pressure (inferred from Zerr and Boehler 1994) and the melt composition of run Z297 at 2270°C (see Figure 2.11). It is emphasised that there is no thermodynamic requirement for the liquidus curves

to be straight, but any curvature cannot be resolved. The melting temperature of majorite has not been determined in the present experiments. Presnall and Walter (1993), however, noted that the melting curves of Mg_2SiO_4 and $MgSiO_3$ cross at approximately 13 GPa due to the higher Clapeyron-slope of the latter component. This results in the melting point of $MgSiO_3$ at 16 GPa being about 20°C higher than that of Mg_2SiO_4. In this way, the melting temperatures of wadsleyite and majorite were determined to be 2190°C and 2210°C, respectively. These temperatures are, however, significantly lower than the values of approximately 2300-2350°C at 16 GPa given by Presnall and Gasparik (1990) and Presnall and Walter (1993). This difference in reported melting temperatures is probably not related to the presence of water, which can have a significant effect on melting temperatures. Estimations of water contents in previous studies are not given, but the reported experimental proceedures suggest that water concentrations may have been similar compared to values estimated in this study. The discrepancies in reported melting temperatures are more likely the result of different pressure cells and/or experimental setups. This demonstrates the difficulties in comparing experimentally determined temperatures in such high-pressure melting experiments.

The congruent melting behaviour of Mj (Presnall and Gasparik 1990) implies that a second eutectic composition must exist between $MgSiO_3$ and SiO_2. Because $MgSiO_3$ melts congruently, this intermediate composition can be regarded as one component. Thus, if the univariant boundary between St+Liq and Liq would intersect the $MgSiO_3$ melting point, the phase rule would be violated because only two phases (majorite and liquid) can be stable at this point. Furthermore, mass balance constraints also pro-

hibit the intersection of the univariant boundary St+Liq/Liq and the majorite melting point. The location of this eutectic point is constrained by experiment Z282 and the melt composition in the sample chamber containing $En_{75}Qz_{25}$ to be between 50 and 51.3 ±0.5 mol% SiO_2. Since this eutectic composition is very close to the Mj bulk composition this implies that the temperature difference between the melting point of Mj and the eutectic temperature from the reaction Mj+St=Liq is most likely very small. Experiment Z295 was performed at the highest temperature of 2360°C. The recovered sample contained completely molten samples, but the measured melt composition in each chamber differs from the inital starting compositions (see Table 2.3). This is most likely the result of either some contamination of the intitial compositions during loading of the capsule or of some melt exchange during the experiment, or both. It is emphasised that only measured melt compositions and identified liquidus phases within the individual sample chambers are used to constuct the phase diagrams. Therefore, a potential contamination of initial starting compositions during capsule loading or during the experiment results only in an uncertainty surrounding the bulk composition.

Melting Along the Join MgO-SiO_2 at 23 GPa

Melting experiments at 23 GPa have been performed in the 10/4 pressure cell using 1 mm Re capsules containing four sample chambers, as shown in Figure 2.3. The thermocouples in these experiments failed during heating to the final temperature. Temperatures were therefore estimated from the calibration shown in Figure 2.4. Run conditions including electrical power used for heating, starting compositions and chemical analyses of the melts are summarised in Table 2.4. Recovered capsules were cut with a diamond wire saw parallel to the rotational axis of the cylindrical capsule to

obtain a section of all sample chambers along the thermal gradient.

Experiment S3462 crystallised subsolidus at approximately 2120°C. The recovered run products contained a phase assemblage of Wads, MgPv and ringwoodite (Rwd). The subsolidus stability field of Wads + MgPv along the join Mg_2SiO_4-$MgSiO_3$ has been reported in an experimental study between 22-23 GPa by Gasparik (1990). It is emphasised that MgPv at this pressure forms from the phase transition of the $MgSiO_3$ component and not by the breakdown of Mg_2SiO_4 wadsleyite. The presence of ringwoodite in experiment S3462 is likely the result of the thermal gradient, which causes ringwoodite to crystallise at the cold end of the capsule, while wadyleyite is stable at the hot end. All sample chambers in the experiments S3468 and S3473 contained small amounts of melt, whereas the melt fractions in chambers containing the same starting composition are almost identical between both experiments. In fact, a temperature difference between these two experiments cannot be resolved from the experimental run textures, although the electrical power in S3473 was about 10 Watts higher than in S3468. The small melt fraction indicates that the experiments were performed close to the eutectic temperature. BSE images of experiment S3473 are shown in Figure 2.12. Assuming a Clapeyron-slope for the eutectic temperature of 5-10°C/GPa the eutectic temperature at 23 GPa should be on the order of 2200°C, which is consistent with the temperature-power curves.

Melts in chambers filled with the same starting material in experiments S3468 and S3473 have, within error, the same chemical compositions. In both experiments, liquids in chambers containing Fo_9En_{91} and $Fo_{25}En_{75}$ mixtures coexist with MgPv and have average SiO_2 contents of 44.6±0.5 mol%. Melts present in chambers contain-

Table 2.4: Run conditions of melting experiments performed along the join MgO-SiO_2 at 23 GPa using the 10/4 pressure cell

run	P [GPa]	T [°C]	t [min]	Mixture	Phases	n	SiO_2	MgO	Mg/Si
S 3462	23	2120[a]	3	Fo9En91	[Wads,Pv,Rwd]		-	-	-
		460 Watts		Fo25En75	[Wads,Pv,Rwd]		-	-	-
				Fo34En66	[Wads,Pv,Rwd]		-	-	-
				Fo50En50	[Wads,Pv,Rwd]		-	-	-
S 3468	23	2220[a]	3	Fo9En91	Liq-[Pv]-[Pv,Wads]	8	42.5 (5)	57.5 (1.7)	1.36 (5)
		470-475 Watts		Fo25En75	Liq-[Pv]-[Pv,Wads]s	22	43.5 (1.2)	56.5 (1.8)	1.30 (5)
				Fo34En66	Liq-[Wads,Pv]-[Wads,Pv]	12	43.4 (1.1)	56.6 (1.7)	1.30 (5)
				Fo50En50	Liq-[Wads]-[Wads,Pv]	14	44.4 (1.3)	55.6 (1.9)	1.25 (6)
S 3473	23	2220[a]	3	Fo9En91	Liq-[Pv]-[Pv,Wads]	2	44.2	55.8	1.26
		480-485 Watts		Fo25En75	Liq-[Pv]-[Pv,Wads]	18	43.2 (1.2)	56.8 (1.9)	1.32 (6)
				Fo34En66	Liq-[Wads,Pv]-[Wads,Pv]	17	44.7 (1.2)	55.3 (1.6)	1.24 (5)
				Fo50En50	Liq-[Wads]-[Wads,Pv]	15	43.7 (6)	56.3 (1.0)	1.29 (3)

a) estimated from electrical power and/or run textures
Abbreviations: Liq: Liquid, Pc: Periclase, Rwd: Ringwoodite
Wads: Wadsleyite, Pv: Mg-perovskite

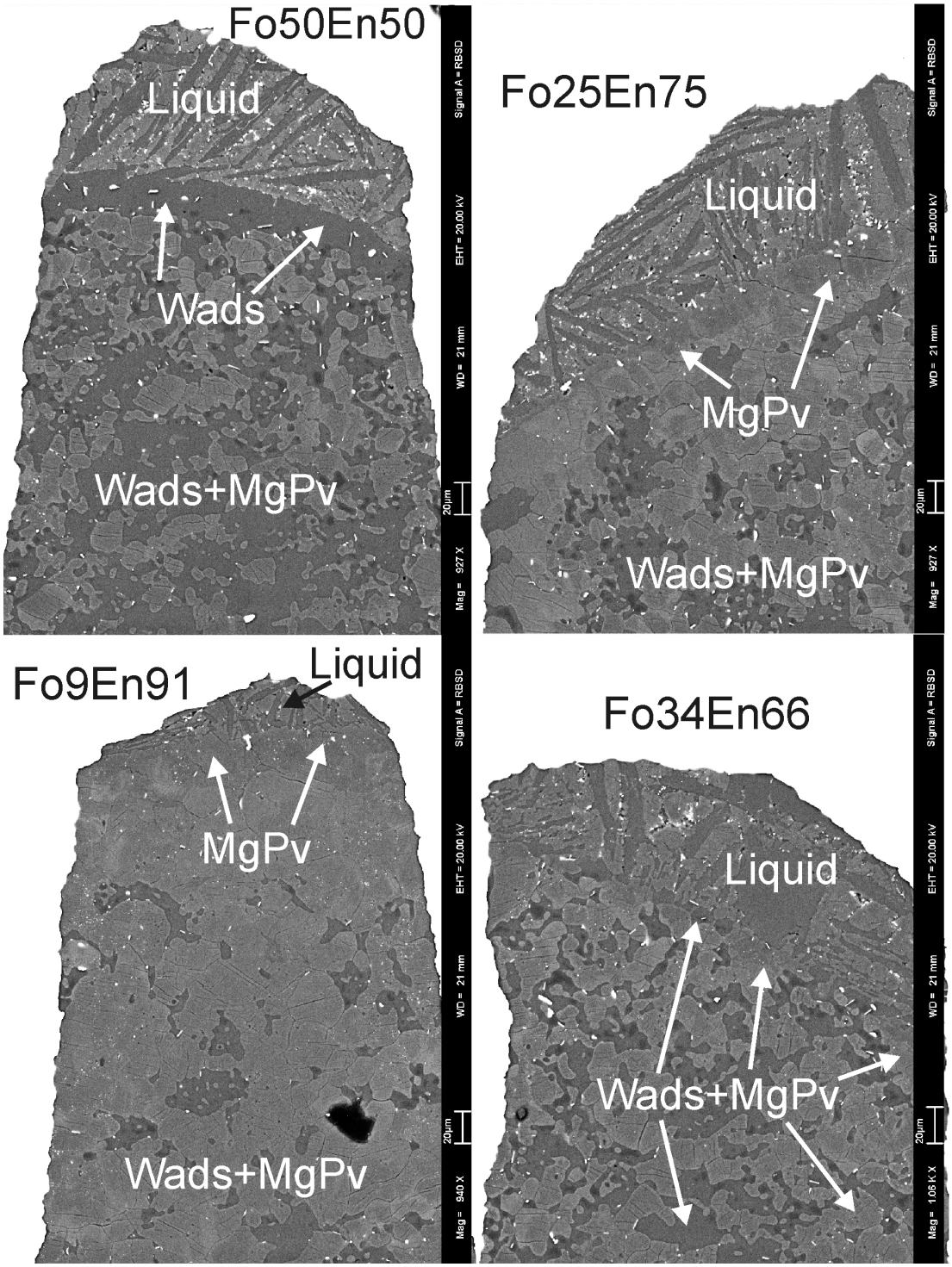

Figure 2.12: BSE images of sample S3473. The sample chamber filled with $Fo_{34}En_{66}$ shows both wadsleyite and Mg-silicate perovskite in contact with the liquid, indicating equilibrium with the eutectic melt composition.

ing $Fo_{50}En_{50}$ have an average SiO_2 content of 43.6±0.5 mol% and are in equilibrium with Wads. In both runs, melts in chambers containing $Fo_{34}En_{66}$ are in contact with MgPv and Wads. Their weighted average chemical composition is 44.0±0.8 mol% SiO_2, which must be at or very close to the eutectic composition, because both phases (MgPv and Wads) are in equilibrium with the liquid. The determined eutectic composition has a slightly higher SiO_2 content than the value of 42.3±0.8 mol% reported by Gasparik (1990) in the wadsleyite plus MgPv stability field. The corresponding phase diagram along the join Mg_2SiO_4 - $MgSiO_3$ is shown in Figure 2.13. To construct the phase diagram, the Clapeyron-slope of the melting curves of Mg_2SiO_4 was estimated to be consistent with the temperature increase of the eutectic between 16 and 23 GPa (50°C). The estimated melting temperature of approximately 2240°C is consistent with the temperatures determined in melting experiments on Mg_2SiO_4 (see below). Because the the Clapeyron-slope of the melting curve of $MgSiO_3$ is steeper than that of Mg_2SiO_4 (e.g. Presnall and Walter 1993) the melting temperature of MgPv was estimated to be 2270°C. This value is in good agreement with the melting temperature of $MgSiO_3$ of 2250°C at 20 GPa reported by Kato and Kumazawa (1985b) but is significantly lower than the temperature of ∼2500°C estimated by Ito and Katsura (1992). The join $MgSiO_3$-SiO_2 was not investigated at this pressure, but it is likely that a second eutectic occurs at compositions slightly more SiO_2-rich than MgPv, as deduced at 16 GPa, because MgPv melts congruently (e.g. Ito and Katsura 1992). The univariant boundary between liquid and Liq+Pc has been constructed to extrapolate to the melting point of MgO at 23 GPa of ∼3500°C (Zerr and Boehler 1994).

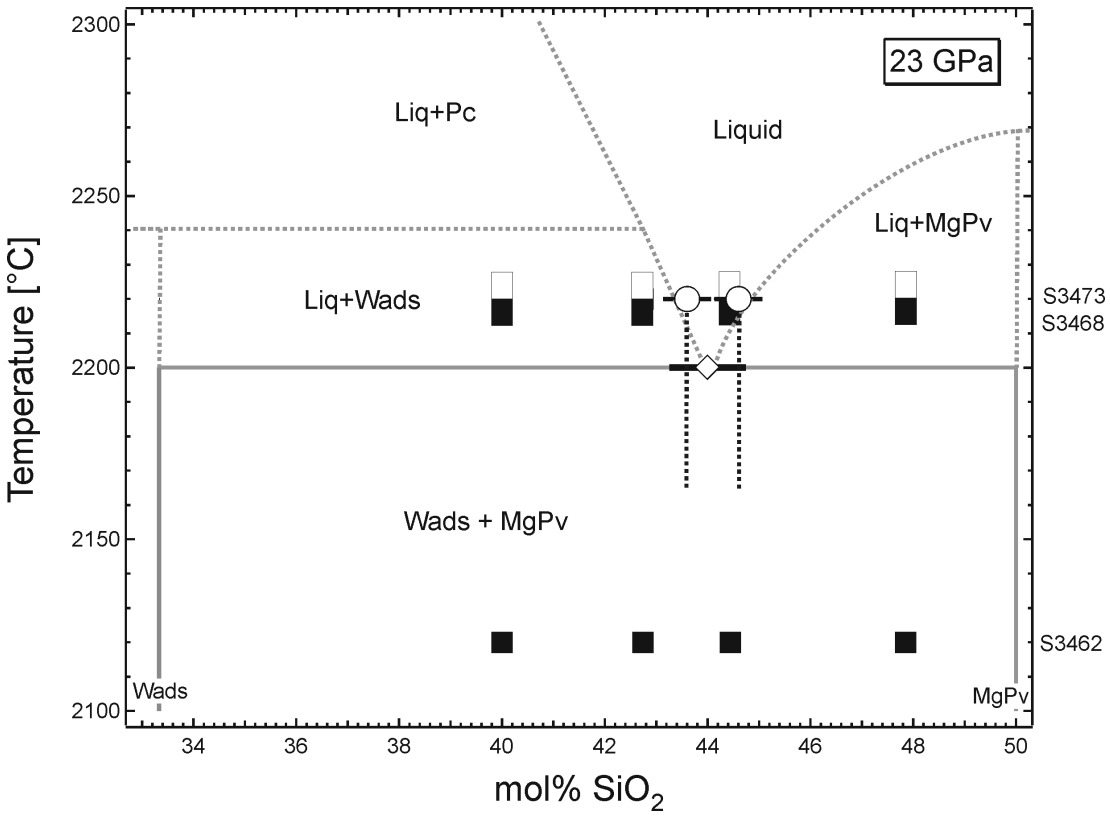

Figure 2.13: Phase diagram along the join Mg_2SiO_4-$MgSiO_3$ constructed from stable mineral phases and melt compositions of high-pressure melting experiments. The eutectic (indicated by the diamond symbol) is located at 44.0 ±0.5 mol% SiO_2. As in Figure 2.11, half-filled rectangles represent the starting compositions of partially molten samples and open circles show average melt compositions. The vertical black dotted lines are indications of the temperature regimes suggested by the run texture, such that the sample was exposed to conditions ranging from subsolidus to liquidus temperatures. The indicated temperature range is not necessarily equivalent to the temperatures present in the capsule during the experiment.

Melting Along the Join MgO-SiO_2 at 24 GPa

Three multi-chamber melting experiments at 24 GPa were performed using the 10/4 assembly. An additional experiment was performed in the 5000 tonne press (Z299). Run conditions, electrical power, observed phases along the thermal gradient and liquid compositions are given in Table 2.5.

Run Z299, performed at 2200°C in the 18/8 pressure cell showed a solid phase assem-

Table 2.5: Run conditions of melting experiments performed along the join MgO-SiO_2 at 24 GPa using the the 10/4 (S3403, S3404, S3415) and 18/8 (Z299) pressure cell

run	P [GPa]	T [°C]	t [min]	Mixture	Phases	n	SiO_2	MgO	Mg/Si
S 3403	24	2150[a)]	3	Fo100	[Pv, Pc]		-	-	-
	(450 bars)	455-460 Watts		Fo75En25	[Pv, Pc]		-	-	-
				Fo50En50	[Pv, Pc]		-	-	-
				Fo25En75	[Pv, Pc]		-	-	-
S 3404	24	2320[a)]	3	Fo100	Liq-[Pc]	14	41.7 (5)	58.3 (6)	1.40 (2)
	(450 bars)	480 Watts		Fo75En25	Liq-[Pc]	20	41.6 (6)	58.4 (9)	1.40 (3)
				Fo50En50	Liq-[Pc]	17	41.8 (4)	58.2 (6)	1.39 (2)
				Fo25En75	Liq	25	43.1 (4)	56.9 (4)	1.32 (1)
S 3415	(450 bars)	2290[a)]	3	Fo34En66	Liq-[Pv]-[Pv,Pc]	25	42.7 (1.1)	57.3 (1.1)	1.34 (4)
		470 Watts		Fo9En91	Liq-[Pv]	25	46.6 (8)	53.4 (7)	1.15 (2)
				En100	Liq	25	49.9 (4)	50.1 (6)	1.01 (1)
				En80Qz20	Liq-[St]	14	50.9 (7)	49.1 (1.0)	0.96 (2)
Z 299	24	2200	4	Fo100	[Pv, Pc]		-	-	-
				En100	[Pv]		-	-	-
				Fo25En75	[Pv, Pc]		-	-	-
				Fo75En25	[Pv, Pc]		-	-	-
				Pc85Qz15	[Pc, Pv, St]		-	-	-

a) estimated from electrical power

blage consisting of MgPv + Pc along the join MgO-$MgSiO_3$ and of MgPv + St along the join $MgSiO_3$-SiO_2. Sample S3403 also crystallised completely subsolidus with a phase assemblage of $MgSiO_3$ perovskite (MgPv) plus MgO periclase (Pc). The run temperature inferred from the calibration shown in Figure 2.4 was ∼2150°C in the latter experiment. The run temperature of S3415 was estimated to be 2290°C. BSE images of this experiment are shown in Figure 2.14. Melt compositions in sample chambers containing Fo_9En_{91} and $Fo_{34}En_{66}$ mixtures are close to the initial compositions and were both found to be in contact with MgPv. The sample chamber containing the $En_{80}Qz_{20}$ mixture contained stishovite (St) liquidus crystals coexisting with a melt containing 50.9 ± 0.7 mol% SiO_2. Since MgPv melts congruently at ∼2280°C this again implies a second eutectic between MgPv and St, which must lie between 50 and 50.9 ± 0.7 mol% SiO_2.

The melt fraction in sample S3404 is higher than in S3415. The run temperature of S3404 was therefore estimated to be ∼2320°C. The sample chambers in S3404 containing Fo_{100}, $Fo_{75}En_{25}$ and $Fo_{50}En_{50}$ compositions show the presence of layers of Pc at the cold end of the capsule, increasing in thickness with increasing bulk Mg-content. The liquid compositions in these chambers are identical within error and have a weighted average SiO_2 content of 41.7 ±0.4 mol%. The $Fo_{25}En_{75}$ starting composition is completely molten. The eutectic melt composition along the join Mg_2SiO_4-$MgSiO_3$ at 24 GPa is therefore bracketed between 41.7 mol% SiO_2 and the melt composition of run S3415, which has the highest SiO_2 content of 42.7 mol%, while still being in equilibrium with MgPv. The eutectic temperature is estimated to be approximately 2210°C.

An interesting observation is that at similar electrical output power values to the fur-

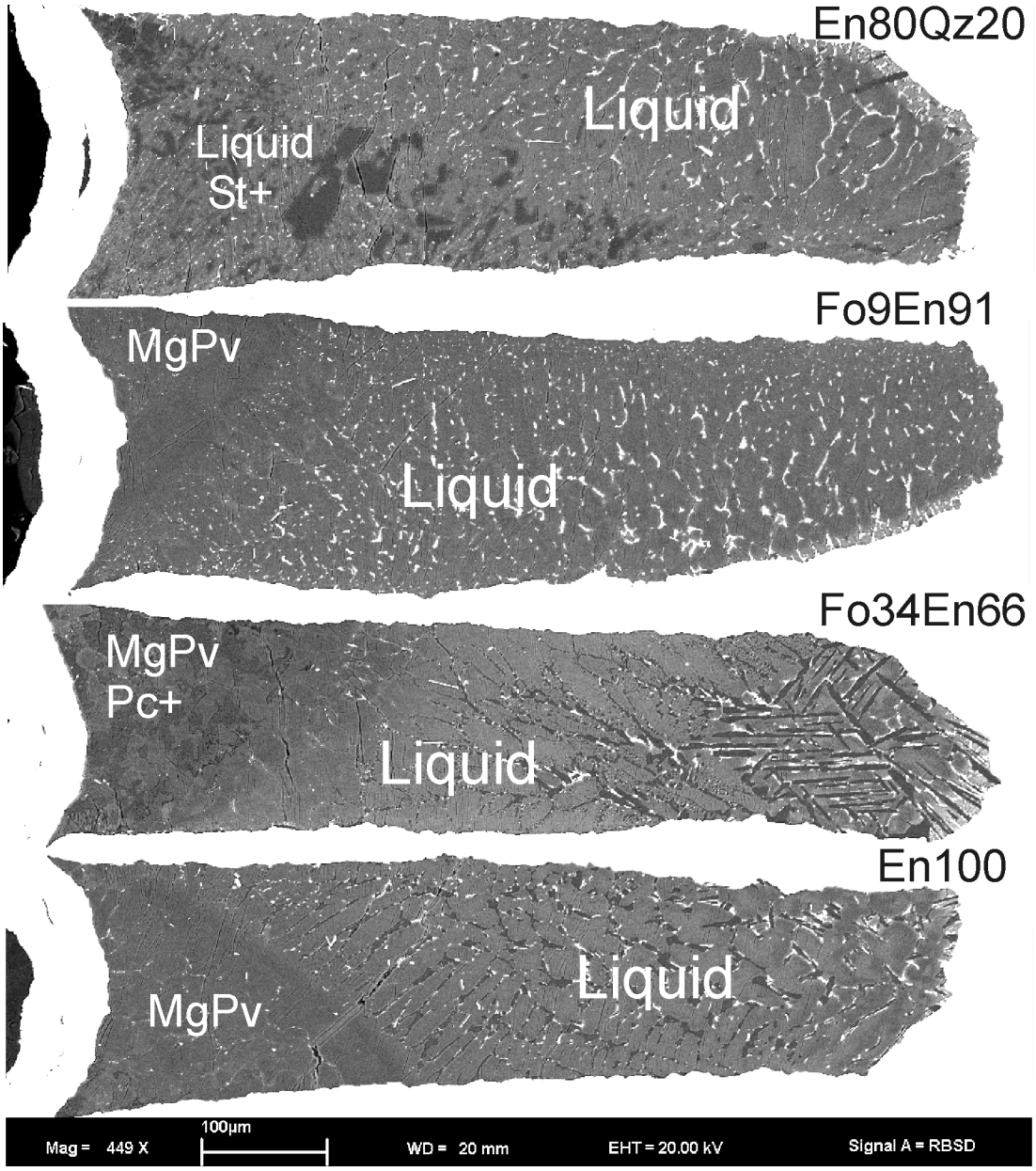

Figure 2.14: BSE images of run S3415 performed at 24 GPa.

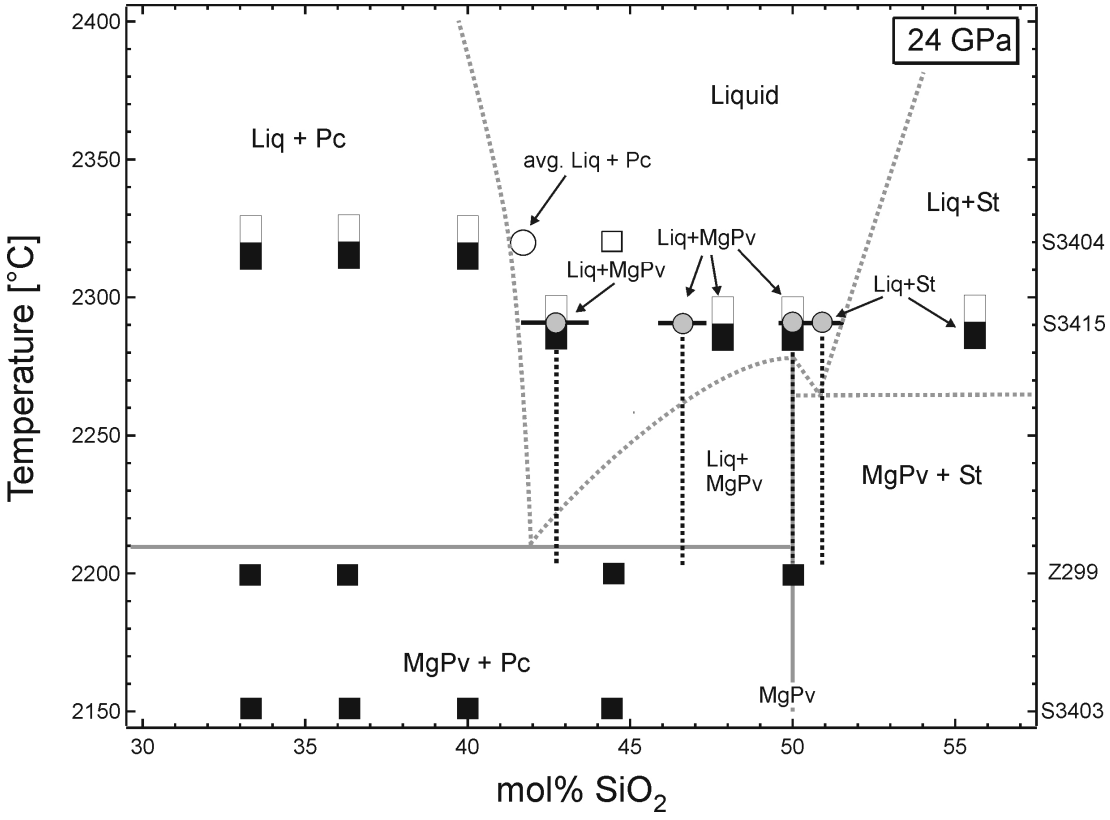

Figure 2.15: Phase diagram along the join MgO-SiO_2 at 24 GPa. Grey circles represent melt compositions in individual sample chambers. Arrows indicate the phase assemblage in partially molten samples and the coexisting liquid compositions. Other symbols are the same as in previous phase diagrams.

nace, the experiments S3404 (480 Watts) and S3415 (470 Watts) at 24 GPa show significantly higher melt fractions than the experiments S3473 (480-485 Watts) and S3468 (475 Watts) at 23 GPa. This may be interpreted to indicate that the eutectic temperature arising from the reaction Pc+MgPv=Liq is lower than that from the reaction Wads+MgPv=Liq. This, however, is precluded because of the invariant point Wads + MgPv + Pc + Liq, which must exist along the binary between the two pressures investigated. This implies that the eutectic melting temperature at the reaction Pc+MgPv=Liq must have a negative Clapeyron-slope, if the aforementioned interpretation is correct. Alternatively, the putative decrease in melting temperature in the

MgPv+Pc stability field may simply reflect the limitations in temperature determination from temperature-power relationships. Another explanation may be related to the presence of small quantities of water in the samples. Wadsleyite is believed to accommodate almost all water present in the experiments. Its breakdown to MgPv plus periclase, however, would likely change the water-partitioning between the phases, which therefore may enhance melting.

Melting Along the Join MgO-SiO_2 at 26 GPa

Two experiments have been performed at 26 GPa using the 8/3 pressure cell. Experimental conditions, coexisting phases and liquid compositions are summarised in Table 2.6.

BSE images of the recovered and polished capsule of experiment H2154, which has been performed at a lower temperature than H2146, is shown in Figure 2.16. Sample chambers containing $Fo_{34}En_{66}$, Fo_9En_{91} and En_{100} compositions show the presence of isolated melt pools coexisting with MgPv. The melt fraction in these sample chambers decreases with increasing En-component and the liquid compositions are close to the initial starting composition. However, the melt composition in the sample chamber containing En_{100} is slightly more Si-rich than the pure $MgSiO_3$-component (51.5 $\pm$1.3 mol% SiO_2). This is probably the result of a small amount of contamination of this sample chamber during capsule loading. The excess Si, relative to $MgSiO_3$, does not cause St to crystallise, which is evidence for a second eutectic along the join $MgSiO_3$ - SiO_2 at 26 GPa. The texture in the highest-temperature region of the chamber containing $En_{80}Qz_{20}$ shows a small amount of interstitial melt between the grains,

Table 2.6: Run conditions of melting experiments performed along the join MgO-SiO_2 at 26 GPa using the 8/3 pressure cell

run	**P [GPa]**	**T [°C]**	**t [min]**	**Mixture**	**Phases**	**n**	**SiO_2**	**MgO**	**Mg/Si**
H 2146	26	2350[a]	3	Fo34En66	Liq	24	42.6 (4)	57.4 (5)	1.35 (2)
				Fo9En91	Liq-[Pv]	20	47.8 (7)	52.2 (8)	1.09 (2)
				En100	Liq	26	50.5 (4)	49.5 (5)	0.98 (1)
				En80Qz20	Liq-[St]	16	52.0 (6)	48.0 (9)	0.92 (2)
H 2154	26	2300[a]	3	Fo34En66	Liq-[Pv]-[Pv,Pc]	15	43.2 (2)	56.8 (3)	1.31 (1)
				Fo9En91	Liq-[Pv]-[Pv,Pc]	6	46.5 (7)	53.5 (1.1)	1.15 (3)
				En100	Liq-[Pv]	7	51.5 (1.3)	48.5 (1.2)	0.94 (3)
				En80Qz20	Liq-[Pv,St]	-	-	-	-

a) estimated from run texture

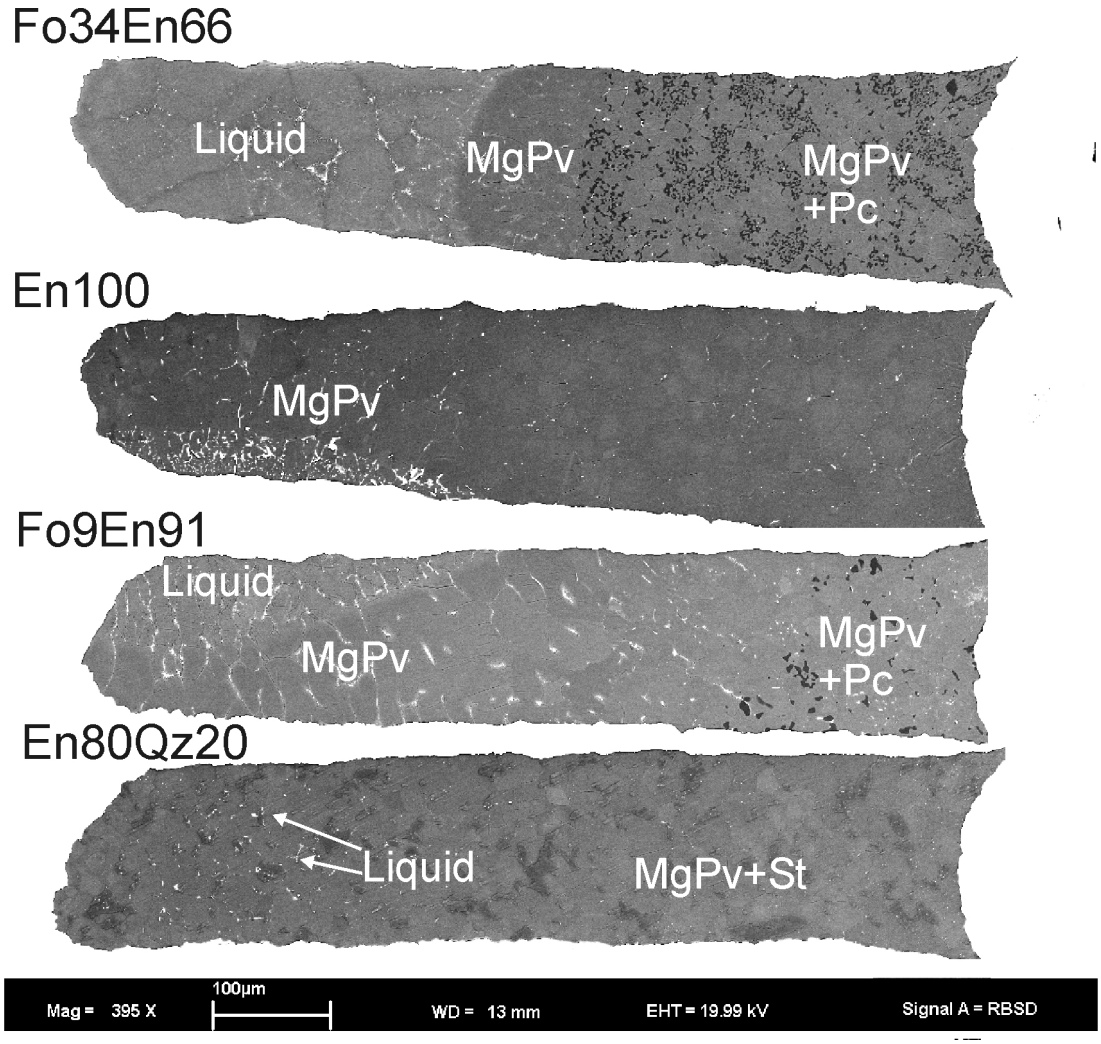

Figure 2.16: BSE images of run H2154 synthesised at 26 GPa in the 8/3 pressure cell. The sample chamber filled with $En_{80}Qz_{20}$ contains small amounts of interstitial melt

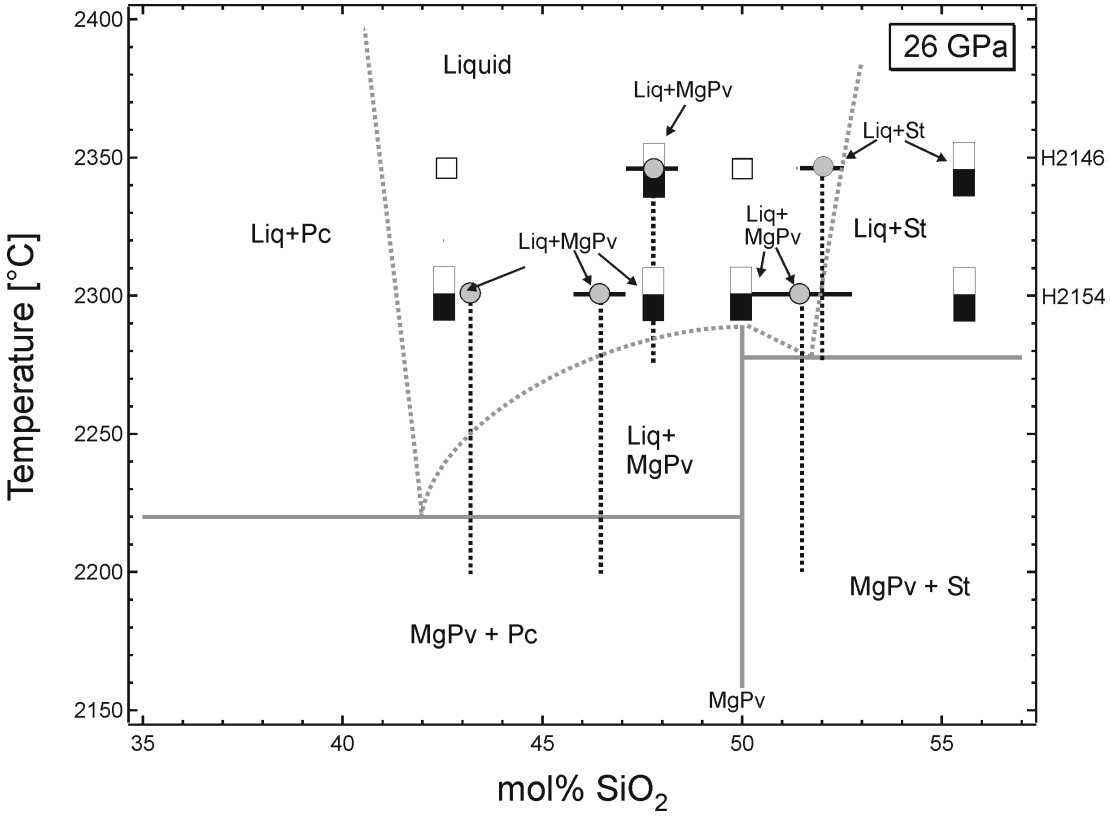

Figure 2.17: Phase diagram along the join MgO-SiO_2 at 26 GPa. Symbols are the same as in previous phase diagrams.

indicating that this part of the capsule was at or slightly above the solidus temperature. Analysis of the melt composition was not possible. The eutectic temperature at the reaction MgPv + St = Liq must be lower than the melting point of MgPv. The observation that the chamber containing En_{100} shows more melt than the chamber containing $En_{80}Qz_{20}$ is probably a result of a small radial thermal gradient across the capsule diameter and variations of sample-chamber positions relative to the furnace. The temperature of the eutectic (2220°C) along the join MgO-$MgSiO_3$ and the melting temperature of MgPv (2290°C) are estimated to be approximately 10°C higher than at 24 GPa. The temperature of experiment H2154 was probably at 2300°C.

In sample H2146, performed at ∼2350°C, the samples En_{100} and $Fo_{34}En_{66}$ were com-

pletely molten, while Fo_9En_{91} and $En_{80}Qz_{20}$ contained minor amounts (approximately less than 5-10 vol%) of MgPv and St crystals, respectively. Although the pure enstatite composition has a higher melting temperature than the Fo_9En_{91} composition, the presence of crystals in the latter sample is likely the result of a slightly longer sample chamber (770 compared to 720 μm) exposed to the thermal gradient, which causes crystallisation in the cold end of the sample chamber. At 26 GPa none of the investigated compositions showed MgO periclase liquidus crystals. The eutectic composition must therefore be located at SiO_2 concentrations less than 42.6 mol% ($Fo_{34}En_{66}$).

Melting of Mg_2SiO_4 Between 10-24 GPa

Additional melting experiment have been performed on pure Mg_2SiO_4 between 10-24 GPa in order to study the melting curve of wadsleyite and to investigate the pressure stability field of phase anhydrous B.

An experiment at 10 GPa was performed using the 14/8 assembly with a 1.6 mm diameter Re-foil capsule, and other experiments, between 15 and 24 GPa, were carried out using 10/4 pressure cells and 1 mm Re-foil capsules. Run conditions, liquid compositions measured by EMPA and determined mineral phases are summarised in Table 2.7. BSE images of experiments S3077 (15 GPa), S3027 (17 GPa), S3051 (22 GPa) and S3118 (24 GPa) are shown in Figure 2.18.

The run temperatures listed in Table 2.7 are nominal run temperatures recorded by the thermocouple and do not correspond to the melting temperatures of wadsleyite. Melt pools in these experiments are always located on the thermocouple side of the capsules. Because the container-walls of Re-foil capsules are thin, ($\sim$50-80 μm) reported temperatures correspond most likely to temperatures above the solidus. The

Table 2.7: Run conditions of melting experiments on Mg_2SiO_4, measured liquid compositions and mineral phases down the thermal gradient.

Run	P [GPa]	Oil P [bars]	T [°C]	t [min]	n	Phases	SiO_2	MgO	Mg/Si
S 3071	10.5	250	2180	5	92	Liq-[Pc]	36.0 (1.2)	64.0 (2.1)	1.78 (9)
S 3077	15	210	2250[a)]	6	n.a.	Liq-[Pc]-[AnhB]-[Fo]	-	-	-
S 2987	16	240	2260	2	42	Liq-[Pc]-[AnhB]-[Wads]	40.1 (9)	59.9 (2.5)	1.49 (7)
S 3027	17	270	2260	5	50	Liq-[AnhB]-[Wads]	38.5 (2.4)	61.5 (4.7)	1.60 (16)
S 3056	18	290	2270	3.3	29	Liq-[Pc]-[Wads]	40.7 (1.4)	59.3 (1.7)	1.46 (7)
S 2988	19	320	2270	3	35	Liq-[Pc]-[Wads]	41.5 (1.2)	58.5 (2.6)	1.40 (7)
S 3057	21	370	2280	4	n.a.	Liq-[Pc]-[Wads]	-	-	-
S 3051	22	400	2290	4	52	Liq-[Pc]-[Wads]	42.9 (1.5)	57.1 (1.9)	1.33 (6)
S 2958	22	400	2300	1.5	35	Liq-[Pc]	41.5 (1.5)	58.6 (2.8)	1.41 (8)
S 3022	23	420	2280	5	12	Liq-[Pc]-[Wads]	43.5 (1.1)	56.5 (1.3)	1.30 (4)
S 3109	24	450	2280	5	51	Liq-[Pc]	43.2 (8)	56.8 (1.1)	1.31 (3)
S 3118	24	450	2250	5	35	Liq-[Pc]-[Pc,Pv]	42.7 (1.0)	57.3 (1.5)	1.34 (5)

a) run temperature estimated from electrical power
n.a. not analysed

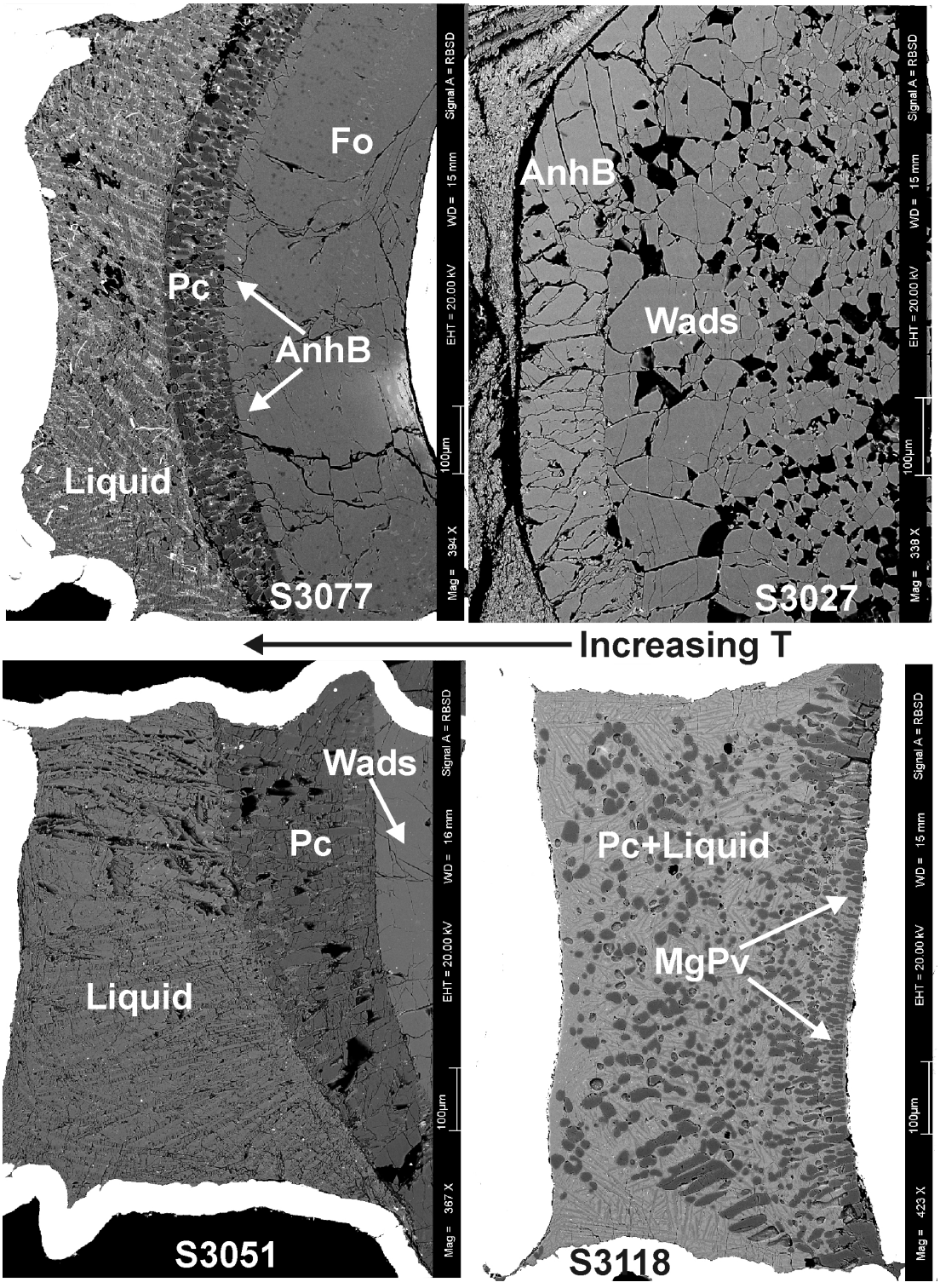

Figure 2.18: BES images of run products per formed on Mg_2SiO_4 at 15, 17, 22 and 24 GPa (from upper left to lower right). Images were rotated by 90°, such that images are shown with decreasing temperature from left to right.

measured temperature of 2260°C±50°C at 16 GPa is consistent therefore with the melting temperature of 2190°C±30°C bracketed from the experiments Z282 and Z294. The reported temperatures in Table 2.7, do not indicate a significant increase of the melting temperature with pressure, which is consistent with the proposed Clapeyron-slope of 5-10°C/GPa (see previous sections). The melting curve has therefore been constructed between the melting temperatures of wadsleyite at 16 GPa (2190°C) and the estimated value of 2240°C at 23 GPa.

Experiments S3071 and S3077 have been performed in the forsterite stability field at 10.5 and 15 GPa, respectively. At 10 GPa forsterite melts incongruently to periclase (Pc) plus liquid. The singular point on the melting curve of Mg_2SiO_4, which marks the beginning of incongruently melting of forsterite to periclase plus liquid, is therefore only constrained to be located at pressures $\leq$10 GPa. At 15 GPa, the recovered run sample S3077 shows liquid followed down temperature by layers of Pc and phase anhydrous B (AnhB) (identified by stoichiometry) and forsterite. This crystallisation sequence is consistent with incongruent melting of forsterite to AnhB plus liquid, which is followed by the melting reaction AnhB + Liq = Pc + Liq at higher temperatures (Presnall and Walter 1993). In Figure 2.19 the run textures of the 10/4 high-pressure experiments are shown schematically in a P-T diagram. Each experiment is represented by a bar indicating the phase proportions down the thermal gradient and the relative lengths of the capsules (between $\sim$750 μm and 280 μm in S3057 and 3109, respectively). The absolute lengths of the bars are chosen arbitrary and are therefore not necessarily equivalent to the temperature ranges that were present during the experiments, because the temperature differences along the capsules are not known. The bars should

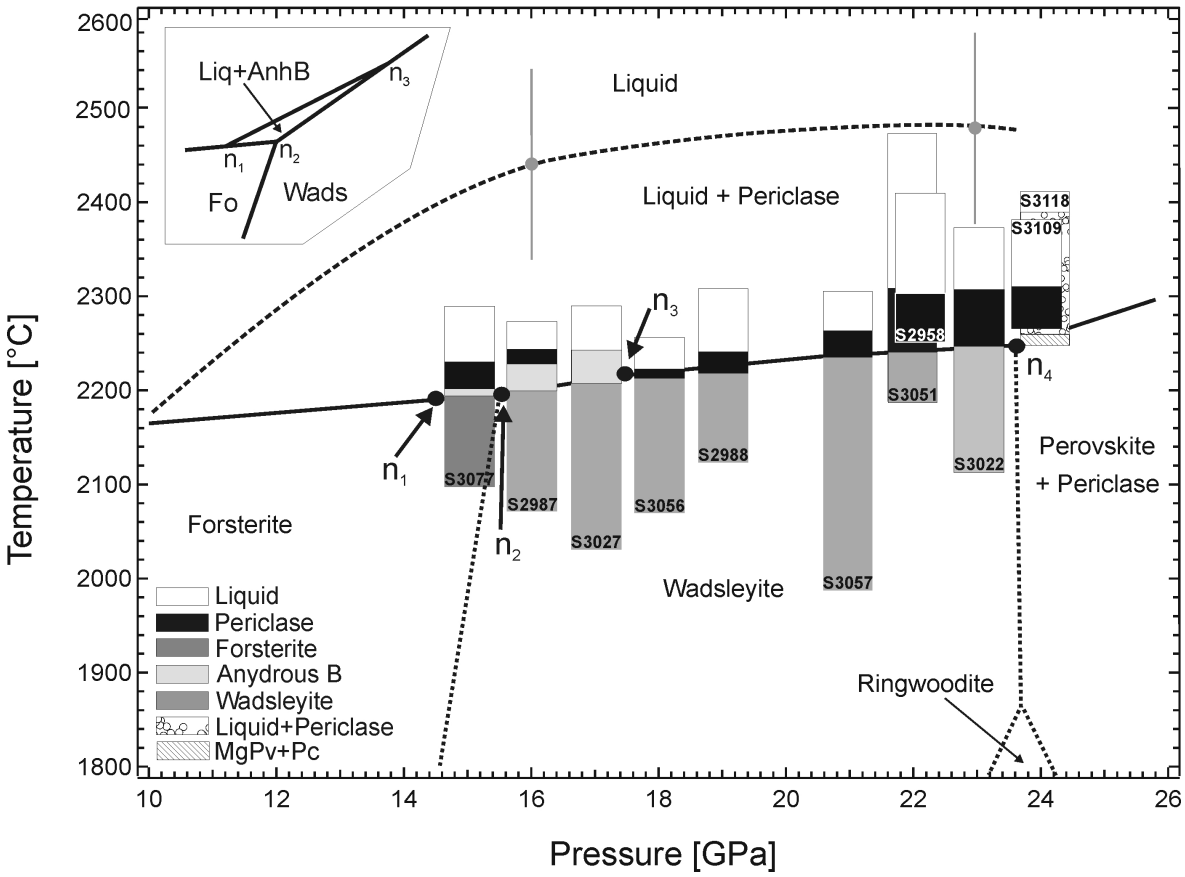

Figure 2.19: Schematic diagram of phases observed along the thermal gradients at experimental run pressures. The length of the bars do not indicate run temperatures (see text for details). The inset in the upper left shows schematically the stability field of phase anhydrous B. Invariant points along the melting curve are denoted n_1 to n_4. Grey data points with error bars are estimated liquidus temperatures. See text for details. The location of invariant point Wads+Rwd+MgPv+Pc was inferred from (Presnall et al. 1998, their Figure 3).

therefore only be interpreted to indicate the relative abundance of the phases. Within each bar the boundary between Mg_2SiO_4 and a liquidus phase (indicated by different colors) has been adjusted such that it coincides with the proposed solidus curve. The liquidus curve has been constrained from the phase diagrams at 16 and 26 GPa and the melting temperatures of periclase at those pressures, inferred from Zerr and Boehler (1994). The estimated liquidus temperatures for a Mg_2SiO_4 bulk composition are 2450 and 2500°C at 16 and 26 GPa, respectively, with an estimated uncertainty of

±100°C. The evolution of the liquidus for this bulk composition towards higher pressures is discussed in section 2.4.6. Anhydrous B is also observed in experiments at 16 and 17 GPa, where it is formed by the melting reaction Wads=AnhB+Liq. At higher pressures up to 23 GPa wadsleyite melts incongruently to periclase + liquid. Between 23 and 24 GPa the melting curve of wadsleyite ends by the breakdown to MgPv and periclase. In addition to the singular point at ≤10 GPa the melting curve of Mg_2SiO_4 must encounter four invariant points (n_1 to n_4). Presnall and Walter (1993) located the invariant point forsterite + periclase + AnhB + liquid (n_1) at 15.6 (2310°C) and n_2, at which forsterite + wadsleyite + anhydrous phase B + liquid are in equilibrium, at 16.7 GPa (2315°C). In the present experiments n_1 is not constrained but it is estimated to be located at 14.5 GPa and 2180°C and thus approximately 1 GPa lower than n_2 (15.5 GPa, 2185°C), similarly to Presnall and Walter (1993). The variations in absolute pressure values compared with the data of the latter study are likely the results of different pressure calibration curves, because Presnall and Walter (1993) used phase transitions in SiO_2 and $MgSiO_3$ as reference points. The invariant point n_3 is constrained to be located at approximately 17.5 GPa and 2200°C, which corresponds the equilibrium of wadsleyite + AnhB + periclase + liquid. The pressure stability field of phase anhydrous B is therefore restricted to about 3 GPa between 14.5 and 17.5 GPa. Ohtani et al. (1998) observed this phase between 18 and 23 GPa in melting experiment on an olivine composition ($(Mg_{0.9}, Fe_{0.1})_2SiO_4$). Ohtani et al. (1998) did not report details of their pressure calibration, but it is likely that the discrepancy in the pressure stability of anhydrous B could be also related to the iron content. At about 23.5 GPa and 2245°C the melting curve of wadsleyite ends, which requires the

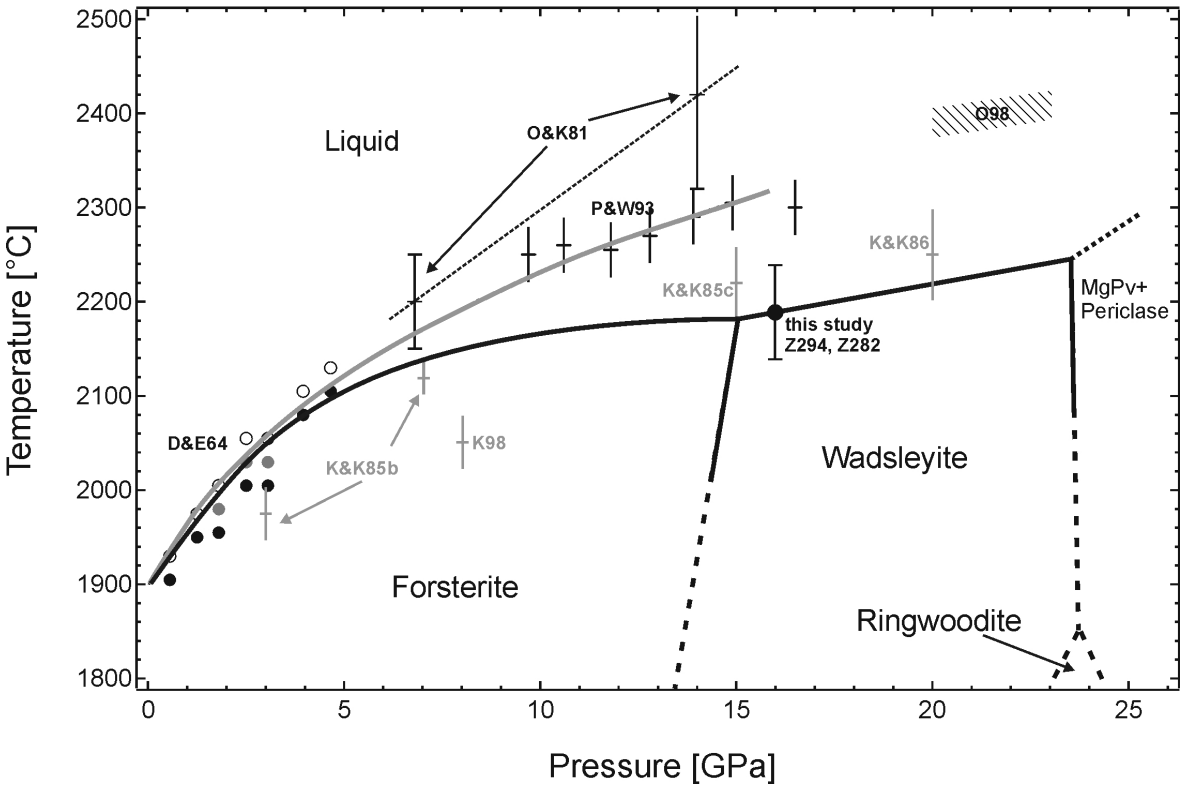

Figure 2.20: Summary of results on melting experiments on Mg_2SiO_4. The solid black line, which marks the solidus, is not mathematically fitted but drawn to the data of Davis and England (1964) (D&E64) and this study. The filled circle at 16 GPa is the melting temperature constrained from experiments in 18/11 pressure cells, which has been used to construct the melting curve. The grey line represents the Simon equation proposed by Presnall and Walter (1993). The hatched region between 20-23 GPa and 2400°C are results on $(Mg, Fe)_2SiO_4$ from Ohtani et al. (1998) (O98). Other data points are from Kato and Kumazawa (1985a) (K&K85b), Kato and Kumazawa (1985c) (K&K85c), Kato and Kumazawa (1986) (K&K86), Kato et al. (1998) (K98) and Ohtani and Kumazawa (1981)

invariant point n_4, where wadsleyite, MgPv, periclase and liquid coexist.

Figure 2.20 summarises results on Mg_2SiO_4 melting experiments from this and previous studies. Data from Ohtani et al. (1998) on $(Mg_{0.9}, Fe_{0.1})_2SiO_4$ are included. Melting temperatures determined in this study are lower than values reported by Ohtani and Kumazawa (1981), Presnall and Walter (1993) and Ohtani et al. (1998), but are in good agreement with temperatures given by Kato and Kumazawa (1985a,c) and Kato

and Kumazawa (1986). It seems that the discrepancies in reported temperatures increase systematically with increasing pressure, which therefore may be attributed to the difficulties in the determination of reliable temperatures along a significant thermal gradient in relatively small multianvil pressure cells.

2.4.6 The Effect of Pressure on the Eutectic Composition Along the Join Mg_2SiO_4-$MgSiO_3$

Figure 2.21 shows the evolution of the eutectic melt composition, arising from the reaction Mg_2SiO_4 + $MgSiO_3$ = liquid, between 16 and 26 GPa. As discussed previously, the eutectic composition moves towards Mg_2SiO_4 between 2 - 16.5 GPa as summarised by Presnall et al. (1998). At 16 GPa the eutectic composition determined in this study (44.3± 0.7 mol% SiO_2) has a higher Si-content than the composition given by Kato and Kumazawa (1986) at 20±2 GPa of 42.9± 0.6 mol%. It is important to note, that the actual pressure of the data point from Kato and Kumazawa (1986) is most likely located at the lower boundary of their pressure uncertainty. The latter authors reported the presence of phase B in their melting experiments, which was most likely phase anhydrous B, as discussed by Presnall and Walter (1993). According to the previous section, the experiments by Kato and Kumazawa (1986), were therefore performed at pressures not higher than 18 GPa, because of the constraints of the stability field of phase anhydrous B. Nonetheless, the data suggest that the increase in Fo-component in the eutectic composition with pressure proceeds to this pressure. If the eutectic composition at 23 GPa determined by the multi-chamber technique in this study is preferred compared to the value from Gasparik (1990), which has been obtained from melt analysis of a single experiment, then the eutectic composition along the join

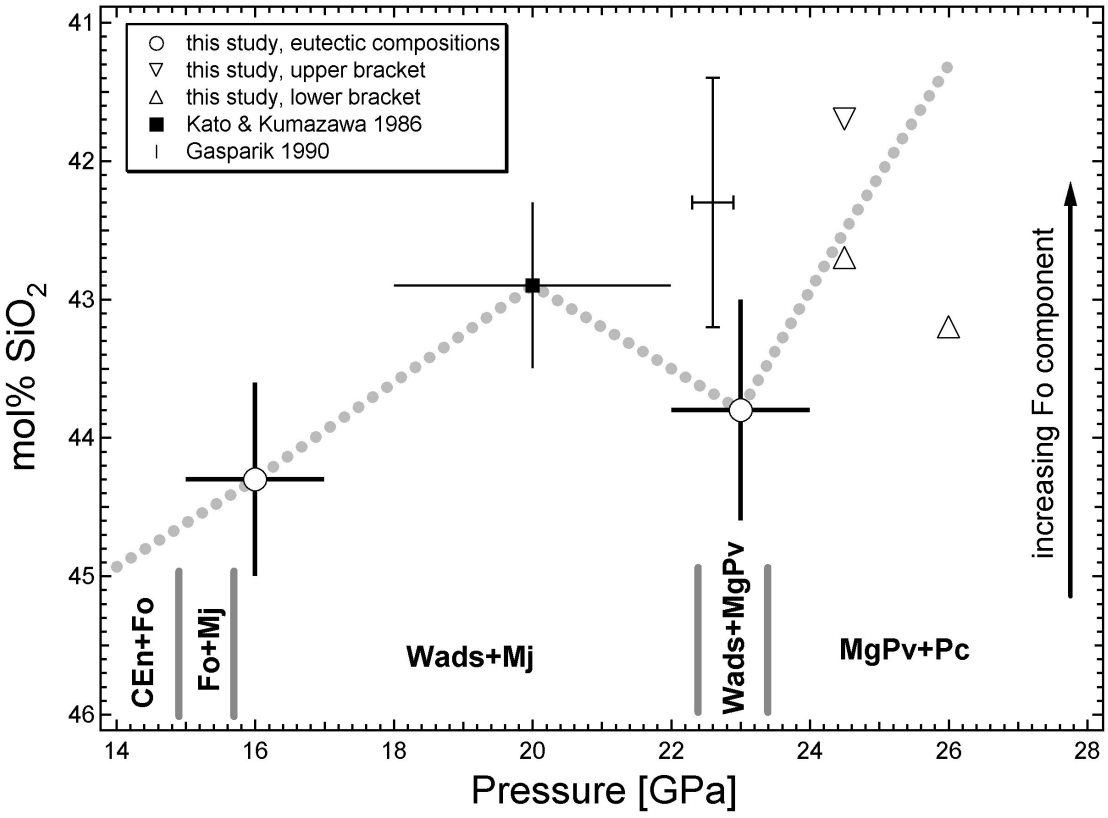

Figure 2.21: Plot of the eutectic composition along the join Mg_2SiO_4-$MgSiO_3$ as a function of pressure. Data points at 20 GPa and 22.6 GPa are taken from Kato and Kumazawa (1986) and Gasparik (1990). Up to 20 GPa the eutectic composition becomes progressively more MgO rich, but the MgO content decreases between 20±2 and 23 GPa

Mg_2SiO_4-$MgSiO_3$ shifts towards the $MgSiO_3$-component between 20±2 and 23 GPa. This trend is therefore similar to the observed melting relations in complex peridotite and chondrite compositions, which also require a shift in the eutectic compositions towards $MgSiO_3$ between 22-25 GPa. Between 23 and 24 GPa the eutectic composition in the simple system moves again towards the MgO-component with increasing pressure. Extrapolating this trend linearly indicates that MgPv should become the liquidus phase in a Mg_2SiO_4 bulk composition at 35-40 GPa.

A change in the eutectic composition along a binary between the components A and B must be related to changes in the chemical potentials of the coexisting phases. At

the eutectic point, the chemical potentials μ_A and μ_B in the solid and the liquid must be equal, such that

$$\mu_A^{solid} = \mu_A^{liq} \tag{2.2}$$

$$\mu_B^{solid} = \mu_B^{liq}, \tag{2.3}$$

which can be written as

$$\mu_A^{solid} = \mu_A^{liq,0} + RTln(a_A) \tag{2.4}$$

$$\mu_B^{solid} = \mu_B^{liq,0} + RTln(1 - a_A), \tag{2.5}$$

where $\mu_A^{liq,0}$ and $\mu_B^{liq,0}$ are the chemical potentials of the pure liquids A and B at a reference state and a_A is the activity of A in the liquid. Since $\mu_A^{liq,0} - \mu_A^{solid}$ equals the molar Gibbs free energy of fusion $\Delta\bar{G}_{f,A}$, these equations can be rewritten as

$$-\Delta\bar{G}_{f,A} = RTln(a_A) \tag{2.6}$$

$$-\Delta\bar{G}_{f,B} = RTln(1 - a_A). \tag{2.7}$$

The molar Gibbs free energy of fusion may be expressed in terms of the molar enthalpy $\Delta\bar{H}_f$ and the entropy $\Delta\bar{S}_f$ of fusion and the volume difference $\Delta\bar{V}_{A,f}$ between phase A in the liquid and solid state:

$$-\left(\Delta\bar{H}_{A,f} - T\Delta\bar{S}_{A,f} + \int \Delta\bar{V}_{A,f}dP\right) = RTln(a_A) \tag{2.8}$$

$$-\left(\Delta\bar{H}_{B,f} - T\Delta\bar{S}_{B,f} + \int \Delta\bar{V}_{B,f}dP\right) = RTln(1 - a_A). \tag{2.9}$$

Assuming that $\Delta\bar{H}_f$, $\Delta\bar{S}_f$ are independent of pressure, the eutectic composition is determined by the activity a_A, temperature and the volume changes of the components A and B during melting. If the thermodynamic parameters $\Delta\bar{H}_f$, $\Delta\bar{S}_f$ and $\Delta\bar{V}_{A,f}$ are

known and assuming that the components A and B mix ideally, such that a_A can be approximated by the mole fraction x_A, then the Equations 2.8 and 2.9 can be solved for temperature and x_A at a given pressure, which thus gives the eutectic point in a temperature-composition diagram. The volume change of the pure components ΔV_f during melting is directly related to the temperature change of the melting temperature with pressure (dT_f/dP) by the Clapeyron equation:

$$\frac{dT_f}{dP} = \frac{\Delta V_f}{\Delta S_f}, \tag{2.10}$$

where ΔS_f is the entropy of fusion. If the changes in the eutectic temperature and ΔS_f with pressure are negligible, then the eutectic composition will move towards the component with the smaller ΔV_f with increasing pressure and thus towards the component with the smaller Clapeyron-slope dT_f/dP.

These simple considerations can be used to explain qualitatively the shift of the eutectic composition with increasing pressure, based on the Clapeyron-slopes of the melting curves of the phases that participate in the melting reaction. The melting curve of the Mg_2SiO_4 components have smaller Clapeyron-slopes than the melting curve of the $MgSiO_3$ component (Presnall and Gasparik 1990, Presnall and Walter 1993). Therefore, the shift in the eutectic composition towards Mg_2SiO_4 up to 20 GPa is consistent with the predictions made from the thermodynamic relations presented above. At pressures within the stability field of periclase plus $MgSiO_3$ perovskite, the melting curve of periclase is significantly less steep than the melting curve of MgPv (Zerr and Boehler 1993, 1994, Zerr et al. 1998). This implies that the eutectic composition in the system MgO-$MgSiO_3$ should move into the direction of MgO above approximately 24 GPa. Although this behaviour is not unambiguously confirmed by the present ex-

periments performed along the join MgO-$MgSiO_3$ at 24 and 26 GPa, it is required by the melting relations in peridotite compositions as discussed above. Figure 2.21 also shows the solidus phases that participate in the eutectic melting reaction, and indicates that the shift of the eutectic composition towards the $MgSiO_3$ component in the simple binary takes place in the stability field of wadsleyite plus majorite. A phase transition of the solid phases and the related volume changes can therefore not account for the reverse of the direction in which the eutectic is moving. This implies that the consideration of the melting curves of the pure components fails to explain the shift of the eutectic composition towards $MgSiO_3$. Another problem is that $\Delta\bar{V}_f$ is integrated over the pressure stability range of a given mineral, which means that even a significant change in $\Delta\bar{V}_f$ over a small pressure range is likely not sufficient to reverse the direction in which the eutectic is moving. Trønnes and Frost (2002) reported that in the pressure range 22-23 GPa, in which the shift in eutectic-like composition in the multi-component system must occur, no olivine polymorph is stable at the solidus, and that the participating phases in the melting reaction are majorite, ferropericlase and CaPv (22 GPa) and MgPv, majorite, ferropericlase and CaPv between 23-24.5 GPa. Thus, the melting reaction in the simple binary and the complex compositions involve different solid phases, although qualitatively the same shift in the eutectic compositions is observed. This may indicate that the evolution of the eutectic composition in this pressure range is predominately determined by the liquid phase. Possible mechanisms that may influence the eutectic composition are cation coordination changes, that would cause volumetric effects and likely influence activity-composition relationships. However, changes in silicate melt structures of depolymerised liquids at these

pressures are not well understood (see Chapter 5). A more detailed discussion of the evolution of the eutectic composition with pressure on the basis of the reported melting experiments is therefore not possible.

2.4.7 Comparison of Melting Relations Between the Simple and Complex Systems

The changes in the eutectic composition in the simple binary between 16-26 GPa are similar to the liquidus phase relations in the more complex peridotite and chondrite compositions, and most importantly, the reversal in which the eutectic composition is moving with pressure is observed in both chemical systems. Figure 2.22 shows the changes in the eutectic melt composition with pressure (as Mg/Si ratio) and the corresponding melting relations of a peridotite model-composition with a fixed Mg/Si ratio of 1.30. Solidus and liquidus temperatures are derived from the phase diagrams reported for pressures between 16-26 GPa. Several observations can be made: First, because the eutectic composition becomes progressively more Mg-rich and approaches the bulk model-composition at approximately 18 GPa, the temperature difference between solidus and liquidus must decrease. This conclusion is consistent with the observation that the temperature interval between the solidus and liquidus in a complex peridotite composition becomes progressively smaller up to 10-15 GPa (e.g. Takahashi 1986, Takahashi et al. 1993, Zhang and Herzberg 1994). Second, the observation that the Clapeyron-solpe of the liquidus between 8-15 GPa in a complex peridotite composition eventually becomes negative (Scarfe and Takahashi 1986, Takahashi 1986) is consistent with the melting relations shown in Figure 2.22. This can be seen most evidently in the changes in the liquidus phases between 18 and 24 GPa. At approximately

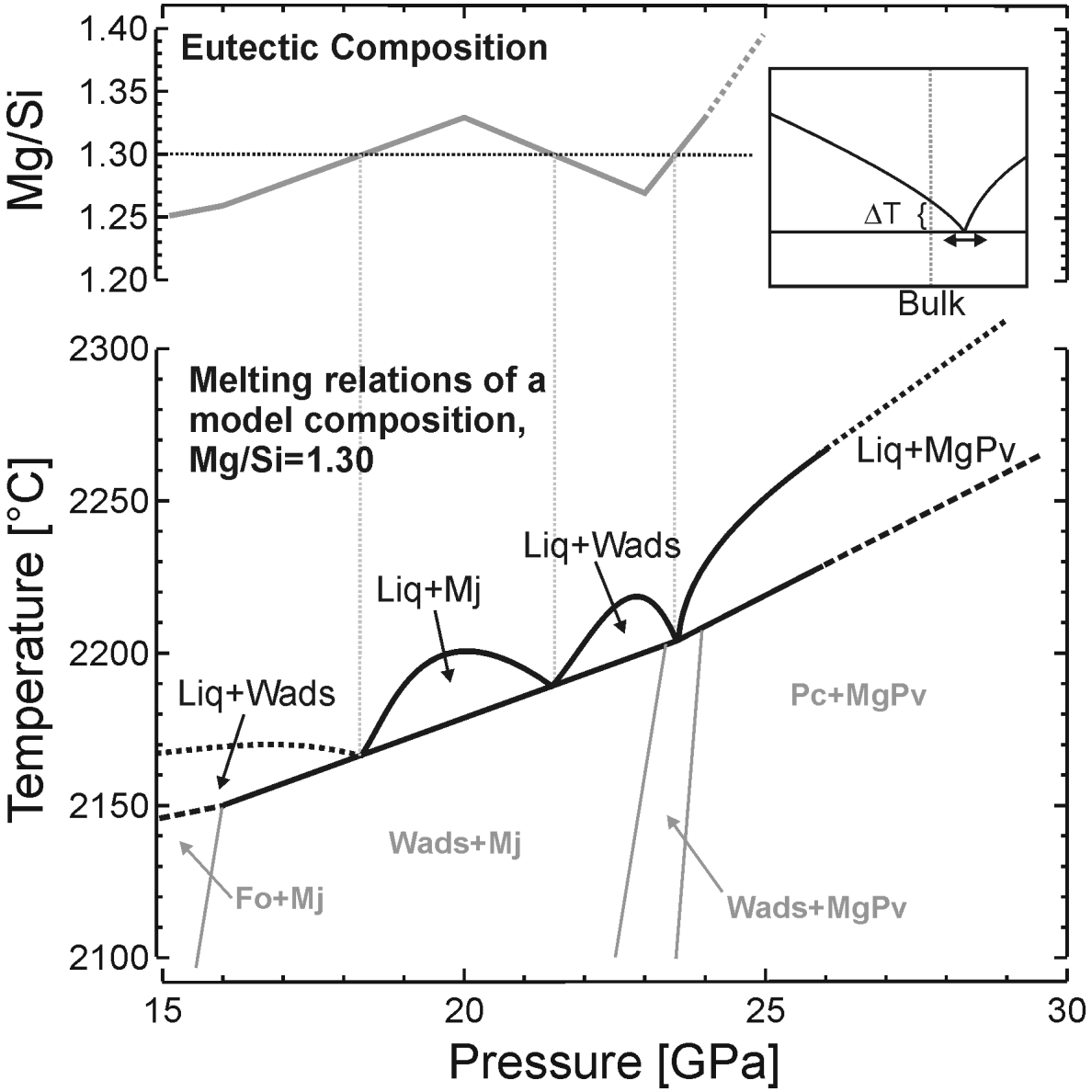

Figure 2.22: Eutectic melt composition along the join MgO-$MgSiO_3$ and phase relations of a model-composition with a Mg/Si ration of 1.30 as a function of pressure. The inset in the upper right indicates schematically how the phase relations were derived from the phase diagrams shown in the previous sections. The absolute temperature difference between solidus and liquidus is not determined unambiguously from the phase diagrams shown in the previous sections due to the uncertainties surrounding the curvatures of the liquidus curves.

18 GPa the eutectic crosses the model-composition from lower to higher Mg/Si ratios and $MgSiO_3$-majorite becomes the liquidus phase between 18 and 21.5 GPa. In the simple system, the temperature difference between solidus and liquidus is at a maxi-

mum, when the compositional difference between the eutectic and the bulk composition is maximum (for a given liquidus phase), but solidus and liquidus converge when the eutectic crosses the bulk composition. Thus, the Clapeyron-slope of the liquidus must become negative. Due to the shift of the eutectic towards $MgSiO_3$ between 20 and 23 GPa the eutectic crosses the bulk model-composition again, which results in Mg_2SiO_4 wadsleyite on the liquidus up to about 23.5 GPa. Above this pressure, MgPv becomes the liquidus phase and the eutectic crosses the model-composition a third time. These multiple changes in liquidus phases result in a relatively narrow difference between the solidus and the liquidus over the investigated pressure range between 16-26 GPa in the simple system. This is also consistent with complex peridotite compositions which show a relatively small solidus-liquidus interval in this pressure range ($\leq$100-200°C between 16-24 GPa, e.g. Zhang and Herzberg 1994, Trønnes and Frost 2002) compared to that at lower pressures (up to 400°C at 2-3 GPa, e.g. Takahashi et al. 1993). It should be noted, that if the shift in the eutectic composition in the stability field of MgPv plus periclase towards MgO proceeds at higher pressures, then the temperature interval between the solidus and liquidus must become increasingly larger with increasing pressure. This implies that also the temperature intervals between the solidus and liquidus in the more complex peridotite and chondrite compositions most likely become significantly larger at higher pressures, relative to values of $\sim$150°C observed at pressures of $\sim$24-26 GPa.

However, Figure 2.22 also demonstrates limitations in describing liquidus phase relations in chemically complex systems by a simple binary. There are significant differences in the pressures at which the liquidus phases change. This implies differences between

the changes in the eutectic composition in the simple system and the changes in the 'eutectic-like' composition in the complex system. For example, in the simple binary system, MgPv becomes the liquidus phase in the model peridotite composition at approximately 24 GPa, whereas in the complex system this is observed to take place at pressures greater than 30 GPa (Ito et al. 2004). In particular, no periclase is observed on the liquidus in the simple system, although in the complex peridotite composition this phase is on the liquidus at a pressure range of approximately 8 GPa at transition zone and lower mantle pressures (Trønnes and Frost 2002, Ito et al. 2004). Melting relations in the simple system also predict a convergence of solidus and liquidus, if the eutectic composition crosses the model-composition. A complete convergence of the solidus and the liquidus in a complex peridotite composition, although it has been suggested on the basis of the reported negative Clapyron-slope of the liquidus (Scarfe and Takahashi 1986), has not been confirmed in subsequent studies (e.g. Zhang and Herzberg 1994).

The deviations between complex and simple system reflect the influence of the other major and minor elements on the liquidus phase relations. Iron most likely stabilises ferropericlase and the effect of Al is probably to extend the stability field of majoritic garnet. Furthermore, the appearance of Ca-silicate perovskite cannot be considered on the basis of the simple binary system. It is important to note, that CaPv has a significantly steeper melting curve than MgPv (Zerr et al. 1997), which may imply that CaPv becomes the liquidus phase in a peridotite composition at pressures higher than 35 GPa, as suggested by Ito et al. (2004). It is therefore reasonable to assume that the most important phases that crystallise from a magma ocean at lower mantle

pressures are MgPv and CaPv. However, modelling liquidus phase relations by taking into account eutectic compositions and solidus and liquidus temperatures along the binary MgO-SiO_2 system enables many observed features of melting relations in complex systems to be related to the simple binary system. Most importantly, these include topological properties of the complex phase relations, such as liquidus Clapeyron-slopes and melting temperature intervals. This provides a more fundamental understanding of melting processes in the Earth's interior, that cannot be derived from melting relations in chemically complex compositions alone.

2.5 Conclusions

The investigation of liquidus phase relations of peridotite and chondrite compositions at 25-26 GPa shows that ferropericlase is the liquidus phase in peridotite compositions, while Mg-silicate perovskite is on the liquidus in chondritic compositions. The difference in liquidus phase relations in such multi-component systems can be explained by changes in the eutectic-like composition with pressure. If such multi-component systems are described by their main components MgO and SiO_2, liquidus phase relations at transition zone and lower mantle conditions can be explained by a shift in the eutectic composition towards Mg_2SiO_4 up to approximately 22 GPa, then by a shift backe towards $MgSiO_3$ between 23-26 GPa, followed again by a shift towards Mg_2SiO_4 at higher pressures.

Liquids phase relations and melt compositions along the join MgO - SiO_2 at pressures ranging from 16 to 26 GPa were studied using a multi-chamber technique, which provides a reliable method for constructing self-consistent phase diagrams and determining

eutectic compositions. Consistent with the phase relations in the complex system, a shift in the eutectic composition towards the $MgSiO_3$ component is observed between 20 and 23 GPa. At high pressures the eutectic composition shifts again towards MgO. A simple thermodynamic approach indicates that the changes in the eutectic composition with pressure are related to volume changes during melting. The change of direction in which the eutectic is moving between 20-23 GPa cannot be attributed solely to the participating solid phases. This most likely requires significant changes of activity-composition relationships of the components in the liquid, which may also have influence on volumetric properties of the melt. Such a process may be initiated by cation-coordination changes in the liquid.

A direct comparison between melting relations of simple and complex compositions shows that the detailed description of a model-peridotite composition in the system MgO-SiO_2 explains many observed features of complex peridotite phase relations. In particular precise melting temperatures and eutectic compositions derived from the simple system enable predictions to be made of Clapeyron-slopes of the liquidus and the solidus-liquidus temperature intervals. Those predictions are qualitatively consistent with reported data on liquidus phase relations of peridotite compositions. However, the liquidus phases predicted from the simple system are different from those observed for a complex peridotite composition. This reflects the influence of other elements on the melting relations of such complex systems.

Chapter 3

Element Partitioning Between Mg-silicate Perovskite and Silicate Melts

3.1 Aims of this Chapter

If a significant proportion of the Earth melted to form a deep magma ocean during the Hadean it is possible that chemical layering resulting from crystal fractionation could still persist in the Earth's lower mantle today. This hypothesis can be tested using element partitioning as has been done in previous studies (e.g. Kato et al. 1988b,a, Drake et al. 1993, McFarlane et al. 1994, Corgne and Wood 2002, Hirose et al. 2004, Corgne et al. 2004, Walter et al. 2004) as summarised in section 1.3.3. The aim of this part of the work is to investigate systematically the influence of varying chemical composition on element partitioning between Mg-silicate perovskite, the most dominant lower mantle phase, and silicate melts. Specifically the effects of varying bulk Mg#'s, Mg/Si ratios and Al_2O_3 concentrations have been investigated. A number of studies have shown that the Al_2O_3 content has a dramatic effect on FeO-MgO partitioning between MgPv and ferropericlase (Fp) (Wood and Rubie 1996, Frost and Langenhorst 2002) and on the oxidation state of iron in MgPv (McCammon 1997, Lauterbach et al. 2000,

Frost et al. 2004a). Little is known, however, about the effects of Al_2O_3 on element partitioning between MgPv and other phases at conditions above the peridotite solidus. A special emphasis was therefore to investigate effects of Al_2O_3 on MgPv/melt partitioning. The application of the lattice strain model to element partitioning (Blundy and Wood 1994) can be used as a crystal chemical probe to investigate element substitution mechanisms, which therefore allows a detailed understanding of compositional effects on element partitioning. These new data are used to examine whether there are plausible magma ocean compositions that could have allowed some proportion of lower mantle fractionation while maintaining a residual liquid composition that is still within the bounds provided by observed upper mantle chondritic element ratios.

3.2 Experimental and Analytical Techniques

Element partitioning between MgPv and silicate melts has been investigated using run products of melting experiments on peridotite and chondrite compositions, which have been described in the previous chapter. These samples were synthesised using a multianvil apparatus at 25 to 26 GPa and temperatures of approximately 2100 to 2250°C. Major and minor element concentrations of solid phases and silicate melts were measured by electron microprobe analysis (EMPA, see section 2.3) on samples S3237, S2342, H2026, H2029, H2033a and H2144 (see Figures 2.6 and 2.7).

3.2.1 Secondary Ion Mass Spectrometry

Trace element analyses were performed on samples S3237 (fertile peridotite + 30 wt% metallic Fe), H2026 (fertile peridotite), H2029 (CI-chondrite analogue) and H2033a

(Al-enriched peridotite) using secondary ion mass spectrometry (SIMS). Measurements were done on a *Cameca IMS-4f* ion probe at the University of Edinburgh. Details of the analytical method are given by Hinton (1995). An O^- primary beam with 10 nA beam current was accelerated by 10 kV before striking the gold-coated sample. To reduce transmission of molecular ion species an offset of 75 V was applied to the secondary ion accelerating voltage of 4500 V. The energy window was set to ± 20 eV. With these conditions, a beam size of 15-20 μm diameter was obtained for both melt and crystal analyses. Measured isotopes were calibrated against ^{30}Si, after calibration on NIST 610 standard. Mass 130.5 was used to monitor background. All analyses reported here have zero background counts. Counting times were adjusted to obtain at least 10^3 total counts per isotope and were typically (for analyses consisting of 5 cycles) around 5 s per cycle for elements present at the ppm level.

3.3 Results

Following the terminology of Beattie et al. (1993), the element partition coefficient $D_i = C_i^{MgPv}/C_i^{melt}$ (where C_i denotes the weight fraction of an element i) was calculated from measured element concentrations in MgPv and silicate melt.

The chemical compositions of coexisting phases measured by EMPA are given in Appendix A. Partition coefficients derived from the electron microprobe are given in Table 3.1. All run products contained MgPv crystals that were sufficiently large (20-40 μm diameter) for ion microprobe trace element analysis. Concentrations of trace elements of coexisting phases are listed in Appendix *B*. Partition coefficients obtained from SIMS are reported in Table 3.2. SIMS analyses are strongly matrix dependent and it

may be possible that very high FeO contents, as observed in the melt of run H2029 (41.4 wt% FeO), may have an effect on derived partition coefficients; in particular a high bulk FeO concentration may result in higher ion yields relative to a low FeO content matrix (R.W. Hinton, personal communication). Partition coefficients for Al and Mg within the Fe-rich samples S3237 and H2029 from SIMS analyses are sigificantly lower than those derived from the electron microprobe (see Table 3.2), which may be related to differences in the relative ion yields. However, the good agreement between the other partition coefficients for major and minor elements obtained from the two techniques does not provide any evidence for a systematic influence of the Fe content on SIMS analyses. For consistency, however, partition coefficients for major and minor elements presented in figures and calculations below were taken from Table 3.1. Major, minor and trace element partition coefficients between MgPv and silicate melts obtained from samples S3237, H2029, H2026 and H2033a are shown in Figure 3.1.

Although partition coefficients among the samples investigated show some variations, the partition coefficient patterns presented in Figure 3.1 demonstrate the same general trends. The majority of elements are found to be incompatible in MgPv and only Si, Sc, Zr, Lu and Hf are consistently compatible in all samples where they have been analysed. Partition coefficients for transition metals (Sc to Ni) systematically decrease with increasing atomic number. Ni appears to be the most incompatible with values of D between 0.19 and 0.33. Partition coefficients for REE increase with atomic number (decreasing ionic radius), from incompatible La (D_{La}=0.01) to compatible Lu (D_{Lu} up to 1.5).

MgPv/melt partition coefficient patterns reported here follow the same general trends

Table 3.1: MgPv/melt partition coefficients determined by electron microprobe analysis

	S3237	**S3242**	**H2026**	**H2029**	**H2033a**	**H2144CI**	**H2144EC**
Si	1.23 (2)	1.21 (4)	1.18 (1)	1.61 (2)	1.19 (1)	1.15 (1)	1.07 (1)
Ti	1.33 (14)	1.38 (21)	1.15 (8)	1.00 (63)	1.49 (6)	1.01 (3)	0.88 (3)
Al	0.93 (3)	0.85 (6)	0.93 (2)	2.14 (6)	0.91 (1)	1.00 (2)	0.93 (2)
Cr	0.64 (6)	0.41 (5)	0.81 (5)	0.75 (4)	0.84 (3)	0.78 (5)	0.76 (5)
Fe	0.36 (1)	0.35 (3)	0.45 (2)	0.35 (1)	0.47 (1)	0.43 (2)	0.49 (1)
Mn	0.42 (7)	0.31 (17)	0.40 (22)	0.44 (4)	0.37 (9)	0.40 (6)	0.52 (6)
Mg	1.13 (4)	1.14 (5)	0.97 (1)	1.83 (4)	1.03 (1)	1.11 (1)	1.32 (1)
Ca	0.25 (2)	0.23 (4)	0.23 (2)	0.33 (2)	0.21 (1)	0.21 (1)	0.21 (2)
Na	0.16 (4)	0.07 (6)	0.19 (12)	0.20 (2)	0.09 (3)	0.10 (4)	0.12 (3)
Ni	0.50 (45)	0.19 (15)	0.19 (13)	0.24 (4)	0.23 (7)	0.27 (6)	0.37 (6)

for experimental details see Chapter 1
Chemical analyses are given in the Appendix

Table 3.2: Experimentally determined partition coefficients obtained from SIMS measurements

Element	**S3237** fertile peridotite + Fe	**H2026** fertile peridotite
Li		0.055 (33)
Be		0.03 (3)
B		0.02 (2)
Na	0.26 (12)	0.06 (6)
Mg	0.86 (7)	0.92 (3)
Al	0.77 (3)	0.88 (2)
Si	1.23	1.18
P	0.64 (11)	0.28 (7)
K	0.54 (25)	0.12 (4)
Ca	0.28 (6)	0.22 (2)
Sc		2.15 (68)
Ti	1.07 (10)	1.08 (4)
V		
Cr	0.65 (5)	0.75 (1)
Fe	0.30 (4)	0.42 (2)
Mn	0.38 (4)	0.41 (3)
Co		0.257 (5)
Ga		0.46 (4)
Ge		
Rb		
Sr	0.06 (3)	0.010 (5)
Y	0.73 (8)	0.73 (9)
Zr	2.32 (59)	2.06 (44)
Nb	0.69 (9)	0.62 (8)
Mo		
Ba	0.07 (4)	0.01 (1)
La	0.042 (16)	0.006 (2)
Ce	0.06 (2)	0.06 (1)
Nd	0.074 (20)	0.05 (1)
Sm	0.15 (3)	0.13 (3)
Eu	0.20 (3)	0.19 (4)
Lu	1.36 (21)	1.20 (4)
Hf	2.64 (81)	2.22 (47)
Pb	0.43 (8)	1.46 (15)
Th	0.05 (2)	0.03 (2)
U	0.15 (5)	0.12 (4)

Table 3.2 continued

Element	**H2029** chondrite analogue	**H2033a** Al-rich peridotite
Li	0.08 (2)	0.04 (2)
Be	0.015 (6)	0.02 (1)
B	0.007 (7)	0.014 (12)
Na	0.12 (2)	0.08 (2)
Mg	1.70 (5)	1.10 (2)
Al	1.78 (6)	
Si	1.61	1.19
P	0.093 (9)	0.16 (3)
K	0.05 (1)	0.19 (6)
Ca	0.31 (2)	0.22 (4)
Sc	3.02 (15)	2.64 (56)
Ti	0.44 (2)	1.54 (21)
V		1.07 (2)
Cr	0.71 (3)	0.91 (4)
Fe	0.35 (1)	0.57 (6)
Mn	0.41 (1)	0.48 (5)
Co	0.35 (1)	0.37 (3)
Ni		0.36 (3)
Ga	0.37 (2)	0.58 (5)
Ge		0.54 (7)
Rb		0.28 (5)
Sr	0.010 (4)	0.010 (6)
Y	0.51 (3)	0.9 (1)
Zr	1.23 (4)	2.38 (68)
Nb	0.10 (1)	1.25 (40)
Mo		0.52 (15)
Ba	0.008 (4)	0.02 (2)
La	0.009 (3)	0.009 (7)
Ce	0.023 (2)	0.08 (5)
Nd	0.029 (3)	0.08 (5)
Sm	0.071 (8)	0.16 (6)
Eu	0.10 (1)	0.22 (8)
Lu	1.04 (5)	1.46 (25)
Hf	1.54 (7)	2.73 (88)
Pb	0.09 (1)	1.37 (57)
Th	0.017 (8)	0.07 (6)
U	0.026 (4)	0.2 (1)

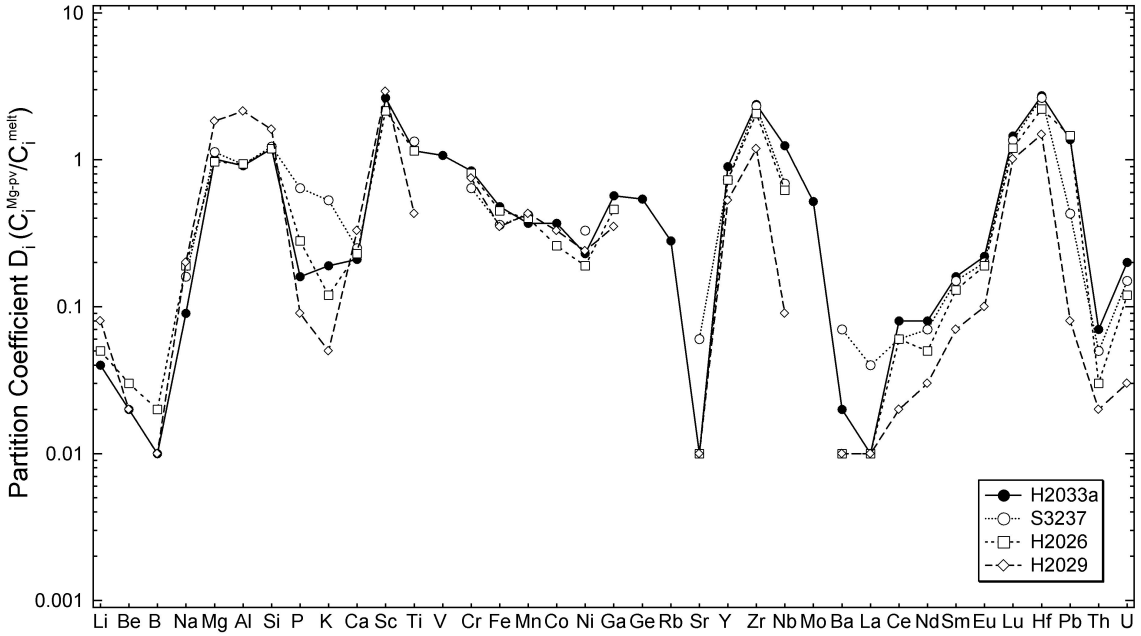

Figure 3.1: Element partition coefficients (MgPv/melt) for all elements analysed in this study

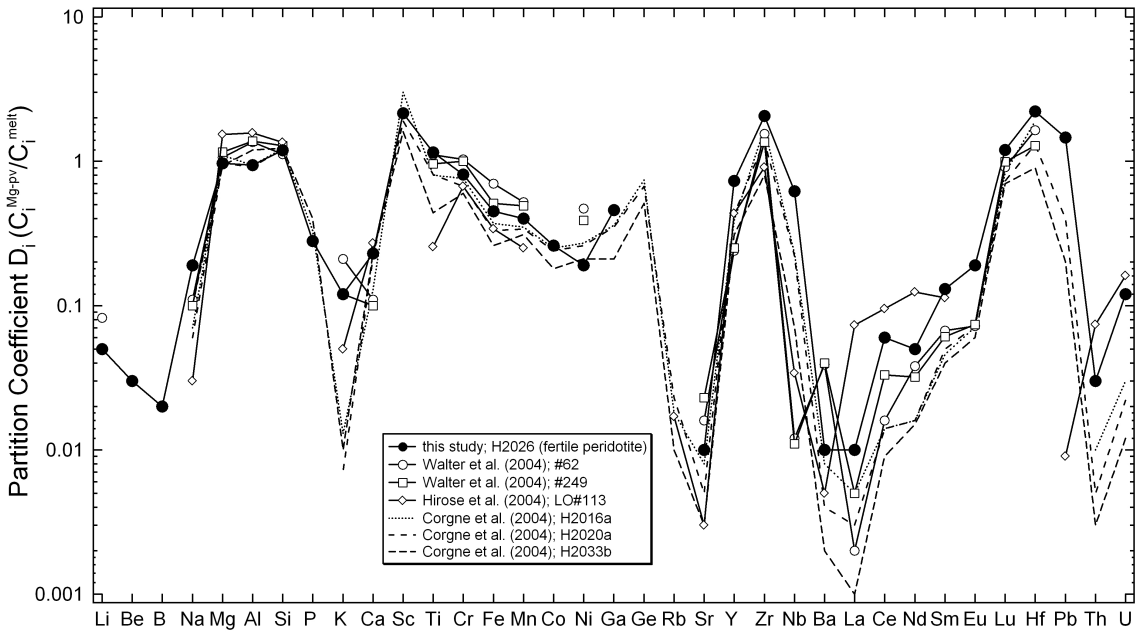

Figure 3.2: Comparison between partitioning data from run H2026 with recent MgPv partitioning coefficients for major, minor and trace elements from Corgne et al. (2004), Walter et al. (2004) and Hirose et al. (2004)

as reported in previous studies (Kato et al. 1988b, Drake et al. 1993, McFarlane et al. 1994, Kato et al. 1996, Taura et al. 2001, Trønnes and Frost 2002, Corgne et al. 2004, Walter et al. 2004, Hirose et al. 2004). As shown in Figure 3.2, the partition coefficient pattern of sample H2026 (fertile peridotite) is comparable with the most recent MgPv/melt partitioning data from Corgne et al. (2004), Walter et al. (2004) and Hirose et al. (2004). Most of the variation in individual partition coefficients between these studies is related to compositional effects, as discussed below.

The various compositions reveal effects of bulk Mg#, Mg/Si ratios and Al_2O_3 contents on MgPv/melt element partitioning. Partition coefficients for Mg and Si show a dependence on the chemical composition of the coexisting liquid. Both Mg and Si become more strongly partitioned into MgPv (increasing MgPv/melt partition coefficient) with decreasing Mg# of the melt as shown in Figure 3.3. D_{Si} and D_{Mg} also vary with the Mg/Si ratio of the melt, as shown in Figure 3.4. To exclude the effect of Mg# on Mg and Si partition coefficients only results from experiments with almost peridotitic Mg#'s > 0.85 have been considered in Figure 3.3. At high Mg/Si ratios D_{Si} is higher than D_{Mg} but with decreasing Mg/Si ratio of the melt both partition coefficients converge and show a crossover at Mg/Si ≈ 0.95. At lower Mg/Si ratios Mg, relative to Si, becomes more effectively partitioned into MgPv. No systematic compositional influence on partition coefficients of the other major elements can be resolved, but D_{Al} and D_{Ca} are higher in the CI-chondritic sample H2029, compared to samples with peridotitic Mg#'s. No systematic influence of bulk FeO content on minor and trace element partitioning is observed, which is consistent with partition coefficients derived from the laser-ablation ICPMS data from Corgne et al. (2004) (samples H2016a,

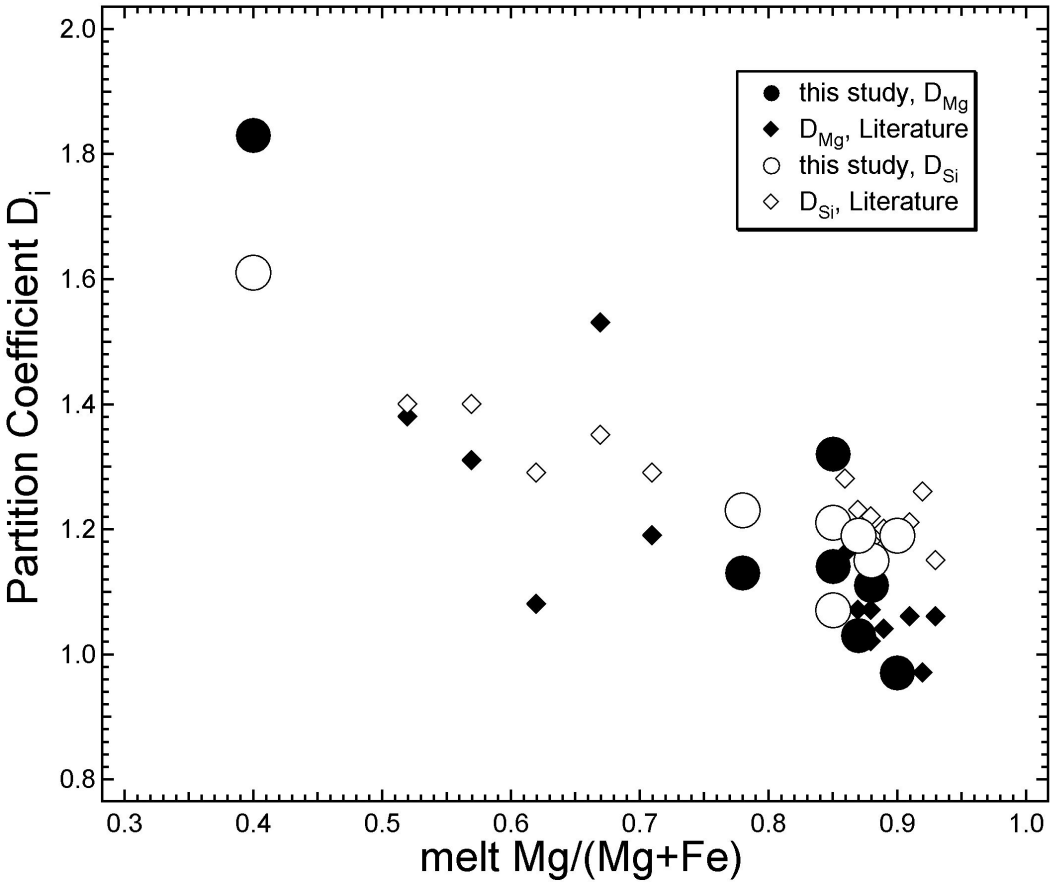

Figure 3.3: Partition coefficients (MgPv/melt) for Mg and Si as a function of the Mg# of the melt. Data from the literature were taken from Corgne et al. (2004), Walter et al. (2004), Hirose et al. (2004), Trønnes and Frost (2002), Trønnes (2000), Asahara et al. (2004), Ito et al. (2004), McFarlane et al. (1994) and Agee (1993)

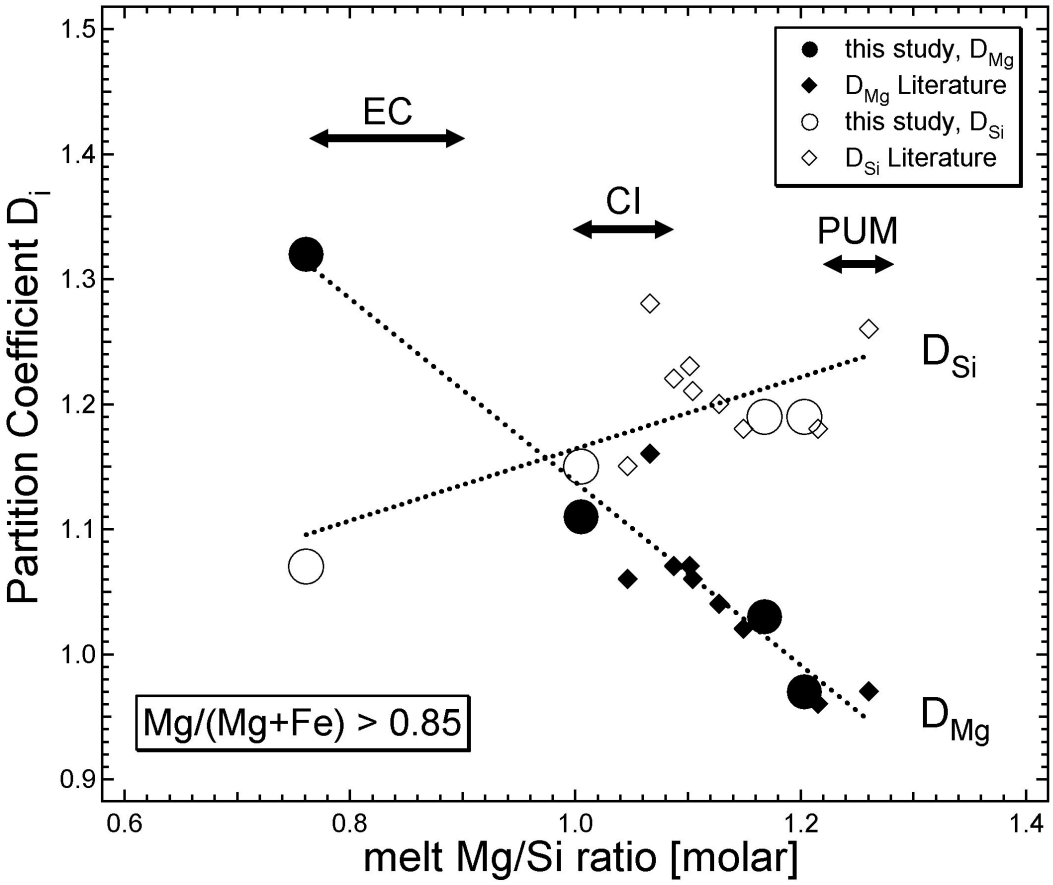

Figure 3.4: MgPv/melt partition coefficients for Mg and Si as a function of the Mg/Si ratio of the melt. Only melt compositions with peridotitic Mg#'s have been considered here. Arrows indicate ranges of Mg/Si ratios from enstatite chondrites (EC) over CI- and carbonaceous chondrites (CI) to primitive upper mantle (PUM) values. Data from previous studies are from Corgne et al. (2004), Walter et al. (2004), Trønnes and Frost (2002), Ito et al. (2004) and McFarlane et al. (1994). Dotted lines are least square fits to the data.

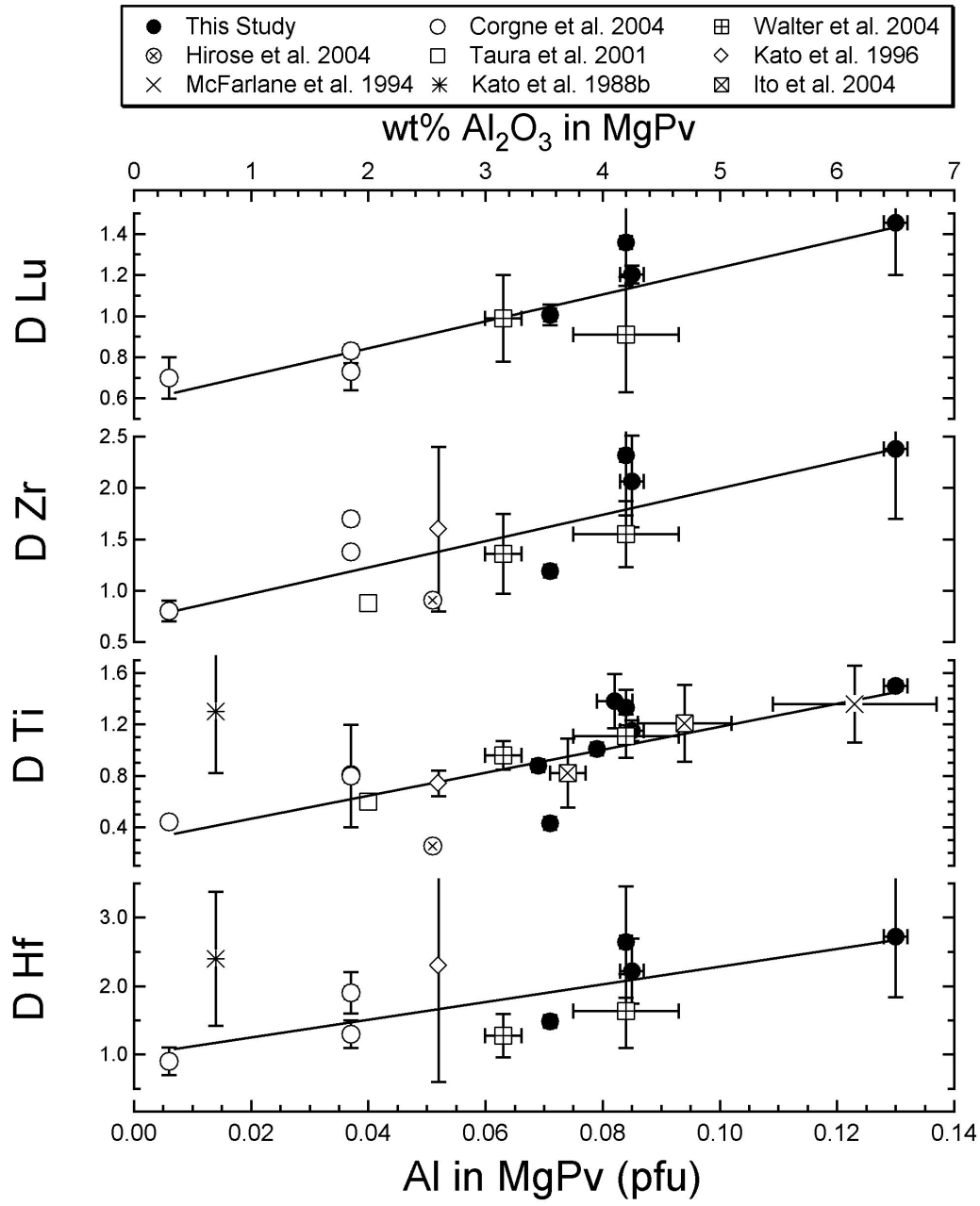

Figure 3.5: MgPv/melt partition coefficients for selected elements as function of Al per formula unit in $MgSiO_3$ (normalised to two cations). Very high partition coefficients around 6 for Zr from Kato et al. (1996) and Kato et al. (1988b) are not shown in this diagram

H2020a and H1625), spanning bulk FeO contents of 8-15 wt%.

Partition coefficients for tri- and tetravalent elements increase with the Al_2O_3 concentration of MgPv. In Figures 3.5 and 3.6, a strong correlation can be seen between

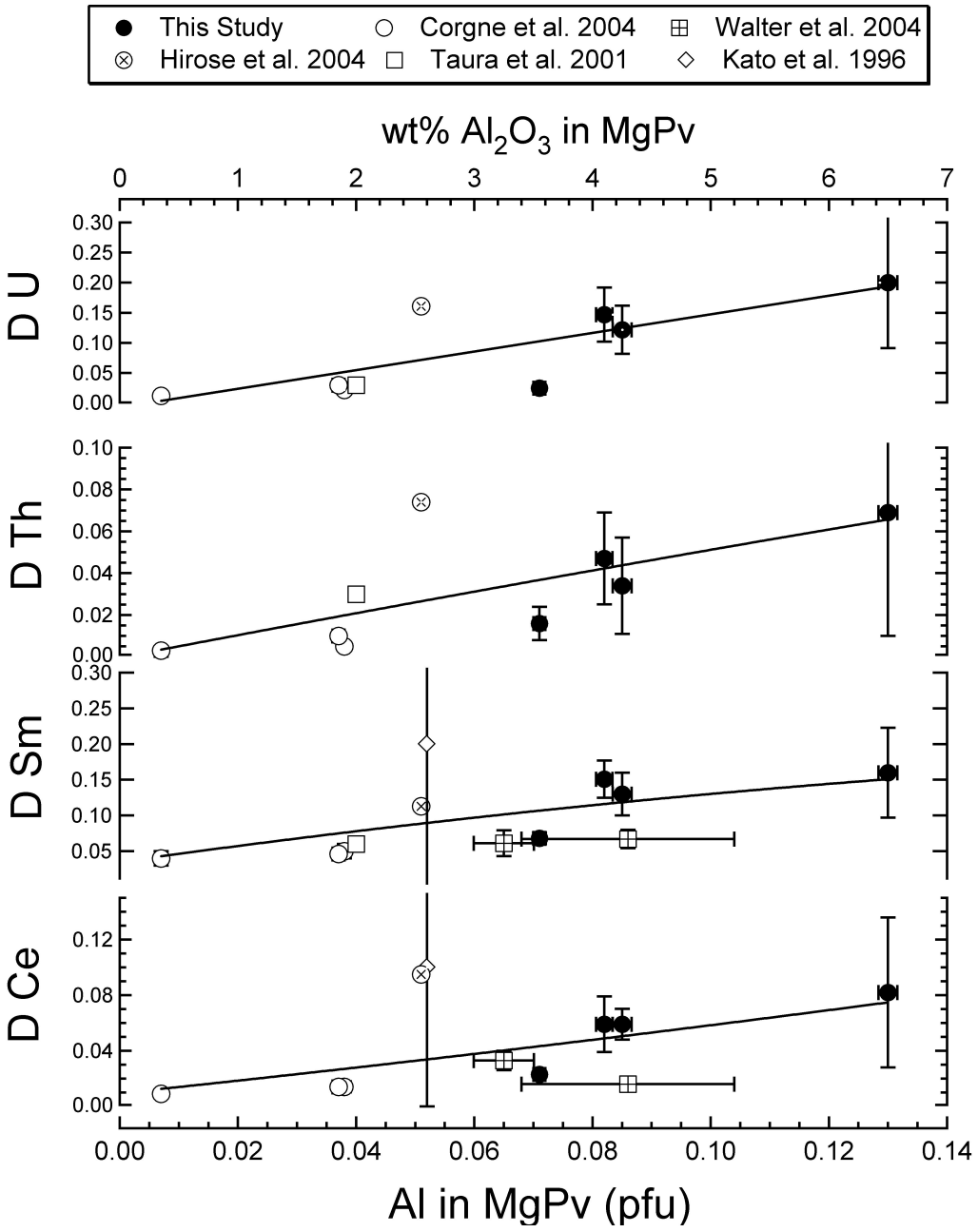

Figure 3.6: Partition coefficients for incompatible elements as a function of the Al content of MgPv

absolute values of partition coefficients and the Al content (per two cations formula unit) of MgPv. Data from the literature are also included (see Figures 3.5 and 3.6 for references). Ti, Lu and Zr change from incompatible to compatible with increasing Al content. It would seem that most of the variations observed in previously reported minor and trace element data are best explained by the effect of Al on MgPv/melt partitioning, which is supported by the crystal chemical considerations presented below. However, some of the variations could also be a result of disequilibrium arising from short experimental run times in the experiments of Kato et al. (1988a) for example (see discussions in Corgne et al. 2004, Walter et al. 2004) and possibly temperature.

3.4 Discussion

3.4.1 Crystal Chemistry of Mg-Silicate Perovskite

By exploring MgPv/melt partition coefficients in the framework of the 'lattice strain model' (Brice 1975, Blundy and Wood 1994) a useful parameterisation of the results can be derived, and information can be gained about site preferences of various elements. In this model, a partition coefficient for a particular element, D_i, is expressed as

$$D_i = D_0 \cdot exp\left[\frac{-4\pi E N_a}{RT}\left(\frac{r_0}{2}\left(r_i - r_0\right)^2 - \frac{1}{3}\left(r_i - r_0\right)^3\right)\right] \tag{3.1}$$

where D_0 is the partition coefficient for a fictive cation with the radius r_0 that enters a cation site without causing elastic strain. E is the apparent Young's modulus of that site, N_A is Avogadro's number, R and T are the gas constant and absolute temperature, respectively. This model predicts an energy penalty for incorporation of cations that deviate from the ideal cation radius r_0, resulting in a partition coefficient that is smaller than D_0.

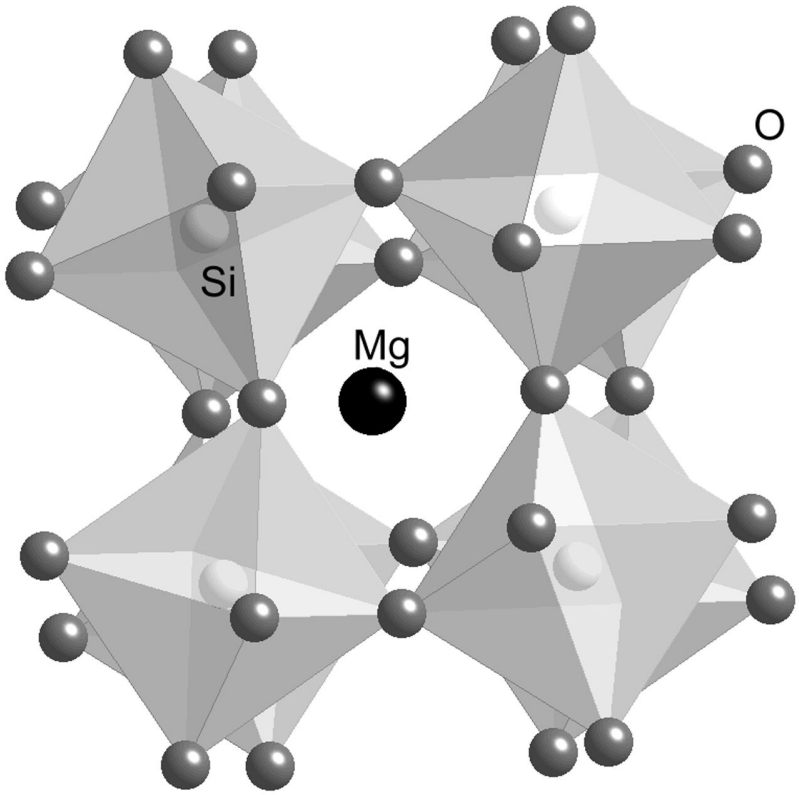

Figure 3.7: Crystal structure of Mg-silicate perovskite. Redrawn from Corgne et al. (2003)

MgPv has an orthorhombic *Pbnm* structure with two cation sites, a small site, the host of 6-fold coordinated Si^{4+} and a larger distorted site occupied by 12-fold coordinated Mg^{2+}. Compared to the cubic $Pm\bar{3}m$ $CaTiO_3$ perovskite structure the SiO_6 octahedra are tilted such that eight of the oxygen anions are closer to Mg^{2+} than the remaining four. A sketch of the crystal structure of MgPv is shown in Figure 3.7. In the following considerations, cations on the Mg-site are assumed to be in 8-fold coordination. Results of lattice strain fits for MgPv/melt partition coefficients are summarised in Figure 3.8, and the fit parameters are listed in Table 3.3. The required ionic radii have been taken from Shannon (1976). It should be noted that ionic radii for 12-fold coordinated cations are not available for most elements. Sets of parabolas with maxima close to

the effective ionic radii of Si^{4+} = 0.40 Å and Mg^{2+} =0.89 Å, corresponding to the two cation sites of MgPv, can be distinguished. Some uncertainty arises from the unknown effective radii of Be^{2+}, Al^{3+} and Ga^{3+} for 8-fold coordination. These radii have been estimated by extrapolating differences in ionic radii between 6- and 8-fold coordination of other cations of the second and third group of elements in the periodic table.

Anomalously high values for the very incompatible elements Sr and La in sample S3237 (fertile peridotite with added metallic Fe) most likely indicate a small amount of melt contamination in the ion probe analyses of the MgPv. The level of this contamination is such that it only affects these highly incompatible elements and the other samples show no evidence of melt contamination.

The partitioning behaviour of some transition metal elements is poorly described by the lattice strain model as a result of either crystal field stabilisation energies (CFSE's) (Burns 1993) or the possibility of heterovalent element substitution. The former effect may explain the deviation of Co^{2+} and Ni^{2+} from the lattice strain curves shown in Figure 3.8, while both effects may influence partition coefficients for multivalent Fe, Mn and Cr. D_{Mn} is in poor agreement with the divalent curve even though Mn^{2+} has a 5d electron configuration and should be insensitive to crystal-field effects. It is emphasised that if Mn were totally in the 3+ state, there would be much better agreement for D_{Mn} with the trivalent lattice strain curve. A similar observation can be made for D_{Fe}, which would be an excellent fit to the trivalent curve if all Fe in the system is assumed to be ferric. A detailed analysis of ferric iron incorporation in MgPv presented in Chapter 4 indicates maximum $Fe^{3+}/\sum Fe$ ratios of 0.4-0.5. As the lattice strain curves predict that $D_{Fe^{2+}}$ should be greater than $D_{Fe^{3+}}$, this implies that some

other influence, such as CFSE in MgPv (Keppler et al. 1994), may indeed complicate the partitioning of Fe.

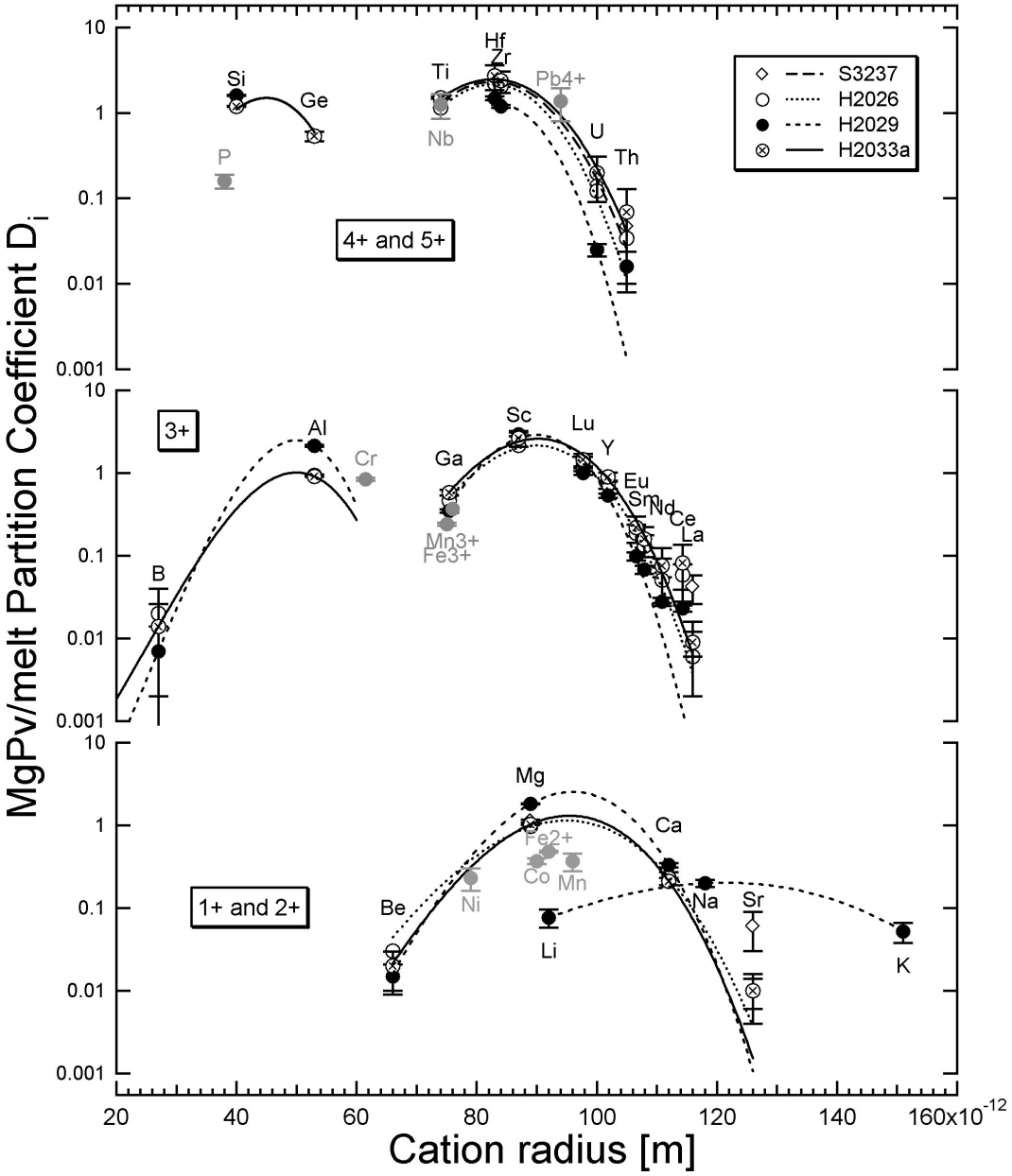

Figure 3.8: Fits of the lattice strain model to experimental determined partition coefficients as a function of cation radius. Fitting was done on Be, Mg, Ca, Sr for 2+ curves; Ga, Sc, Y, REE for 3+ and Ti, Hf, Zr, Th, and U for 4+ elements. Grey circles show partition coefficients from run H2033a that have not been included in the fits of Equation 3.1. Parabolas shown for the Si-site are only estimates since the number of data points is less than the number of adjustable parameters in Equation 3.1.

Table 3.3: Fit parameters obtained from the lattice strain model

run	**D_0**	**E [GPa]**	**r_0** [Å]
1+			
H2029	0.2	60	1.21
2+			
S3237[1]	1.5 (1)	359 (35)	0.96
H2026	1.1 (1)	290 (44)	0.95
H2029	2.5 (1)	403 (26)	0.96
H2033a	1.3 (1)	354 (33)	0.95
3+			
S3237[2]	2.0 (3)	416 (50)	0.9
H2026	1.8 (1)	425 (16)	0.9
H2029[3]	2.1 (1) / 3.0	534 (13) / 661 (8)	0.90 / 0.90
H2033a	2.5 (3)	467 (43)	0.9
4+			
S3237	2.3 (4)	527 (93)	0.83
H2026	2.2 (3)	804 (89)	0.85
H2029	1.3 (1)	1029 (36)	0.86
H2033a	2.5 (5)	482 (107)	0.83
3+ Si-site			
H3033a[4]	1	1300	0.5

T = 2573 K except for H2029 (T=2473 K)
[1] D_{Be} = 0.02 estimated
[2] D_{Ga} = 0.5 estimated
[3] additional values: D_0 fixed to D_{Sc}
[4] r_0 = 0.5 Å fixed in regression

Divalent Elements

There is no indication that divalent cations are influenced by variations in the Al content of MgPv. Be^{2+} is well assigned to the Mg-site, even given its small estimated ionic radius (0.66 Å). Although highly incompatible, Ba has a partition coefficient that is significantly higher than predicted from the lattice strain model, consistent with previous studies (Walter et al. 2004, Corgne et al. 2004, Hirose et al. 2004). Walter et al. (2004) suggested a substitution of Ba^{2+} for O^{2-} by the formation of a Si^{4+} vacancy, based on the observation that Ba^{2+} has a similar ionic radius as O^{2-}. Ba was accordingly excluded from lattice strain fits. Pb^{2+} is significantly more compatible in all samples than predicted by the lattice strain model which may be related to its electronic structure (Blundy and Wood 1994) or possibly arises from a contribution of some Pb^{4+}. However, given that D_{Pb} shows the largest variations among our samples, from 0.08 to 1.5, it is possible that some analytical bias influenced the Pb data, which were therefore excluded from further considerations.

Trivalent Elements

REE's, and Y seem to substitute exclusively onto the Mg-site in MgPv. A comparison between the Ga and Al partition coefficients from our experiments shows that D_{Al} is always higher than D_{Ga} although the estimated effective radius of Al^{3+} of 0.68 Å in 8-fold coordination is smaller than that of Ga^{3+} (0.75 Å). This indicates that Al is predominantly present on the Si-site in MgPv, whereas Ga^{3+} may substitute mainly on the Mg-site. This view is supported by a study of Andrault (2003), who found a high solubility of an [GaAl] component in MgPv. Calculation of 'Mg-site' Al partition

coefficients from lattice strain fits indicate that about 10% of the Al may also be present on this site in MgPv. Sc, which likely substitutes predominantly onto the Mg-site, has a slightly anomalous partition coefficient in sample H2029, such that D_{Sc} is higher than constrained from the lattice strain model, when fitted together with Ga and REE (see Table 3.3). A similar behaviour of Sc can be seen in the data from Corgne et al. (2004) in their runs H2016a and H2020a. This is potentially a result of a small amount of mixing of Al, Ga, and possibly Sc between both sites in MgPv. Parabolas for the Si-site in MgPv shown in Figure 3.8 are only estimates.

Figure 3.9 shows partition coefficients for trivalent elements as a function of cation radius for varying MgPv Al contents. All samples were produced under nearly identical experimental conditions. The figure shows, that the increase of partition coefficient with increasing MgPv Al content is a general feature of trivalent cations. From Figure 3.9, it seems that the most obvious effect of adding Al is to increase the parameter D_0 of the lattice strain model. However, since D_0 is strongly related to D_{Sc}, a direct correlation between the Al content of MgPv and the parameters of the lattice strain model is complicated by uncertainties in some values of D_{Sc} and by strong coupling of D_0 and E during data fitting. Partition coefficients for Ce are significantly higher than the value predicted by the lattice strain model, as indicated in Figure 3.9. This can also be seen in previous data sets (Walter et al. 2004, Corgne et al. 2004). Melt contamination seems to be excluded as a possible explanation, because D_{La} should then also be raised but this is not the case. A good explanation for this 'Ce-anomaly' would be its presence in both trivalent and tetravalent states, as it has been observed in natural zircons (e.g. Hinton and Upton 1991). The lattice strain model predicts that

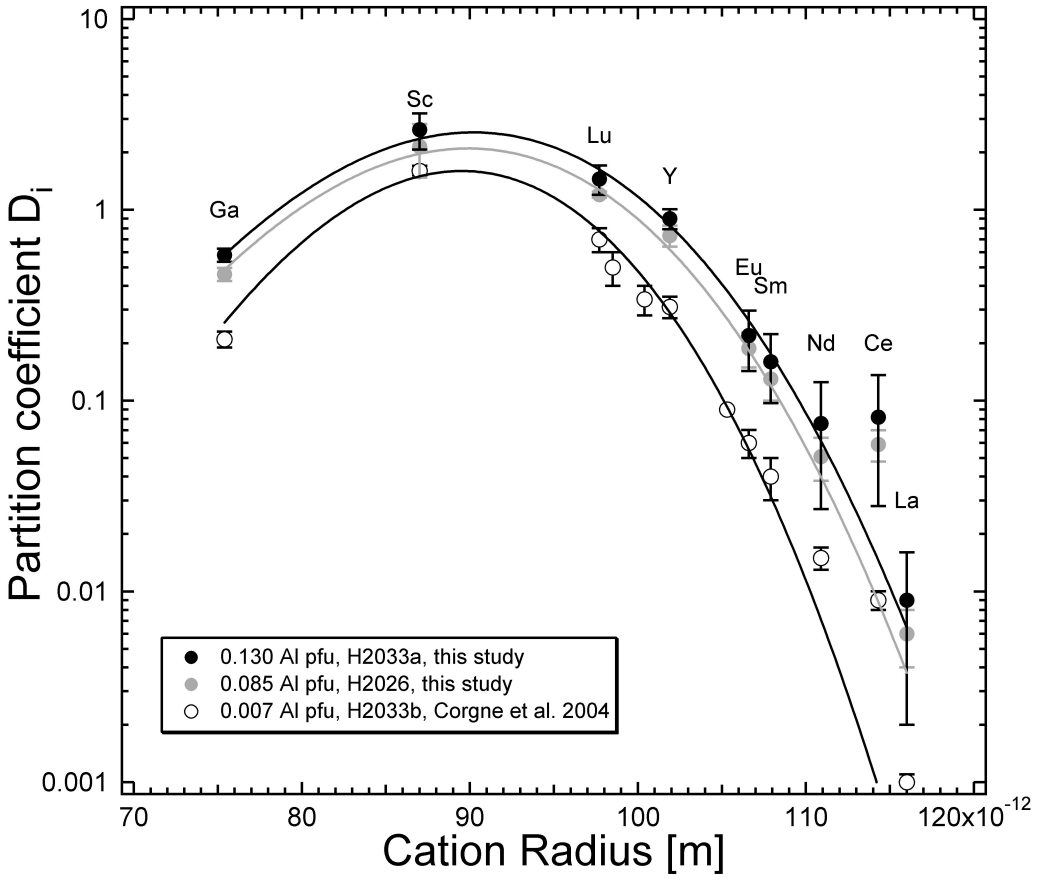

Figure 3.9: Partition coefficients of trivalent elements and lattice strain fits as function of cation radius. The peridotitic samples have different bulk Al concentrations but were equilibrated under nearly identical pressure and temperature conditions. The fit of the lattice strain parabola to the data of Corgne et al. (2004) has been adjusted by fixing D_0= 1.6 in order to match D_{Sc} (E = 646 GPa, r_0 = 0.90)

$D_{Ce^{4+}}$ should be an order of magnitude larger than $D_{Ce^{3+}}$ such that a relatively small component of Ce^{4+} could raise the partition coefficient to its observed level. Although the oxygen fugacity in the present experiments is not constrained and may be quite high, it is important to note that a Ce anomaly of similar magnitude occurs in our experiment performed in the presence of metallic Fe (S3237) and in the experiments of Walter et al. (2004) performed in diamond capsules. Such effects for Ce are not observed at low pressure, even in partitioning studies performed in air (e.g. Hill et al.

2000), which may indicate that either pressure or MgPv crystal chemical effects favour the stability of the smaller Ce^{4+} cation.

Tetravalent Elements

As seen in Figures 3.5 and 3.6 partition coefficients for tetravalent cations also increase with the Al content of MgPv. In accordance with their effective radii, the elements Hf^{4+}, Zr^{4+}, U^{4+} and Th^{4+} substitute exclusively onto the Mg-site. The assignment of Ti^{4+} is more difficult, however, as it may substitute onto both sites and it is also possible that the site preference may change with the Al concentration of MgPv. At high Al contents, D_{Ti} is greater than D_{Si} and much greater than D_{Ge}, which means that if Ti were entirely on the Si site the corresponding elastic strain parabola would require an unrealistically high value of D_0 ($\sim$10) or a very low value of E^{4+} and there would be very poor agreement with Ge. The relationship between Si and Ge in fact implies that only a relatively small amount of Ti is on the Si-site ($<$20%) for high Al contents in MgPv. For low Al concentrations of MgPv (e.g. H2033b of Corgne et al. 2004) D_{Ti} is $\sim$0.4, and would consequently fit closer to an expected tetravalent Si-site parabola. Corgne et al. (2004) assigned Ti at low MgPv Al concentrations predominantly to the Si site and constrained a tighter Mg-site tetravalent parabola that passed through their Sn data point. Unfortunately we lack Sn results at higher Al contents with which to test this observation. Although the tetravalent parabola is rather poorly constrained as a result of the uncertainties surrounding Ti, it would seem that these observations are consistent with Ti being predominately on the Si-site at low Al concentrations but predominantly on the Mg-site at higher Al contents.

Heterovalent Substitution and the Effect of Al on Element Partitioning

As discussed above, Al^{3+} substitutes mainly for Si^{4+} in MgPv. This exchange requires charge compensation through either a charge-coupled substitution onto the Mg-site or the creation of an oxygen vacancy (e.g. Lauterbach et al. 2000). The strong coupling between the Al content of MgPv and trivalent cation partition coefficients supports the former mechanism, which can be expressed in terms of the Kröger-Vink notation (Kröger and Vink 1956, Allan et al. 2003) as

$$\frac{1}{2}Al_2O_3 + \frac{1}{2}M_2O_3 + Si_{Si} + Mg_{Mg} \leftrightarrow Al'_{Si} + M^{\bullet}_{Mg} + SiO_2 + MgO. \qquad (3.2)$$

X_{Si} and X_{Mg} refer to element X on the Mg and Si sites, respectively. This reaction, where the M^{3+} cation can also be Al in the absence of a more suitable cation, also seems to be the currently more favoured mechanism according to spectroscopic (Stebbins et al. 2001) and computational studies (Akber-Knutson and Bukowinski 2004, Yamamoto et al. 2003, Richmond and Brodholt 1998).

In the case of tetravalent cations, different charge-compensating mechanisms can be envisaged that may cause a dependence of D_i^{4+} on the Al concentration of MgPv. One possibility would be substitution of tetravalent cations onto the Mg-site charge balanced by the replacement of two Si^{4+} by two trivalent cations i.e.,

$$\frac{1}{2}Al_2O_3 + \frac{1}{2}M_2O_3 + JO_2 + 2Si_{Si} + Mg_{Mg} \leftrightarrow Al'_{Si} + M'_{Si} + J^{\bullet\bullet}_{Mg} + 2SiO_2 + MgO. \quad (3.3)$$

An additional or alternative substitution mechanism involving Al on the Si-site and tetravalent cations on the Mg-site could lead to the formation of Mg-vacancies similar to substitution trends investigated by Corgne et al. (2003). Incorporation of tetravalent cations may be a result of a combination of substitution trends, but in the absence of

spectroscopic or further computational evidence, it would be hard to unequivocally identify the actual substitution mechanism.

3.4.2 The Mg/Si Ratio of the Upper Mantle and MgPv Fractionation

An attractive aspect of MgPv fractionation in a deep magma ocean is that this could have raised the Mg/Si ratio of the residual liquid that formed the primitive upper mantle (PUM) and therefore explain the compositional difference between the Earth's upper mantle and the array of chondritic compositions from which the Earth likely formed (e.g. Liu 1982). However, the compositional dependence of D_{Mg} and D_{Si} on the Mg/Si ratio of the melt (see Figure 3.4) indicates that for relatively Si-rich melt compositions an increasingly larger degree of MgPv fractionation would be required to evolve the residual liquid Mg/Si ratio to that of PUM. At Mg/Si ratios less than unity (equivalent to bulk Mg/Si ratios of enstatite chondrites) MgPv fractionation would produce a residual melt which is enriched in Si. Based on these observations, it is highly unlikely that PUM is a derivative of large scale MgPv fractionation from an initially chondritic magma ocean and it cannot be possibly derived from enstatite chondrites as suggested by Javoy (1995).

3.4.3 Constraints on the Size of a possible Perovskitic Reservoir in the Lower Mantle

Constraints can be placed on the maximum amount of MgPv and CaPv that could have fractionated from a Hadean magma ocean by examining the evolution of refractory lithophile element ratios during crystallisation. If an element ratio is chondritic in PUM then the maximum amount of perovskite fractionation must not drive this ratio

outside of the uncertainty of the chondritic value. The concentration C_i of an element i can be calculated from the equation for fractional crystallisation

$$C_i = C_i^{0,l} \cdot f^{D_i - 1}, \tag{3.4}$$

where $C_i^{0,l}$ is the initial bulk concentration of i, f is the weight fraction of the residual liquid and D_i represents the bulk partition coefficient

$$D_i = \sum X^a D_i^a, \tag{3.5}$$

whereas D_i^a is the mineral/melt partition coefficient of phase a and X^a is its weight fraction. The concentration ratio between two elements i and j is then given by

$$\frac{D_i}{D_j} = \frac{C_i^{0,l}}{C_j^{0,l}} \cdot f^{(D_i - D_j)}. \tag{3.6}$$

The most discerning element ratios for the constraining degree of MgPv fractionation, therefore, have $D_i >> D_j$. It is emphasised, that the following considerations do not depend on the actual fractionation model and that equilibrium or batch melting equations would provide almost identical results. There are two problems, however, with applying this methodology to determining the extent of maximum possible perovskite fractionation. The first is that most of the aforementioned 'discerning element ratios' have also been strongly fractionated in the mantle as a result of extraction of the continental crust and cannot, therefore, be assumed to be chondritic in PUM. The second is that since the majority of elements that are incompatible in MgPv are actually compatible in CaPv (e.g. REE's), the combined fractionation of MgPv and CaPv will partly compensate the leverage of one phase on an element concentration ratio. This thereby extends the possible amount of fractionated material and creates two unknowns, the

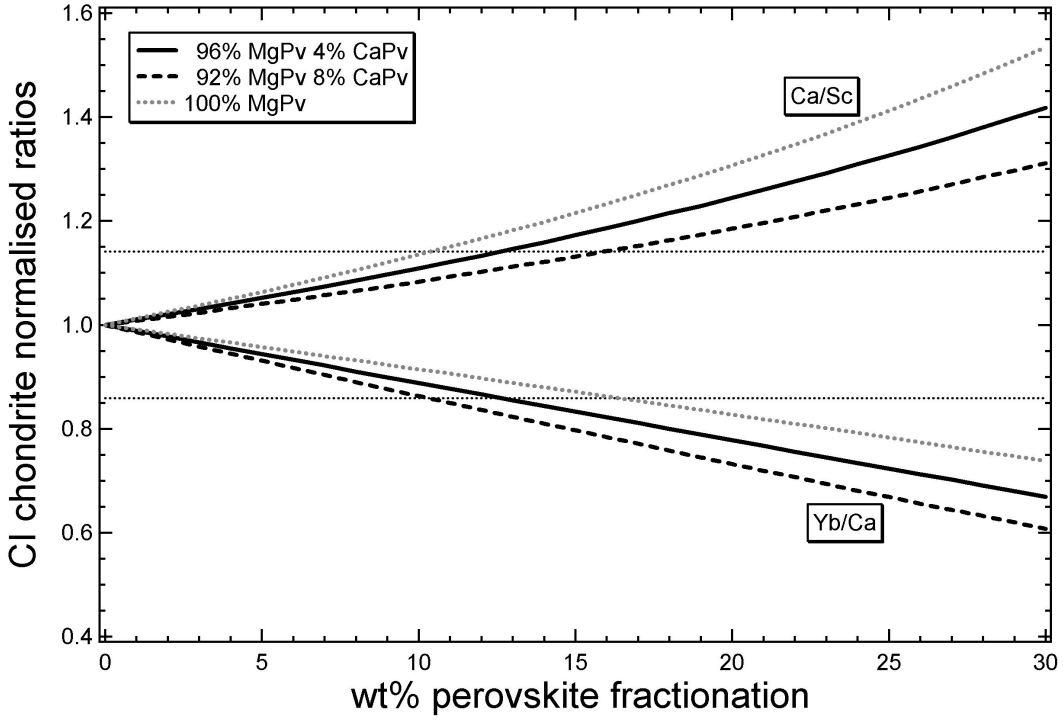

Figure 3.10: Chondrite normalised ratios for Ca/Sc and Yb/Ca as function of perovskite fractionation calculated from Equation 3.6. MgPv/melt partition coefficients were taken from experiment H2026 with D_{Yb} being calculated from Equation 3.1 and parameters given in Table 3.3. Data for CaPv are from Corgne et al. (2004). Horizontal dashed lines represent the uncertainty on both element ratios. Solid and dashed lines show the effect of different proportions of MgPv and CaPv.

total amount of plausible perovskitic fractionation and the proportion of MgPv and CaPv in the crystallising assemblage.

In Figure 3.10 the evolution of two refractory lithophile element ratios (Ca/Sc and Yb/Ca) are plotted as a function of perovskite fractionation. These ratios are, with suitable uncertainties, chondritic in PUM (Walter et al. 2004) but have complimentary sensitivities to the fractionation of each perovskite phase. Partition coefficients for CaPv are taken from experiment H2020b of Corgne et al. (2004). We use a 10% uncertainty on each element concentration consistent with estimates by Walter et al. (2004). The amount of pure MgPv fractionation is constrained by Ca/Sc to be ap-

proximately 10% but if we add CaPv to the fractionating assemblage the amount of allowable fractionation increases and can reach 100% for a 70:30 assemblage of MgPv and CaPv. The ratio Yb/Ca constrains the maximum amount of pure MgPv fractionation to be approximately 17%, however, this is reduced if CaPv is added to the crystallising assemblage. The maximum amount of fractionation allowed by both of these ratios is approximately 13% of a 96:4 MgPv:CaPv mixture. These ratios are the most discriminating for determining the maximum allowable fraction of a lower mantle perovskitic layer as a number of other possibly useful and reliably chondritic ratios (e.g. Al/Yb, Sc/Yb, Sm/Yb, Zr/Y; see Walter et al. 2004) all remain within their PUM uncertainties for this amount and proportion of fractionation. This estimate is significantly larger than values from previous studies (Kato et al. 1988b,a) which had to employ less reliable partitioning data and did not consider the effect of CaPv fractionation.

Using the new partitioning results the influence of varying chemical composition on the allowable size of a perovskitic layer can be investigated. Assuming a crystallising assemblage of 96% MgPv and 4% CaPv, bulk partition coefficients for Fe and Ca are $\sim$0.4 and $\sim$0.5, respectively and the concentration of both oxides would, therefore, increase in the liquid as fractionation proceeds. As described in previous sections, even extreme enrichment of a melt in FeO does not have a pronounced effect on trace element MgPv/melt partitioning and will therefore not have major consequences on the allowable amount of perovskite fractionation. The CaO content of the melt, however, is negatively correlated with CaPv/melt partition coefficients for trivalent and divalent cations (Corgne et al. 2004, Hirose et al. 2004). All currently available partition coeffi-

cients for CaPv come from experiments with enriched bulk CaO contents (e.g. Corgne and Wood 2002, Corgne et al. 2004, Hirose et al. 2004), as CaPv does not appear near the liquidus of normal peridotite assemblages at conditions equivalent to the top of the lower mantle. In determining the plausible amount of perovskite fractionation above, values for CaPv/melt partitioning from H2020b of Corgne et al. (2004) have been used, an experiment which contained ∼8 wt% CaO in the melt. Any plausible magma ocean composition likely had a lower CaO content. Using data from Corgne and Wood (2002), Corgne et al. (2004) and Hirose et al. (2004) a rough parameterisation of partition coefficients verses the melt CaO content can be performed, which allows extrapolation to a typical peridotite value (3.5 wt% CaO). Using these extrapolated values shows that the permissible amount of total total perovskite fractionation decreases to 10 wt% fractionation in the proportion 97% MgPv and 3% CaPv as a result of the increase in CaPv/melt partition coefficients. The Al_2O_3 concentration has a strong effect on MgPv/melt partition coefficients but given that the bulk Al_2O_3 partition coefficient is close to unity, the concentration of Al_2O_3 in MgPv will not vary enough during fractionation to significantly affect the conclusions concerning the size of a potential perovskitic layer.

Any perovskitic reservoir is likely to be FeO and CaO depleted and thus probably less dense compared to the rest of the mantle, which may violate the requirements for a dynamically stable reservoir in the lower mantle (Kellogg et al. 1999). If, however, a magma ocean extended to pressures corresponding to the present day core-mantle boundary, an initially perovskite-rich layer could have become more dense as a result of phase transformation to a post-MgPv phase (Murakami et al. 2004). This could

have stabilised such a chemically distinct layer in the D'' region at the bottom of the mantle against subsequent mantle convection.

In addition to chemical variables it is likely that pressure also influences partition coefficients. In recent studies it has been proposed that D_0 can be related to the free energy of fusion of a hypothetical trace element component (Blundy et al. 1995, Wood and Blundy 1997, van Westrenen et al. 2001). As silicates usually show a positive Clapeyron slope of fusion, this may contribute to an increase in D_0 with increasing pressure. In this case, however, increasing absolute values of mineral/melt partition coefficients will increase their leverage on RLE ratios, and therefore decrease the total amount of allowable perovskite fractionation. This implies that the 10-13 wt% MgPv/CaPv fractionation, that is still consistent with upper mantle RLE ratios, is an upper bound and that the effects of pressure in a magma ocean significantly deeper than 700 km may even reduce this value.

Figure 3.11 shows BSE normalised element abundances of a 'perovskite depleted mantle' (PDM) and the complementary perovskitic reservoir formed by 13 wt% fractionation (96:4 MgPv:CaPv). The remarkable flat element abundance pattern of the PDM is a result of bulk partition coefficients close to unity and the relatively high melt fraction. The calculated element patterns for the depleted mantle with and without perovskite fractionation are almost indistinguishable, assuming the continental crust was formed by 1.5 wt% melt extraction (Hofmann 1988) and using partitioning data and mineral modes from Salters and Stracke (2004). Although there is no direct evidence for the presence of a lower mantle perovskitic reservoir, the geochemistry of the upper mantle is not inconsistent with $\sim$13 wt% MgPv/CaPv fractionation. This reservoir could of

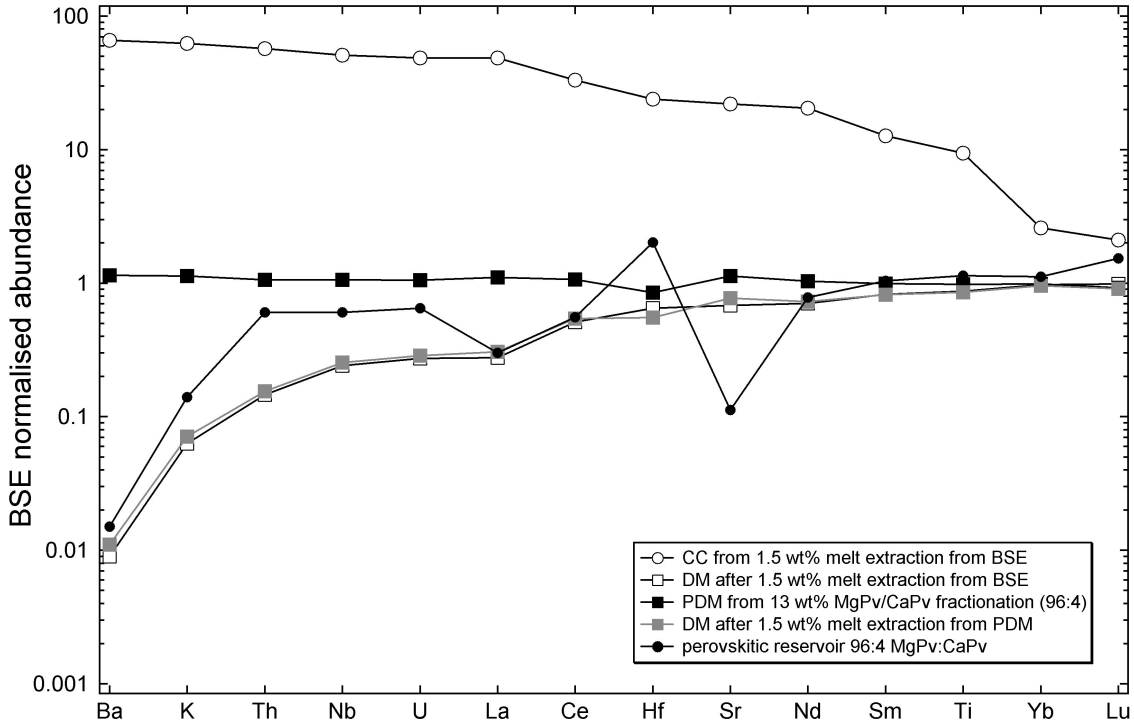

Figure 3.11: BSE normalised abundance pattern for highly incompatible elements during formation of the continental crust (CC). Elements are sorted by decreasing incompatibility. BSE concentrations are taken from McDonough and Sun (1995). Filled black symbols represent a 'perovskite depleted mantle' (PDM) and the complementary perovskitic reservoir after 13 wt% MgPv/CaPv (96:4) crystallisation calculated from Equation 3.6 (partition coefficients for MgPv from H2026; CaPv data are from Corgne et al. (2004). Grey and open squares show the depleted mantle (DM) with and without previous perovskite fractionation as a residual of 1.5 wt% melt extraction to form the CC (open circles, see text for details). The latter 'low melt fraction' processes have been calculated using the batch melting equation.

course be smaller or could have been homogenised by subsequent mantle convection. Assuming ∼13 wt% fractionation and taking least square regressions of the Mg and Si partitioning coefficients presented in Figure 3.4 together with the present day Mg/Si ratio of the PUM (1.26, Walter et al. 2004), shows that a magma ocean (assumed to be the BSE) would have an initial Mg/Si ratio of 1.23, which is essentially peridotitic. This demonstrates that the depletion of Si in PUM relative to Mg and CI-chondrites is a feature of the bulk silicate Earth, that was caused by either volatilisation during

accretion (e.g. Ringwood 1979), incorporation of Si into the core (e.g. Allegre et al. 1995) or was simply inherited from an as yet unsampled proto Earth material.

Chapter 4

The Oxidation State of Iron in Mg-Silicate Perovskite

4.1 Aim of this Chapter

Previous studies have shown that aluminous Mg-silicate perovskite (MgPv) can contain significant amounts of ferric iron under subsolidus conditions (McCammon 1997, Xu et al. 1998, Frost and Langenhorst 2002, McCammon et al. 2004), even at very low oxygen fugaciies (Lauterbach et al. 2000). These experiments were performed in relatively simple four-component systems and the bulk composition was therefore not equivalent to a typical lower mantle peridotite compositions. Although McCammon et al. (2004) reported two $Fe^{3+}/\sum Fe$ ratios measured on MgPv in a peridotitic sample, the Al_2O_3 concentrations in the MgPv-phase were $\leq$2.6 wt%, which is significantly lower than expected for the lower mantle (4-5 wt% Al_2O_3 , Wood 2000). Most importantly, no measurements of $Fe^{3+}/\sum Fe$ of MgPv's at conditions above or at the peridotite solidus are available. Such data, however, are crucial in order to understand the distribution of heterovalent iron during crystallisation of a deep magma ocean.

In this chapter, results of measurements of $Fe^{3+}/\sum Fe$ ratios of Mg-silicate perovskite synthesised at conditions close to or above the peridotite solidus are presented. The

new data are used to estimate possible effects of MgPv crystallisation on the evolution of the oxidation state of the Earth's lower mantle during the Hadean.

4.2 Experimental and Analytical Techniques

Measurement of Fe^{3+} concentrations of MgPv were performed on samples synthesised at approximately 25 GPa using a multianvil apparatus. Two samples have been investigated. Experiment S3242, performed an a the fertile peridotite composition, has already been described in the previous chapter. The starting material in this experiment was encapsuled in a graphite container the run temperature was approximately 2250°C. Experiment S3224 has was performed using the 10/3.5 pressure cell and graphite as capsule material. This experiment was performed under subsolidus consitions at approximately 2000°C, which was estimated from the electrical power. Run conditions and phase assemblages are summarised in Table 4.1.

Table 4.1: Run conditions and phase assemblages of experiments used for ferric iron determinations

run	**T [°C]**	**t [min]**	**Phase assemblage**
S3224	2000	120	[MgPv,Fp,Mj,CaPv]
S3242	2000-2250	12	Liq-[Fp]-[Fp,MgPv,(CaPv)]

Pressure: 25 GPa
Starting material: fertile peridotite
Capsule material: graphite

4.2.1 Electron Energy Loss Spectroscopy

Measurements of $Fe^{3+}/\sum Fe$ ratios of MgPv by electron energy loss spectroscopy (EELS) using the transmission electron microscopy (TEM) have been performed in collaboration with P.D. Dr. Falko Langenhorst at the Bayerisches Geoinstitut. For TEM investigations, thin sections of the sample (20-30 μm) were mounted on 3 mm diameter molybdenum grids and then thinned to electron transparency by argon ion bombardment in a *Gatan DUO-MILL* machine at an acceleration voltage of 3 kV and 1 mA beam current. To avoid amorphisation of the MgPv, thinning was done in a sample holder that was cooled by liquid nitrogen.

Electron energy-loss spectra were recorded using a *Gatan PEELS 666* parallel electron spectrometer attached to a *Philips CM20-FEG* (field emission gun) transmission electron microscope operating at 200 kV. The measurement of the $Fe^{3+}/\sum Fe$ ratio is based on the white line intensities at the Fe $L_{2,3}$ edges, which have been calibrated for minerals in the high-spin state (van Aken et al. 1998). Details of this method are reported in the latter reference and by Lauterbach et al. (2000). To minimise electron irradiation damage during measurements, samples were cooled to nearly liquid nitrogen temperature (ca. 100 K) in a Gatan cooling stage. Iron $L_{2,3}$ edges were recorded at the thinnest part of the sample in diffraction mode of the TEM at small scattering angles. To improve counting statistics six spectra with integration times of 10-20 s were recorded.

The chemical composition of MgPv grains used for $Fe^{3+}/\sum Fe$ determinations have been analysed by a *ThermoNoran Vantage* energy dispersive x-ray (EDX) analysis system attached to the TEM. EDX spectra were collected under 200 kV for 60 s total

counting times, while the sample was tilted at an angle of 14° towards the Ge solid-state detector.

4.2.2 Mössbauer Analysis

Mössbauer analyses have been performed with Catherine A. McCammon at the Bayerisches Geoinstitut. Samples were prepared as sections with thicknesses of 100-150 μm. Mössbauer spectra were recorded at 298 K on a constant acceleration micro-Mössbauer spectrometer with a nominal 1.85 GBq ^{57}Co source in a 12 μm Rh matrix. Further details of this method can be found in McCammon et al. (1991) and McCammon (1994). The velocity scale was calibrated relative to 25 μm α-Fe foil using the positions certified for National Bureau of Standards reference material no. 1541. Line widths of 0.36 mm/s for the outer lines of α-Fe were obtained at room temperature. The spectra were fitted to Lorentzian lineshapes using the program NORMOS, written by R.A. Brand and distributed by *Wissenschaftliche Elektronik GmbH, Germany.*

4.3 Results

Sample S3224 crystallised at subsolidus conditions with the phases Mg-silicate perovskite, ferropericlase, Ca-silicate perovskite and majoritic garnet. Sample S3242 crystallised under a range of conditions from subsolidus to the silicate liquidus as a result of a thermal gradient. BSE images of the latter sample with magnifications of the liquidus and subsolidus region are shown in Figure 4.1. Although no additional Fe-metal had been added to either experiment, homogeneously distributed, mostly sub-micron Fe-rich metal particles are observed on grain boundaries in both samples. The metal

Table 4.2: Chemical compositions of MgPv determined by EMPA or by TEM-EDX as cations per formula unit (pfu) $MgSiO_3$ (normalised to two cations), and $Fe^{3+}/\sum Fe$ rations measured by Mössbauer- (M) or electron energy loss (E) spectroscopy. Chemical compositions for S3224 and S3242-1,2 are bulk analyses from EMPA. Compositions for S3242-3,4 were derived from TEM-EDX analyses from individual MgPv grains.Numbers in parenthesis are uncertainties in terms of the last cites units

	S3224 subsolidus	**S3242-1** subsolidus	**S3242-2** liquidus	**S3242-3**	**S3242-4**
$Fe^{3+}/\sum Fe$	M 0.20 (11)	M 0.30 (9)	M 0.39 (10)	E 0.46 (10)	E 0.39 (10)
Si	0.939 (6)	0.901 (8)	0.926 (8)	0.913	0.927
Ti	0.005 (1)	0.004 (1)	0.004 (1)	0.002	0.003
Al	0.071 (4)	0.095 (6)	0.082 (3)	0.099	0.073
Cr	0.005 (1)	0.003 (1)	0.002 (1)	0.003	0.003
Fe^{3+}	0.014 (8)	0.025 (8)	0.019 (5)	0.020	0.016
Fe^{2+}	0.056 (8)	0.059 (8)	0.030 (5)	0.023	0.026
Mn	0.002 (1)	0.002 (1)	0.001 (1)	-	-
Mg	0.887 (9)	0.884 (12)	0.911 (12)	0.916	0.927
Ca	0.020 (7)	0.025 (2)	0.024 (4)	0.025	0.024
Ni	0.001 (1)	0.001 (1)	0.001 (1)	-	-

must have formed during the experiment, which will be discussed below. Chemical analysis of coexisting phases are reported in Tables A.1 and A.3 in Appendix A. In sample S3242, the chemical composition of MgPv changes with temperature, such that the FeO^{total} content increases from 3.5 wt% close to the liquidus to approximately 6 wt% in the subsolidus assemblage. The MgPv compositions, expressed as cations per formula unit determined by EMPA and TEM-EDX are given in Table 4.2. Mass balance calculations performed on the subsolidus composition of sample S3242 indicate a phase assemblage of 78 wt% MgPv, 14 wt% Fp, 2 wt% Mj and 6 wt% CaPv, which is therefore close to a typical lower mantle phase assemblage.

In sample S3224 both Fp and CaPv could not be analysed accurately by EMPA due to small grain sizes. However, using the measured chemical compositions of MgPv and

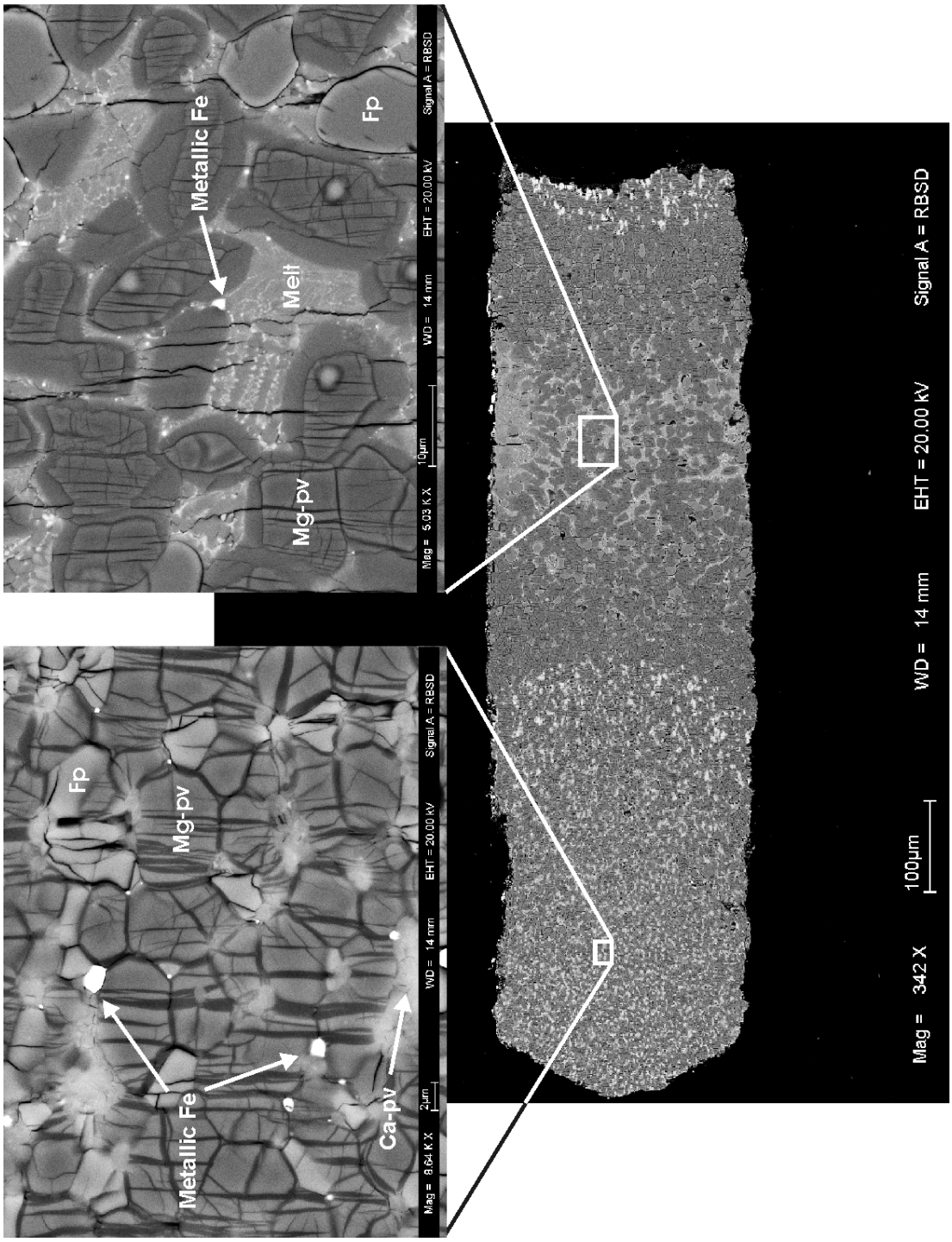

Figure 4.1: Backscattered electron images of run S3242 with close-ups of the liquidus and subsolidus regions. Although no metallic Fe was added to this experiment, Fe^0 of sub-micron size was observed to be homogeneously distributed over the sample

majorite from S3224 and taking the subsolidus chemical composition of ferropericlase and CaPv from experiment S3242, phase proportions of 66 wt% MgPv, 17 wt% Fp, 13 wt% Mj and 4 wt% CaPv are estimated. The higher amount of majorite is consistent with the lower concentration of Al_2O_3 in MgPv in S3224 (3.6 wt%) compared to sample S3242 (4.8 wt% Al_2O_3 in MgPv). In sample S3242, some particles of the precipitated metallic phase were large enough to perform chemical analysis by EMPA. They contain 88.5 wt% Fe and 11.5 wt% Ni. Using these data and the chemical composition of Fp, the oxygen fugacity fO_2 during this experiment can be calculated. The oxygen fugacity is controlled by the distribution of Fe between the metallic and the oxide phase, such that

$$2Fe_{Metal} + O_2 = 2FeO_{Oxide}. \tag{4.1}$$

The equilibrium constant K is then given by

$$K = \frac{a^2_{FeO,Oxide}}{a^2_{Fe,Metal} \cdot fO_2}, \tag{4.2}$$

whereas $a_{c,p}$ denotes the activity of component c in phase p. In case of pure Fe and FeO the activities of both components equal 1 and the equilibrium constant becomes

$$K = fO_2(IW)^{-1}, \tag{4.3}$$

where $fO_2(IW)$ is the oxygen fugacity of the iron-wüstite buffer. The oxygen fugacity during an experimental run may therefore be expressed relative to the iron-wüstite buffer as

$$\Delta IW = log(fO_2) - log(fO_2)(IW), \tag{4.4}$$

which can be calculated from reaction 4.1 as

$$\Delta IW = 2log\left(\frac{a_{FeO,Oxide}}{a_{Fe,Metal}}\right). \tag{4.5}$$

Assuming that FeO and MgO in the oxide phase and Fe and Ni in the metallic phase mix ideally, the activity coefficients in equation 4.5 can be replaced by the mole fractions $X_{FeO,Fp}$ and $X_{Fe,metal}$. Using the mole fractions determined from run S3242 gives an oxygen fugacity of approximately 1.3 log-units below the iron-wüstite buffer. It is expected that the oxygen fugacity in run S3224 had a comparable value, since this experiment has been performed under similar conditions.

EELS measurements have been performed on two individual MgPv grains in sample S3242. The relative positions of the two grains could not be determined unambiguously, but the low total Fe content suggest that both analyses were obtained from grains in or close to the subliquidus region. Raw spectra were corrected for dark current and channel-to-channel gain variation of the detector. The background was subtracted by an inverse power-law and multi-scattering effects were eliminated by a Fourier-ratio technique (Egerton 1996). After data reduction the white-line intensities (L_3, L_2) used for $Fe^{3+}/\sum Fe$ determination, were obtained by integrating energy windows from 708.5 eV to 710.5 eV and 719.7 eV to 721.7 eV, respectively.

Mössbauer measurements have been performed on both samples S3224 and S3242. In the latter sample, spectra were obtained from both the subsolidus and subliquidus regions. Spectra were collected from bulk phase assemblages over circular areas of approximately 50 μm diameter, and are shown in Figure 4.2. The spectra show overlapping peaks from all iron containing phases. To derive $Fe^{3+}/\sum Fe$ ratios of MgPv the deconvolution model of McCammon et al. (2004) was used. Spectra were evaluated by fitting doublets for Fe^{2+}_{MgPv}, Fe^{3+}_{MgPv}, Fe^{2+}_{Fp} and Fe^{2+}_{Mj} to the data. Thus both Fp and Mj were assumed to be free of ferric iron. Empirical relations for $Fe^{3+}/\sum Fe$ ratios of

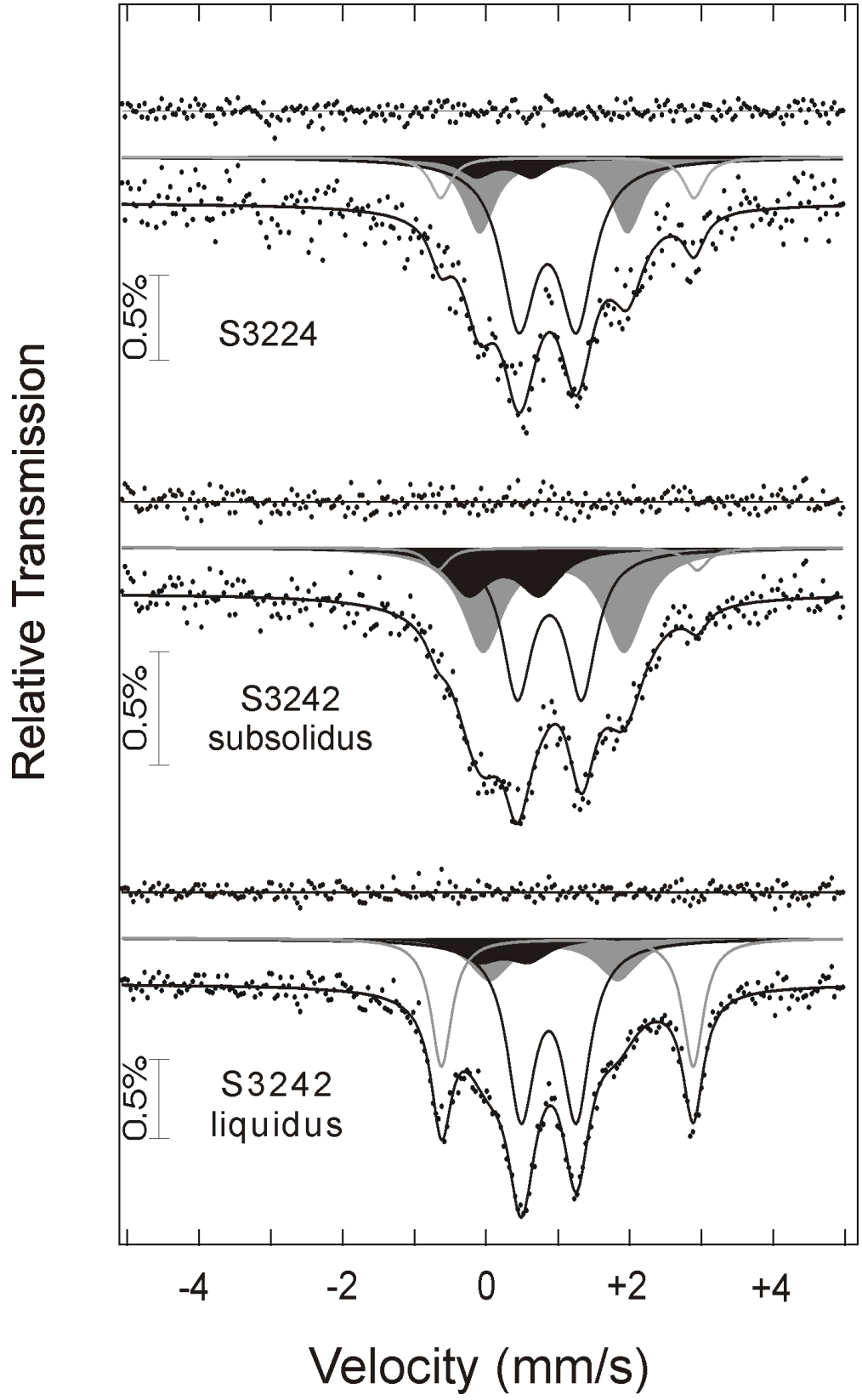

Figure 4.2: Mössbauer spectra obtained at room temperature from samples S3224 and S3242. Doublets correspond to Fe^{2+}_{MgPv} (dark grey area), Fe^{3+}_{MgPv} (black area), Fe^{2+}_{Fp} (black line) and Fe^{2+}_{Mj} (grey line)

Mj and Fp indicate maximum values of 0.05-0.10 (Mj) and 0.01-0.02 (Fp), respectively, based on the mineral total Fe content and experimentally adjusted redox conditions (McCammon and Ross 2003, McCammon et al. 2004). Although the assumption that all of the Fe^{3+} of the system is incorporated in MgPv may cause its $Fe^{3+}/\sum Fe$ ratio as determined from Mössbauer analysis to be slightly overestimated, the comparison with EELS data (see discussion below) suggest an overall small contribution of Fe^{3+} from other phases. $Fe^{3+}/\sum Fe$ ratios from both EELS and Mössbauer analysis are included in Table 4.2.

Despite relatively low oxygen fugacities, the measured $Fe^{3+}/\sum Fe$ ratios reach values between 0.2 and 0.5. Figure 4.3 shows the concentration of ferric iron as a function of the Al concentration of MgPv as cations per formula unit (normalised to two cations), similar to Figure 3.5 in section 3.3. There is good agreement between $Fe^{3+}/\sum Fe$ ratios determined from Mössbauer- and EEL spectroscopy at similar Al concentrations of the MgPv phase. The amount of ferric iron is positively correlated with the concentration of Al in MgPv. Similar observations have been made in the studies of Lauterbach et al. (2000), Frost and Langenhorst (2002), Frost et al. (2004a) and McCammon et al. (2004). In Figure 4.4, data from the latter studies have been added to the results shown in Figure 4.3. Data from Lauterbach et al. (2000) were obtained from high pressure experiments performed on aluminous pyroxene compositions under relatively reducing conditions in Fe capsules but also in a more oxidising environment in the presence of a Re-ReO_2 oxygen buffer. Their results show no systematic difference in the concentration of ferric iron in MgPv as a function of redox conditions. Frost and Langenhorst (2002) performed their experiments on aluminous pyroxene mixed

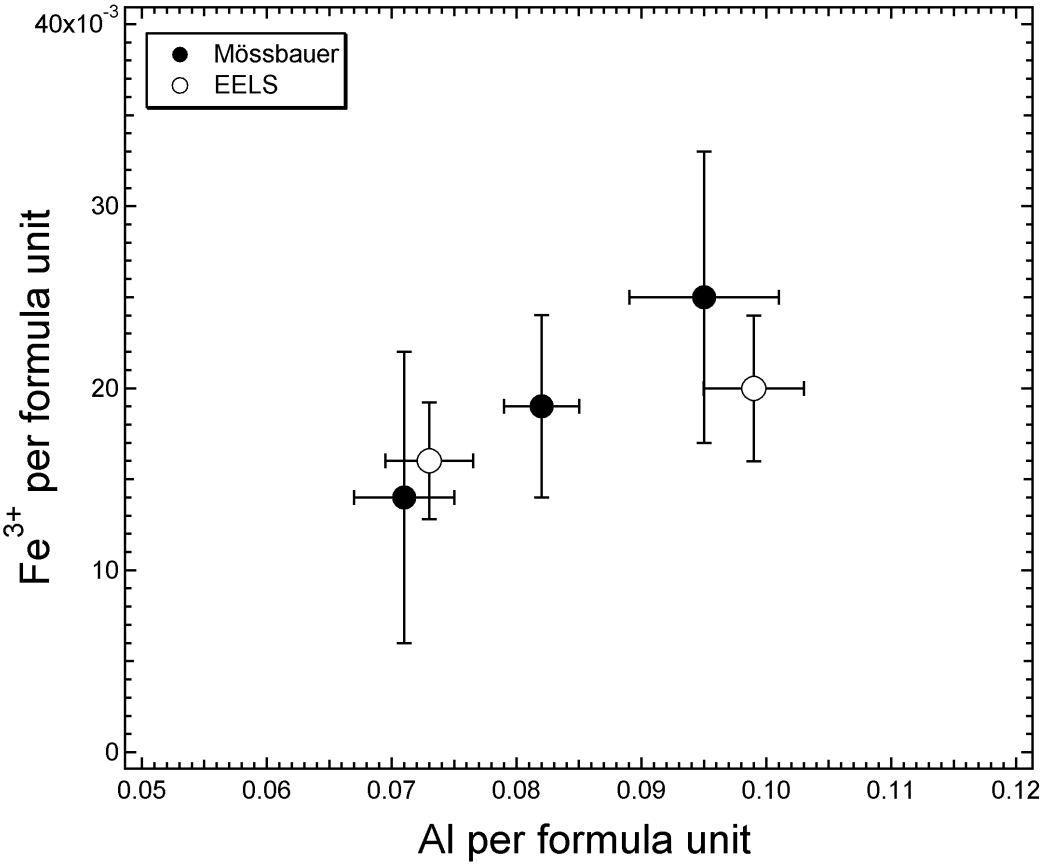

Figure 4.3: Ferric iron concentration plotted against the amount of Al in formula units (normalised to two cations) in MgPv

with ferropericlase under oxygen fugacities constrained by the Re-ReO_2 oxygen buffer. Experiments by Frost et al. (2004a) on similar starting compositions encapsuled in Fe-metal capsules. The data from McCammon et al. (2004) were also obtained on mixtures of MgPv and Fp. These studies were performed on a four-component system SiO_2-Al_2O_3-FeO-MgO at temperatures between 1650-1850°C, although McCammon et al. (2004) also presented two data points obtained from $Fe^{3+}/\sum Fe$ measurements on MgPv's crystallised in a subsolidus phase assemblage of a chemically more complex synthetic KLB-1 peridotite composition.

In general, the data shown in Figure 4.4 indicate that the amount of Fe^{3+} in MgPv increases with increasing Al concentration but the ferric iron concentrations in the

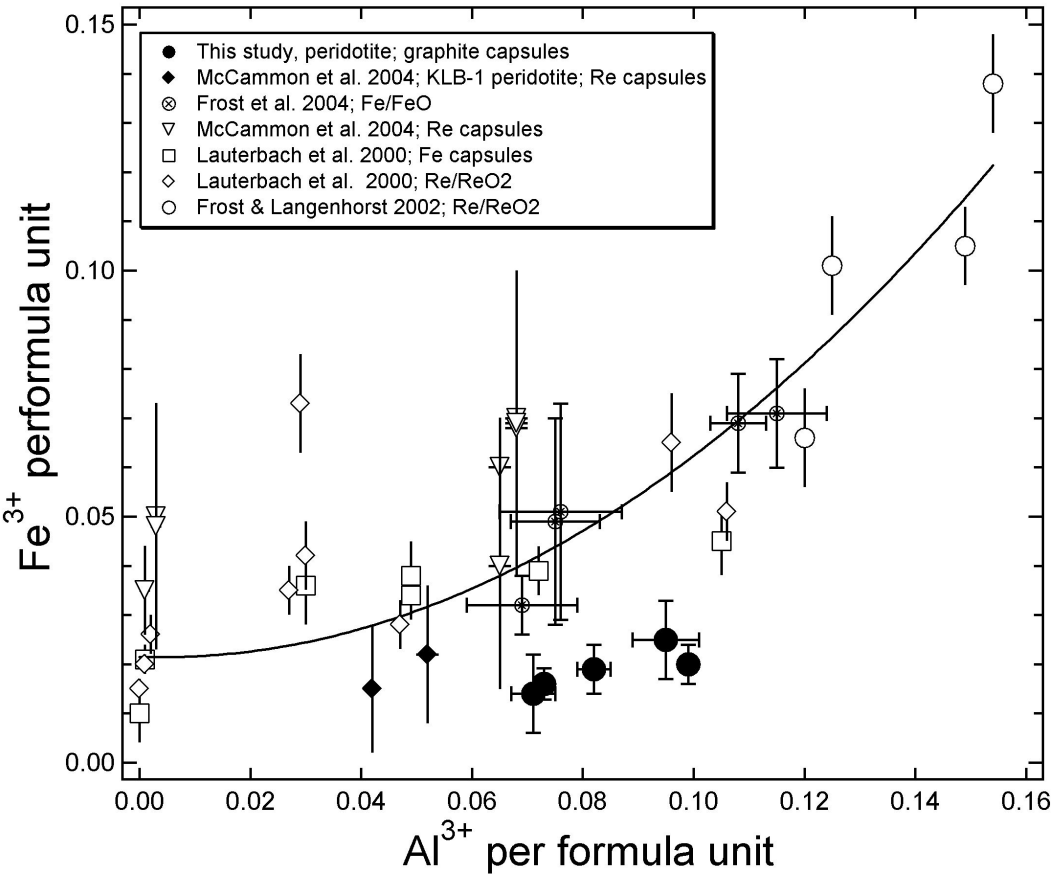

Figure 4.4: Comparison of ferric iron concentrations as a function of Al content in MgPv presented with recently pubslished data from Lauterbach et al. (2000), Frost and Langenhorst (2002), McCammon et al. (2004) and Frost et al. (2004a). The solid line is a least square polynomial fit to results from previous studies.

chemically more complex peridotitic compositions fall systematically below the trend followed by the simpler four-component system. Compared to the peridotite data from McCammon et al. (2004) obtained from samples quenched from 1750 and 1850°C, the amounts of ferric iron in MgPv compositions from this study are similar, although the Al content is significantly higher. However, it is emphasised, that experiments from this study have been performed at higher temperatures of 2000-2250°C.

4.4 Discussion

4.4.1 Oxygen Fugacity and Fe^{3+} in MgPv

The positive correlation between ferric iron and Al in MgPv can well be understood on the basis of a charge coupled substitution mechanism as described in section 3.4.1 by Equation 3.2 for trivalent elements. The charge balance of Fe^{3+} by creation of an oxygen vacancy, as discussed by Lauterbach et al. (2000), is not supported by the present data or by the trace element partitioning results (Chapter 3). However, it may be a feasible substitution mechanism at very low Al concentrations (Frost and Langenhorst 2002).

The lower concentrations of ferric iron in MgPv from complex peridotitic compositions compared to samples produced in the more simple four-component system is likely a result of substitution of other tri- and tetravalent minor and trace elements onto the Mg-site in MgPv such as Ti^{4+}, Cr^{3+} or Mn^{3+} which in total reach almost the 1 wt% level in MgPv. Furthermore, the high-temperature MgPv compositions from this study have higher CaO concentrations compared to compositions reported by McCammon et al. (2004) or Wood (2000) from experiments at 1750-1900°C, which suggests that the solubility of Ca into MgPv is temperature dependent. In the framework of the lattice strain model (section 3.4.1) a high abundance of large Ca^{2+} cations on the Mg-site in MgPv will increase the average lattice-site (e.g. manifested in an increase of r_0), which may stabilise the larger Fe^{2+} against the smaller Fe^{3+} cation. In addition, the high synthesis temperatures applied in this study will most likely also lead to high concentrations of intrinsic defects, such as Schottky pairs (i.e. cation and anion vacancies), since the abundance of the latter are strongly temperature dependent (e.g.

Poirier 1985). The relatively high ferric iron concentrations in MgPv even in equlibrium with precipitated metal implies a relatively weak influence of oxygen fugacity on the $Fe^{3+}/\sum Fe$ in MgPv. The amount of Fe^{3+} in aluminous MgPv may consequently be controlled predominately by its crystal chemistry and a charge coupled substitution mechanism and not by oxygen fugacity. This would be consistent with results from Lauterbach et al. (2000) and McCammon et al. (2004), suggesting little or no influence of oxygen fugacity on the ferric iron content of alumina bearing MgPv.

Lauterbach et al. (2000) and Frost et al. (2004a) suggested that in the absence of sufficient amounts of oxygen (low oxygen fugacities) the required proportion of ferric iron for the coupled substitution in MgPv can be produced by a disproportionation reaction according to

$$3FeO_{System} = Fe_2O_{3,MgPv} + Fe_{Metal}. \tag{4.6}$$

This reaction could therefore explain the presence of the observed Fe-rich metal in both runs of this study, while the MgPv phase still contains significant amounts of Fe^{3+}. The observation that high levels of ferric Fe in MgPv occur in the presence of metallic iron implies that this equilibrium must shift to the right hand side of Equation 4.6 in the MgPv stability field.

4.4.2 Implication for Magma Ocean Crystallisation

The disproportionation of FeO to ferric iron and Fe metal may have important consequences for the crystallisation of MgPv from a deep magma ocean. A magma ocean was likely in or close to equilibrium with core-forming metallic liquids and thus very reduced, which implies that almost the entire iron of the silicate system was expected

to be in the Fe^{2+} state and the $Fe^{3+}/\sum Fe$ ratio was therefore close to zero. As aluminous MgPv formed, however, disproportionation to produce Fe^{3+} plus Fe-metal must also have occurred if no other likely component is available to oxidise FeO. In the following discussion it is assumed that all Fe^{3+} forms by disproportionation of FeO and likely consequences of the formation of the lower mantle with and without crystal fractionation from a magma ocean are considered. An additional or alternative oxidation mechanism is presented at the end of this section.

In the previous chapter it was shown that the present day upper mantle geochemistry is not inconsistent with the existence of a MgPv-dominated crystal accumulate that could comprise up to 13 wt% of the entire mantle in the proportion 96% MgPv and 4% CaPv, and could have formed during crystallisation of a Hadean magma ocean. MgPv crystallising at approximately 700 km depth would typically contain about 4.0-4.5 wt% Al_2O_3 and 3.5 wt% FeO^{total}. At this relatively low total Fe content (compared to subsolidus compositions) the $Fe^{3+}/\sum Fe$ ratio can be up to 50% as observed in analysis S3242-3 (see Table 4.2). This results in approximately 0.6 mol% Fe_2O_3 component in MgPv. Assuming that all the ferric iron is produced by the disproportionation of FeO, the formation of a MgPv dominated reservoir must have been accompanied, according to equation 4.6, by precipitation of a similar amount (0.6 mol%) of Fe-rich metal. Considering that the molar weight for the given MgPv composition of 53 g/mol is similar to the molar weight of Fe-metal (55.8 g/mol), and ignoring the effect of small amounts of CaPv, an MgPv crystal accumulate would contain approximately 0.5-1 wt% of a Fe-rich metallic phase.

If a peridotitic magma ocean solidified without any significant amount of crystal frac-

tionation, a Fe-rich metal phase should have formed below a depth of 670 km, probably in a similar mode as it has been observed in the subsolidus assemblage of sample S3242 (Figure 4.1). Taking the subsolidus chemical compositions and mineral abundances of the latter experiment and the measured $Fe^{3+}/\sum Fe$ ratio of 0.30, the bulk rock $Fe^{3+}/\sum Fe$ ratio should be approximately 0.2. It is emphasised that the $Fe^{3+}/\sum Fe$ ratio at subsolidus conditions is lower when compared to subliquidus conditions, because the bulk Fe-content of MgPv in the former case is higher. This implies a lower $Fe^{3+}/\sum Fe$ ratio at a similar Al_2O_3 concentration in MgPv. In this example, the MgPv composition would contain 0.6-0.7 mol% Fe_2O_3, which thus results in a similar amount of Fe-metal relative to MgPv. Considering a molar abundance of 80% MgPv the amount of Fe-metal in the bulk phase assemblage is on the order of 0.5-0.6 mol%, which thus corresponds to a similar weight fraction of metallic iron in the lower mantle, because the molar weight of a peridotite bulk composition of ∼52 g/mol is again similar to the molar weight of Fe-metal. In this approximation the effect of Fe-Mg partitioning (e.g. Frost and Langenhorst 2002) between MgPv and Fp on Fe-metal precipitation is ignored, since it is expected to have a relatively minor influence on the total amount of precipitated Fe^0.

Analysis of mantle xenoliths suggest that upper mantle rocks have bulk $Fe^{3+}/\sum Fe$ ratios of ≤0.03 (e.g. O'Neill et al. 1993, Canil et al. 1994). Although ferrous iron is by far the most dominant species, the ferric iron content in the present day upper mantle is therefore higher than it probably was during core-formation ($Fe^{3+}/\sum Fe \approx 0$). Although the disproportionation of FeO to Fe_2O_3 and metallic iron in the lower mantle does not change the net oxygen content, the separation of this precipitated metallic

phase into the core, eventually by percolation (e.g. Shannon and Agee 1998, Takafuji et al. 2004) or by a mechanism as envisaged in Figure 4.5, would leave behind a region which is enriched in oxygen (or Fe_2O_3) relative to the rest of the mantle. Subsequent rehomogenisation between the lower mantle (or a MgPv dominated reservoir) and the overlying upper mantle by whole-mantle convection could therefore have increased the relative oxygen content of the bulk mantle.

In a peridotite bulk mantle composition the amount of excess oxygen that is required to raise the $Fe^{3+}/\sum Fe$ ratio from zero to a bulk mantle value of 0.03 (as observed for the upper mantle) is on the order of 0.03 is 0.04 mol%. Considering that the lower mantle contains approximately 70% of the bulk mantle implies that the total mole-fraction of precipitated metal in a solidified lower mantle (following the example given above) relative to the bulk mantle is $0.7 \cdot 0.5 mol\% \approx 0.4 mol\%$. Taking into acount that the removal of one mole of Fe^0 leaves behind one mole of O^{2-}, suggests that segregation of approximately 10% of the metal phase into the core, followed by subsequent rehomogenisation of upper and lower mantle, is sufficient to explain the present-day redox state of the Earth's upper mantle. It is emphasised that Fe-metal and ferric iron in MgPv would recombine to FeO outside the stability field of MgPv, which therefore excludes the presence of a metal phase in upper mantle rocks.

If MgPv crystal fractionation or solidification of the lower mantle occurred before core-formation was completed, then the precipitated Fe-rich metal could have been a sink for siderophile elements in the lower mantle, which inhibited extraction of these elements into the Earth's core. Subsequent whole-mantle convection after core-formation, however, could have redistributed the element content of the metallic phase in the en-

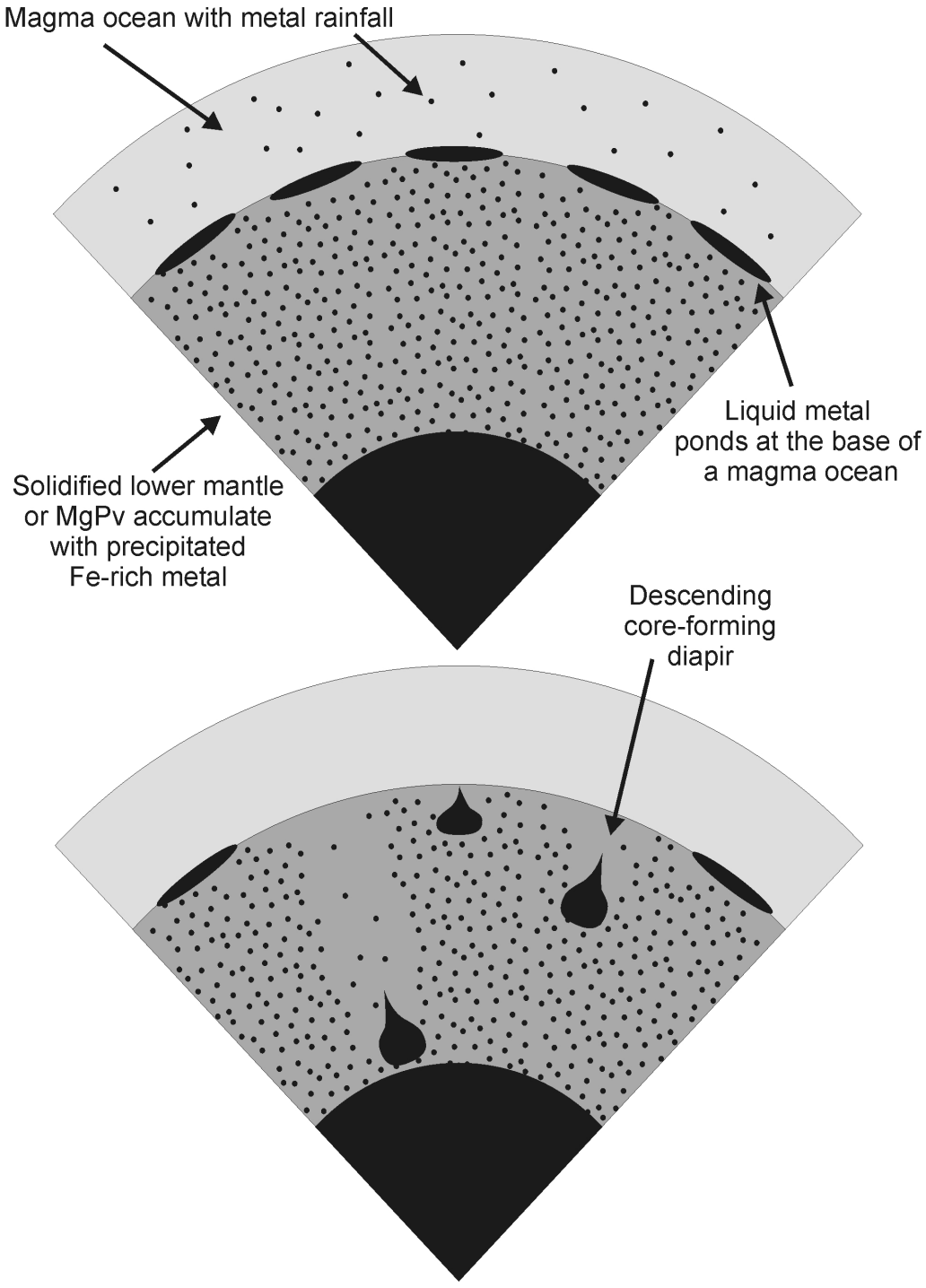

Figure 4.5: Possible mechanism leading to mantle oxidation. Upper part: Liquid metal ponds form at the base of a magma ocean as a result of metal 'rainfall' (see Righter and Drake 1997, Rubie et al. 2003, for details). Lower part: Due to their high density, the metal ponds become dynamically unstable and descend through the solid lower mantle or a MgPv dominated reservoir. This situation would most likely lead to removal of some precipitated Fe-metal from the lower mantle.

tire mantle and could therefore explain the observed overabundance of moderately- and highly-siderophile elements in the upper mantle. Thus two major geochemical features of the present day upper mantle, its oxidation state and the 'overabundance' of siderophile elements, can be derived from the existence of Fe-rich metal in the Earth's lower mantle. The addition of approximately 1% of the Earth's total mass of oxidised chondritic material to acount for those properties, known as the 'late veneer' (e.g. Kimura et al. 1974, Holzheid et al. 2000), is therefore not necessarily required.

Another mechanism may be envisaged for the oxidation of the mantle. It has been suggested that a Hadean magma ocean contained a substantial amount of water (Abe et al. 2000, and references therein). Righter and Drake (1999) suggested that a magma ocean may have contained up to 4 wt% dissolved H_2O. These authors pointed out that reaction of water and core-forming liquids could have increased the FeO content of the mantle by the reduction of H_2O. However, if significant amounts of water were present in a deep magma ocean, possibly even after core-formation, then H_2O, or other volatile species, could have been reduced during the formation of aluminous MgPv to produce ferric iron. Such a reaction would therefore not necessarily involve the disproportionation of FeO, and thus no precipitation of metallic Fe. Subsequent degassing of the mantle and loss of the reduced volatile species, however, could have been another effective mechanism to leave behind an oxygen enriched bulk mantle. In such a model the overabundance of siderophile elements in the present day Earth's mantle cannot be related to the formation of the lower mantle.

4.5 Conclusions

Measurements of $Fe^{3+}/\sum Fe$ ratios of aluminous Mg-silicate perovskite (MgPv) suggest that the concentration of ferric iron is mainly a function of the Al content in MgPv but not of oxygen fugacity, and is best explained by crystal chemical controls constrained by a charge-coupled substitution mechanism. At low oxygen fugacities, the required amount of Fe^{3+} can be produced by disproportionation of FeO to Fe_2O_3 and metallic iron. Precipitation of metallic Fe in the presence of aluminous MgPv, either by MgPv dominated crystal fractionation during the Hadean or generally by formation of the lower mantle, could have had a significant effect on the present-day upper mantle geochemistry. Segregation of a certain fraction of this Fe-rich metal into the core could have raised the relative oxygen content of the mantle and therefore increased the $Fe^{3+}/\sum Fe$ ratio from a value close to zero during core-formation to the observed value of 0.03 at present. This requires rehomogenisation of upper and lower mantle regions which also provides a possibility to increase the concentration of siderophile elements in the upper mantle, if those were partitioned into the metallic phase before core-formation was completed. An alternative or additional process, that could have created an oxidised mantle, involves reduction of volatile species during formation of a MgPv dominated lower mantle. Subsequent degassing of the reduced species could have also raised the net oxygen content of the mantle.

Chapter 5

Viscosity of Peridotite Liquid at High Pressure

5.1 Introduction

Early differentiation processes and the possibility of crystal fractionation in a deep magma ocean depend on the fluid dynamical properties of a molten mantle, in which the viscosity of the silicate liquid as a function of depths is a crucial parameter. As pointed out in section 1.5, the viscosity of a magma ocean has been estimated in previous studies of magma ocean dynamics (Tonks and Melosh 1990, Solomatov and Stevenson 1993b,a, Rubie et al. 2003) but the effect of pressure on viscosity has not been considered. The viscosity of peridotite liquid, as a likely magma ocean composition, has recently been determined as a function of temperature at 1 bar, but the effect of pressure on a melt of peridotitic composition has not been studied so far.

5.1.1 Falling Sphere Viscometry

Experimentally, the viscosity of a melt at super-liquidus temperatures and high pressures can be determined by the 'falling sphere' method. This method has first been applied to silicate liquids by Shaw (1963). Viscosity measurements are based on the determination of the velocity of a sphere falling through a liquid. Melt viscosity can be

derived from *Stokes formula* (Eqn. 5.1), which describes the drag force F_d on a sphere of radius r moving with the velocity v through a liquid:

$$F_d = 6\pi\eta r v \tag{5.1}$$

where η denotes the dynamic viscosity of the fluid. In case of a sphere falling through a liquid, its velocity is determined by the drag force, the gravitational force $F_g = \rho_s V g$ and the buoyancy force $F_b = \rho_l V g$, where V is the volume of the sphere, g the acceleration due to gravity and ρ_s and ρ_l are the densities of the sphere and liquid, respectively. At a constant terminal velocity v_s, all three forces are balanced, such that

$$F_g = F_b + F_d \tag{5.2}$$

and

$$\rho_s V g = \rho_l V g + 6\pi\eta r v_s. \tag{5.3}$$

Substituting for the volume of the sphere and solving for the viscosity of the liquid gives

$$\eta = \frac{2r^2 g\,(\rho_s - \rho_l)}{9 v_s}. \tag{5.4}$$

Equation 5.4 can be used to calculate the viscosity of the liquid when the falling velocity of the sphere, its density ρ_s and the density of the liquid ρ_l are known. In the case of spheres falling through a liquid contained in a finite cylindrical sample capsule, the viscosities can be corrected for wall-effects by multiplicating Equation 5.4 by a correction factor F:

$$F = 1 - 2.104 \cdot \left(\frac{r}{r_c}\right) + 2.09 \cdot \left(\frac{r}{r_c}\right)^3 - 0.95 \cdot \left(\frac{r}{r_c}\right)^5, \tag{5.5}$$

where r_c is the diameter of sample capsule (Faxen 1923).

5.1.2 The Radiographic Method

The falling sphere technique has been used widely to investigate silicate melt viscosities as a function of pressure and temperature in piston-cylinder or gas-pressure apparatus using a quench technique (e.g. Shaw 1963, Kushiro et al. 1976, Brearley et al. 1986, Schulze et al. 1996). In these studies, the sphere velocity was determined from experimental run times and relative sphere positions in samples before and after the experiments. The sphere position after the experiment could be determined in the recovered sample, while the initial sphere position was either assumed to be very close the top of the capsule (Shaw 1963) or it was marked by fine grained metal powder, which was assumed to sink only a negligible distance compared to metal sphere (Schulze et al. 1996). This approach only allows viscosities to be determined with reasonable precision if the experimental run times are long enough that acceleration and deacceleration of the sphere during heating and quenching and the uncertainty surrounding the initial sphere position can be neglected. Thus, falling sphere viscometry in quench-type experiments is mainly suitable for investigating relatively polymerised, high-viscosity melts, such as liquids of granitic, andesitic or dacitic compositions. This technique is also limited to pressure ranges that are covered by the piston-cylinder technique (<3-4 GPa), because the much smaller sample sizes in multianvil experiments are not sufficient for obtaining viscosity data with acceptable uncertainties.

Significant improvement in investigating silicate melt viscosities with high precision has been provided by *in-situ* falling sphere viscometry using the 'radiographic method' (Kanzaki et al. 1987). Using this technique, the descent of a metal sphere through silicate liquid can be monitored in real-time by the use of intense x-ray synchrotron

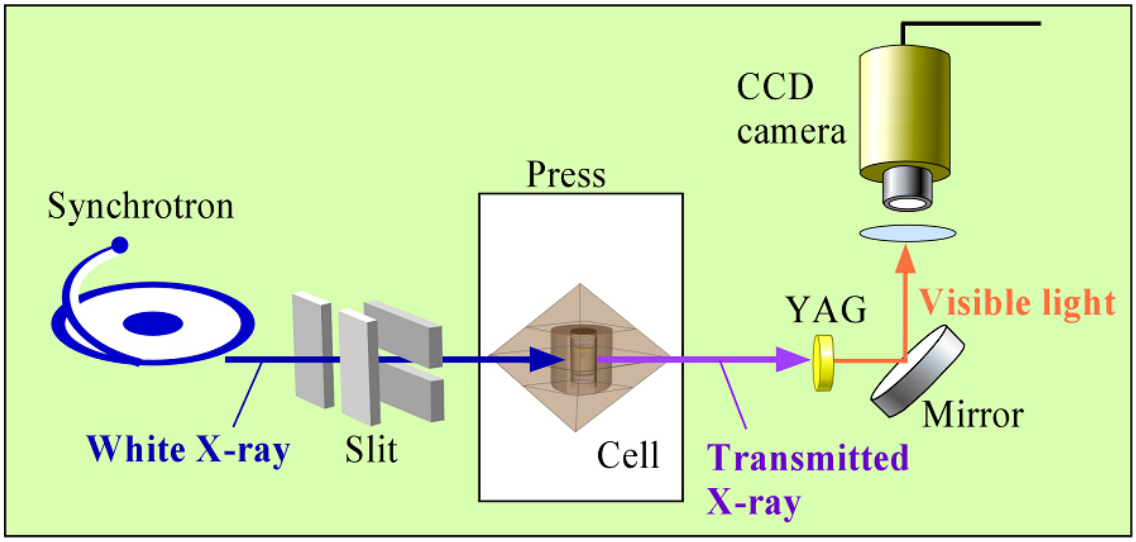

Figure 5.1: Schematic diagram of the radiographic method.

radiation for imaging, because of the large difference in x-ray absorption coefficients between metals and silicates. A schematic experimental setup of this method is shown in Figure 5.1. Synchrotron x-ray radiation passes through the sample (here contained in an octahedral pressure cell) and the transmitted x-ray radiation falls onto a mirror, which acts as a fluorescence screen, from where a x-ray density contrast image (x-ray shadowgraph) as visible light is recorded by a CCD-camera. This method can be combined readily with a multianvil technique because the gaps between the tungsten-carbide anvils (see Figure 2.1) allow transmission of x-rays through the pressure cell at high pressure and temperature.

5.1.3 Aim of this Chapter

Although the development of a radiographic in-situ falling sphere technique has greatly improved the ability to investigate directly silicate liquid viscosities as a function of pressure, highly depolymerised silicates liquids have not been studied extensively so far.

Only in one study has this technique been used to measure the viscosity of $CaMgSi_2O_6$-liquid (NBO/T=2) (Reid et al. 2003) up to 13 GPa. Thus, the pressure dependence of the viscosity of highly depolymerised silicate liquids is not well constrained at high pressure. Viscosity measurements on ultramafic compositions are complicated by very high melting temperatures but also very low viscosities. The latter results in very short falling times of the spheres (∼1-2 s, Reid et al. 2003), which make the determination of sphere velocities difficult, even using the radiographic method. In viscosity measurements on peridotite melts (NBO/T∼2.5) there is an additional complication because such a multi-component composition has a broad temperature interval between the solidus and liquidus. At 2-3 GPa the melting interval can reach up to 400°C (e.g. Takahashi et al. 1993), which means that the sphere may start to fall during heating before the final temperature above the liquidus has been reached. Here, in order to provide viscosity data that may be used to make modelling of magma ocean dynamics more realistic, viscosity measurements on peridotite liquid have been performed. To circumvent experimental problems related to ultramafic compositions, new technical developments on the high-pressure multianvil cells used for viscosity experiments were required.

5.2 Experimental Methods

5.2.1 Experimental Procedure and Description of High-Pressure Cells

The fine-grained synthetic powder of peridotitic composition used for viscosity experiments was kindly provided by Dr. Bettina Schmickler from Bayerisches Geoinstitut.

The nominal chemical composition of this material is given in Table 5.1 and is similar to the fertile peridotite composition described in Chapter 2.

High pressure falling sphere viscometry has been performed on beamline BL04B1 at SPring-8 synchrotron radiation facility in Japan in collaboration with Drs. Bettina Schmickler, Hidenori Terasaki (Bayerisches Geoinstitut), Dr. Akio Suzuki (Tohoku, University, Japan) and Dr. Ken-ichi Funakoshi (SPring-8 synchrotron radiation facility). Pressure was generated using a two-stage 1500 t multianvil system (SPEED 1500) consisting of an inner set of eight truncated tungsten carbide cubes with edge lengths of 26 mm, that were compressed by six outer tool-steel anvils in a DIA type geometry (Utsumi et al. 1998, Funakoshi et al. 2000). The inner tungsten-carbide cubes had corner truncations of either 12 or 8 mm and were used with Cr_2O_3-doped MgO octahedra as pressure cells with edge lengths of either 18 or 14 mm, respectively.

Rhenium spheres for falling sphere viscometry have been fabricated by applying a potential of 220 V and a maximum current of 16 A to thin stripes of 25 μm thick Re-foil. Resulting metal blobs were quenched into liquid nitrogen. Sphere diameters obtained from this technique were typically 50-500 μm. Diameters were determined by scanning electron microscopy with an accuracy of ± 2 μm. Spheres of 100-160 μm diameter were used for viscosity measurements.

Three different pressure cells, as shown in Figure 5.2, have been used for viscosity measurements. The first setup consisted of an octahedra of 18 mm edge length (Figure 5.2, pressure cell A) and contained a stepped graphite heater to minimise thermal gradients. The cylindrical heater was surrounded by a ZrO_2 sleeve for thermal insulation, except for the central region surrounding the capsule, because the high x-ray absorption co-

Table 5.1: Nominal chemical composition of the peridotite used for in-situ viscometry

	wt%
SiO_2	46.1
Al_2O_3	4.0
FeO	8.8
MgO	37.5
CaO	3.6
total	100
NBO/T	2.55

efficient of the ZrO_2 would reduce the density contrast information of the transmitted x-rays. Electrical contact to the heating element was provided by electrodes made from Re or Mo foil. Sample powders were encapsuled in Mo containers. Using pressure cell A, the viscosity of peridotite melt could not be measured successfully as a function of temperature, because the spheres started falling before a stable temperature above the liquidus was reached. This was due to the broad temperature interval between the liquidus and solidus and very short falling times of spheres in this low-viscosity liquid. To overcome this problem a high pressure cell having a new capsule design (Figure 5.2, pressure cell B) has been developed. This stepped Mo capsule contains a recessed reservoir (∼6 vol% of the total capsule volume) at one end in which a second sphere is embedded in a 50:50 (by mole) mixture of synthetic Mg_2SiO_4 forsterite (Fo) and $MgSiO_3$ enstatite (En), which has a higher solidus temperature than the peridotite (approximately 150-250°C at 4 GPa, inferred from Takahashi 1986, Presnall et al. 1998). In addition, this recessed reservoir is located outside central part of the stepped graphite heater, which means that it is at a lower temperature than the main part of the capsule. Thus the release of the sphere is delayed, until the main part of the

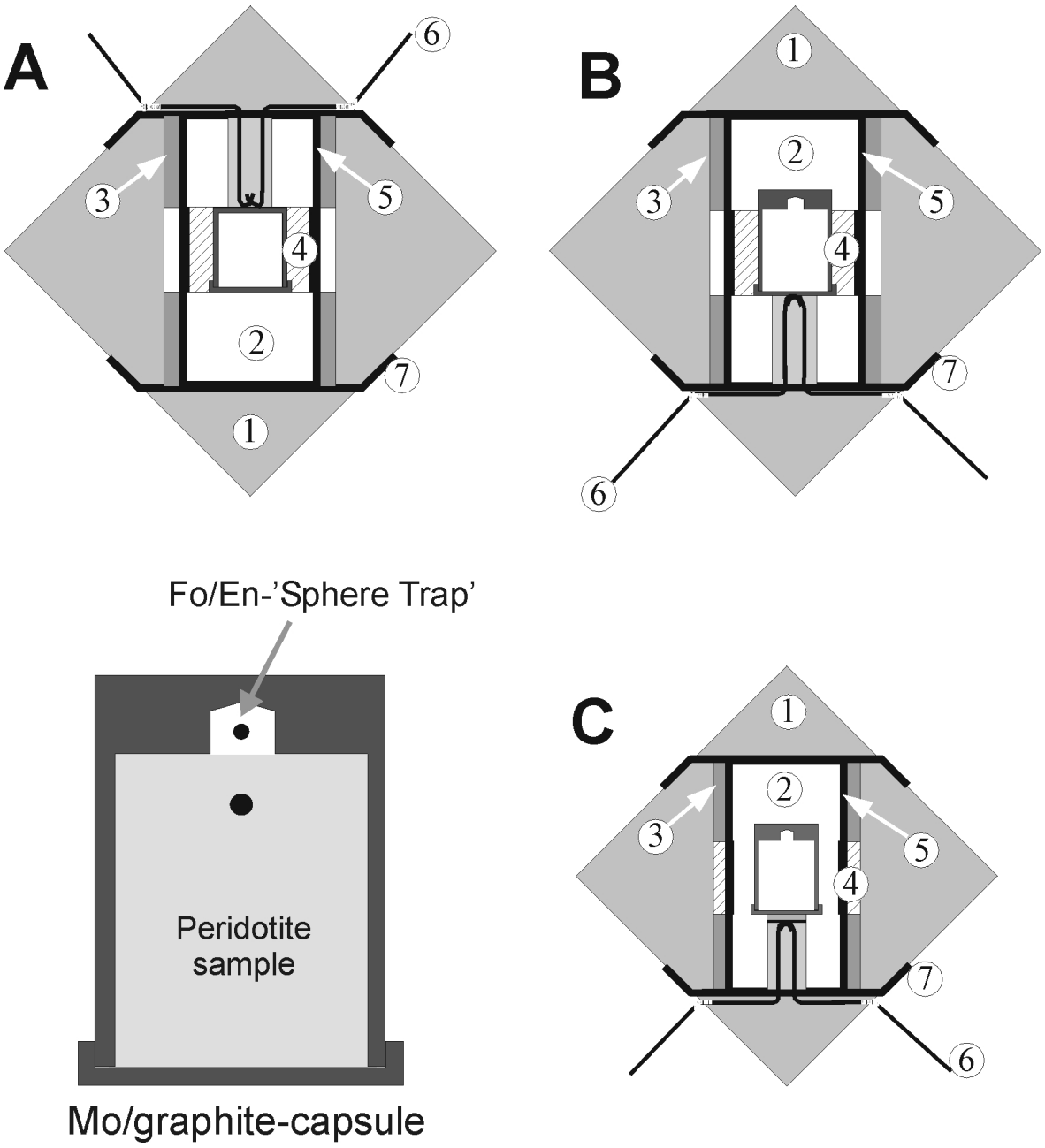

Figure 5.2: High-pressure cells used for in-situ falling sphere viscometry. A) 18 mm cell. B) 18 mm cell with a recessed capsule. The capsule is shown as a close-up (bottom-left). The recessed reservoir is located outside the hotspot of the furnace and contains a second (upper) sphere embedded in a mixture of $Fo_{50}En_{50}$ having a higher melting temperature than peridotite. The volume of this recessed 'sphere trap' is restricted to ∼6 vol% of the total container volume to minimise chemical contamination. C) 14 mm cell with a graphite capsule of a similar design as used in assembly B. Numbers: 1) Cr_2O_3 doped MgO; 2) polycrystalline MgO; 3) ZrO_2 insulation; 4) h-BN/MgO pressure calibrant; 5) stepped graphite (cells A, B) and $LaCrO_3$ (cell C) furnace; 6) W/Re thermocouples; 7) Re (cells A, B), Mo (cell C) electrodes.

sample is completely molten. The sphere in the recessed region can be used in addition to a sphere in the 'normal' position (see Figure 5.2), which allows two viscosity values to be determined in a single experiment.

The accessible pressure range using the pressure cells A and B is limited to approximately 7 GPa at ∼2000 K by the graphite-diamond transition of the furnace material. In order to investigate peridotite liquid viscosities at higher pressures, a 14 mm edge-length pressure cell with a stepped $LaCrO_3$ furnace, similar to that used by Reid et al. (2003) (Figure 5.2, pressure cell C) was developed. To obtain density contrast information that is adequate for imaging the falling sphere, capsules made from graphite instead of Mo were used to compensate for the high x-ray absorption of the $LaCrO_3$ furnace material.

Experiments were conducted as follows: To ensure anhydrous conditions, pressure cell components were, depending on the material, either fired at 800°C or stored in an oven at 110°C prior to preparation. The assembled pressure cell was then stored at 110°C before being used. Cells were first pressurised before raising the temperature to values 50-100 K below the peridotite solidus temperature (Takahashi 1986, Takahashi et al. 1993). Temperatures in all assemblies were measured using axially inserted $W_{97}\%Re_3\% - W_{75}\%Re_{25}\%$ thermocouples with no correction for the effect of pressure on the thermocouple *emf*. Based on an extrapolation of the relationship of temperature and electrical power, the required power for the target temperature above the liquidus was estimated. Heating to the final temperature was then performed by heating directly to the desired power, at the maximum possible heating rate. Heating to a defined electrical power value also prevents the interruption of ramping in the case of

thermocouple failures. X-ray shadowgraphs of the descent of the spheres were recorded with CCD-cameras with frame rates between 30 frames per seconds (fps) (Hamamatsu Photonics, Japan, model C4880-80-14A, assembly A) and 30-60 fps (Kodak, Megaplus ES 310 turbo, assemblies B and C).

A 'pressure marker' consisting of a mixture of h-BN and MgO (1:1 by volume), served as a calibrant when using x-ray diffraction for in-situ pressure determination. Pressures were derived by fitting the equation of state of Jamieson et al. (1982) to lattice parameters of MgO obtained from energy dispersive x-ray diffraction patterns. The presence of h-BN minimised the grain growth of the MgO during annealing at high temperature. X-ray diffraction patterns were collected at 1273 K for 300-600 s before heating to the target temperature and at target temperatures after the spheres had fallen. In many cases, when using pressure cells A and B, however, the capsules collapsed several seconds after the descent of the spheres which prevented final pressure determinations. In some recovered samples a reaction rim between the Mo-capsule and the h-BN/MgO mixture was observed, indicating that reaction between the h-BN and the Mo capsule may have led to the collapse of the sample containers. Reported run pressures are therefore values obtained at 1273 K. Because thermal expansion and plastic flow of the pressure cell at melting temperatures have opposing effects, the higher temperatures may only affect the pressure slightly; the uncertainty in pressure at the final temperature is estimated to be ± 0.3 GPa. Due to the problems associated with potential reaction between the pressure calibrant and the Mo-capsules, some experiments with pressure cell B were performed without in-situ pressure calibration. In such cases h-BN/MgO sleeves were replaced by pure polycrystalline MgO. Pressures were estimated

using a calibration of pressure versus applied multianvil press load derived from previous experiments performed on the same pressure cells. Uncertainties in pressures for such runs were estimated to be ±0.7 GPa and are comparable to normal quench-type multianvil experiments.

Using pressure cell C, collection of diffraction patterns for pressure determinations from materials inside the furnace area was not possible because of the high x-ray absorption of the heater (Reid et al. 2003). Spectra were therefore obtained from outside the furnace region. The temperature T_{PM} at this position, required for calculating the pressure, has been calibrated by an experiment on an identical pressure cell at Bayerisches Geoinstitut, by adding a second thermocouple at the position of the pressure calibrant. T_{PM} was observed to be related linearly to the sample temperature according to $T_{PM} \sim 0.57 \cdot T_{Sample}$. X-ray spectra were taken at $T_{Sample} = 1773$ K. The temperature of the pressure calibrant was estimated to be within ±150 K of the calculated T_{PM}, which resulted in pressure uncertainties of approximately ±1 GPa.

5.3 Results

The velocities of falling spheres, required for viscosity determinations, were derived by tracking the relative positions of spheres in individual images from recorded video files. Time intervals were derived from recording frame rates. An example of a typical x-ray shadowgraph is shown in Figure 5.3. The absolute falling distance has been calibrated by the density contrast image of an reference object (a multianvil-cube), which has been moved in steps of 50 μm in vertical direction. This enables a calibration-curve, such as 'number of pixels' in an image versus relative distance, to be constructed. Plots of the

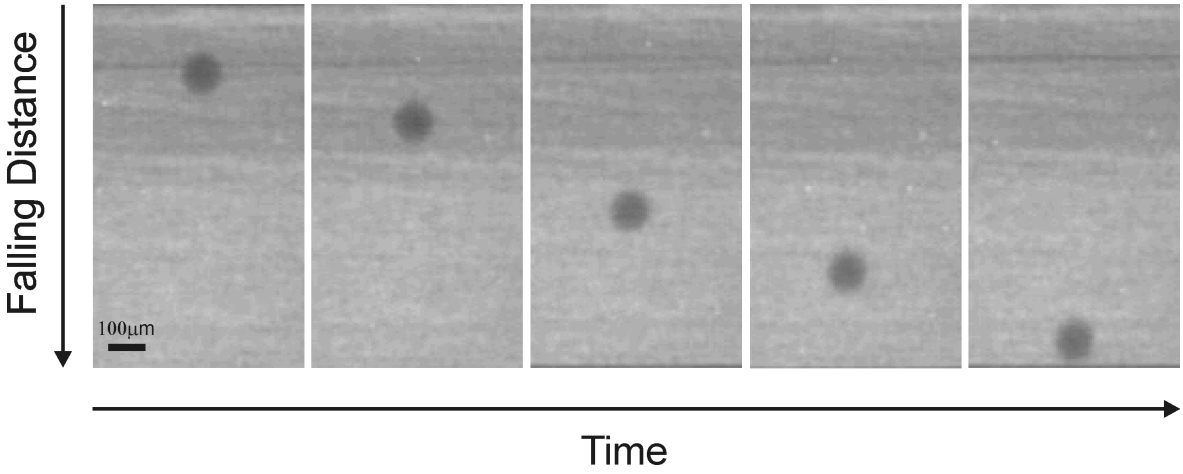

Figure 5.3: Example of an x-ray shadowgraph. The velocity of the sphere is determined by tracking its position in individual pictures of the video files and from recording frame rates.

falling distance of spheres as a function of time for experiment S982 performed at 2.5 GPa using assembly B are shown in Figure 5.4. The sphere in the lower position (within the peridotite powder) fell during heating before the final temperature was reached. After acceleration, the sphere reached a constant velocity indicated by the solid line in Figure 5.4a. The sphere embedded in the Fo/En-mixture in the recessed region of the capsule fell ∼8 s later after an additional temperature increase of ∼180 K. The falling velocity of the second sphere was constant over the observable region of the capsule. Effects of convection or thermal gradients in the molten samples would have likely resulted in variations or discontinuities in the distance vs. time plots, but have not been observed in the present experiments. With increasing pressure the time interval between the falling of the two spheres in a given experiment became progressively shorter (∼1 s at 13 GPa), which is consistent with a decreasing temperature interval between the solidus and liquidus as pressure is increased (e.g. Takahashi 1986, or see Chapter 2).

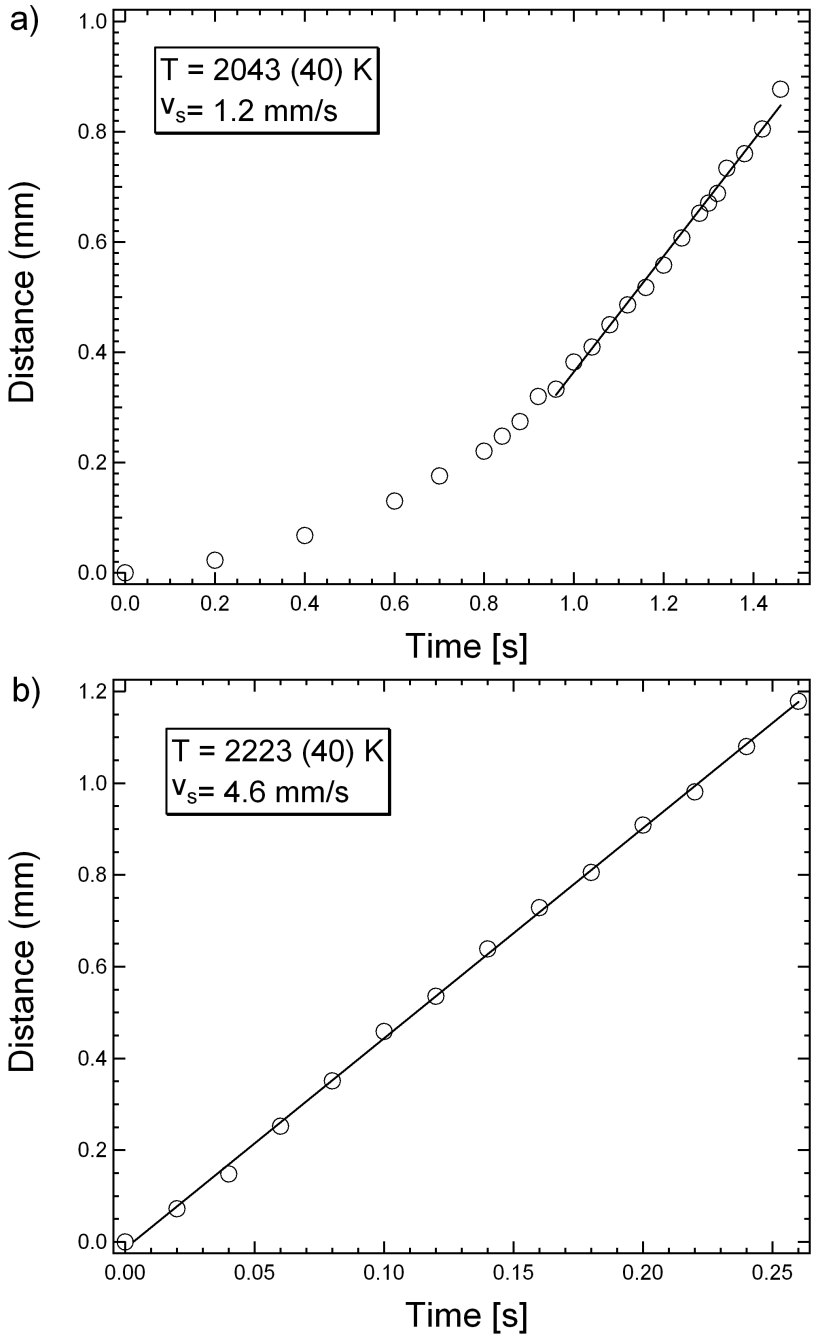

Figure 5.4: Plots of distance versus time for experiment S 982 at 2.5 GPa. Distances have been determined from relative positions of spheres in individual images of recorded video files. a) The sphere in the lower position of pressure cell A fell at 2043 ±40 K. b) The sphere in the recessed 'sphere trap' embedded in forsterite and enstatite fell ∼8 s later and after the temperature had increased to 2223 ±40 K. The lines have been fitted to regions of constant falling velocities. The recording frame rate was 50 fps.

Knowing the falling velocity v_s of the spheres, melt viscosities can be calculated from Equations 5.4 and 5.5. Densities of Re spheres and peridotite liquid at high pressures have been calculated using equations of states and compressibility data from Vohra et al. (1987) and Suzuki and Ohtani (2003), respectively. The required zero pressure density of peridotite melt at high temperature was determined using the model of Lange and Carmichael (1987). The uncertainty in the $\Delta\rho$ term of Equation 5.4 is estimated to be $\pm 5\%$.

Experimental run conditions and calculated viscosities are summarised in Table 5.2. Errors in falling velocities are based on the reproducibility of tracking sphere positions in x-ray shadowgraphs and on choice of the points in distance versus time plots (e.g. Figure 5.4) at which the terminal velocity was reached. Reported uncertainties in viscosities are based on normal error propagation. Temperatures measured during the descent of spheres in pressure cell A or of spheres in the lower positions of cells B and C are systematically lower by 50-100 K than reported liquidus temperatures for KLB-1 peridotite (Takahashi 1986, Takahashi et al. 1993, Zhang and Herzberg 1994). Uncertainties in reported liquidus temperatures are expected to be on the order of 30 K, which indicates that spheres most likely fell through a partially molten sample. Only the results of experiments in which spheres fell along a straight path and at a constant velocity were evaluated (e.g. Figure 5.4), but it is clear in such cases that the presence of a small proportion of crystals may have led to a slight overestimation of viscosities determined at near-liquidus conditions. The consequences of such an overestimation when extrapolating viscosities to higher temperatures is discussed below.

Since viscosity of silicate melts generally depends on the iron oxidation state (e.g.

Table 5.2: Experimental run conditions (pressure P, temperature T), sphere diameters (SD) terminal sphere velocities (v) and calculated viscosities (η) obtained from in-situ falling sphere viscometry. Indices on T, v and η correspond to spheres in the peridotite sample (1) and in the recessed capsule reservoir (2), respectively. Numbers in parentheses are uncertainties in terms of the last units cited

Run	**Cell**	**P [GPa]**	$\mathbf{T_1}$**[K]**	$\mathbf{T_2}$**[K]**	**SD [μm]**	$\mathbf{v_1}$**[mm/s]**	$\mathbf{v_2}$**[mm/s]**	η_1**[Pas]**	η_2**[Pas]**
S 866	A	2.5 (3)	2053 (50)		107	1.69 (10)	-	0.057 (5)	-
S 875	A	4.2 (3)	2073 (100)		129	1.60 (8)	-	0.084 (7)	-
S 883	A	6.9 (3)	2223 (70)		148	2.09 (50)	-	0.093 (23)	-
S 884	A	3.4 (3)	2093 (50)		161	3.89 (51)	-	0.050 (7)	-
S 972	B	4.0 (7)	1)	2283 (30)	137	-	6.55 (13)	-	0.0230 (15)
S 976	B	4.0 (7)	1)	2173 (30)	108	-	3.77 (8)	-	0.0282 (16)
S 982	B	2.5 (3)	2043 (40)	2223 (40)	119, 105	1.21 (10)	4.61 (9)	0.096 (10)	0.0203 (15)
S 989	B	6.0 (3)	2143 (40)	2)	174	1.77 (10)	-	0.127 (10)	-
S 1109	B	5.0 (7)	2123 (50)	2)	144	2.00 (7)	-	0.094 (11)	-
S 1110	C	7.0 (1.0)	2293 (50)	3)	120, 117 (Mo)	2.22 (4)	-	0.056 (7)	-
S 1114	C	11.0 (1.0)	2173 (50)	2373 (30)	155, 135	4.47 (67)	8.97 (1.35)	0.048 (8)	0.019 (3)
S 1120	C	10.0 (1.0)	2373 (50)	2403 (30)	159, 134	4.39 (18)	5.27 (28)	0.052 (4)	0.031 (3)
S 1123	C	9.0 (1.0)	2443 (50)	2523 (30)	135, 123	3.83 (25)	6.08 (91)	0.043 (4)	0.023 (4)
S 1129	B	1.9 (3)	2123 (40)	2283 (30)	123, 120	1.9 (1)	6.0 (1)	0.071 (5)	0.022 (2)
S 1131	C	12.5 (1.0)	2253 (50)	2273 (30)	129, 133	4.70 (31)	8.84 (1.33)	0.032 (3)	0.018 (3)

1) Capsule contained only one sphere in upper position
2) Second sphere in upper position did not fall
3) Mo sphere not visible

Cukierman and Uhlmann 1974, Dingwell 1989, 1991, Liebske et al. 2003) Mössbauer analyses have been performed on sample S976, quenched from ∼2170 K and 4 GPa, to estimate the redox state of the molten peridotite. No evidence for Fe^{3+} was found in this sample, which suggests that the melts were reduced under the experimental run conditions. This is consistent with empirical models of ferric-ferrous equilibria in silicate melts, which predict low concentrations of ferric iron at high temperatures and low alkali contents (Sack et al. 1980, Kilinc et al. 1983, Kress and Carmichael 1991).

The experimental conditions of this study cover pressure and temperature intervals of ∼10 GPa and approximately 450 K, respectively. Measured viscosities are, to our knowledge, the lowest values measured on silicate liquids at high pressure, which is consistent with the peridotite composition being the most depolymerised liquid so far investigated by falling sphere viscometry. The degree of depolymerisation expressed as NBO/T is 2.5 for the investigated composition. Determined viscosities range from 0.018 Pa s at 13 GPa and 2283 K to 0.127 Pa s at 6.0 GPa and 2143 K. Experimentally determined viscosities plotted as a function of pressure are shown in Figure 5.5. Viscosities obtained at similar temperatures but different pressures suggest that viscosity increases with increasing pressure (referred to as a positive pressure effect on viscosity) to approximately 9 GPa. Data derived from higher pressures indicate that viscosity decreases isothermally between 9 and 13 GPa (negative pressure effect). Compared to viscosity data for the slightly less depolymerised $CaMgSi_2O_6$ liquid (e.g. Reid et al. 2003, NBO/T=2.0), measured over a similar pressure range, the viscosity of peridotite melt is approximately one order of magnitude lower.

Viscosity as a function of pressure and temperature may be described by an Arrhenius

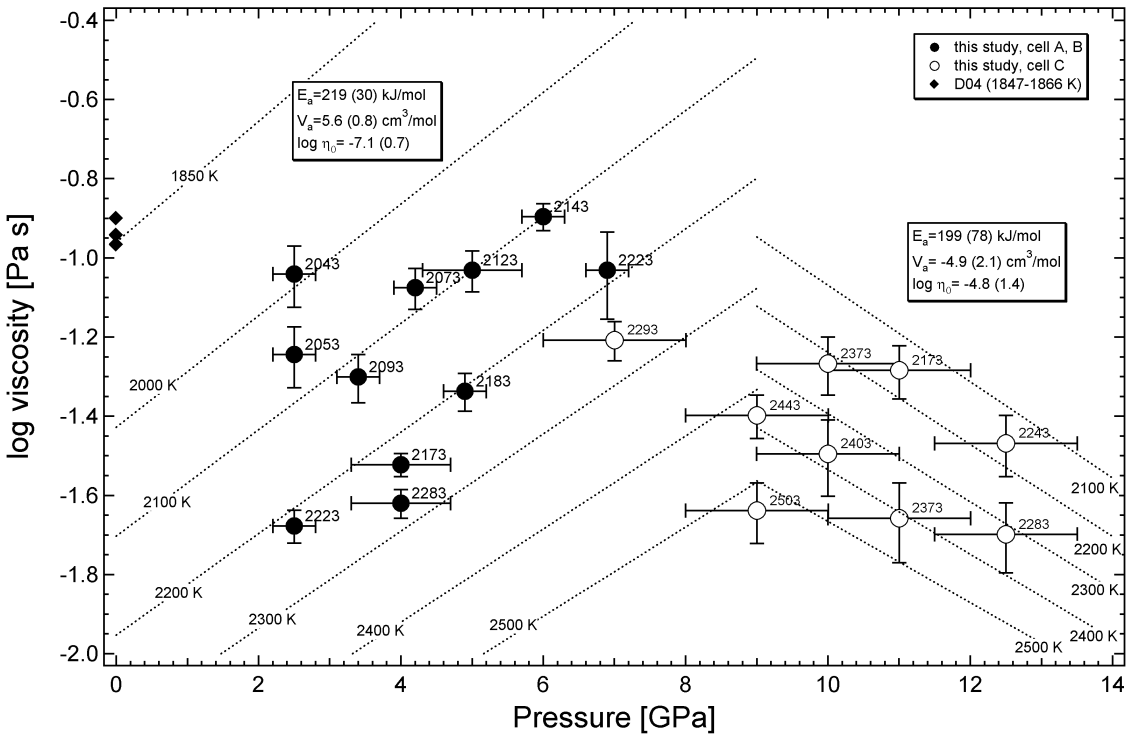

Figure 5.5: Experimentally determined viscosities as a function of pressure. Filled circles represent data obtained from pressure cells A and B, open circles from C. Dotted lines are isotherms calculated from the fits of the Arrhenius relationship (Equation 5.6). Data from experiment S1129 at 1.9 GPa (at 2123 and 2283 K), represented by crosses, have not been considered for data fitting (see text for details). D04 denotes data points from Dingwell et al. (2004).

relationship:

$$\eta = \eta_0 \cdot exp\left(\frac{E_a + P \cdot V_a}{R \cdot T}\right) \tag{5.6}$$

where E_a and V_a are the activation energy and activation volume for viscous flow, respectively. R and T are the gas constant and absolute temperature, respectively and η_0 is a preexponential factor. In order to fit the data, recent peridotite melt viscosity data obtained at 0.1 MPa and temperatures ranging from 1847-1867 K (Dingwell et al. 2004) were included to constrain viscosity at ambient pressure. Data points from Dingwell et al. (2004) and fits of Equation 5.6 to the data are included in Figure 5.5. Data in pressure regions that indicate different effects of pressure on melt viscosity (0-9

Table 5.3: Parameters and uncertainties obtained from fitting an Arrhenius relationship to high pressure viscosity data including high temperature data from Dingwell et al. (2004)

Pressure range [GPa]	10^{-4} -9 GPa	9-13 GPa
Actication energy E_a [kJ/mol]	219 (30)	199 (78)
Activation Volume V_a [cm^3/mol]	5.6 (0.8)	-4.9 (2.1)
log η_0 [Pa s]	-7.1(0.7)	-4.8 (1.4)

GPa, 9-13 GPa), corresponding to positive and negative activation volumes, have been fitted separately. Within each pressure and temperature interval, both the activation volume and energy, are assumed to be constant. Viscosities derived from run S1129 at 1.9 GPa are significantly higher than predicted from this approach (see Fig. 5.5). This is likely related to an experimental problem based on the observation of an exceptionally long time interval of 23 s between the descent of the two spheres, suggesting lower run temperatures than recorded by the thermocouple. Therefore, run S1129 was excluded from the data fitting. Fit parameters and their uncertainties were determined by Monte-Carlo simulations. Fitting of Equation 5.6 to the data was performed 500 times in each pressure range, while the input parameters pressure, temperature and viscosity were randomly varied within their range of absolute uncertainties. Viscosities as a function of pressure, together with isotherms calculated from Equation 5.6, are shown in Figure 5.5. Average fit parameters and uncertainties at the 1σ level are listed in Table 5.3.

5.4 Discussion

5.4.1 The Effect of Pressure on the Viscosity of Depolymerised Silicate Liquids

Previous experimental studies performed at pressures below 3 GPa (e.g. Brearley et al. 1986, Scarfe et al. 1987, Behrens and Schulze 2003), showed that the pressure dependence of the viscosity of silicate liquids changes with the degree of melt depolymerisation, and ranges from a negative effect for polymerised liquids, (e.g. $NaAlSi_3O_8$, NBO/T=0) to a positive effect for relatively depolymerised liquids (e.g. $CaMgSi_2O_6$). However, other recent studies reveal a more complex behaviour of transport properties as a function of pressure, involving maxima and minima (e.g. Poe et al. 1997, Tinker and Lesher 2001, Persikov and Bukhtiyarov 1999, Reid et al. 2001, 2003), especially in the pressure range 5-10 GPa. The viscosity of peridotite liquid shows a pressure dependence that is similar to that of $CaMgSi_2O_6$ liquid (Reid et al. 2003), which can be explained by the similar degree of depolymerisation of both melts.

The observed positive pressure effect on viscosity of peridotite and $CaMgSi_2O_6$ liquids below 9-10 GPa is generally consistent with a pressure dependence that is predicted from the 'free volume theory' (Cohen and Turnbull 1959). However, a negative effect of pressure on viscosity as observed between 9 and 13 GPa cannot be explained on the basis of a 'hard sphere' model. Several studies on simple binary or ternary systems have shown that compression of silicate melts and glasses is accompanied by increasing coordination numbers of network-forming cations such as Si^{4+} or Al^{3+} (e.g. Waff 1975, Williams and Jeanloz 1988, Xue et al. 1991, Yarger et al. 1995, Bryce et al. 1999) particular for highly polymerised melts and/or decreasing intertetrahedral bond

angles (e.g. Kubicki et al. 1992, Poe et al. 2001). The latter structural modification is a means of reducing free volume without any significant change in bond strength. The reduction of intertetrahedral angels may therefore explain the observed positive pressure dependence up to 9 GPa. Above this pressure another structural modification must be involved in order to reverse the pressure dependence of viscosity. As observed for more polymerised melts, the coordination of network-forming cations may increase in highly depolymerised melts. Highe-coordinated Si and Al cations are characterised by longer, and thus weaker, Si-O and Al-O bonds compared to those of tetrahedral TO_4 (T=Si^{4+}, Al^{3+}) units, which has been related to decreasing viscosity at increasing pressures (Waff 1975, Poe et al. 1997, Suzuki et al. 2002). In particular, an enhanced oxygen exchange via a mechanism that involves intermediate $^{[5]}$Si or $^{[5]}$Al species, as shown in Figure 1.9, is therefore facilitated. The decrease in viscosity of peridotite and $CaMgSi_2O_6$ liquids at pressures greater than 9-10 GPa is therefore likely related to changes in cation coordination numbers. High pressure spectroscopic data however, which provide information about cation coordination or bond angles and distances, are not available for liquids and glasses of such highly depolymerised melts.

However, it is likely that any silicate melt structure will converge into a 'densely packed' state at sufficiently high pressure, with no further changes in cation coordination that would result in a negative pressure effect on viscosity. This is generally consistent with results from molecular dynamics (Bryce et al. 1999), that predict the disappearance of the negative pressure effect on viscosity in simple sodium-alumino-silicate liquids at pressures >25 GPa. As a consequence, it is expected that the viscosity of peridotite liquid must increase again with increasing pressure above 13 GPa, due to further re-

duction of free volume.

5.4.2 Parameterisation of the Viscosity of Peridotite Liquid

The experiments performed by Dingwell et al. (2004) showed that the viscosity of peridotite liquid, when investigated from glass transition to superliquidus temperatures, exhibits strongly non-Arrhenian behaviour. This implies that the activation energy of viscous flow is temperature dependent, such that E_a decreases with increasing temperature. A consequence is that extrapolating experimental results from low to high temperatures using Equation 5.6, would result in an underestimation of viscosities. Therefore, to account for the non-Arrhenian behaviour, Dingwell et al. (2004) fitted the widely-used empirical three-parameter Vogel-Fulcher-Tamman (VFT) equation:

$$log_{10}\eta = A_{VFT} + \frac{B_{VFT}}{T - T_0} \tag{5.7}$$

to their viscosity data, where A_{VFT}, B_{VFT}, and T_0 are constants. A_{VFT} represents log η at infinite temperature, B_{VFT} corresponds to an energy barrier of viscous flow and T_0 can be regarded as the temperature at infinitely high viscosity. Analysis of one-atmosphere viscosity data for silicate liquids over a wide range of chemical compositions and temperatures, from the glass-transition to superliquidus temperatures, indicate that A_{VFT} may have a unique value of -4.31 ($\pm$ 0.74) (Russell et al. 2003), which physically corresponds to a high temperature limit of viscosity. However, the original VFT equation does not account for the effect of pressure on melt viscosity. To fit both the ambient- and high-pressure viscosity data, from Dingwell et al. (2004) and this study respectively, using a non-Arrhenian model, the VFT equation may be extended,

according to Behrens and Schulze (2003), as

$$log_{10}\eta = A_{VFT} + \frac{B_{VFT} + C_{VFT} \cdot P}{T - T_0} \tag{5.8}$$

where C_{VFT} is related to the pressure dependence of viscous flow analogous to the parameter V_a in Equation 5.6 and A_{VFT}, B_{VFT} and T_0 are assumed to be independent of pressure. As noted above, the experimental viscosity data clearly show a complex pressure dependence, such that C_{VFT} cannot be constant over the investigated pressure range. Therefore, C_{VFT} is replaced by an empirical pressure-dependent term $C(P)$, such that

$$log_{10}\eta = A_{VFT} + \frac{B_{VFT} + C(P)}{T - T_0} \tag{5.9}$$

and

$$C(P) = C_1 \cdot P + C_2 \cdot P^2 + C_3 \cdot P^3. \tag{5.10}$$

Fitting Equation 5.9 to all available viscosity data for peridotite liquid over pressure and temperature ranges from 0.1 MPa to 13 GPa and ∼1000-2500 K with A_{VFT}= -4.3, reproduces experimental values to within 0.08 log-units on average with a maximum deviation of 0.23 log-units. This fit is shown in Figure 5.6 together with the experimental data from this study. Given the wide range of experimental conditions and considering the pressure and temperature uncertainties in falling sphere viscometry, this represents an excellent fit to the data. Fit parameters and uncertainties were determined using the aforementioned Monte-Carlo technique and are presented in Table 5.4. Viscosities measured up to 9 GPa, plotted as a function of reciprocal temperature, and VFT-fits of Equation 5.9 are presented in Figures 5.7a and 5.7b. Figure 5.7b shows the difference between VFT and Arrhenian models, with the latter leading to a possible underestimation of viscosity between 2500-5000 K. Using a constant value of A_{VFT}

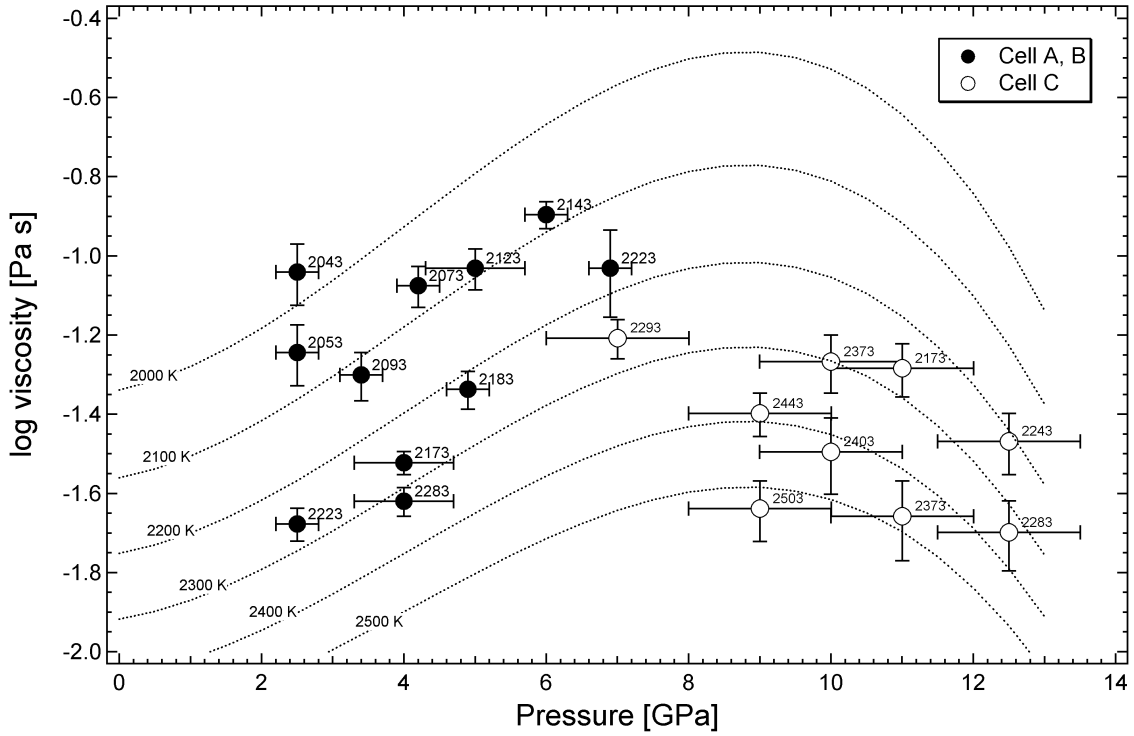

Figure 5.6: Experimentally determined viscosities from this study as a function of pressure and isotherms calculated from the modified VFT Equation (Eqn. 5.9). Experimental data are reproduced with an average deviation of 0.08 log-units. The current model cannot be used to extrapolate viscosities to pressures greater than 13 GPa, because of the empirical nature of the fitted pressure dependence.

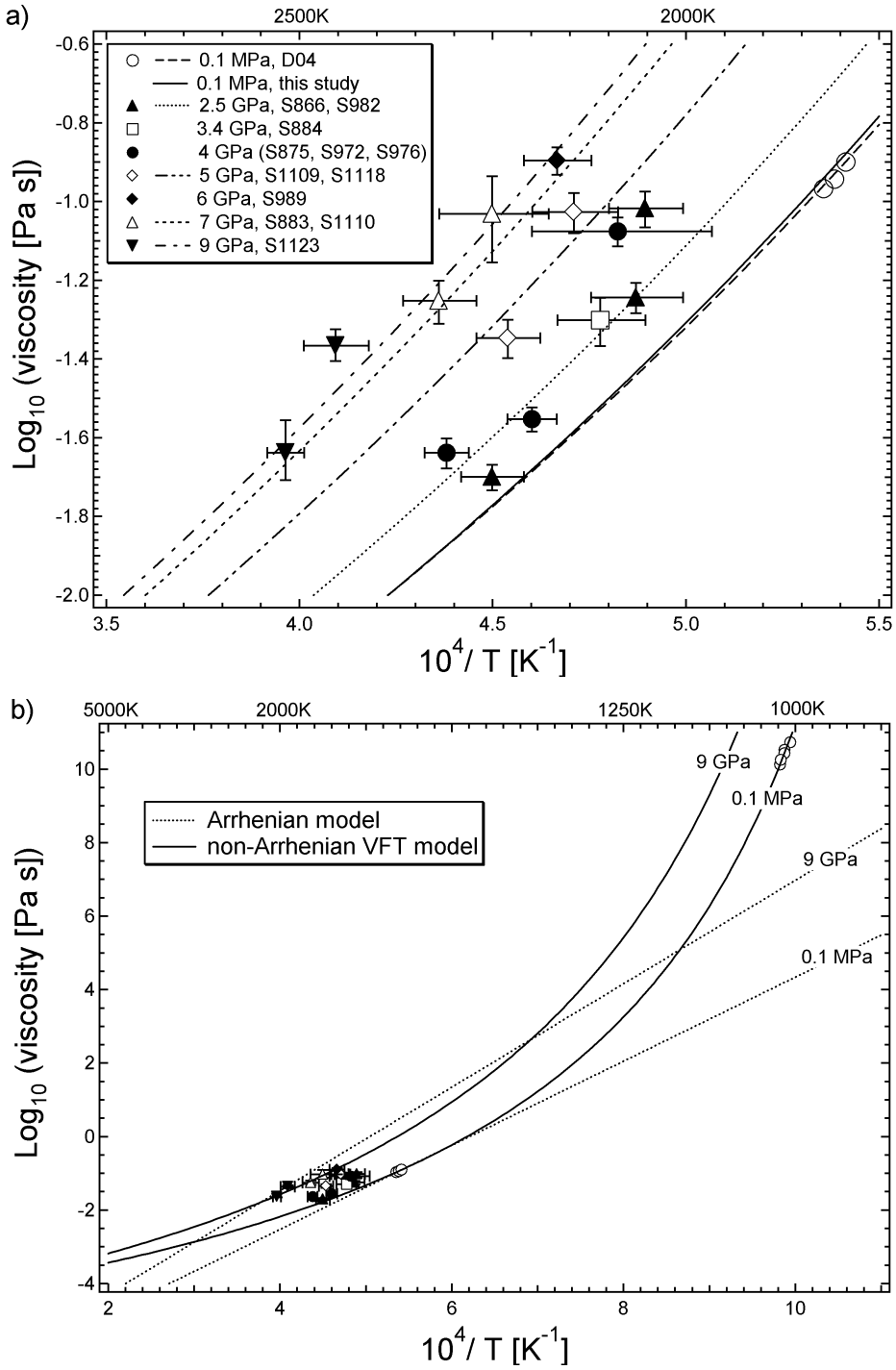

Figure 5.7: Experimentally determined viscosities up to 9 GPa as a function of reciprocal temperature. Solid and dashed lines are isobars calculated from the pressure modified VFT-equation (Eqn. 5.9). The temperature ranges from 1800 to 2850 K. b) The same plot including the high-viscosity data from peridotite glass at ambient pressure (D04, Dingwell et al. 2004), demonstrating the strong non-Arrhenian behaviour of peridotite liquid. Dotted and solid lines represent isobars calculated from the Arrhenian and non-Arrhenian VFT model, respectively.

Table 5.4: Parameters obtained from fitting Equation 5.9 to available viscosity data for peridotite liquid. Parameters denoted as D04 are from Dingwell et al. (2004)

Parameter	**this study**	**D04**
A_{VFT}	-4.3	-4.31
$B_{VFT}[K^{-1}]$	3700 (30)	3703 (54)
T_0 [K]	762 (3)	762 (4)
C_1 [K/GPa]	42 (44)	-
C_2 [K/GPa^2]	30 (12)	-
C_3 [K/GPa^3]	-2.5 (0.7)	-

also compensates for the effects of a potential overestimation of measured viscosities at subliquidus conditions due to the presence of crystals. An overestimation of viscosity at low subliquidus temperatures relative to values at high temperatures overestimates the effect of temperature on viscosity, from which the activation energy E_a is derived. An overestimation of E_a results in an underestimation of viscosity when extrapolated to higher temperatures. A defined viscosity at infinite temperature as inferred from A_{VFT}, however, circumvents such a problem.

Positive and negative effects of pressure on melt viscosity in Equation 5.9 are described by the pressure derivative $\partial C(P)/\partial P$. Positive values of $\partial C(P)/\partial P$ correspond to an increase of viscosity with increasing pressure, while a negative $\partial C(P)/\partial P$ causes a decrease of viscosity, analogous to positive and negative activation volumes, respectively. The change in sign of $\partial C(P)/\partial P$ at approximately 9 GPa can be seen clearly in Figure 5.6. It is emphasised that the given fit parameters from Equation 5.9 cannot be used outside the pressure range of the data (<13 GPa), because the presented approach is purely empirical and has no theoretical basis.

5.4.3 Viscosity of a Magma Ocean

In order to predict the viscosity of a deep terrestrial magma ocean as a function of its depth, a temperature distribution is required. The absolute temperature and depth of a magma ocean will be constrained by the thermal state of the planet. Estimates about magma ocean depths have been derived from metal-silicate partitioning or solubilities of light elements in core-forming liquids and range from <700 km up to ∼2000 km (e.g. Righter and Drake 1997, Gessmann and Rubie 2000, Li and Agee 2001, Rubie et al. 2004). We assume an adiabatic temperature gradient and use thermodynamic data for komatiite liquid (Miller et al. 1991a) as an analogue material to calculate the temperature profile of a molten mantle. Following Rubie et al. (2003) the base of the magma ocean is defined by the onset of crystallisation at the peridotite liquidus. It is emphasised that complete solidification will occur at higher pressures than defined by the intersection of the pure liquid adiabat with the peridotite solidus, because the entropy of fusion causes subliquidus adiabats to lie between the liquidus and solidus over a large pressure interval (Miller et al. 1991b).

The viscosity of a peridotitic magma ocean is likely be determined primarily by the effects of pressure and temperature. Other variables such as volatile content and iron oxidation state are expected to be less important and have been discussed by Dingwell et al. (2004). However, the peridotite melts in this study were likely reduced under the experimental conditions, as indicated by Mössbauer spectroscopy, and the oxidation state is therefore compatible with that of a magma ocean that is in equilibrium with core-forming Fe-rich liquids.

As an example, a magma ocean adiabat leading to crystallisation at 1800 km depth

(inferred from Zerr et al. 1998) is calculated, with the depth of the magma ocean being consistent with a recent estimate of Rubie et al. (2004). The pressure and temperature conditions at the base of the magma ocean correspond to approximately 100 GPa and 3500-4000 K with a potential surface temperature of ∼2800 K. The viscosity along this adiabat to a pressure of 13 GPa or a depth of ∼400 km can be calculated using Equation 5.9. As discussed above, extrapolating to higher pressures is not justified on the basis of the present parameterisation. A temperature profile and the calculated magma ocean viscosity as a function of pressure are shown in Figure 5.8. Liquid adiabats are characterised by a steep initial temperature increase at shallow depth followed by a moderate increase at higher pressures. The corresponding viscosities are on the order of 3 mPa s and change less than half an order of magnitude between the surface and transition zone depths. This value is close to the viscosity of water at ambient conditions ($\eta_{H_2O} \approx 1$ mPa s) and thus extremely low. The viscosity at the base of a deep magma ocean remains uncertain, because neither the pressure to which the observed decrease in viscosity continues, nor the magnitude of the likely positive pressure effect on viscosity at still higher pressures are known. However, for an approximation we use the Arrhenius relationship (Equation 5.6) and fit parameters obtained at 0-9 GPa (Table 5.3) to estimate possible pressure effects on viscous flow at pressures >13 GPa, based on the assumption that the pressure dependence of viscosity can be described by a constant positive activation volume. Figure 5.9 shows the estimated viscosity increase (relative to ambient conditions) at 100 GPa and 3500 and 4000 K as a function of activation volume V_a. Although absolute viscosities at these temperatures may be more accurately described by the VFT-model, the magnitude of the pressure effect

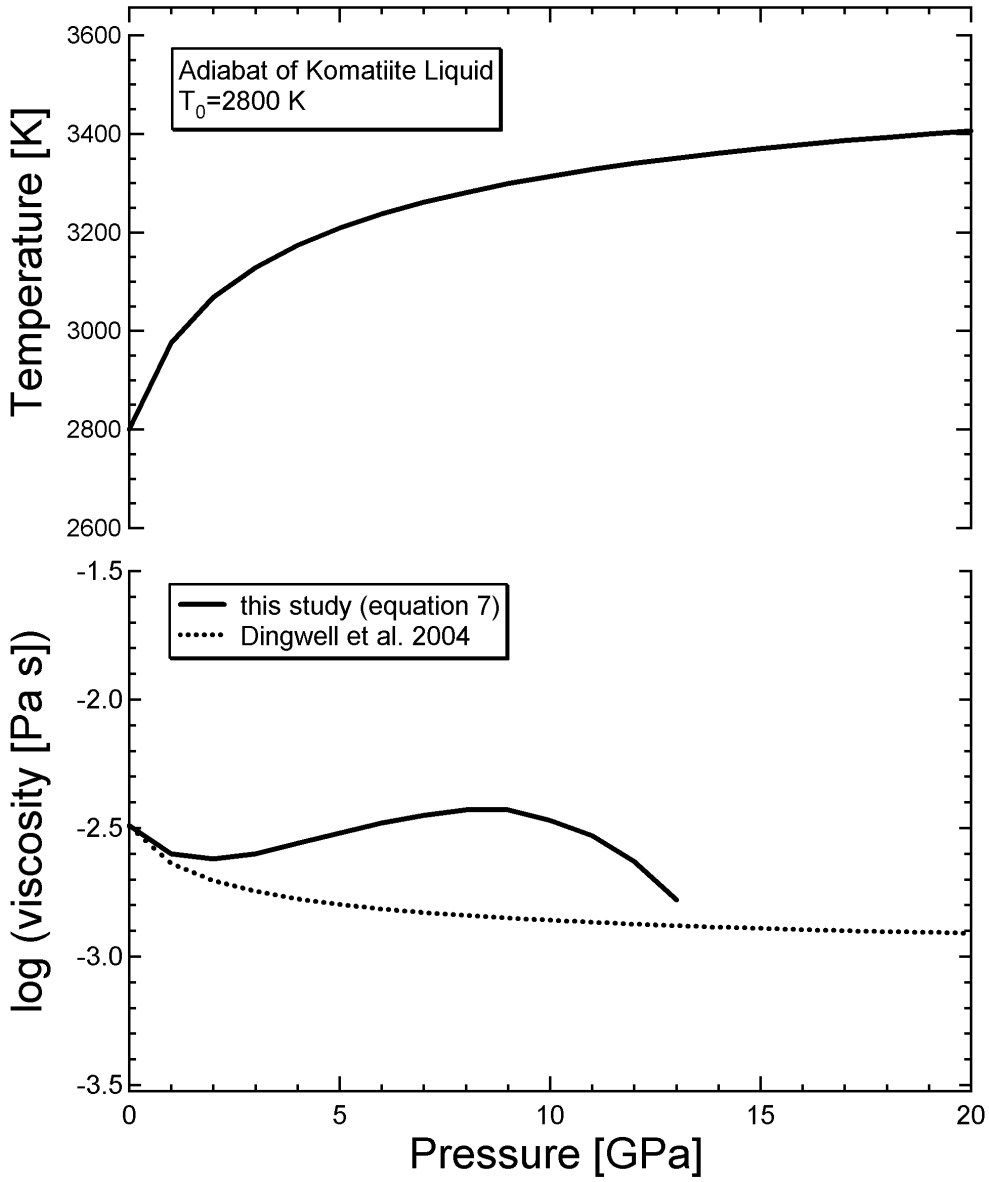

Figure 5.8: Adiabatic temperature gradient for komatiite liquid (Miller et al. 1991a) as an example of temperature of a magma ocean of ∼1800 km depth with a potential surface temperature of ∼2800 K. The lower part of the figure shows calculated viscosities along this adiabat. Viscosities calculated from Eqn. 5.9 are on the order of 3 mPa s and change by less than half an order of magnitude down to transition zone pressures. The dotted line shows the pressure-independent model of Dingwell et al. (2004)

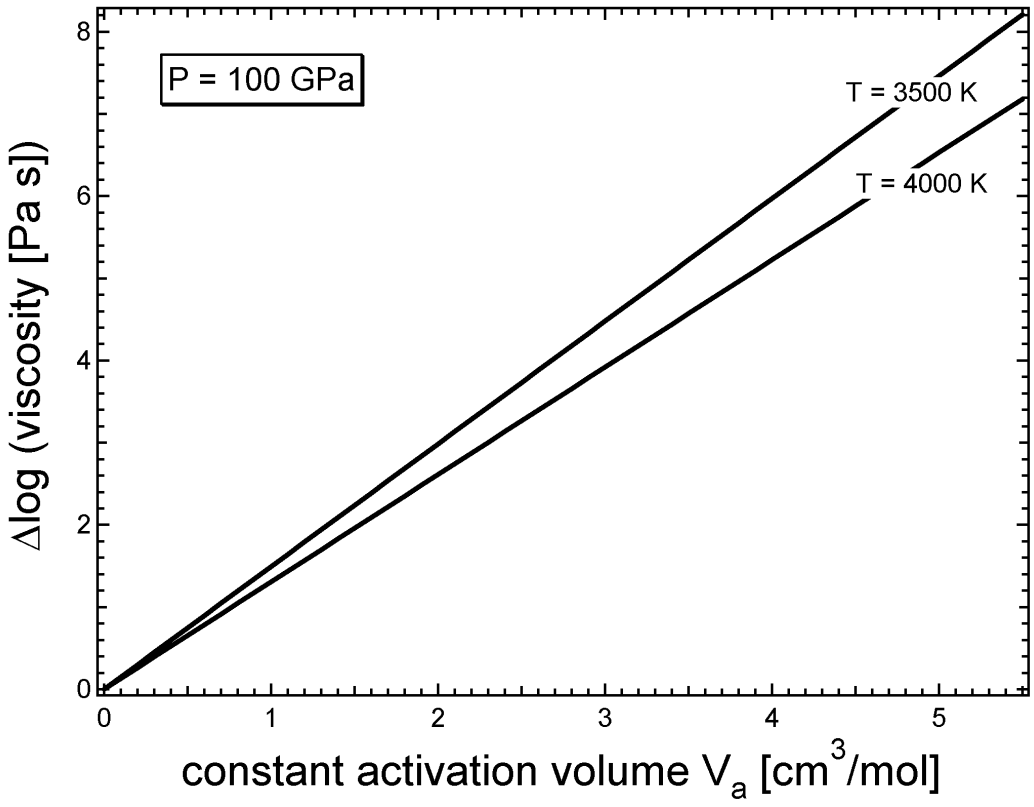

Figure 5.9: Change in viscosity extrapolated to 100 GPa at 3500 and 4000 K as a function of activation volume assuming that this parameter does not change with pressure. The conditions correspond to the base of a magma ocean of 1800 km depth. The figure indicates that melt viscosity could increase by several orders of magnitude over a pressure range of 100 GPa. The activation volume determined up to 9 GPa is $\sim$5 cm^3/mol, although this could decrease significantly at higher pressures. The negative pressure effect (9-13 GPa) has been ignored here.

should be similar for both the Arrhenian and non-Arrhenian models. At a constant activation volume of $\sim$5 cm^3/mol, as observed up to 9 GPa, the viscosity at the base of a 1800 km deep magma ocean would be up to seven orders of magnitude higher than inferred from a pressure independent model. The latter magnitude is not completely realistic, because the negative activation volume observed at 9-13 GPa has not been taken into account. Nonetheless, even significantly smaller positive activation volumes above 13 GPa would have a strong effect on viscosity when calculated for pressures of 100 GPa or more. Other investigations of transport properties of peridotite liquids at

higher pressures, such as studies of the self-diffusion of Si^{4+} and O^{2-} (Schmickler et al. 2004) will be required to explore the dynamics of terrestrial magma oceans at depths greater than 400 km.

5.4.4 Crystal Fractionation in a Magma Ocean

The physics of crystal fractionation or suspension in a molten mantle are quite complex and depend strongly on the fluid dynamics of a convecting magma ocean but also critically on the crystal size (Tonks and Melosh 1990, Solomatov and Stevenson 1993b). In particular, the vigour of convective flow (expressed as Rayleigh number, e.g. Rubie et al. 2003) is an important parameter, such that turbulent convection (at high Rayleigh numbers) may effectively inhibited crystal fractionation (Tonks and Melosh 1990). As shown above, the viscosity in the upper 400 km of a 1800 km deep peridotitic magma ocean is extremely low with values in the order 3 mPa s. Low viscosities support turbulent convection, because viscosity and Rayleigh number are inversely correlated. Solomatov and Stevenson (1993b) pointed out that strong turbulence is likely to occur at viscosities lower than $10^4 - 10^7$ Pa s. This may be interpreted to indicate that crystal fractionation in a shallow magma ocean may not have occurred because such viscosity values are not possible at transition zone pressures. Although the pressure dependence on magma ocean viscosities below a depth of 400 km is not very well constrained, it is unlikely that the viscosity of peridotite melt can reach such values even at conditions close to the core-mantle boundary. However, Solomatov and Stevenson (1993b) pointed out that the crystal size is a critical parameter in modelling fractionation or suspension in a magma ocean. Solomatov and Stevenson (1993a) argued that the likely crystal sizes in a magma ocean are close to a critical value of 10^{-2}-1 cm that enhances crystal

fractionation at pressures greater than 15 GPa. Solomatov (2000) however, reported that the crystal sizes increase with the square-root of viscosity. Thus, increasing viscosity with increasing pressure at significantly greater depth than 400 km may support crystal fractionation. Probably more important than the pure liquid viscosity is the rheological behaviour of a 'mush' of partial melt and crystals and crystal fractions of 70-80% may be sufficient to suppress the turbulence in a convecting magma ocean (Solomatov and Stevenson 1993b). However, the present data do not allow a detailed discussion on the likelihood of crystal fractionation, but the observed low viscosities do not exclude a priori the settling of crystals in a deep terrestrial magma ocean.

5.5 Conclusions

In-situ falling sphere viscometry has been performed on peridotite liquid up to 13 GPa and ∼2500 K. In order to overcome problems associated with viscosity marker spheres falling through a partially molten sample before super-liquidus temperatures can be reached in the experiments, we have developed a new capsule design, in which the sphere is initially contained in a small recessed region, at lower temperature than the main part of the sample. In addition, the sphere is embedded in a material having a similar chemical composition but a higher melting temperature than the sample peridotite. These developments result in spheres falling at superliquidus temperatures. This technique should also be applicable for other chemical systems and could be of great benefit for the investigation of all low viscosity melts at high pressure.

The viscosity of peridotite liquid first increases isothermally to 9-10 GPa but then decreases up to at least 13 GPa. This behaviour is almost identical to that of simi-

larly depolymerised $CaMgSi_2O_6$ liquid. The new data support the proposal that the effect of pressure on the viscosities of silicate liquid is strongly coupled to the degree of melt depolymerisation. Although there is no direct evidence, it appears likely that the negative pressure effect observed between 9-13 GPa is caused by cation coordination changes taking place in this pressure range. At still higher pressures, once the coordination changes are complete, the pressure dependence should be reversed to be positive, as a result of further melt compaction.

To account for the strong non-Arrhenian rheology of peridotite liquid, we described the available viscosity data, at conditions ranging from the glass-transition to superliquidus temperatures and pressures up to 13 GPa, by an empirical Vogel-Fulcher-Tamman (VFT) equation to which a pressure-dependent term has been added. This model describes the observed pressure dependence and reproduces experimentally determined viscosities well, but it cannot be used to extrapolate viscosities to pressures above 13 GPa.

The viscosity of a peridotitic magma ocean can be calculated to a depth of ∼400 km using the new results. Although the viscosity will depend on the absolute temperature (and magma ocean depth), changes in viscosity along a liquid adiabat are less than half an order of magnitude to 13 GPa or ∼400 km depth. Determination of viscosities at the base of a deep magma ocean requires further experimental and/or computational studies. The likelihood of crystal fractionation in a deep magma ocean is not determined by the presented data, but the latter may be used in the future for studies on the physics of crystal fractionation in a molten mantle.

Chapter 6

Implications for Magma Ocean Crystallisation

The investigation of liquidus phase relations of peridotite and chondrite compositions, which represent plausible magma ocean compositions, shows that Mg-silicate perovskite and probably Ca-silicate perovskite are the dominant phases that crystallise from a deep Hadean magma ocean, if the latter extends into the lower mantle. As deduced from the melting relations in the simple MgO-SiO_2 system, the temperature interval between the solidus and the liquidus of a magma ocean composition becomes increasingly larger with increasing pressure (above 26 GPa), because the eutectic composition most likely moves towards MgO. This implies that the depth interval over which crystallisation takes place is significantly larger in a deep magma ocean (e.g. >1000 km depth), compared with the crystallisation interval in a magma ocean that extends only to transition zone conditions. The phase relations in the simple MgO-SiO_2 system may be used to estimate crystallisation depths and sub-liquidus adiabats over a large proportion of the mantle.

The new high-pressure viscosity data for peridotite liquid have been used to derive an empirical model that enables magma ocean viscosities to be calculated to depths of ∼400 km. The extremely low viscosities in the upper ∼400 km of a magma ocean

may be interpreted to indicate that convective velocities are sufficiently high to keep crystals in suspension, and thus preclude crystal fractionation. However, the proposed increase in viscosity at significantly greater depths than 400 km may support fractional crystallisation of a magma ocean, because of the constraints of the viscosity on crystal sizes and the turbulence of convection. The new data, however, may be used for a more detailed investigation of magma ocean dynamics to determine the likelihood of crystal fractionation. The simple phase relations in the MgO-SiO_2 system would also allow the proportion of solids and liquids at a given pressure and temperature to be estimated based on the lever-rule. This may be used to constrain the rheological behaviour of a 'mush' of crystals and liquid depending on the magma ocean depth. This rheology is probably quite different from the that of pure liquid and may also determine the possibility for crystal fractionation.

The results of element partitioning show that the present day geochemistry of the upper mantle is not inconsistent with a chemically distinct reservoir in the lower mantle, that may have formed by crystal fractionation from a magma ocean. Based on the evolution of refractory lithophile element ratios, the amount of a potential Mg-silicate perovskite (MgPv) and Ca-silicate perovskite (CaPv) reservoir has been determined to be 13 wt% of the total mantle at maximum. This amount of fractionation is possible for a proportion of 96 wt% MgPv and 4 wt% CaPv. It is important to note, that the amount of possible fractionation is not significantly influenced by variations of the chemical composition of the magma ocean liquid. However, the MgPv/CaPv reservoir is likely not dynamically stable against solid-state mantle convection (Kellogg et al. 1999), because such a crystal accumulate is depleted in Fe and Ca relative to

the residual liquid. This indicates a lower density of the crystal reservoir compared with the overlying mantle after complete solidification. Nonetheless, even temporary mantle differentiation by fractional crystallisation of a magma ocean may have left behind geochemical signatures, as have been observed in ancient Archean rocks (e.g. Caro et al. 2003). Based on such indications and the likely density contrast between a MgPv-dominated crystal reservoir and the overlying mantle, it follows that crystal fractionation probably took place but that the resulting crystal accumulate was rehomogenised with the overlying mantle by subsequent solid-state mantle convection. If a crystal accumulate extended to depths close to the present-day core-mantle boundary, parts of the fractionated perovskite reservoir may have been stabilised against mantle convection by a phase-transformation to the denser post-perovskite structure (Murakami et al. 2004). By such a process, evidence of early mantle differentiation may be still preserved until the present day.

Independent of the path of solidification of a magma ocean, the capability of aluminum-bearing Mg-silicate perovskite to incorporate significant amounts of Fe^{3+}, even in chemical equilibrium with metallic iron, may have influenced the oxidation state of the Earth's mantle. The disproportionation of ferrous iron to ferric iron plus Fe-metal during the emplacement of a MgPv dominated lower mantle (or fractionated crystal reservoir) must have occurred, if the silicate Earth was in equilibrium with metallic liquids during core-formation and no other components, such as volatile species, could have been reduced instead. The physical separation of precipitated Fe-metal from the Fe_2O_3-component could have produced an oxygen enriched reservoir. Subsequent whole mantle convection may have increased the relative oxygen content of the bulk mantle,

and redistribution of some precipitated metal in the upper mantle may have raised the abundance of siderophile elements. An alternative oxidation mechanism possibly involved the reduction of volatile species followed by subsequent degassing of the reduced components. Both oxidation mechanisms are consistent with a relatively short time scale of mantle oxidation (e.g. Delano 2001).

Acknowledgments

First of all, I would like to thank Dan Frost for his enthusiasm in almost every situation and for his support, whenever it was necessary, especially in the last couple of months during writing up the thesis. I would also like to thank Dave Rubie for his support and, particularly, for his activity during Christmas 2004! Many thanks also to Falko Langenhorst and Catherine McCammon for the help with the $Fe^{3+}/\sum Fe$ determinations.

Mein Dank gebührt ebenfalls vielen anderen Personen am BGI, die das Leben und Arbeiten wesentlich einfacher und angenehmer machten: Vielen Dank an Heinz Fischer and Georg Hermannsdörfer für die unzähligen kleinen 'Gimmicks' (am besten sofort, natürlich!), ohne die diese Arbeit nicht möglich gewesen wäre. Ein besonderer Dank gilt natürlich auch Hubert Schulze und Oskar Leitner, die meine Proben 'gründlich aufpoliert' haben. Vielen Dank auch an Detlef Krauße für die Hilfe an der Mikrosonde und bei diversen Computerproblemen! Vergessen möchte ich natürlich nicht Petra Ständner, Lydia Kison-Herzing und Stefan Keyssner die mir den ein oder anderen organisatorischen Weg abgenommen haben. Vielen Dank an Euch alle!

Zu guter Letzt noch vielen Dank an Anne-Rose, Hasche, Martin und Annika. Auf Euch kann ich mich immer verlassen!

Bibliography

Abe, Y., Ohtani, E., Okuchi, T., Righter, K., and Drake, M. (2000). Water in the early Earth. In Canup, R. and Righter, K., editors, *Origin of the Earth and Moon*, pages 413–433. The Universtity of Arizona Press, Tuscon, USA.

Agee, C. B. (1990). A new look at differentiation of the Earth from melting experiments on the Allende meteorite. *Nature*, 346:834–837.

Agee, C. B. (1993). High-pressure melting of carbonaceous chondrite. *Journal of Geophysical Research*, 98, E3:5419–5426.

Agee, C. B., Li, J., Shannon, M. C., and Circone, S. (1995). Pressure-temperature phase diagram for the Allende meteorite. *Journal of Geophysical Research*, 100, B9:17725–17740.

Akber-Knutson, S. and Bukowinski, M. S. T. (2004). The energetics of aluminium solubility into $MgSiO_3$ perovskite at lower mantle conditions. *Earth and Planetary Science Letters*, 220:317–330.

Albarede, F., Blichert-Toft, J., Vervoort, J. D., Gleason, J. D., and Rosing, M. (2000). Hf-Nd isotope evidence for a transient dynamic regime in the early terrestrial mantle. *Nature*, 404(6777):488–490.

Allan, N. L., Du, Z. M., Lavrentiev, M. Y., Blundy, J. D., Purton, J. A., and van Westrenen, W. (2003). Atomistic simulation of mineral-melt trace-element partitioning. *Physics of the Earth and Planetary Interiors*, 139:93–111.

Andrault, D. (2003). Cation substitution in $MgSiO_3$ perovskite. *Physics of the Earth and Planetary Interiors*, 136:67–78.

Angell, C. A., Cheeseman, P. A., and Tamaddon, S. (1982). Pressure enhancement of ion mobilities in silicate liquids from computer simulation studies to 800 kbar. *Science*, 118:87–97.

Angell, C. A., Cheeseman, P. A., and Tamaddon, S. (1983). Water-like transport property anomalies in liquid silicates investigated at high-T and high-P by computer simulation techniques. *Bulletin de Mineralogie*, 106:87–97.

Asahara, Y., Kubo, T., and Kondo, T. (2004). Phase relations of a carbonaceous chondrite at lower mantle conditions. *Physics of the Earth and Planetary Interiors*, 143-144:421–432.

Ballhaus, C., Berry, R. F., and Green, D. H. (1991). High pressure experimental calibration of the olivine-orthopyroxene-spinel oxygen geobarometer: implications for the oxidation state of the upper mantle. *Contributions to Mineralogy and Petrology*, 107:27–40.

Beattie, P., Drake, M., Jones, J., Leeman, W., Longhi, J., McKay, G., Nielsen, R., Palme, H., Shaw, D., Takahashi, E., and Watson, B. (1993). Terminology for Trace-Element Partitioning. *Geochimica Et Cosmochimica Acta*, 57:1605–1606.

Behrens, H. and Schulze, F. (2003). Pressure dependence of melt viscosity in the system $NaAlSi_3O_8$-$CaMgSi_2O_6$. *American Mineralogist*, 88:1351–1363.

Belonoshko, A. B. and Dubrovinsky, L. S. (1995). Molecular dynamics of stishovite melting. *Geochimica et Cosmochimica Acta*, 59:1883–18891.

Blundy, J. D., Falloon, T. J., Wood, B. J., and Dalton, J. A. (1995). Sodium partitioning between clinopyroxene and silicate melts. *Journal of Geophysical Research*, 100 B8:15501–15515.

Blundy, J. D. and Wood, B. J. (1994). Prediction of crystal-melt partition coefficients from elastic moduli. *Nature*, 372:452–454.

Bolfan-Casanova, N. (2000). *The distribution of water in the Earth's mantle: an experimental and infrared spectroscopic study.* PhD thesis, Universtität Bayreuth, Germany.

Bolfan-Casanova, N., Keppler, H., and Rubie, D. C. (2000). Water partitioning between nominally anhydrous minerals in the MgO-SiO_2-H_2O system up to 24 GPa: implications for the distibution of water in the Earth's mantle. *Earth and Planetary Science Letters*, 182:209–221.

Bouhifd, A. M. and Jephcoat, A. P. (2003). The effect of pressure on partitioning of Ni and Co between silicate and iron-rich metal liquids: a diamond-anvil cell study. *Earth and Planetary Science Letters*, 209:245–255.

Bowen, N. L. and Anderson, O. (1914). The binary system MgO-SiO_2. *American Journal of Science*, 37:487–500.

Bowring, S. A. and Housh, T. (1995). The Earth Early Evolution. *Science*, 269(5230):1535–1540.

Boyd, F. R., England, J. L., and Davis, B. T. C. (1964). Effects of pressure on the melting and polymorphism of enstatite, $MgSiO_3$. *Journal of Geophysical Research*, 69:2101–2109.

Boyet, M., Blichert-Toft, J., Rosing, M., Storey, M., Telouk, P., and Albarede, F. (2003). ^{142}Nd evidence for early Earth differentiation. *Earth and Planetary Science Letters*, 214(3-4):427–442.

Brearley, M., Dickinson, J. E., J., and Scarfe, C. M. (1986). Pressure dependence of melt viscosities on the join diopside-albite. *Geochimica et Cosmochimica Acta*, 50:2563–2570.

Brice, J. C. (1975). Some thermodynamic aspects of the growth of strained crystals. *Journal of Crystal Growth*, 28:249–253.

Bryce, J. G., Spera, F. J., and Stein, D. J. (1999). Pressure dependence of self-diffusion in the $NaAlO_2$-SiO_2 system: Compositional effects and mechanisms. *American Mineralogist*, 84:345–356.

Burns, R. G. (1993). *Mineralogical applications of crystal field theory*. Cambridge University Press, Cambridge, UK, 2nd edition edition.

Canil, D. (1994). Stability of clinopyroxene at pressure-temperature conditions of the transition zone. *Physics of the Earth and Planetary Interiors*, 86:25–34.

Canil, D. (2002). Vanadium in peridotites, mantle redox and tectonic environments: Archean to present. *Earth and Planetary Science Letters*, 195:75–90.

Canil, D., O'Neill, H. S. C., Pearson, D. G., Rudnick, R. L., McDonough, W. F., and Carswell, D. A. (1994). Ferric iron in peridotites and mantle oxidation state. *Earth and Planetary Science Letters*, 123:205–220.

Caro, G., Bourdon, B., Birck, J. L., and Moorbath, S. (2003). Sm-146-Nd-142 evidence from Isua metamorphosed sediments for early differentiation of the Earth's mantle. *Nature*, 423:428–432.

Chen, C. H. and Presnall, D. C. (1975). The system Mg_2SiO_4-SiO_2 at pressures up to 25 kilobars. *American Mineralogist*, 60:398–406.

Chipman, J. (1926). The Soret effect. *J. Am. Chem. Soc.*, 48:2577–2589.

Cohen, M. H. and Turnbull, D. (1959). Molecular transport in liquids and glasses. *The Journal of Chemical Physics*, 31:1164–1169.

Corgne, A., Allan, N. L., and Wood, B. J. (2003). Atomistic simulations of trace element incorporation into the large site of $MgSiO_3$ and $CaSiO_3$ perovskites. *Physics of the Earth and Planetary Interiors*, 139:113–127.

Corgne, A., Liebske, C., Wood, B. J., Frost, D. J., and Rubie, D. C. (2004). Silicate

perovskite-melt partitioning of trace elements and geochemical signature of a deep perovskitic reservoir. *Geochimica et Cosmochimica Acta*, in press.

Corgne, A. and Wood, B. J. (2002). $CaSiO_3$ and $CaTiO_3$ perovskite-melt partitioning of trace elements: Implications for gross mantle differentiation. *Geophysical Research Letters*, 29(19):1903, doi: 10.1029/2001GL014398.

Cukierman, M. and Uhlmann, D. R. (1974). Effects of iron oxidation state on viscosity, Lunar composition 15555. *Journal of Geophysical Research*, 79:1594–1598.

Davis, B. T. C. and England, J. L. (1964). The melting of forsterite up to 50 kilobars. *Journal of Geophysical Research*, 69:1113–1116.

Delano, J. W. (2001). Redox history of the Earth's interior since 3900 Ma: Implications for prebiotic molecules. *Origins of Life and Evolution of the Biosphere*, 31:311–341.

Dingwell, D. B. (1989). Shear viscosities of ferrosilicate liquids. *American Mineralogist*, 74:1038 – 1044.

Dingwell, D. B. (1991). Redox viscometry of some Fe-bearing silicate melts. *American Mineralogist*, 76:1560–1562.

Dingwell, D. B., Courtial, C., Giordano, D., and Nichols, A. (2004). Viscosity of peridotite liquid. *Earth and Planetary Science Letters*, 226:127–138.

Drake, M. J., McFarlane, E. A., Gasparik, T., and Rubie, D. C. (1993). Mg-perovskite/silicate melt and majorite garnet/silicate melt partition coefficients in the system CaO-MgO-SiO_2 at high temperatures and pressures. *Journal of Geophysical Research*, 98 (E3):5427–5431.

Egerton, R. F. (1996). *Electron energy loss spectroscopy in the electron microscope*. Plenum, New York.

Eyring, H. (1936). Viscosity, plasticity, and diffusion as examples of absolute reaction rates. *Journal of Chemical Physics*, 4:283–291.

Farnan, I. and Stebbins, J. F. (1994). The nature the glass-transition in a silica-rich oxide. *Science*, 265:1206–1209.

Faxen, H. (1923). Die Bewegung einer starren Kugel längs der Achse eines mit zäher Flüssigkeit gefüllten Rohres. *Arkiv för Matematik, Astronomi och Fysik*, 17:1–28.

Fei, Y. and Bertka, C. M. (1999). Phase transitions in the Earth's mantle and mantle mineralogy. In Fei, Y., Bertka, C., and Mysen, B., editors, *Mantle Petrology: Field observation and high pressure experimentation: A tribute to Francis R. (Joe) Boyd*, volume Special Publication No.6, pages 189–207. The Geochemical Society.

Finger, L. W., Hazen, R. M., and Prewitt, C. T. (1991). Crystal structures of $Mg_{12}Si_4O_{19}(OH_2)$ (phase B) and $Mg_{14}Si_5O_{22}$ (phase AnhB). *American Mineralogist*, 76:1–7.

Frost, D. J. and Langenhorst, F. (2002). The effect of Al_2O_3 on Fe-Mg partitioning between magnesiowüstite and magnesium silicate perovskite. *Earth and Planetary Science Letters*, 199:227–241.

Frost, D. J., Liebske, C., Langenhorst, F., McCammon, C. A., Trønnes, R. G., and Rubie, D. C. (2004a). Experimental evidence for the existence of Fe-rich metal in Earth's lower mantle. *Nature*, 428:409–412.

Frost, D. J., Poe, B. T., Trønnes, R. G., Liebske, C., Duba, A., and Rubie, D. C. (2004b). A New Large-Volume 6-8 Multianvil System. *Physics of the Earth and Planetary Interiors*, 143-144:507–514.

Funakoshi, K., Kanzaki, M., Yasuda, A., Suzuki, A., Terasaki, H., and Yamashita, S. (2000). Viscosity measurement of albite melt under high pressure using an in-situ x-ray radiographic technique. In Manghnani, M., Nellis, W., and Nicol, M., editors, *Science and Technology of High Pressure, Proceedings of AIRAPT-17*. Universities Press, Hyderabad, India.

Galer, S. J. G. and Goldstein, S. L. (1991). Early Mantle Differentiation and Its Thermal Consequences. *Geochimica Et Cosmochimica Acta*, 55:227–239.

Gasparik, T. (1990). Phase relations in the transition zone. *Journal of Geophysical Research*, 95 (B10):15751–15769.

Gessmann, C. K. and Rubie, D. C. (2000). The origin of the depletions of V, Cr and Mn in the mantles of the Earth and Moon. *Earth and Planetary Science Letters*, 184(1):95–107.

Hart, S. R. and Zindler, A. (1986). In search of a bulk Earth composition. *Chemical Geology*, 57:247–267.

Herzberg, C., Gasparik, T., and Sawamoto, H. (1990). Origin of mantle preidotite: Constraints from melting experiments to 16.5 GPa. *Journal of Geophysical Research*, 95 (B10):15779–15803.

Hill, E., Wood, B. J., and Blundy, J. D. (2000). The effect of Ca-Tschermaks component on trace element partitioning between clinopyroxene and silicate melt. *Lithos*, 53:203–215.

Hinton, R. W. (1995). Ion microprobe analysis in geology. In Potts, P., Bowles, J., Reed, S., and Cave, M., editors, *Microprobe Techniques in Earth Sciences*, pages 235–289. Chapman and Hall, London.

Hinton, R. W. and Upton, B. G. J. (1991). The chemistry of zircon - variations within and between large crystals from syenite and alkali basalt xenoliths. *Geochimica et Cosmochimica Acta*, 55:3287–3302.

Hirose, K., Shimizu, N., van Westrenen, W., and Fei, Y. (2004). Trace element partitioning in Earth's lower mantle and implications for geochemical consequences of partial melting at the core-mantle boundary. *Physics of the Earth and Planetary Interiors*, 146:249–260.

Hofmann, A. W. (1988). Chemical differentiation of the Earth: the relationship between mantle, continental crust, and oceanic crust. *Earth and Planetary Science Letters*, 90:297–314.

Holzapfel, C. (2004). *Fe-Mg interdiffusion at high pressures in mineral phases relevant for the Earth's mantle*. PhD thesis, Universität zu Köln.

Holzheid, A., Sylvester, P., O'Neill, H. S. C., Rubie, D. C., and Palme, H. (2000). Evidence for a late chondritic veneer in the Earth's mantle from high-pressure partitioning of palladium and platinum. *Nature*, 406:396–399.

Irifune, T. (1994). Absence of an aluminous phase in the upper part of Earth's lower mantle. *Nature*, 370:131–133.

Irifune, T. (2002). Application of synchrotron radiation and Kawai-type apparatus to various studies in high-pressure mineral physics. *Mineralogical Magazine*, 66:769–790.

Ito, E. and Katsura, T. (1992). Melting of ferromagnesian silicates under the lower mantle conditions. In Syono, Y. and Manghnani, M., editors, *High-Pressure Research: Application to Earth and Planetary Sciences*, pages 315–322. American Geophysical Union, Washington D.C.

Ito, E., Kubo, A., Katsura, T., and Walter, M. J. (2004). Melting experiments of mantle materials under lower mantle conditions with implications for magma ocean differentiation. *Physics of the Earth and Planetary Interiors*, 143-144:397–406.

Ito, E. and Takahashi, E. (1987). Melting of peridotite at uppermost lower-mantle conditions. *Nature*, 328:514–517.

Ito, E. and Takahashi, E. (1989). Postspinel transformations in the system Mg_2SiO_4-Fe_2SiO_4 and some geophysical implications. *Journal of Geophysical Research*, 94 (B8):10637–10646.

Jamieson, J. C., Fritz, J. N., and Manghnani, M. H. (1982). Pressure measurement at high temperature in x-ray diffraction studies: Gold as primary standard. In Akimoto,

S. and Manghnani, M., editors, *High pressure research in geophysics*, pages 27–48. Center for Akademic Publications, Tokyo.

Javoy, M. (1995). The integral enstatite chondrite model of the Earth. *Geophysical Research Letters*, 22:2219–2222.

Kanzaki, M., Kurita, K., Fujii, T., Kato, T., Shimomura, O., and Akimoto, S. (1987). A new technique to measure viscosity and density of silicate melts at high pressure. In Manghnani, M. and Syono, Y., editors, *High-Pressure Research in Mineral Physics*, pages 195–200. America Geophysical Union, Washington, D.C.

Kato, T. and Kumazawa, M. (1985a). Effect of high pressure on the melting relation in the system Mg_2SiO_4-$MgSiO_3$, I, eutectic relation up to 7 GPa. *J. Phys. Earth*, 33:514–254.

Kato, T. and Kumazawa, M. (1985b). Garnet phase of $MgSiO_3$ filling the pyroxene-ilmenite gap at very high temperature. *Nature*, 316:803–805.

Kato, T. and Kumazawa, M. (1985c). Stability of phase B, a hydrous magnesium silicate to 2300°C at 20 GPa. *Geophysical Research Letters*, 12:534–535.

Kato, T. and Kumazawa, M. (1986). Melting and phase relation in the system Mg_2SiO_4 - $MgSiO_3$ at 20 GPa under hydrous conditions. *Journal of Geophysical Research*, 91 B9:9351–9355.

Kato, T. and Kumazawa, M. (1990). High pressure effect on melting relations in the system Mg_2SiO_4-$MgSiO_3$: Phase transitions in the constituent phases and differentiation by melting in the Earth's mantle. In Marumo, F., editor, *Dynamic Processes of material transport and transformation in the Earth's interior*, pages 277–308. Terra Scientific Publishing Company, Tokyo.

Kato, T., Nakata, N., Ohtani, E., and Onuma, K. (1998). Melting experiments on the forsterite - pyrope system at 8 and 13.5 GPa. *Physics of the Earth and Planetary Interiors*, 107:97–102.

Kato, T., Ohtani, E., Ito, Y., and Onuma, K. (1996). Element partitioning between silicate perovskite and calcic ultrabasic melt. *Physics of the Earth and Planetary Interiors*, 96:201–207.

Kato, T., Ringwood, A. E., and Irifune, T. (1988a). Constraints on element partition coefficients between $MgSiO_3$ perovskite and liquid determined by direct measurements. *Earth and Planetary Science Letters*, 90:65–68.

Kato, T., Ringwood, A. E., and Irifune, T. (1988b). Experimental determination of element partitioning between silicate perovskites, garnets and liquids: constraints on early differentiation in the mantle. *Earth and Planetary Science Letters*, 89:123–145.

Katsura, T. and Ito, E. (1989). The system Mg_2SiO_4 - Fe_2SiO_4 at high pressures and temperatures: precise determination of stabilities of olivine, modified spinel, and spinel. *Journal of Geophysical Research*, 94 B11:15663–15670.

Kawai, N. and Endo, S. (1970). The genaration of ultrahigh hydrostatic pressures by a split sphere apparatus. *Reviews in Scientific Instruments*, 41:1178–1181.

Kellogg, L. H., Hager, B. H., and van der Hilst, R. D. (1999). Compositional stratification in the deep mantle. *Science*, 283:1881–1884.

Keppler, H., McCammon, C. A., and Rubie, D. C. (1994). Crystal-Field and Charge-Transfer Spectra of $(Mg,Fe)SiO_3$ Perovskite. *American Mineralogist*, 79:1215–1218.

Kilinc, A., Carmichael, I. S. E., Rivers, M. L., and Sack, R. O. (1983). The ferric - ferrous ratio of natural silicate liquids equilibrated in air. *Contributions to Mineralogy and Petrology*, 83:136–140.

Kimura, K., Lewis, R. S., and Anders, E. (1974). Distribution of gold and rhenium between nickel-iron and silicate melts: implications for the abundance of siderophile elements on the Earth and Moon. *Geochimica et Cosmochimica Acta*, 38:683–701.

Kleine, T., Mezger, K., Palme, H., and Münker, C. (2004). The W isotope evolution of the bulk silicate Earth: constraints on the timing and mechanism of core formation and accretion. *Earth and Planetary Science Letters*, 228:109–123.

Kleine, T., Münker, C., Mezger, K., and Palme, H. (2002). Rapid accretion and early core formation on asteroids and the terrestrial planets from Hf-W chronometry. *Nature*, 418:952–954.

Kohlstedt, D., Keppler, H., and Rubie, D. C. (1996). Solubility of water in the α, β, and γ phases of $(Mg, Fe)_2SiO_4$. *Contributions to Mineralogy and Petrology*, 123:345–357.

Kress, V. C. and Carmichael, I. S. E. (1991). The compressibility of silicate liquids containing Fe_2O_3 and the effect of composition, temperature, oxygen fugacity and pressure on their redox states. *Contributions to Mineralogy and Petrology*, 108:82–92.

Kröger, F. A. and Vink, H. J. (1956). Relation between the concentration of imperfections in crystalline solids. *Solid State Physics*, 3:307–435.

Kubicki, J. D., Hemley, R. J., and Hofmeister, A. M. (1992). Raman and infrared study of pressure-induced structural changes in $MgSiO_3$, $CaMgSi_2O_6$ and $CaSiO_3$ glasses. *American Mineralogist*, 77:258–269.

Kushiro, I. (1976). Changes in viscosity and structure of melt of $NaAlSi_2O_6$ composition at high pressure. *Journal of Geophysical Research*, 81:6347–6350.

Kushiro, I., Yoder, J. R., and Mysen, B. O. (1976). Viscosities of basalt an andesite melts at high pressures. *Journal of Geophysical Research*, 81:6351–6356.

Lange, R. A. and Carmichael, I. S. E. (1987). Densities of Na_2O- K_2O - CaO - MgO - FeO - Fe_2O_3-Al_2O_3-TiO_2 -SiO_2 liquids: New measurements and derived partial molar properties. *Geochimica et Cosmochimica Acta*, 51:2931–2946.

Lauterbach, S., McCammon, C. A., van Aken, P., Langenhorst, F., and Seifert, F. (2000). Mössbauer and ELNES spectroscopy of $(Mg, Fe)(Si, Al)O_3$ perovskite: a

highly oxidised component of the lower mantle. *Contributions to Mineralogy and Petrology*, 138:17–26.

Lee, S. K., Cody, G. D., Fei, Y., and Mysen, B. O. (2004). Nature of polymerization and properties of silicate melts and glasses at high pressure. *Geochimica et Cosmochimica Acta*, 68:4189–4200.

Lesher, C. E. and Walker, D. (1988). Cumulate maturation and melt migration in a temperature gradient. *Journal of Geophysical Research*, 93:10295–10311.

Li, J. and Agee, C. B. (1996). Geochemistry of mantle-core differentiation at high pressure. *Nature*, 381:686–689.

Li, J. and Agee, C. B. (2001). The effect of pressure, temperature, oxygen fugacity and composition of nickel and cobalt between liquid Fe-Ni-S alloy and liquid silicate: Implications for the Earth's core formation. *Geochimica et Cosmochimica Acta*, 65:1821–1832.

Li, Z. X. A. and Lee, C. T. A. (2004). The constancy of upper mantle fO_2 through time inferred from V/Sc ratios in basalts. *Earth and Planetary Science Letters*, in press.

Liebske, C., Behrens, H., Holtz, F., and Lange, R. A. (2003). The influence of pressure and composition on the viscosity of andesitic melts. *Geochimica et Cosmochimica Acta*, 67:473–485.

Liu, L. G. (1982). Chemical inhomogeneity of the mantle: geochemical considerations. *Geophysical Research Letters*, 9:124–126.

Liu, S. B., Stebbins, J. F., Schneider, E., and Pines, A. (1988). Diffusive Motion in Alkali Silicate Melts - an NMR-Study at High-Temperature. *Geochimica Et Cosmochimica Acta*, 52:527–538.

Liu, T. C. and Presnall, D. C. (1990). Liquidus phase relationships on the join anorthite-forsterite-quartz at 20 kbar with application to basalt petrogenesis and igneous saphirine. *Contributions to Mineralogy and Petrology*, 104:735–742.

Mao, H. K. and Bell, P. M. (1971). Behavior of thermocouples in the single-stage piston-cylinder apparatus. *Carnegie Institution of Washington Year Book*, 76:207–216.

McCammon, C. A. (1994). A Mössbauer milliprobe: practical considerations. *Hyperfine Interactions*, 92:1235–1239.

McCammon, C. A. (1997). Perovskite as a possible sink for ferric iron in the lower mantle. *Nature*, 387:694–696.

McCammon, C. A., Chaskar, V., and Richards, G. G. (1991). A technique for spatially resolved Mössbauer spectroscopy applied to quenched metallurgical slags. *Meas. Sci. Technol.*, 2:657–662.

McCammon, C. A., Lauterbach, S., Seifert, F., Langenhorst, F., and van Aken, P. A. (2004). Iron oxidation state in lower mantle mineral assemblages I. Emperical relations derived from high-pressure experiments. *Earth and Planetary Science Letters*, 222:435–449.

McCammon, C. A. and Ross, N. L. (2003). Crystal chemistry of ferric iron in $(Mg, Fe)(Si, Al)O_3$ majorite with implications for the transition zone. *Physics and Chemistry of Minerals*, 30:206–216.

McDonough, W. F. and Sun, S. s. (1995). The composition of the Earth. *Chemical Geology*, 120:223–253.

McFarlane, E. A., Drake, M. J., and Rubie, D. C. (1994). Element partitioning between Mg-perovskite, magnesiowüstite, and silicate melt at conditions of the Earth's mantle. *Geochimica et Cosmochimica Acta*, 58:5161–5172.

McMillan, P. F., Hemley, R. J., and Gillet, P. (1996). Vibrational spectroscopy of mantle minerals. In Dyar, M., McCammon, C., and Schaefer, M., editors, *Mineral Spectroscopy: A Tribute to Roger G. Burns*. The Geochemical Society, Special Publication No. 5.

McMillan, P. F. and Hofmeister, A. M. (1988). Infrared and raman spectroscopy. In Hawthorne, F., editor, *Spectroscopic methods in mineralogy and geology*, volume 18 of *Reviews in Mineralogy*, pages 99–160. Minalogical Scociety of America.

Melosh, H. J. (1990). Giant impacts and the thermal state of the early Earth. In Newsom, N. and Jones, J., editors, *Origin of the Earth*, pages 69–83. Oxford University Press, New York.

Miller, G. H., Stolper, E. M., and Ahrens, T. J. (1991a). The Equation of State of a Molten Komatiite. 1. Shock-Wave Compression to 36 GPa. *Journal of Geophysical Research-Solid Earth and Planets*, 96:11831–11848.

Miller, G. H., Stolper, E. M., and Ahrens, T. J. (1991b). The Equation of State of a Molten Komatiite. 2. Application to Komatiite Petrogenesis and the Hadean Mantle. *Journal of Geophysical Research-Solid Earth and Planets*, 96:11849–11864.

Mori, S., Ohtani, E., and Suzuki, A. (2000). Viscosity of the albite melt to 7 GPa at 2000 K. *Earth and Planetary Science Letters*, 175:87–92.

Morishima, H., Kato, T., Suto, M., Ohtani, E., Urakawa, S., Utsumi, W., Shimomura, O., and Kikegawa, T. (1994). The phase boundary between *alpha-* and *beta-* Mg_2SiO_4 determined by in situ x-ray observation. *Science*, 265:1202–1203.

Mosenfelder, J. L., Connolly, J. A. D., Rubie, D. C., and Liu, M. (2000). Strength of $(Mg, Fe)_2SiO_4$ wadsleyite determined by relaxation of transformation stress. *Physics of the Earth and Planetary Interiors*, 120:63–78.

Murakami, M., Hirose, K., Kawamura, K., Sata, N., and Ohishi, Y. (2004). Post-perovskite phase transition in $MgSiO_3$. *Science*, 304:855–858.

Mysen, B. O. (1991). Relation between structure, redox equlibria of iron, and properties of magmatic liquids. *Advances in Physical Chemistry*, 9:41–98.

Mysen, B. O. (2003). Physics and chemistry of silicate glasses and melts. *European Journal of Mineralogy*, 15:781–802.

Ohtani, E., Kato, T., and Sawamoto, H. (1986). Melting a model chondritic mantle to 20 GPa. *Nature*, 322:352–353.

Ohtani, E. and Kumazawa, M. (1981). Melting of forsterite Mg_2SiO_4 up to 15 GPa. *Physics of the Earth and Planetary Interiors*, 27:32–38.

Ohtani, E., Moriwaki, K., Kato, T., and Onuma, K. (1998). Melting and crystal-liquid partinioning in the system Mg_2SiO_4 - Fe_2SiO_4 to 25 GPa. *Physics of the Earth and Planetary Interiors*, 107:75–82.

Ohtani, E. and Sawamoto, H. (1987). Melting experiment on a model chondritic mantle composition at 25 GPa. *Geophysical Research Letters*, 14:733–736.

O'Neill, H. S. C. and Palme, H. (1998). Composition of the silicate Earth: Implication for Accretion and core formation. In Jackson, I., editor, *The Earth's mantle*, pages 3–182. Cambridge University Press, Cambridge, UK.

O'Neill, H. S. C., Rubie, D. C., Canil, D., Geiger, C. A., Ross II, C. R., Seifert, F., and Woodland, A. B. (1993). Ferric iron in the upper mantle and in transition zone assemblages: implications for relative oxygen fugacities in the mantle. *Geophysical Monographs, IUGG*, 74:73–88.

O'Neill, H. S. C. and Wall, V. J. (1987). The olivine-orthopyroxene-spinel oxygen geobarometer, the nickel precipitation curve, and the oxygen fugacity of the Earth's upper mantle. *Journal of Petrology*, 28:1169–1191.

Paterson, M. S. (1982). The Determination of Hydroxyl by Infrared-Absorption in Quartz, Silicate-Glasses and Similar Materials. *Bulletin De Mineralogie*, 105:20–29.

Persikov, E. S. and Bukhtiyarov, P. G. (1999). Influence of temperature and pressure on the viscosity of model and magmatic melts of acid-ultrabasic compositions. *Geochemistry International*, 37:1256–1267.

Poe, B. T., McMillan, P. F., Rubie, D. C., Chakraborty, S., Yarger, J., and Diefenbacher, J. (1997). Silicon and oxygen self-diffusivities in silicate liquids measured to 15 Gigapascals and 2800 Kelvin. *Science*, 176:1245–1248.

Poe, B. T., Romano, C., Zotov, N., Cibin, G., and Marcelli, A. (2001). Compression mechanisms in aluminosilicate melts: Raman and XANES spectroscopy of glasses quenched from pressures up to 10 GPa. *Chemical Geology*, 174:21–31.

Poirier, J. P. (1985). *Creep of crystals. High-temperature deformation processes in metals, ceramics and minerals*. Cambridge University Press, Cambridge, UK.

Presnall, D. C. and Gasparik, T. (1990). Melting of enstatite ($MgSiO_3$) from 10 to 16.5 GPa and the forsterite (Mg_2SiO_4) - Majorite ($MgSiO_3$) eutectic at 16.5 GPa: Implications for the origin of the mantle. *Journal of Geophysical Research*, 95 (B10):15771 – 15777.

Presnall, D. C. and Walter, M. J. (1993). Melting of forsterite, Mg_2SiO_4, from 9.7 to 16.5 GPa. *Journal of Geophysical Research*, 98 (B11):19777–19783.

Presnall, D. C., Weng, Y. H., Milholland, C. S., and Walter, M. J. (1998). Liquidus phase relations in the system MgO-Mg_2SiO_4 at pressures up to 25 GPa - constraints on crystallisation of molten Hadean mantle. *Physics of the Earth and Planetary Interiors*, 107:83–95.

Reed, S. J. B. (1975). *Electron microprobe analysis*. Cambridge Monographs on Physics. Cambridge Universtity Press, Cambridge, United Kingdom.

Reid, J. E., Poe, B. T., Rubie, D. C., Zotov, N., and Wiedenbeck, M. (2001). The self-diffusion of silicon and oxygen in diopside ($CaMgSi_2O_6$) liquid up to 15 GPa. *Chemical Geology*, 174:77–86.

Reid, J. E., Suzuki, A., Funakoshi, K. I., Terasaki, H., Poe, B. T., Rubie, D. C., and Ohtani, E. (2003). The viscosity of $CaMgSi_2O_6$ liquid at pressures up to 13 GPa. *Physics of the Earth and Planetary Interiors*, 139:45–54.

Richmond, N. C. and Brodholt, J. P. (1998). Calculated role of aluminum in the incorporation of ferric iron into magnesium silicate perovskite. *American Mineralogist*, 83:947–951.

Righter, K. and Drake, M. J. (1997). Metal-silicate equilibrium in a homogeneously earth: new results for Re. *Earth and Planetary Science Letters*, 146:541–553.

Righter, K. and Drake, M. J. (1999). Effect of water on metal-silicate partitioning of siderophile elements: a high pressure and temperature terrestrial magma ocean and core formation. *Earth and Planetary Science Letters*, 171:383–399.

Ringwood, A. E. (1979). *Origin of the Earth and Moon*. Springer Verlag, New York, USA.

Rubie, D. C. (1999). Characterising the sample environment in multianvil high-pressure experiments. *Phase Transitions*, 68:431–451.

Rubie, D. C., Gessmann, C. K., and Frost, D. J. (2004). Partitioning of oxygen during core formation of the Earth and Mars. *Nature*, 429:58–61.

Rubie, D. C., Melosh, H. J., Reid, J. E., Liebske, C., and Righter, K. (2003). Mechanisms of metal-silicate equilibration in the terrestrial magma ocean. *Earth and Planetary Science Letters*, 205:239–255.

Rubie, D. C., Ross, C. R., Carroll, M. R., and Elphick, S. C. (1993). Oxygen Self-Diffusion in $Na_2Si_4O_9$ Liquid up to 10 GPa and Estimation of High-Pressure Melt Viscosities. *American Mineralogist*, 78:574–582.

Russell, J. K., Giordano, D., and Dingwell, D. B. (2003). High-temperture limits on viscosity of non-Arrhenian silicate melts. *American Mineralogist*, 88:1390–1394.

Sack, R. O., Carmichael, I. S. E., Rivers, M., and Ghiorso, M. S. (1980). Ferric-ferrous equilibria in naturel silicate liquids at 1 bar. *Contributions to Mineralogy and Petrology*, 75:369–376.

Salters, V. J. M. and Stracke, A. (2004). Composition of the depleted mantle. *Geochemistry Geophysics Geosystems*, 5:Q05004, doi:10.1029/2003GC000597.

Scarfe, C. M., Mysen, B. O., and Virgo, D. (1987). Pressure dependence of the viscosity of silicate melts. In Mysen, B., editor, *Magmatic processes: physicochemical principles*, volume Special Publication No. 1, pages 504–511. The Geochemical Scociety.

Scarfe, C. M. and Takahashi, E. (1986). Melting of garnet peridotite to 13 GPa and the early history of the upper mantle. *Nature*, 322:354–356.

Schmickler, B., Rubie, D. C., Liebske, C., and Poe, B. T. (2004). Diffusion of Si, O, Mg, Ca, Ni and Co in peridotite liquid at high pressures. *Lithos*, 73:S98–S98.

Schmidt, M. W. and Ulmer, P. (2004). A rocking multianvil: Elimination of chemical segregation in fluid-saturated high-pressure experiments. *Geochimica et Cosmochimica Acta*, 68:1889–1899.

Schulze, F., Behrens, H., Holtz, F., Roux, J., and Johannes, W. (1996). The influence of H_2O on the viscosity of a haplogranitic melt. *American Mineralogist*, 81:1155–1165.

Shannon, M. C. and Agee, C. B. (1998). Perculation of core melts at lower mantle conditions. *Science*, 280:1059–1061.

Shannon, R. D. (1976). Revised effective ionic radii and systematic studies of interatomic distances in halides and chalcogenides. *Acta Crystallography*, A32:751–767.

Shaw, H. R. (1963). Obsidian - H_2O viscosities at 100 and 200 bars in the temperature range 700 to 900°C. *Journal of Geophysical Research*, 68:6337–6342.

Smyth, J. R. (1987). Beta-Mg_2SiO_4 - a potential host for water in the mantle. *American Mineralogist*, 72(11-12):1051–1055.

Solomatov, V. S. (2000). Fluid dynamics of a terrestrial magma ocean. In Canup, R. and Righter, K., editors, *Origin of the Earth and Moon*, pages 323–338. University of Arizona Press, Tucson, AZ, USA.

Solomatov, V. S. and Stevenson, D. J. (1993a). Kinetics of crystal growth in a terrestrial magma ocean. *Journal of Geophysical Research*, 98, E3:5407–5418.

Solomatov, V. S. and Stevenson, D. J. (1993b). Suspension in convective layers and style of differentiation of a terrestial magma ocean. *Journal of Geophysical Research*, 98 (E3):5375–5390.

Stebbins, J. F., Kroeker, S., and Andrault, D. (2001). The mechanism of solution of aluminum oxide in $MgSiO_3$ perovskite. *Geophysical Research Letters*, 28:615–618.

Stebbins, J. F. and McMillan, P. (1989). 5-Coordinated and 6-Coordinated Si in $K_2Si_4O_9$ Glass Quenched from 1.9 GPa and 1200°C. *American Mineralogist*, 74:965–968.

Stebbins, J. F. and Poe, B. T. (1999). Pentacoordinate silicon in high-pressure crystalline and glassy phases of calcium disilicate ($CaSi_2O_5$). *Geophysical Research Letters*, 26:2521–2523.

Suzuki, A. and Ohtani, E. (2003). Density of peridotite melts at high pressure. *Physics and Chemistry of Minerals*, 30:449–456.

Suzuki, A., Ohtani, E., Funakoshi, K., Terasaki, H., and Kubo, T. (2002). Viscosity of albite melt at high pressure and high temperature. *Physics and Chemistry of Minerals*, 29:159–165.

Takafuji, N., Hirose, K., Ono, S., Xu, F., Mitome, M., and Bando, Y. (2004). Segregation of core melts by permeable flow in the lower mantle. *Earth and Planetary Science Letters*, 224:249–257.

Takahashi, E. (1986). Melting of dry peridotite KLB 1 up to 14 GPa: Implications on the origin of peridotitic upper mantle. *Journal of Geophysical Research*, 91 (B9):9367–9382.

Takahashi, E. and Scarfe, C. M. (1985). Melting of peridotite to 14 GPa and the genesis of komatiite. *Nature*, 315:566–568.

Takahashi, E., Shimazaki, T., Tsuzaki, Y., and Yoshida, H. (1993). Melting study of a peridotite KLB-1 to 6.5 GPa, and the origin of basaltic magmas. *Philosophical Transactions of the Royal Society of London Series A*, 342:105–120.

Taura, H., Yurimoto, H., Kato, T., and Sueno, S. (2001). Trace element partitioning between silicate perovskites and ultracalic melt. *Physics of the Earth and Planetary Interiors*, 124:25–32.

Tinker, D. and Lesher, C. E. (2001). Self diffusion of Si and O in dacitic liquid at high pressures. *American Mineralogist*, 86:1–13.

Tinker, D., Lesher, C. E., Baxter, G. M., Uchida, T., and Wang, Y. (2004). High-pressure viscometry of polymerized silicate melts and limitations of the Eyring equation. *American Mineralogist*, 89:1701–1708.

Tonks, W. B. and Melosh, H. J. (1990). The physics of crystal settling and suspension in a turbulent magma ocean. In Newsom, N. and Jones, J., editors, *Origin of the Earth*, pages 151–174. Oxford University Press, New York.

Tonks, W. B. and Melosh, H. J. (1993). Magma ocean formation due to giant impacts. *Journal of Geophysical Research*, 98 (E3):5319–5333.

Trønnes, R. G. (2000). Melting relations and major element partitioning in an oxidized bulk Earth model composition at 15-26 GPa. *Lithos*, 53:233–245.

Trønnes, R. G. and Frost, D. J. (2002). Peridotite melting and mineral-melt partitioning of major and minor elements at 22 - 24.5 GPa. *Earth and Planetary Science Letters*, 197:117–131.

Utsumi, W., Funakoshi, K., Urakawa, S., Yamakata, M., Tsuji, K., Konishi, H., and Shimomura, O. (1998). SPring-8 beamlines for high pressure science with multi-anvil apparatus. *Rev. High Press. Sci. Technol.*, 7:1484–1486.

van Aken, P. A., Liebscher, B., and Styrsa, V. J. (1998). Quantitative determination of iron oxidations states in minerals using Fe $L_{2,3}$-edge electron energy-loss near-edge structure spectroscopy. *Physics and Chemistry of Minerals*, 25:323–327.

van der Hilst, R. D. and Karason, H. (1999). Compositional heterogeneity in the bottom 1000 kilometers of Earth's mantle: Toward a hybrid convection model. *Science*, 283:1885–1888.

van Westrenen, W., Wood, B. J., and Blundy, J. D. (2001). A predictive thermodynamic model of garnet-melt trace element partitioning. *Contributions to Mineralogy and Petrology*, 142:219–234.

Vohra, Y. K., Duclos, S. J., and Ruoff, A. L. (1987). High-pressure x-ray diffraction studies on rhenium up to 216 GPa (2.16 Mbar). *Physical Review B*, 36:9790–9792.

Waff, H. S. (1975). Pressure-induced coordination changes in magmatic liquids. *Geophysical Research Letters*, 2:193–196.

Walter, M. J. (1998). Melting of garnet peridotite and the origin of komatiite and depleted lithosphere. *Journal of Petrology*, 39:29–60.

Walter, M. J., Nakamura, E., Trønnes, R. G., and Frost, D. J. (2004). Experimental constraints on crystallization differentiation in a deep magma ocean. *Geochimica et Cosmochimica Acta*, 68:4267–4284.

Walter, M. J., Thibault, Y., Wei, K., and Luth, R. W. (1995). Characterizing experimental pressure and temperature conditions in multianvil apparatus. *Canadian Journal of Physics*, 73:273–286.

Williams, Q. and Jeanloz, R. (1988). Spectroscopic evidence for pressure-induced coordination changes in silicate glasses and melts. *Science*, 239:902–905.

Wolf, G. H., Durben, D. J., and McMillan, P. F. (1990). High-pressure raman spectroscopic study of sodium tetrasilicate ($Na_2Si_4O_9$) glass. *Journal of Chemical Physics*, 93:2280–2288.

Wood, B. J. (2000). Phase transformations and partitioning relations in peridotite under lower mantle conditions. *Earth and Planetary Science Letters*, 174:341–354.

Wood, B. J. and Blundy, J. D. (1997). A predictive model for rare earth element partitioning between clinopyroxene and anhydrous silicate melt. *Contributions to Mineralogy and Petrology*, 129:166–181.

Wood, B. J. and Rubie, D. C. (1996). The effect of alumina on phase transformations at the 660-kilometer discontinuity from Fe-Mg partitioning experiments. *Science*, 273:1522–1524.

Xu, Y., McCammon, C. A., and Poe, B. T. (1998). The effect of alumina on the electrical conductivity of silicate perovskite. *Science*, 282:922–924.

Xue, X. Y., Stebbins, J. F., Kanzaki, M., McMillan, P. F., and Poe, B. (1991). Pressure-induced silicon coordination and tetrahedral structural-changes in alkali oxide-silica melts up to 12 GPa - NMR, Raman, and infrared-spectroscopy. *American Mineralogist*, 76:8–26.

Yamamoto, T., Yuen, D. A., and Ebisuzaki, T. (2003). Substitution mechanism of Al ion in $MgSiO_3$ perovskite under high pressure conditions from first-principles calculations. *Earth and Planetary Science Letters*, 206:617–625.

Yarger, J., Smith, K. H., Nieman, R. A., Diefenbacher, J., Wolf, G. H., Poe, B. T., and McMillan, P. F. (1995). Al coordination changes in high pressure aluminosilicate liquids. *Science*, 270:1964–1967.

Zerr, A. and Boehler, R. (1993). Melting of $(Mg, Fe)SiO_3$ - perovskite to 625 kilobars: indication of a high melting temperature in the lower mantle. *Science*, 262:553–555.

Zerr, A. and Boehler, R. (1994). Constraints on the melting temperature of the lower mantle from high-pressure experiments on MgO and magnesiowüstite. *Nature*, 371:506–508.

Zerr, A., Diegeler, A., and Boehler, R. (1998). Solidus of Earth's deep mantle. *Science*, 281:243–245.

Zerr, A., Serghiou, G., and Boehler, R. (1997). Melting of $CaSiO_3$ perovskite to 430 kbar and first in-situ measurements of lower mantle eutectic temperatures. *Geophysical Research Letters*, 24:909–912.

Zhang, J. and Herzberg, C. (1994). Melting experiments on anhydrous peridotite KLB-1 from 5.0 to 22.5 GPa. *Journal of Geophysical Research*, 99 (B9):17729–17742.

Appendix A

Chemical Compositions of Coexisting Phases

Table A.1: Run S3224

	S 3224 (fertile peridotite)			
	MgPv		**Mj**	
	n=15	2σ	n=11	2σ
SiO_2	55.55	0.51	48.43	0.93
TiO_2	0.38	0.03	0.04	0.02
Al_2O_3	3.56	0.21	14.04	0.59
Cr_2O_3	0.36	0.09	0.66	0.38
FeO^{total}	4.97	0.25	4.67	0.23
MnO	0.14	0.05	0.17	0.05
MgO	35.22	0.76	27.77	0.30
CaO	1.11	0.36	4.62	0.35
NiO	0.05	0.05	0.05	0.03
total	101.34		100.44	

Table A.2: Run S3237

	S3237 (fertile peridotite + Fe)					
	melt		**Fp**		**MgPv**	
	n=22	2σ	n=17	2σ	n=38	2σ
SiO_2	43.81	0.58	0.19	0.02	53.96	0.13
TiO_2	0.23	0.02	0.03	0.005	0.30	0.005
Al_2O_3	4.47	0.13	1.54	0.01	4.17	0.03
Cr_2O_3	0.29	0.03	0.35	0.01	0.18	0.00
FeO	15.48	0.53	23.45	0.12	5.61	0.07
MnO	0.14	0.02	0.12	0.01	0.06	0.004
MgO	31.11	1.04	73.86	0.09	35.13	0.12
CaO	4.52	0.39	0.08	0.004	1.15	0.04
Na_2O	0.08	0.01	0.05	0.003	0.01	0.002
NiO	0.03	0.02	0.05	0.01	0.01	0.004
total	100.15		99.71		100.60	

Table A.3: Run S3242

	melt		**MgPv (melt)**		**Fp (melt)**		**MgPv**		**Fp**		**Mj**		**CaPv**	
	n=8	2σ	n=15	2σ	n=16	2σ	n=10	2σ	n=7	2σ	n=10	2σ	n=6	2σ
SiO_2	45.90	1.21	55.56	0.91	0.18	0.03	53.86	0.50	0.55	0.43	47.44	1.04	43.91	3.44
TiO_2	0.25	0.03	0.34	0.02	0.02	0.02	0.31	0.04	0.04	0.02	0.04	0.03	0.17	0.07
Al_2O_3	4.93	0.34	4.17	0.12	1.73	0.04	4.81	0.31	1.61	0.11	15.52	1.28	2.69	0.20
Cr_2O_3	0.44	0.02	0.18	0.02	0.35	0.03	0.23	0.03	0.56	0.06	0.38	0.08	0.10	0.04
FeO^{total}	9.93	0.79	3.48	0.19	16.14	0.32	6.04	0.23	29.66	3.87	4.92	0.26	2.23	0.71
MnO	0.20	0.02	0.06	0.03	0.16	0.04	0.16	0.05	0.36	0.09	0.19	0.04	0.08	0.04
MgO	32.19	1.10	36.70	0.80	80.32	0.49	35.42	0.68	66.11	4.21	26.55	1.12	7.27	3.15
CaO	5.81	0.31	1.36	0.22	0.09	0.02	1.38	0.12	0.20	0.03	5.38	0.97	35.78	2.56
NiO	0.13	0.03	0.01	0.01	0.07	0.01	0.02	0.02	0.27	0.08	0.11	0.04	0.04	0.01
Na_2O	0.23	0.05	0.04	0.03	0.96	0.09	0.07	0.03	1.21	0.13	0.04	0.05	0.07	0.05
total	100.00		101.90		100.01		102.30		100.57		100.56		92.33	

Table A.4: Run H2026

H 2026 (fertile peridotite)						
	melt		**Fp**		**MgPv**	
	n=50	2σ	n=10	2σ	n=10	2σ
SiO_2	45.93	0.17	0.18	0.01	54.41	0.61
TiO_2	0.27	0.01	0.01	0.005	0.31	0.02
Al_2O_3	4.54	0.04	1.73	0.02	4.25	0.08
Cr_2O_3	0.46	0.01	0.62	0.01	0.37	0.02
FeO	7.44	0.14	10.10	0.06	3.33	0.16
MnO	0.14	0.01	0.10	0.01	0.05	0.03
MgO	37.08	0.27	84.94	0.52	36.04	0.46
CaO	3.40	0.13	0.04	0.003	0.78	0.07
Na_2O	0.05	0.004	0.04	0.003	0.01	0.01
NiO	0.23	0.01	1.04	0.02	0.04	0.03
total	99.54		98.80		99.60	

Table A.5: Run H2029

H2029 (chondrite analogue)						
	melt		**MgPv**		**Fp**	
	n=32	2σ	n=22	2σ	n=20	2σ
SiO_2	31.41	0.34	50.60	0.47	0.29	0.01
TiO_2	0.01	0.01	0.01	0.01	0.01	0.002
Al_2O_3	1.59	0.04	3.39	0.05	0.57	0.01
Cr_2O_3	0.61	0.01	0.45	0.02	0.86	0.01
FeO	41.40	0.46	14.67	0.49	60.60	0.30
MnO	0.48	0.02	0.21	0.02	0.45	0.01
MgO	15.79	0.28	28.93	0.19	32.25	0.30
CaO	3.20	0.08	1.06	0.04	0.09	0.004
Na_2O	0.69	0.02	0.14	0.01	0.95	0.01
NiO	0.81	0.03	0.20	0.04	2.99	0.02
total	96.00		99.68		99.07	

Table A.6: Run H2033a

	H2033a (Al-rich peridotite)							
	melt		**Fp**		**MgPv**		**Mj**	
	n=23	2σ	n=16	2σ	n=23	2σ	n=2	2σ
SiO_2	43.51	0.22	0.26	0.01	51.57	0.16	48.32	0.01
TiO_2	0.25	0.01	0.02	0.01	0.38	0.01	0.03	0.02
Al_2O_3	7.04	0.04	3.02	0.04	6.43	0.08	14.43	0.37
Cr_2O_3	0.40	0.01	0.59	0.02	0.34	0.01	0.37	0.02
FeO	9.01	0.05	13.14	0.11	4.28	0.11	3.34	0.22
MnO	0.18	0.01	0.13	0.02	0.07	0.02	0.10	0.03
MgO	34.10	0.10	80.86	0.37	35.21	0.14	28.31	0.30
CaO	4.07	0.02	0.06	0.01	0.87	0.06	4.45	0.07
Na_2O	0.10	0.004	0.06	0.01	0.01	0.00	0.07	0.01
NiO	0.24	0.01	1.15	0.02	0.05	0.02	0.05	0.04
total	98.90		99.29		99.20		99.47	

Table A.7: Run H2144 CI

	H2144 (CI mantle)			
	melt		**MgPv**	
	n=63	2σ	n=49	2σ
SiO_2	49.99	0.40	57.27	0.25
TiO_2	0.23	0.00	0.23	0.01
Al_2O_3	4.11	0.05	4.09	0.06
Cr_2O_3	0.36	0.01	0.28	0.02
FeO^{total}	7.81	0.29	3.39	0.08
MnO	0.16	0.01	0.06	0.01
MgO	33.70	0.17	37.53	0.24
CaO	3.76	0.12	0.81	0.04
NiO	0.21	0.01	0.06	0.01
Na_2O	0.07	0.01	0.01	0.00
total	100.40		103.73	

Table A.8: Run H2144 EC

	H2144 (EC mantle)					
	melt		**MgPv**		**St**	
	n=25	2σ	n=38	2σ	n=9	2σ
SiO_2	53.98	0.31	57.86	0.17	103.41	0.52
TiO_2	0.21	0.00	0.19	0.01	0.01	0.00
Al_2O_3	3.85	0.02	3.57	0.07	0.31	0.00
Cr_2O_3	0.37	0.01	0.28	0.02	0.01	0.01
FeO^{total}	8.95	0.10	4.41	0.11	0.25	0.01
MnO	0.18	0.01	0.09	0.01	0.01	0.01
MgO	27.56	0.23	36.34	0.21	0.05	0.01
CaO	4.90	0.05	1.04	0.08	0.03	0.00
NiO	0.27	0.01	0.10	0.02	0.02	0.01
Na_2O	0.13	0.01	0.02	0.00	0.00	0.00
total	100.40		103.88		104.11	

Appendix B

Trace Element Analyses

Table B.1: Element concentrations measured by SIMS (in ppm)

	S3237 (fertile peridotite+Fe^0)				**H2026 (fertile peridotite)**			
	melt (4)	±	MgPv (5)	±	melt (3)	±	MgPv (2)	±
Li					242	19	13	8
Be					92	19	3	3
B					83	19	2	2
Na	396	52	103	46				
Mg	203960	15803	175676	4622	207604	6935	191456	835
Al	25757	119	19927	657	23254	329	20399	205
Si	204732		253536		214688		25331	
P	309	39	198	25	168	23	47	9
K	114	31	61	24	38	7	5	1
Ca	27696	1797	7727	1492	18929	1483	4252	714
Ti	1245	107	1342	47	1263	45	1367	28
Cr	2409	145	1584	75	3526	61	2651	5
Mn	1290	52	489	47	1123	51	463	32
Fe	199402	18998	60028	6292	77750	1081	32967	
Ni								
Sc					554	17	1191	372
V								
Co					102	2	26	0
Ga					210	6	96	7
Ge								
Rb								
Sr	103	5	6	3	64	15	1	0
Y	97	10	71	3	88	2	64	8
Zr	86	14	200	38	102	5	210	44
Nb	81	9	56	4	80	2	50	7
Mo								
Ba	90	5	6	4	34	11	0.4	0.4
La	94	5	4	2	227	24	1	1
Ce	92	8	5	2	62	3	4	1
Nd	487	50	36	9	333	16	17	4
Sm	477	52	72	10	355	7	46	11
Eu	186	20	38	5	145	1	27	6
Lu	401	55	544	39	438	14	527	8
Hf	296	62	782	175	409	19	908	189
Pb	66	9	28	3	17	1	24	2
Th	114	23	5	2	93	4	3	2
U	103	23	15	3	91	2	11	4

numbers in parentheses are the numbers of analysis

Table B.1 continued

	H2029 (Chondrite)				H2033a (Al-rich peridotite)			
	melt (4)	±	MgPv (3)	±	melt (6)	±	MgPv (5)	±
Li	518	41	40	9	532	24	19	10
Be	963	94	14	6	311	70	6	2
B	1025	89	7	8	322	68	5	4
Na	6817	591	757	132	793	116	62	17
Mg	104264	2885	171929	153	164308	3076	180592	980
Al	10092	339	17421	155				
Si	151726		236525		203377		241056	
P	433	39	40	2	261	39	43	5
K	610	36	32	9	146	23	28	8
Ca	29721	1334	8940	386	22567	1319	4988	822
Ti	95	2	41	1	1036	142	1591	22
Cr	5743	208	3927	38	2807	102	2562	69
Mn	4857	86	1920	24	1271	86	606	47
Fe	518601	8846	173507	2707	75747	5880	43412	2574
Ni					2014	120	722	30
Sc	179	9	524	7	427	13	1127	240
V					36	0	38	1
Co	132	4	44	1	85	7	32	2
Ga	436	17	155	3	222	12	128	8
Ge					28	3	15	1
Rb					10	1	3	0.2
Sr	360	30	3	1	137	49	1	1
Y	186	6	100	5	80	4	72	8
Zr	84	1	100	3	90	20	215	39
Nb	372	22	33	3	65	21	82	5
Mo					18	5	10	1
Ba	432	31	3	2	201	97	4	4
La	182	17	2	0.5	94	40	1	1
Ce	330	30	7	0.3	94	40	8	4
Nd	209	16	6	0.4	474	169	36	19
Sm	281	18	19	2	451	128	72	20
Eu	268	16	27	2	177	45	39	9
Lu	180	3	181	9	396	68	576	15
Hf	162	3	241	10	341	81	929	203
Pb	97	12	8	1	17	6	24	6
Th	157	17	3	1	104	45	7	5
U	187	19	5	1	97	47	19	5

numbers in parentheses are the numbers of analysis